Doctoral Thesis

# Fermi Surface and Superconducting Properties of $Sr_2RuO_4$

by

YOSHIYUKI YOSHIDA

Department of Physics
Graduate School of Science
Osaka University

January, 2000

## Abstract

Since the discovery of superconductivity of $Sr_2RuO_4$, many interests have been attracted to its non-$s$ wave superconducting properties. $Sr_2RuO_4$ is the first non-cuprate superconductor with the same layered perovskite structure as in high-$T_c$ $La_{2-x}Sr_xCuO_4$. We succeeded in growing high-quality single crystals with the superconducting transition temperature $T_c$=1.52 K by using a floating-zone technique and measured the magnetoresistance, de Haas-van Alphen (dHvA) effect and specific heat to clarify the two-dimensional Fermi surface and superconducting properties.

First, we clarified the quasi-two dimensional electronic states in $Sr_2RuO_4$ from the magnetoresistance and dHvA effect experiments. The Yamaji effect, which is a characteristic feature for a quasi-two dimensional Fermi surface, is observed as the oscillatory angular dependence of the magnetoresistance. From the angular dependence of the dHvA amplitude, we also determined the Yamaji angle for three quasi-cylindrical Fermi surfaces named $\alpha$, $\beta$ and $\gamma$ to be 30.6° for the Fermi surface $\alpha$, about 30° for $\beta$ and 15.3° for $\gamma$. The cyclotron masses of sum and difference oscillatory components, $m^*_{\beta\pm\alpha}$ and $m^*_{\gamma\pm\alpha}$, are found to be highly different from $m^*_\beta + m^*_\alpha$ and $m^*_\gamma + m^*_\alpha$, respectively, for any field direction. The dHvA oscillation due to sums and differences is found to be not due to the magnetic interaction but to the chemical potential oscillation related to the quasi-two-dimensional Fermi surfaces. We determined the cyclotron mass for each Fermi surface: $3.3m_0$ for $\alpha$, $6.9m_0$ for $\beta$ and $17m_0$ for $\gamma$ for the field along [001]. These total masses correspond to the electric specific heat coefficient of 40 mJ/K$^2$·mol, which is in excellent agreement with 39.8 mJ/K$^2$·mol, determined from the specific heat experiment.

Next, the superconducting properties were studied by the specific heat measurement. A residual electronic specific heat coefficient $\gamma_{res}$ at $T \to 0$ in the superconducting state decreases with increasing the quality of the sample. The $\gamma_{res}$-value, estimated at 0 K, is 8 mJ/K$^2$·mol. We concluded that the existence of $\gamma_{res}$ is not intrinsic in superconductivity of $Sr_2RuO_4$. The temperature dependence of the electronic specific heat in the superconducting state $C_e$ shows the $T^2$ dependence at low temperatures. A characteristic power law of $C_e \sim T^2$ at low temperatures claims line nodes in the superconducting energy gap. This is direct evidence that the superconducting state of $Sr_2RuO_4$ is of the non-$s$ wave type. The Maki parameters $\kappa_2$ obtained from the specific heat in magnetic fields is found to be highly anisotropic, which was discussed on the basis of the quasi-two-dimensional electronic states and the existence of the paramagnetic effect.

# Contents

# *Chapter 1* Introduction

Strongly correlated electron systems attract strong interests with respect to the non-BCS superconducting property. For example, $UPt_3$, which is a typical heavy fermion compound, is well known to possess two superconducting transition temperatures and three phases called A, B and C in the superconducting phase diagram. [1] The existence of multiple superconducting phases is reminiscent of superfluid $^3$He and is very strong evidence that $UPt_3$ is a reduced symmetry superconductor. It was recently reported that $UPt_3$ is of odd parity in symmetry from the NMR-Knight shift and magnetization experiments. [2,3] High-$T_c$ cuprates also show the non-BCS behavior, which is known as a spin-singlet superconductor. The mechanism of high-$T_c$ superconductivity in the layered perovskite copper oxides is also one of the most important issues to be solved urgently.

$Sr_2RuO_4$ is an interesting superconductor, in which the superconductivity was discovered in 1994, to bridge the above two electron systems. [4] Its crystal structure with the tetragonal $K_2NiF_4$-type is the same as the high $T_c$-superconductor $La_{2-x}Sr_xCuO_4$, although the superconducting transition temperature $T_c$ is about 1 K, in contrast with $\sim$40 K in $La_{2-x}Sr_xCuO_4$ and the quasi-two-dimensional network of $CuO_2$ plane is replaced by the $RuO_2$ one.

The electronic state in the normal state is two-dimensional, reflecting the layered structural character. The temperature dependence of $\rho_{ab}$ is metallic, while that of $\rho_c$ is nonmetallic at room temperature, but becomes metallic below about 130 K. The Fermi surface consists of three kinds of cylindrical Fermi surfaces, named $\alpha$, $\beta$ and $\gamma$, by the quantum oscillation measurements and the results of energy band structure calculations. [5-7]. Their cyclotron masses are rather heavy, ranging from 3 to 12 $m_0$. $Sr_2RuO_4$ is therefore an enhanced Pauli paramagnet. Recently, an interesting phenomenon was observed in the Shubnikov-de Haas oscillation at an angle $\theta = 31°$, where $\theta$ denotes a tilt angle measured from the $c$-axis or the [001] direction.[8] The cyclotron effective masses of the sum and difference oscillatory components $m^*_{\beta\pm\alpha}$ are found to be highly different from $m^*_\beta + m^*_\alpha$, which is derived from the usual magnetic interaction. This phenomenon was explained on the basis of the dHvA oscillation derived under the constant total electron number, so-called chemical potential oscillation, which is in contrast with the Lifshiz-Kosevich formula derived under the constant chemical potential. [9]

In the superconducting state, the anisotropic pairing state was claimed from the specific heat and NMR experiments as in heavy fermion and high-$T_c$ superconductors. [11,10] There was found no coherence peak just below $T_c$ in the Ru-NMR-relaxation rate, indicating the non-$s$-wave superconductivity in $Sr_2RuO_4$. [10] The large residual density of states was observed at lower temperature from early Ru-NQR and specific heat measurement.[11,12] Recently, the result of $\mu$SR experiments indicates that the superconducting state is characterized by the breaking of time-reversal symmetry. [13] The recent Knight shift measure-

ments for $^{17}$O-NMR also revealed that the spin susceptibility for the field perpendicular to [001] remains unchanged through $T_c$.[14] This result is inconsistent with the spin-singlet pairing, where the spin susceptibility becomes zero as $T \rightarrow 0$.

Triplet superconductivity was theoretically discussed on the basis of two-dimensionality. There were proposed five possible $p$-wave pairing states without any gap nodes in a weak spin-orbit coupling scheme.[15] Several ideas have been proposed in order to explain the intrinsic residual density of states. Agterberg *et al.* proposed the orbital dependent superconductivity.[16] A part of the Fermi surfaces $(\alpha, \beta)$ or $\gamma$ opens up a large superconductivity gap, where Fermi surfaces $(\alpha, \beta)$ and $\gamma$ are considered to be domained by Ru $d_{xz,yz}$ and $d_{xy}$ orbitals, respectively. If the $\gamma_{\rm res}$-value is intrinsic, only the Fermi surface named $\gamma$ is expected to open up the energy gap. Theoretically, there is a possibility that the gap size of the Fermi surface $\gamma$ is one order of magnitude larger than those of the other two Fermi surfaces ($\alpha$, $\beta$). [16] If it is true, the electronic specific heat in the form of $C_e/T$ might be reduced at temperatures lower than 0.3 K. Recently, Miyake and Narikiyo have done anther theoretical approach, in which the exchange-enhanced ferromagnetic coupling dominated between the nearest-neighbor Ru spins leads to the spin-triplet wave function with a strong four-fold anisotropy in the superconducting gap.[17] The ratio between the maximum and minimum of the magnitudes of the gap is of the order of ten. The specific heat may be explained even if all the bands equally contribute to superconductivity.

To clarify the topology of the cylindrical Fermi surface in detail, we have grown a high-quality single crystal of $Sr_2RuO_4$ and have measured magnetoresistance and the de Haas-van Alphen (dHvA) effect. We have extended our investigations, especially on the chemical potential oscillation by measuring the de Haas-van Alphen oscillation at low temperatures and in high magnetic fields. There are still some open questions on the superconducting state. One of them is whether a residual density of states is intrinsic or not. The other is the to confirm experimentally the existence of the anisotropic energy gap. For this purpose, we have measured the specific heat in magnetic fields up to 20 kOe and at low temperatures down to 70 mK.

In this paper we will introduce a review of the low-dimensional electronic system, strongly correlated electron system and type II superconductor including an anisotropic superconductor in Chap. 2. Next, we will present the sample preparation of $Sr_2RuO_4$ and experimental methods in Chap. 3, and experimental results and discussion are presented in Chap. 4. Finally we will give a conclusion in Chap. 5.

# *Chapter 2* Review

## 2.1 Fermiology and strongly correlated electron systems

### *2.1.1 Fermi surface topology of low-dimensional electronic system*

1) Yamaji effect

Low-dimensional conductors are characterized by an anisotropy in the electrical conduction, strong electron-phonon coupling and strong Coulomb interaction. When the electron conduction along a certain crystallographic axis is larger than those in the other directions, we call it a quasi-one dimensional conduction. This occurs when the electron transfer energy $t_{\parallel}$ for a particular direction is much stronger than the other direction $t_{\perp}$. In organic conductors this occurs in linear polymers and charge-transfer salts composed of stacks of planar molecules.[18] For example, for polyacetylene the electron transfer energy between atoms is given by the resonance integral. For columnar arrays of molecular stacks, the overlap of $\pi$-orbitals on adjacent molecules within a stack is usually stronger than that between stacks. The transfer energy between molecules is given in the extended Hückel approximation by

$$t = \frac{1}{2}K(E_i + E_j)S_{ij}, \tag{2.1.1}$$

where $E_i$ is the energy level of the $i$th atomic orbital and $K$ is a constant which is conventionally taken as a value 1.75. $S_{ij}$ is the overlap integral between the atomic orbitals $i$ and $j$.

By applying the tight-binding band approximation to the quasi-one dimensional system, an energy band can be written as a cosine form

$$\epsilon(k_a) = 2t_a \cos(k_a a). \tag{2.1.2}$$

Here, we take the direction of highest conductivity as the a-axis, and $a$ and $k_a$ are the lattice spacing and the wave number of the a-axis, respectively. Figures 2.1.1(a) and (b) show the energy dispersion and the density of states $N(\epsilon)$ of the one-dimensional band with a bandwidth of $4t_a$. The Fermi surface for this quasi-one dimensional system is given by a pair of flat planes, as shown by solid lines in the $k_a - k_b$ plane in Fig 2.1.2, since the energy in this system is determined by $k_a$, and it is independent of both $k_b$ and $k_c$. When the inter-stack electron-transfer energy $t_b$ in the $b$-axis is not negligible, the energy dispersion is modified to

$$\epsilon(\boldsymbol{k}) = 2t_a \cos(k_a a) + 2t_b \cos(k_b b), \tag{2.1.3}$$

where $b$ and $k_b$ are the lattice spacing and the wave number of the b-axis, respectively. When the $t_b$ term is not negligible, the Fermi surface is warped, as shown by dashed lines in Fig 2.1.2. If $t_b$ is much less than $t_a$, e.g., less than 10% of $t_a$, the Fermi surface cannot

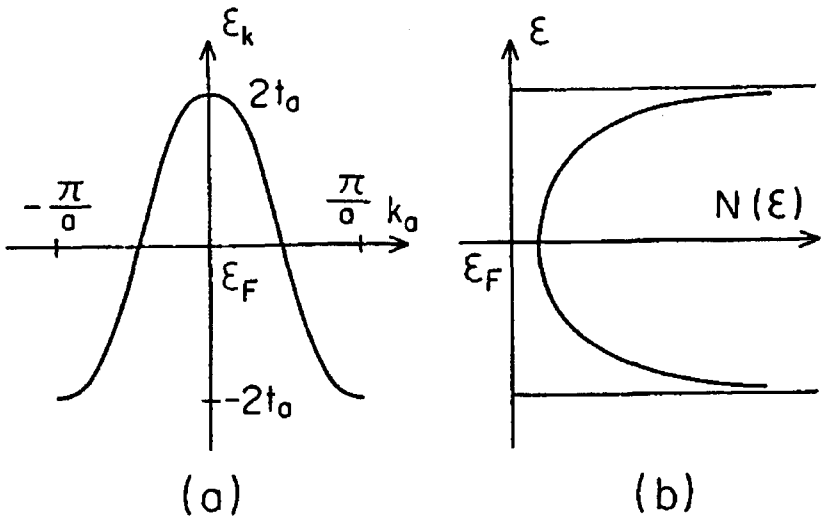


**Fig. 2.1.1** (a)Energy-dispersion relation for a one-dimensional electronic system in the tight-binding band model and (b)the corresponding density of the states.[18)]

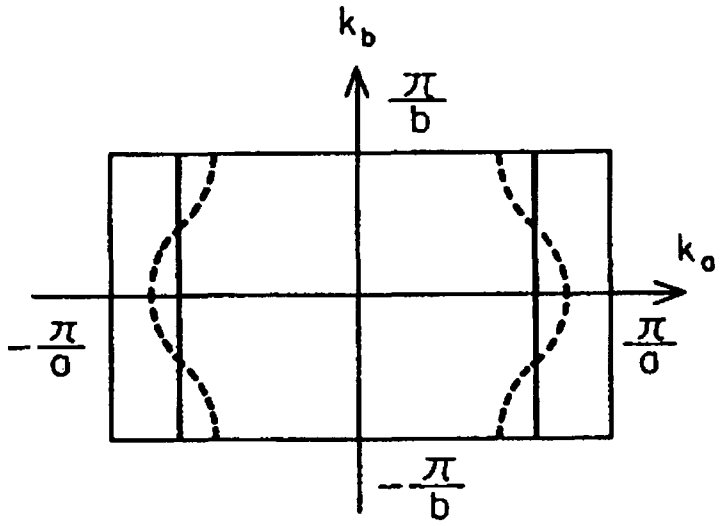


**Fig. 2.1.2** Fermi surface for the one-dimensional(solid lines) and quasi-one dimensional metal(dashed lines) in the $k_a - k_b$ plane.[18)]

be closed within the Brillouin zone, whereas if $t_b$ reaches more than about 30% of $t_a$, it is closed and has a shape something like a cylinder parallel to the $k_c$-axis (two-dimensional Fermi surface).

In general, the lattice is three-dimensional but it exhibits obvious anisotropy between the stacking direction and the perpendicular directions. Due to the interstack couplings, the crystal is not very rigid. Thus, changes in the electronic system affect the lattice, and electron-phonon interactions may be strong and result in Peierls instability.

In quasi-one dimensional metals, the electronic system tends to become unstable against perturbations with the wave number $2k_F$, $k_F$ being the Fermi wave number. As the result, the electron density is modulated predominantly with the wave number $2k_F$. In reality the electron system is more or less coupled to the underlying lattice system, and hence the lattice is also deformed when the electron density is perturbed through electron-phonon interactions. Then, the lattice becomes unstable against perturbations below the critical temperature. The critical temperature $T_{\rm P}$ for instability is given by

$$k_B T_{\rm P} = 1.13\epsilon_B \exp(\frac{-\pi\hbar^2\omega_0 v_F}{2g^2 a}), \tag{2.1.4}$$

where $\epsilon_B$ specifies the energy region where the electron distribution may be perturbed, $\omega_0$ is the normal-mode frequency in the absence of an electron-phonon interaction and $g$ is the electron-phonon coupling constant. Below $T_{\rm P}$ the lattice is modulated with the wave number $2k_F$ and the phase transition to this lattice is called a Peierls transition. In this structure Bragg reflections occur for electrons with the modulation wave number $2k_F$. As a consequence an energy gap, called the Peierls gap, appears in the electron energy spectrum; in this situation the quasi-one dimensional metal changes into an insulator.

The $2k_F$-modulated electronic structure corresponds to an electron density modulation, and hence is called a Charge Density Wave (CDW). Since this is usually accompanied by a lattice modulation through electron-phonon coupling, CDW is regarded as a collective mode of coupled electron and lattice systems. There are two kinds of CDW. One is the bond ordering wave in which the charge density is spatially modulated according to the distribution of bonding electrons. The bond alternation between single and double bonds splits the conduction band, resulting in an insulator. The other CDW is the charge ordering wave, where the charge density is determined from the distribution of conduction electrons. Hereafter, we discuss the latter case.

In quasi-one dimensional conductors, the Fermi surface consists of a pair of planar sheets. With increasing transverse interactions, the sheets are warped. If the degree of the warping is low, two unique features emerge. First, one sheet can be nested with the other by a shift of the wave vector $\boldsymbol{Q}$ given by $(\pm 2k_F, \pi/b, 0)$. The nesting is necessary to induce the CDW instability, but with increased warping the nesting is deteriorated, the CDW instability is weakened, and finally it is suppressed. The second characteristic feature of the weakly warped Fermi surface is its openness. In ordinary metals, the Fermi surfaces are mostly closed within the Brillouin zone, or the surface is opened and connected

to an adjacent zone in limited regions. For quasi-one dimensional metals a Fermi surface exists only in one direction; in other directions no surfaces, which confine electrons in momentum space, exist. Thus the Fermi surface is thoroughly open in two directions.

In quasi-two dimensional conductors, the Fermi surface consists of a cylindrical one with conducting planes. When the inter-plane electron transfer energy $t_c$ is not negligible, the Fermi surface is warped along a direction perpendicular to the conducting plane. For simplify, we assume the following band-energy relation:

$$\epsilon_{\boldsymbol{k}} = \frac{\hbar^2(k_x^2 + k_y^2)}{2m^*} - 2t_c \cos(ck_z), \tag{2.1.5}$$

where $k_x$ and $k_y$ are the conducting plane components of the crystal wave vector $\boldsymbol{k}$, and $c$ and $k_c$ are, respectively, the spacing between neighboring conducting plane and the component of the wave vector perpendicular to the plane; $m^*$ is the effective mass in the conduction plane. The transfer energy $t_c$ is assumed to be much smaller than the Fermi energy $\epsilon_F = \hbar^2 k_F^2/2m^*$, $k_F$ being the Fermi wave number in the case we can neglect $t_c$. An intersection of the Fermi surface in the extended Brillouin zone is shown in Fig 2.1.3.

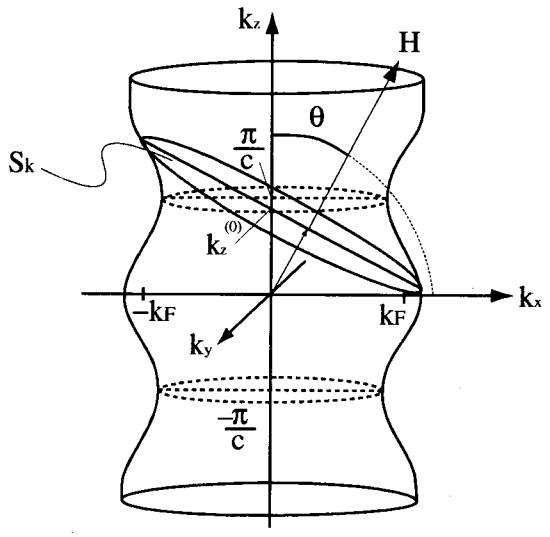


**Fig. 2.1.3** Fermi surface for quasi-two dimensional metal in the extended Brillouin zone.

The oscillatory angular dependence of the magnetoresistance is often observed in the quasi-two dimensional organic conductors.[19] Yamaji explained this phenomenon in terms of geometrical consideration.[20] This explanation is as follows. When the applied magnetic field $H$ is tilted by the angle $\theta$ from the $k_z$-direction to the $k_x$-direction, the trajectories of semiclassically closed orbits are given by the intersection $\boldsymbol{k}$-space of the Fermi surface with the plane normal to the field, as

$$k_x \sin\theta + k_z \cos\theta = p = k_z^{(0)} \cos\theta, \tag{2.1.6}$$

where $k_z^{(0)}$ denotes the point of intersection at the $k_z$-axis with the orbital plane. By employing the polar coordinates $k$ and $\phi$ in the $k_xk_y$ plane, the area $S_F(k_z)$ of orbit in the $\boldsymbol{k}$-space can be calculated with a precision of up to the first order of $\epsilon_F$ in the following way:

$$S_F(k_z) = \left\{\pi k_F^2 + 4\pi m^* t \cos(ck_z)\, J_0(ck_F \tan\theta)\right\}/\cos\theta, \tag{2.1.7}$$

where $k_F$ is the Fermi wave number having relations with $S_F = \pi k_F^2$ of a cylinder, $m^*$ is the effective mass, $t_c$ is transfer energy, $J_0$ is the Bessel function and $c$ is the lattice constant along the $z$-axis. Since $J_0(z)$ is proportional to $\cos(z - \pi/4)$ for $z \geq 1$, the $k_z$-dependent term in eq.(2.1.7) vanishes periodically for the value of $\theta_n$ satisfying

$$ck_F \tan\theta_n - \pi/4 = \pi n \tag{2.1.8}$$

with integer $n$.

This is noteworthy because for these values of $\theta_n$, all orbits on a corrugated Fermi surface have the same cross-sectional area of $\pi k_F^2/\cos\theta_n$. The peak angles in the oscillatory angular dependence of the magnetoresistance were explained by Yamaji on the basis of eq.(2.1.8). Therefore, the similar behavior are observed in the quantum oscillations. We will apply this relation to the dHvA effect and call "Yamaji effect".

2) Chemical potential oscillation

In principle, the two-dimensional (2D) system is simpler than the three-dimensional system, so that basic problems such as the magnetic breakdown (MB) effect can be investigated more thoroughly.[21] With this in mind, an experiment[22] and a numerical simulation[23] were performed on the de Haas-van Alphen (dHvA) effect of $\kappa$-$(ET)_2Cu(NCS)_2$, which is a simple and typical 2D MB system. We show in Fig. 2.1.4 the Fermi surface schematically. The results of both the experiment and simulation indicate the existence of an expected frequency component in the dHvA oscillation. It is a novel phenomenon which cannot be explained by existing theories. On the Fermi surface structure in Fig. 2.1.4, a small orbit is named $\alpha$, and a large orbit due to the MB is named $\beta$. These orbits produce the oscillation components of frequencies $f_\alpha$ and $f_\beta$, which are determined by the $k$-space areas enclosed by the respective orbits. In addition to these, components of frequencies $f_{\beta\pm\alpha} = f_\beta \pm f_\alpha$ are observed. As we take into account of MB, the $f_{\beta+\alpha}$ component is naturally expected, while the $f_{\beta-\alpha}$ component cannot be explained conventionally, The origin of $f_{\beta-\alpha}$ is as follows:

1) It is not due to MB in the conventional sense, because it is not permitted in the standard Falicov-Stachowiak (FS) theory[24] based on the network model.[25,26]

2) It is not due to the Shoenberg magnetic interaction (SMI),[28] because of its large magnitude in the dHvA experiment. In the simulation, no electron interaction is included, so that the possibility of SMI is excluded from the first.

3) It is not due to a Stark quantum interference effect,[27] because the $f_{\beta-\alpha}$ oscillation appears not in a transport coefficient but in a thermodynamic quantity.

The origin of $f_{\beta-\alpha}$ remained mystery. Recently, the interference though the chemical potential oscillation (CPO) is proposed to cause this unexpected frequency components in the quantum oscillation.[21] The chemical potential is not constant in the two-dimensional

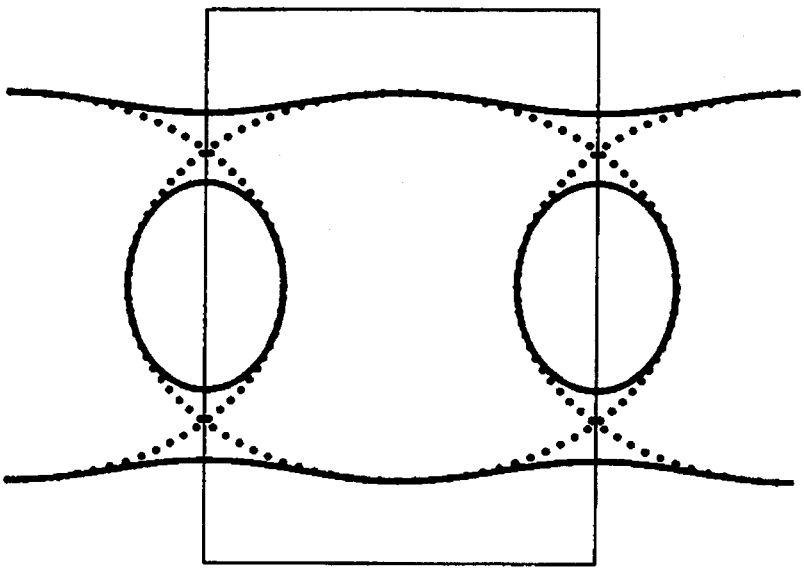

**Fig. 2.1.4** Schematic Fermi surface of $\kappa$-$(ET)_2Cu(NCS)_2$, which is a simple and typical 2D MB system.[21]

system, while it is constant in the usual three-dimensional system.

The thermodynamic potential $\Omega$ for a chemical potential $\mu$, and the free energy $F$ for a electron number $N$ are obtained as

$$\Omega(\mu, B) = \sum_i \Omega_i(\mu, B), \quad F(N, B) = \sum_i F_i(N, B). \tag{2.1.9}$$

Note that the total $\Omega$ is literally a simple sum of each $\Omega_i$, but the total $F$ is not so. The parameter $\mu$ in the formula for $F_i$ depends on $B$ and $N$, where $N$ is the total electron number, not the electron number of each band. Therefore, $F_i$ is affected by the existence of the other band through $\mu(N, B)$. On the other hand, all the parameters in the formula $\Omega_i$ are external parameters, so that $\Omega_i$ is not affected by the existence of the other band. The chemical potential $\mu(N, B)$ oscillates as a function of $B$. Thus, we designate the coupling among the bands through $\mu$ in the fixed $N$ case as the interference through CPO.

CPO affects all the thermodynamic quantities in the fixed $N$ case, because it affects the free energy. As an example, we consider the magnetization $M$ in the following. The

corresponding magnetization are derived as

$$M(\mu, B) = -\frac{\partial \Omega}{\partial B}, \quad M(N, B) = -\frac{\partial F}{\partial B}. \tag{2.1.10}$$

The dHvA effect is the oscillation of the magnetization. The numerical calculation of the dHvA oscillations for fixed $\mu$ and $N$ cases are shown in Fig. 2.1.5: while $M(\mu, B)$ is simply $M_\alpha(\mu, B) + M_\beta(\mu, B)$, the fast oscillation in $M(N, B)$ is clearly modulated by the slow one. This means that some new frequency components should exist in $M(N, B)$. Actually, in its Fourier spectrum shown in Fig. 2.1.6(a), both of the $f_{\beta \pm \alpha}$ components are present, while they do not exist in Fig. 2.1.6(b) for $M(\mu, B)$. From these, CPO is important for the 2D system when we discuss the dHvA experiments.

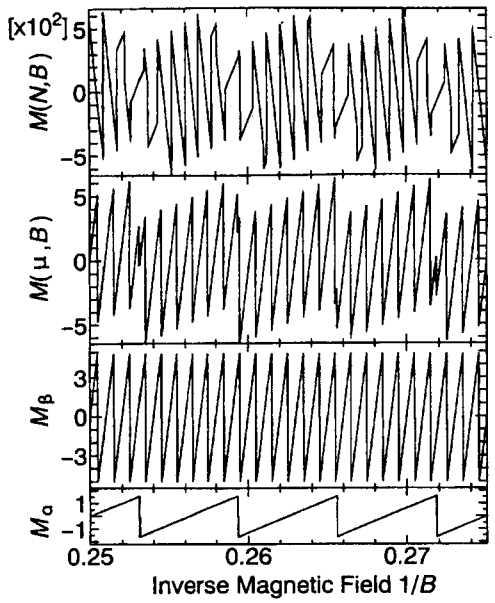


**Fig. 2.1.5** dHvA oscillations of the two-independent-band system. The lower three are for fixed $\mu$. The amplitudes for $M_\beta$ and $M_\alpha$ can be calculated analytically to be 1000 and 320 in this unit, which is reproduced in the numerical result.[21)]

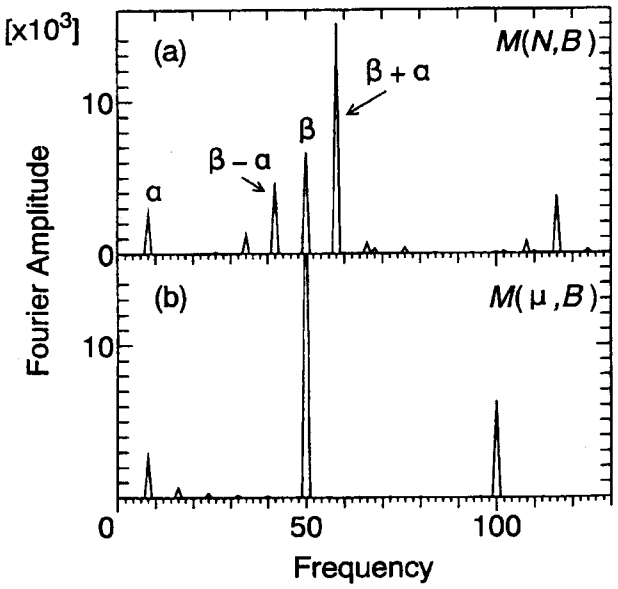


**Fig. 2.1.6** Fourier amplitudes of dHvA oscillation. (a)constant $N$ case and (b) constant $\mu$ case.[21)]

*2.1.2 Strongly correlated electron systems*

(1) $3d$ itinerant system

a) Hubbard model

The $3d$ electron system is often described as the following Hubbard model:

$$\mathcal{H} = \sum_{ij\sigma} t_{ij} c_{i\sigma}^{\dagger} c_{j\sigma} + U \sum_{j} n_{j\uparrow} n_{j\downarrow} \quad , \tag{2.1.11}$$

where $t_{ij}$ is a transfer integral, $U$ is Coulomb energy, $c_{i\sigma}^{\dagger}$ and $c_{i\sigma}$ are anihiation and creation operators of the $3d$ electron, respectively and $n_j$ is a number operator denoted as $n_j = c_j^{\dagger} c_j$. First term means a kinetic energy when the electron moves into the neighbor site, which is proportional to a band width. The second term is a Coulomb repulsion energy when the two electrons set on one site. Relative difference between two terms provides the different character for the $3d$ electron. For example, the $3d$-electron is localized on the lattice and shows a ferro- or antiferromagnetism when $U$ is extremely large. The limit of $U/t \gg 1$ provides the Heisenberg Hamiltonian $\mathcal{H} = -\sum_{ij} J_{ij} \boldsymbol{S}_i \cdot \boldsymbol{S}_j$, which is useful model for magnetism of an insulator, where $\boldsymbol{S}$ is spin of localized electron and $J_{ij}$ is an exchange interaction between $i$ and $j$ sites.

From the band theory and dHvA experiment, however, the $3d$ electron in Fe and Ni can be described as a one-body band picture in the ground state, that is, the $3d$ electron is itinerant. Here, the one-body band picture means the theory which treats the correlated electron under the mean field approximation. This contradiction was explained by Stoner.

b) Stoner's theory

The itinerant $3d$ electron system such as Fe or Ni shows the Curie-Weiss law at higher temperatures, just like a localized moment system, whereas they are described by the itinerant band picture, as mentioned above. Stoner added the molecular field theory into Pauli paramagnetism and introduced a spontaneous magnetization:

$$M = \chi_{\mathrm{p}}(H + \alpha M) \quad . \tag{2.1.12}$$

This is transformed into

$$\chi = \frac{M}{H} = \frac{\chi_{\mathrm{p}}}{1 - \alpha\chi_{\mathrm{p}}} \quad , \tag{2.1.13}$$

where $M$ is the magnetization, $\chi_{\mathrm{p}}$ is the Pauli susceptibility and $H$ is a magnetic field. The susceptibility is enhanced by the molecular field . Ferromagnetism appears when a denominator $1 - \alpha\chi_{\mathrm{p}} < 0$, namely,

$$2\alpha{\mu_{\mathrm{B}}}^2 D(E_{\mathrm{F}}) > 1 \quad , \tag{2.1.14}$$

where $\mu_{\mathrm{B}}$ is Bohr magneton and $D(E_{\mathrm{F}})$ is the density of states at the Fermi energy. This is called the Stoner's condition, and large $\alpha$ or $D(E_{\mathrm{F}})$ is a condition of ferromagnetism.

Difficulty of this theory is that it can not explain the Curie-Weiss law at higher temperatures and it gives a large Curie temperature.

c) SCR theory

Difficulty in the Stoner model was removed by Moriya on the basis of SCR (self consistent renormalization) theory, which treats the spin fluctuation in the band electron.

We show the spatial distribution of the spin density $\rho_s(r)$ in Fig. 2.1.7[29]. $\rho_s(r)$ can be expressed as a deviation between the wave functions of up-spin and down-spin, namely, $\rho_s(r) = |\psi_\uparrow(r)|^2 - |\psi_\downarrow(r)|^2$. In the Stoner model, there is no difference between the density of states of up- and down-spins above a Curie temperature $T_{\mathrm{c}}$, and thus $\rho_s(r) = 0$ (Fig. 2.1.7(a)). On the other hand, in the localized spin model, the magnitude of each moment is constant, but the spin takes any directions by the thermal motion above $T_{\mathrm{c}}$ (Fig. 2.1.7(b)). Considering the spin fluctuation effect, the spin at the finite temperature varies not only the direction but also its amplitude, as seen in Fig. 2.1.7(c).

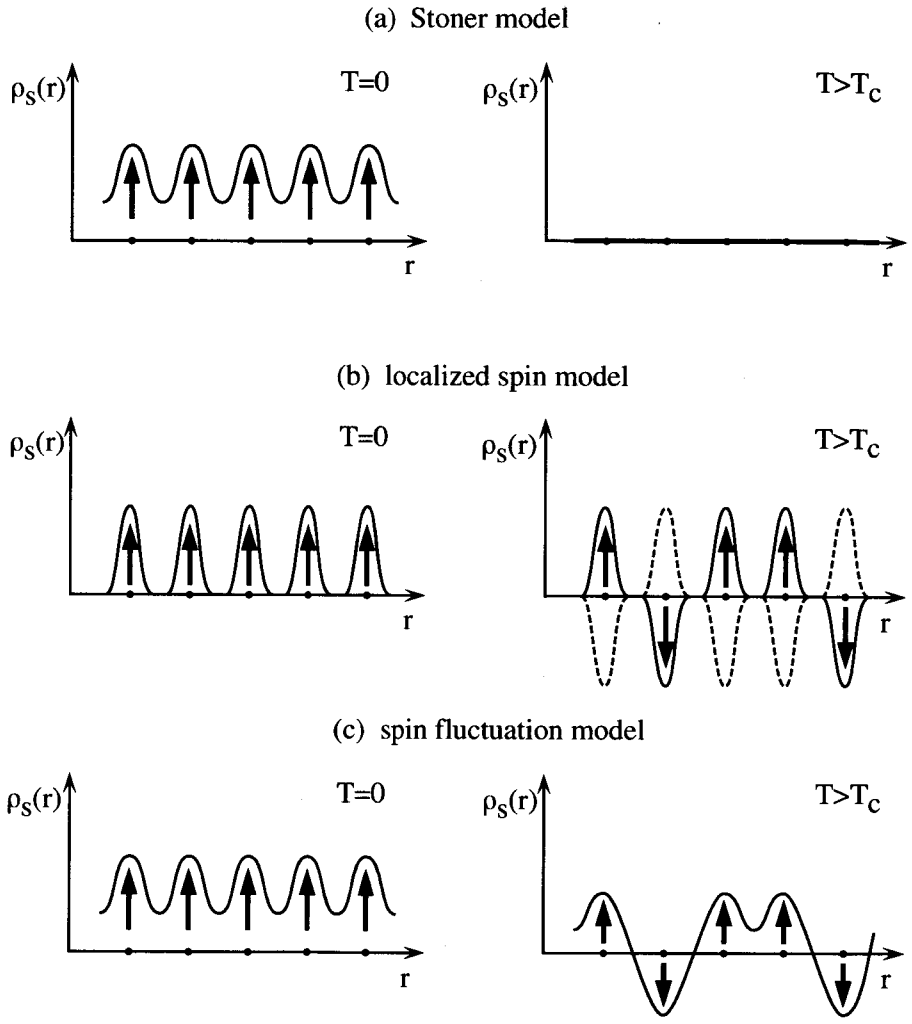


**Fig. 2.1.7** Spatial distribution of the spin density $\rho_s(r)$ for (a) Stoner model, (b) localized spin model and (c) spin fluctuation model. Left side is at $T = 0$, right side is $T > T_c$. In (a) $\rho_s(r)$ vanishes, in (b) $\rho_s(r)$ is unchanged and in (c) the local density of spin is slightly diminished at $T > T_c$[29].

(2) Heavy fermion aspects

a) RKKY interaction

The $4f$ electrons in the Ce atom are pushed into the interior of the closed $5s$ and $5p$ shells because of the strong centrifugal potential $l(l+1)/r^2$, where $l = 3$ holds for the $f$ electrons. This is a reason why the $4f$ electrons possess an atomic-like character in the crystal[30]. On the other hand, the tail of their wave function spreads to the outside of the closed $5s$ and $5p$ shells, which is highly influenced by the potential energy, the relativistic effect and the distance between the Ce atoms. This results in hybridization of the $4f$ electrons with the conduction electrons. These cause various phenomena such as valence fluctuations, Kondo lattice, heavy fermions, Kondo insulator and unconventional superconductivity.

The Coulomb repulsive force of the $4f$ electron $U$ at the same atomic site is so strong, for example $U \approx 5\,\mathrm{eV}$ in Ce compounds (see Fig. 2.1.8[31]). In Ce compounds the tail of

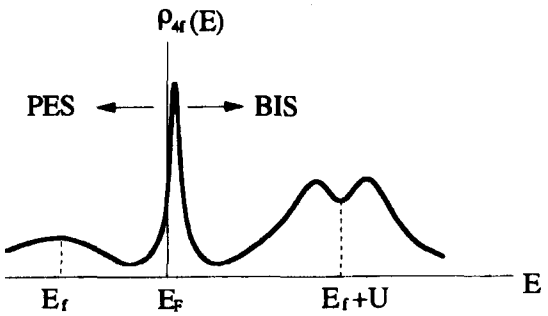


**Fig. 2.1.8** Density of states of $4f$ electrons in the Ce compound $(Ce^{3+})$[31].

the $4f$ partial density of states extends to the Fermi level even at room temperature, and thus the $4f$ level approaches the Fermi level in energy and the $4f$ electrons hybridize strongly with the conduction electron. This $4f$-hybridization coupling constant is denoted by $V$. When $U$ is strong and/or $V$ is ignored, the freedom of the charge in the $4f$electron is suppressed, while the freedom of the spin is retained, representing the $4f$-localized state. Naturally, the degree of localization depends on the level of the $4f$ electrons $E_f$, where larger $E_f$ helps to increase the localization. This situation is applied to most of the lanthanide compounds in which the Ruderman-Kittel-Kasuya-Yosida (RKKY) interaction plays a predominant role in magnetism. Therefore, the mutual magnetic interaction between the $4f$ electrons occupying different atomic sites cannot be of a direct type, such as in $3d$ metal magnetism, but should be indirect, which occurs only through the conduction electrons.

In the RKKY interaction, a localized spin $S_i$ interacts with a conduction electron with spin $s$, which leads to a spin polarization of the conduction electron. This polarization interacts with another spin $S_j$ localized on ion $j$ and therefore creates an indirect interaction between the spins $S_i$ and $S_j$. This indirect interaction extends to the far distance

and damps with a sinusoidal $2k_F$ oscillation. When the number of $4f$ electrons increases in such a way that the lanthanide element changes from Ce to Gd or reversely from Yb to Gd in the compound, the magnetic moment becomes larger and the RKKY interaction stronger, leading the magnetic order of which the ordering temperature roughly follows the de Gennes relation, $(g_J - 1)^2 J(J+1)$. Here $g_J$ and $J$ are the Landé $g$ factor and the total angular momentum, respectively.

b) Dense Kondo effect

Higher $V$ tends to enhance the hybridization of $4f$ electrons with conduction electrons, thus accelerating the delocalization of the $4f$ electrons[32]. The delocalization of $4f$ electrons tends to make the $4f$ band wide. When $E_f > V$, we have still better localization and expect the Kondo regime in the Ce (or Yb) compounds such as CeSb and $CeB_6$.

The Kondo effect was studied for the first time in a dilute alloy where a ppm range of the $3d$ transition metal is dissolved in a pure metal of copper. Kondo showed that the third-order scattering of the conduction electron with the localized moment of the transition impurity diverges logarithmically with decreasing temperature, and clarified the origin of the long standing problem, and it took ten years for theorists to solve this divergence problem at the Fermi energy.

The many-body Kondo bound state is now understood as follows. For the simplest case of no orbital degeneracy, the localized spin $S(\uparrow)$ is coupled antiferromagnetically with the spin of the conduction electron $s(\downarrow)$. Consequently the singlet state $\{S(\uparrow)\cdot s(\downarrow) \pm S(\downarrow)\cdot s(\uparrow)\}$ is formed with the binding energy $k_B T_K$. Here the Kondo temperature $T_K$ is the single energy scale. In other words, disappearance of the localized moment is thought to be due to the formation of a spin-compensating cloud of the conduction electron around the impurity moment.

Kondo-like behavior was observed in the lanthanide compounds, typically in Ce and Yb compounds[33-35]. For example, the electrical resistivity in $Ce_xLa_{1-x}Cu_6$ increases logarithmically with decreasing temperature for all the $x$-values[36], as shown in Fig. 2.1.9. The Kondo effect occurs independently at each Ce cite even in a dense system. Therefore, this phenomenon is called the dense Kondo effect. The Kondo temperature in the Ce (Yb) compound is large compared to the magnetic ordering temperature based on the RKKY interaction. For example, the Ce ion is trivalent ($J = 5/2$), and the $4f$ energy level is split into three doublets by the crystalline electric field, namely possessing the splitting energies of $\Delta_1$ and $\Delta_2$ (see Fig. 2.1.10[31]). The Kondo temperature is given as follows[37];

$$T_K^h = D\exp\left(-\frac{1}{3|J_{ex}|D(E_F)}\right) \quad \text{when} \quad T > \Delta_1, \Delta_2, \tag{2.1.15}$$

and

$$T_K = \frac{D^2}{\Delta_1\Delta_2} D\exp\left(-\frac{1}{|J_{ex}|D(E_F)}\right) \quad \text{when} \quad T < \Delta_1, \Delta_2. \tag{2.1.16}$$

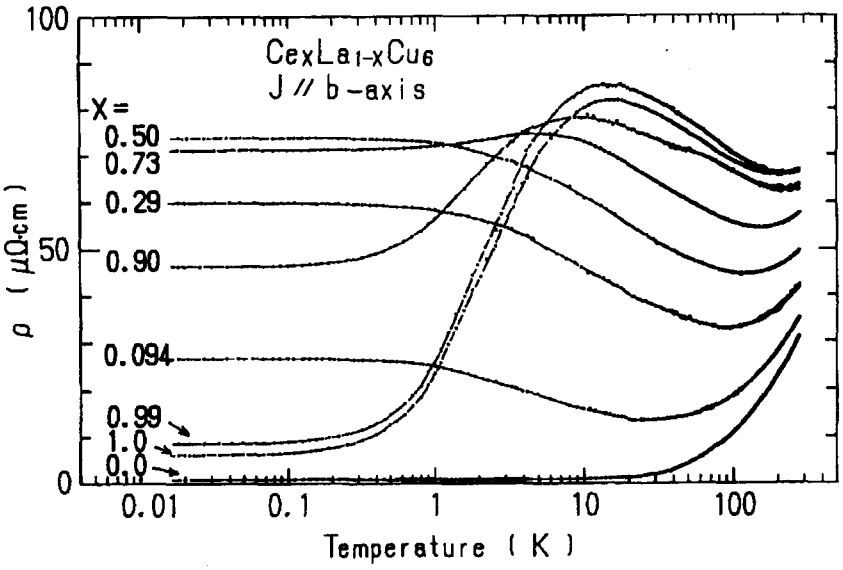


**Fig. 2.1.9** Temperature dependences of electrical resistivity of $La_{1-x}Ce_xCu_6$[36].

Here $D$, $|J_{ex}|$ and $D(E_F)$ are the band width, exchange energy and density of states, respectively. If we postulate $T_K \approx 5\,K$, for $D = 10^4\,K$, $\Delta_1 = 100\,K$ and $\Delta_2 = 200\,K$, the value of $T_K^h \approx 50\,K$ is obtained, which is compared to the $S = \frac{1}{2}$-Kondo temperature of $10^{-3}\,K$ defined as $T_K^0 = D\exp(-1/|J_{ex}|D(E_F))$. These large values of Kondo temperatures shown in eqs.(2.1.15) and (2.1.16) are due to the orbital degeneracy of the $4f$ levels. Therefore, the Kondo effect occurs from the room temperature. Even at low temperatures the Kondo temperature is not $T_K^0$ but $T_K$ shown in eq.(2.1.16).

On the other hand, the magnetic ordering temperature is about 5 K in the Ce (Yb) compound, which can be simply estimated from the de Gennes relation under the consideration of the Curie temperature of about 300 K in Gd. Therefore, it depends on the compound whether or not magnetic ordering occurs at low temperatures.

c) Heavy Fermion system

The ground state properties of dense Kondo system are interesting in magnetism, which is highly different from the dilute Kondo effect. In the Ce intermetallic compounds such as $CeCu_6$, Ce ions are periodically aligned whose ground state can not be a scattering state but becomes a coherent Kondo-lattice state. The electrical resistivity $\rho$ decreases steeply with decreasing temperature, following $\rho \approx AT^2$ with a large value of the coefficient $A$[38]. The $\sqrt{A}$-value is proportional to the effective mass of the carrier and thus inversely proportional to the Kondo temperature. Correspondingly, the electronic specific heat coefficient $\gamma$, which is proportional to the effective mass, roughly follows the simple relation $\gamma \approx 10^4/T_K$ (mJ/K$^2$mol) because the Kramers doublet of the $4f$ levels is changed

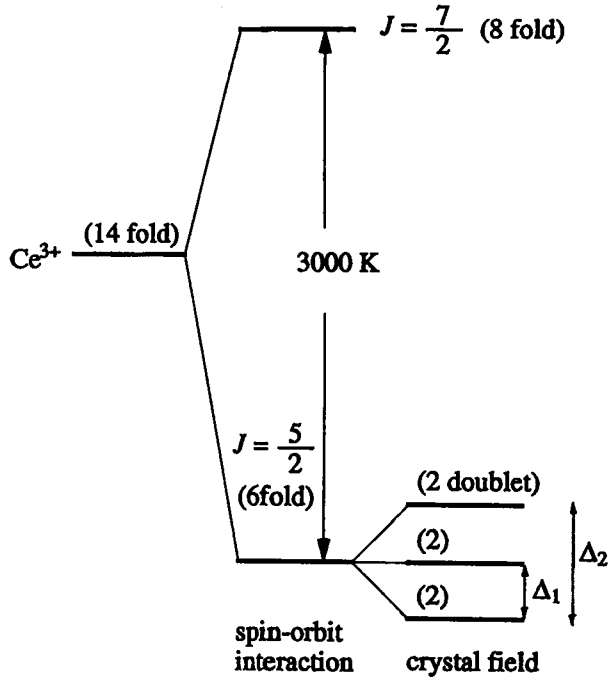


**Fig. 2.1.10** Level scheme of $4f$ electrons in $Ce^{3+}$[31].

into the $\gamma$ value in the Ce compound, namely $\gamma = R \ln 2/T_K = 5.8 \times 10^3/T_K$ (mJ/K$^2$mol). It reaches 1600 mJ/K$^2$mol for $CeCu_6$ because of a small Kondo temperature. The Ce Kondo-lattice compound with magnetic ordering also possesses the large $\gamma$ value even if the RKKY interaction overcomes the Kondo effect at low temperatures. For example, the $\gamma$ value of $CeB_6$ is 250 mJ/K$^2$mol, which is roughly one hundred times larger than that of $LaB_6$, 2.6 mJ/K$^2$mol. The conduction electrons possess large effective masses and thus move slowly in the crystal. Therefore the Kondo-lattice system is called a heavy fermion or a heavy electron system.

When $E_f < V$, the $4f$ electrons may tend to be delocalized, manifesting the valence fluctuation regime. $CeSn_3$ and CeNi were once called valence fluctuation compounds or mixed valent compounds. The magnetic susceptibility in these compounds follows the Curie-Weiss law at higher temperatures than room temperature, possessing the magnetic moment near $Ce^{3+}$, while it becomes approximately temperature-independent with decreasing temperature, showing a broad maximum around 150−200 K[39]. Thus the valence of Ce atoms seems to change from $Ce^{3+}$ into $Ce^{4+}$ (non-magnetic state) with decreasing temperature.

A significant correlation factor is thought to be the ratio of the measured magnetic susceptibility $\chi$, which is proportional to the effective mass for Pauli paramagnetism, to the one calculated from the observed $\gamma$ value[40]:

$$R_W \equiv \left(\frac{\pi^2 {k_B}^2}{\gamma}\right)\left(\frac{\chi(T=0)}{{\mu_B}^2 {g_J}^2 J(J+1)}\right) \quad . \tag{2.1.17}$$

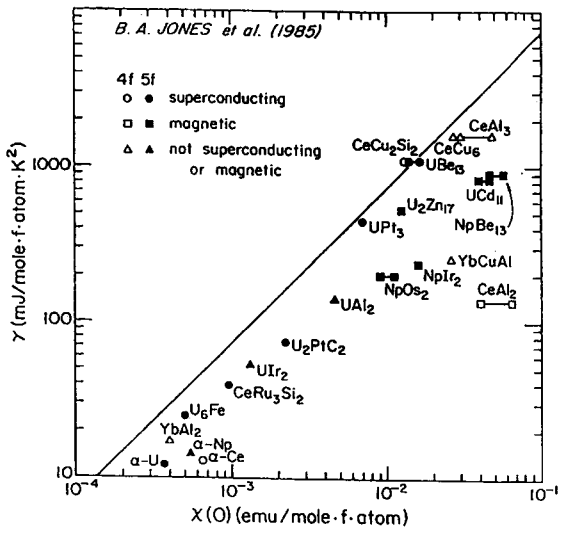


**Fig. 2.1.11** $\gamma$ versus $\chi$ plot[42].

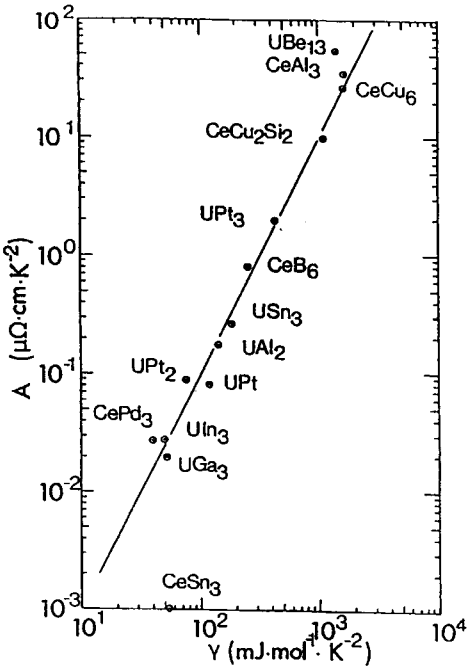


**Fig. 2.1.12** $A$ versus $\gamma^2$ plot[43].

This ratio $R_W$ is called Wilson ratio. Stewart evaluated $R_W$ for the heavy fermion system[41], as shown in Fig. 2.1.11[42]. He suggested that for the heavy fermion system $R_W$ is not 1 but 2. Kadowaki and Woods stressed the importance of a universal relationship between the $A$ and $\gamma$, as shown in Fig. 2.1.12[43]. They noted that the ratio $A/\gamma^2$ has a common value of $1.0\times10^{-5}\,\mu\Omega\cdot\mathrm{cmK^2mol^2/(mJ)^2}$. Thus obtained relations of $\rho \approx \mathrm{AT}^2$, $\chi \approx \chi(T=0)$ and $C = \gamma T$ at low temperatures are a characteristic feature of Fermi liquid. Namely, $\sqrt{A} \sim \chi(T=0) \sim \gamma$ is hold for the heavy fermion system.

d) Fermi surface study

Fermi surface studies are very important to know the ground state properties of the various magnetic compounds[44,45]. Even in the localized system, the presence of $4f$ electrons alters the Fermi surface through the $4f$ electron contribution to the crystal potential and through the introduction of new Brillouin zone boundaries and magnetic energy gaps which occur when $4f$ electron moments order. The latter effect may be approximated by a band-folding procedure where the paramagnetic Fermi surface, which is roughly similar to the Fermi surface of the corresponding La compound, is folded into smaller Brillouin zone based on the magnetic unit cell, which is larger than the chemical unit cell.

If the magnetic energy gaps associated with the magnetic structure are small enough, conduction electrons undergoing cyclotron motion in the presence of a magnetic field can tunnel through these gaps and circulate the orbits on the paramagnetic Fermi surface. If

this magnetic breakthrough (or breakdown) occurs, the paramagnetic Fermi surface may be observed in the de Haas-van Alphen (dHvA) effect even in the presence of magnetic order.

For Kondo lattice compounds with magnetic ordering, the Kondo effect is expected to have minor influence on the topology of the Fermi surface, representing that Fermi surfaces of the Ce compounds are roughly similar to those of the corresponding La compounds, but are altered by the magnetic Brillouin zone boundaries mentioned above. Nevertheless, the effective masses of the conduction carriers are extremely large compared to those of La compounds mentioned above. In this system a small amount of $4f$ electron most likely contributes to make a sharp density of states at the Fermi energy. Thus the energy band becomes flat around the Fermi energy, which brings about the large mass.

There is a big difference in $f$-electron character between the Kondo regime and the valence-fluctuation regime. One may be tempted to think that $4f$ electrons in a Kondo lattice compound with a large value of $T_{\mathrm{K}}$ are itinerant. This is true, as shown in $CeSn_3$. Recently, it has been furthermore clarified that $f$-electrons in a heavy fermion compound $CeRu_2Si_2$ as well as $UPt_3$ are itinerant at low temperatures.

## 2.2 Anisotropic superconductivity

### *2.2.1 Magnetic and thermodynamic properties of type II superconductors*

A macroscopic cylinder of type II superconductor placed in a field $H$ parallel to its axis exhibits the properties shown in Fig. 2.2.1. There are three regions of interest depending

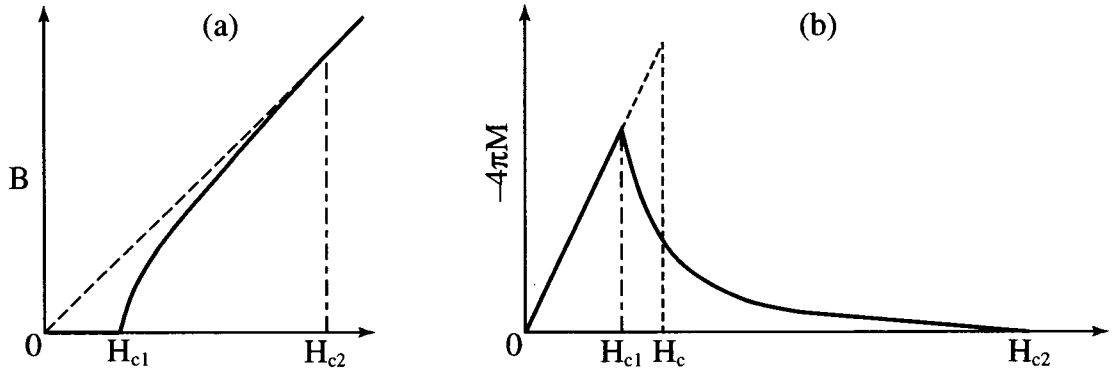


**Fig. 2.2.1** Schematic variation of (a) the induction $B$ versus the field $H$ and (b) the magnetization $-4\pi M$ versus the field $H$ in a type II superconductor.

on the value of the external field.

(1) The exclusion of the field from the sample (Meissner effect) is total only for values of field $H$ smaller than $H_{c1}$, where $H_{c1}$ is a critical field smaller than the thermodynamic critical field $H_c$, called the lower critical field.

(2) For $H_{c2} > H > H_{c1}$ flux gradually penetrates the sample, but even at the thermodynamic equilibrium this flux is small than in the normal state. A new state appears in which a lattice of quantization flux-enclosing supercurrent vortices (or filaments) is formed: this state is usually called the "mixed state" or the "vortex state".

(3) For $H > H_{c2}$ the specimen becomes normal and the transition at $H = H_{c2}$ is of the second order. The critical field $H_{c2}$ is greater than $H_c$ and can be very high, where $H_{c2}$ is called the upper critical field.

$H_{c1}$ and $H_{c2}$ vary with the temperature. This variation is shown in Fig. 2.2.2. The curves $H_{c1}(T)$ and $H_{c2}(T)$ are the boundaries of three regions (1) for which $B = 0$ (Meissner effect), (2) for which $B < H$ (mixed state), (3) for which $B = H$ (normal state). The magnetic properties of type II materials at a fixed temperature may be displayed as the induction inside the material (Fig. 2.2.1(a)) or as the magnetization (Fig.2.2.1(b)):

$$-4\pi M = H - B, \tag{2.2.1}$$

The concept of a "thermodynamic critical field" $H_c$ for a type II superconductor can be introduced:

$$F_n(T) - F_s(T) = \frac{H_c^2(T)}{8\pi}, \tag{2.2.2}$$

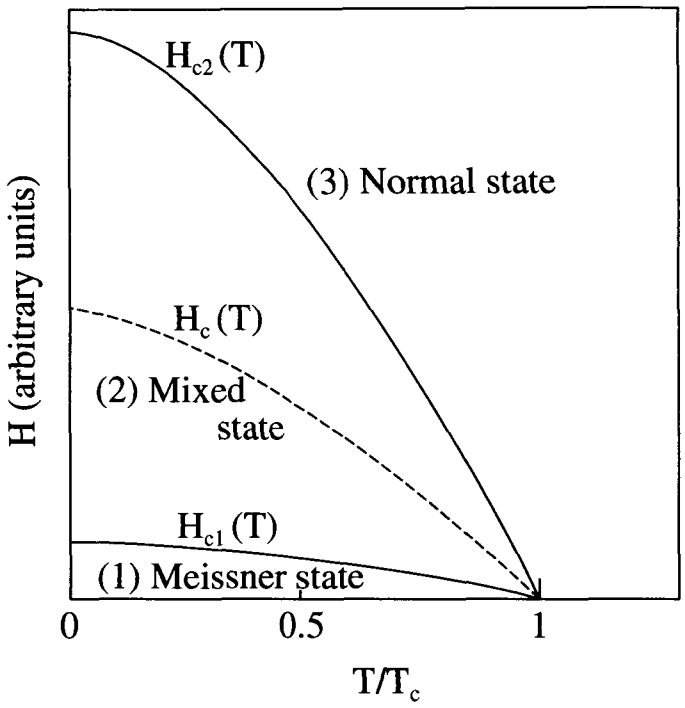


**Fig. 2.2.2** Schematic variation of the critical fields $H_{c1}$, $H_c$ and $H_{c2}$ versus the reduced temperature $T/T_c$ in a type II superconductor.

where $F_n(T)$ and $F_s(T)$ are the free energies of the normal and superconducting states in zero field, respectively. It must be emphasized that for a type I superconductor, this equation defines an actual critical field, while for a type II superconductor it defines only a convenient concept. The magnetic properties of type I and type II superconductors having the same shape and the same value of $H_c$ are compared in Figs. 2.2.1 and 2.2.2 where the dashed line gives the variation of the magnetization versus $H$ and of $H_c$ versus $T$ for the type I superconductor.

In the former, for $H < H_c$, $B = 0$ and it has the property that

$$\int_0^{H_c} M \mathrm{d}H = -\frac{H_c^2}{8\pi}. \tag{2.2.3}$$

A type II superconductor has the analogous property

$$\int_0^{H_{c2}} M \mathrm{d}H = -\frac{H_c^2}{8\pi}. \tag{2.2.4}$$

The Gibbs thermodynamic potential can be generally written as

$$G = F(B) - \frac{BH}{4\pi}, \tag{2.2.5}$$

The equilibrium value $B(H)$ being obtained from

$$\left(\frac{\partial G}{\partial B}\right)_H = 0. \tag{2.2.6}$$

In the normal state, where the induction $B_n$ is equal to $H$, the suitable form for $G$ is

$$G_n = F_n(0) + \frac{B^2}{8\pi} - \frac{BH}{4\pi}, \tag{2.2.7}$$

while $G_s$ is given by eq. (2.2.5) with $F(B) = F_s(B_s)$.

Then

$$\frac{\partial}{\partial H}(G_n - G_s) = \frac{B_s - B_n}{4\pi} = \frac{B_s - H}{4\pi}. \tag{2.2.8}$$

According to eq. (2.2.6),

$$\frac{\partial}{\partial H}(G_n - G_s) = \frac{\mathrm{d}}{\mathrm{d}H}(G_n - G_s) \tag{2.2.9}$$

and

$$\int_0^{H_{c2}} M \mathrm{d}H = |G_n - G_s|_0^{H_{c2}}. \tag{2.2.10}$$

For $H = H_{c2}$, $G_n = G_s$ and for $H = 0$, $G_n - G_s = F_n - F_s = -H_c^2/8\pi$ which proves eq. (2.2.4). Hence, the thermodynamic critical field can be found from the reversible magnetization curve by evaluating the area under the curve $M = f(H)$.

Another interesting feature of type II superconductors is that the transition at $H_{c1}(T)$ and $H_{c2}(T)$ are of the second order. There should be no latent heat and a discontinuity of the specific heat should exist. Several interesting thermodynamic relations have been deduced by Goodman for these transitions[46].

Defining the thermodynamic potential $G_i$ corresponding to phase $i$ ($i$ = (1), (2) and (3)), then

$$G_i = F_i(T, B_i) - \frac{B_i H}{4\pi}. \tag{2.2.11}$$

$G_i$ must be a minimum for fixed $H$ and $T$, so that

$$\left(\frac{\partial F}{\partial B_i}\right)_{H,T} = \frac{H}{4\pi}. \tag{2.2.12}$$

The corresponding entropy is

$$S_i = -\left(\frac{\partial G_i}{\partial T}\right)_H = -\frac{\partial F_i}{\partial T}. \tag{2.2.13}$$

At the equilibrium between the two phases $i$ and $j$, the field is equal to the critical field $H_{ij}(T)$, the thermodynamic potentials are equal, and if the transition is of the second order, there is no latent heat, and the entropies are also equal. As a result of this, it can be shown that the induction is continuous at the transition.

Calculating the variation of $G_i$ for a variation $\mathrm{d}H$ of the field along the curve $H = H_{ij}(T)$ i.e. for $\mathrm{d}H = (\mathrm{d}H_{ij}/\mathrm{d}T)\mathrm{d}T$:

$$\begin{aligned}\frac{\mathrm{d}G_i}{\mathrm{d}T} &= \frac{\mathrm{d}F_i}{\mathrm{d}T} - \frac{B_i}{4\pi}\frac{H_{ij}}{\mathrm{d}T} - \frac{H_{ij}}{4\pi}\frac{\mathrm{d}B_i}{\mathrm{d}T} \\ &= \frac{\partial F_i}{\partial T} + \frac{\partial F_i}{\partial B_i}\frac{\mathrm{d}B_i}{\mathrm{d}T} - \frac{B_i}{4\pi}\frac{\mathrm{d}H_{ij}}{\mathrm{d}T} - \frac{H_{ij}}{4\pi}\frac{\mathrm{d}B_i}{\mathrm{d}T} \\ &= -S_i - \frac{B_i}{4\pi}\frac{\mathrm{d}H_{ij}}{\mathrm{d}T}.\end{aligned} \tag{2.2.14}$$

In establishing eq. (2.2.14), eqs. (2.2.12) and (2.2.13) have been used. On the transition curve $H = H_{ij}(T)$. $G_i \equiv G_j$, i.e. $\mathrm{d}G_i/\mathrm{d}T \equiv \mathrm{d}G_j/\mathrm{d}T$. If there is no latent heat, $S_i \equiv S_j$, so that

$$B_i \equiv B. \tag{2.2.15}$$

Let us now calculate the discontinuity of specific heat. For a fixed $H$ in the phase $i$

$$C_i = T\left(\frac{\partial S_i}{\partial T}\right)_H. \tag{2.2.16}$$

Along the equilibrium curve $H = H_{ij}(T)$, the total derivative of the entropy is

$$\frac{\partial S_i}{\partial T} = \left(\frac{\partial S_i}{\partial T}\right)_H + \left(\frac{\partial S_i}{\partial H}\right)_T \frac{\mathrm{d}H_{ij}}{\mathrm{d}T}. \tag{2.2.17}$$

As there is no latent heat, $S_i \equiv S_j$ along the curve $H = H_{ij}(T)$ and

$$\frac{\mathrm{d}S_i}{\mathrm{d}T} = \frac{\mathrm{d}S_j}{\mathrm{d}T}. \tag{2.2.18}$$

The discontinuity in the specific heat is

$$C_j - C_i = T\left(\frac{\partial S_j}{\partial T}\right)_H - T\left(\frac{\partial S_i}{\partial T}\right)_H \tag{2.2.19}$$

$$= T\frac{\mathrm{d}H_{ij}}{\mathrm{d}T}\left[\left(\frac{\partial S_i}{\partial T}\right)_T - \left(\frac{\partial S_j}{\partial T}\right)_T\right] \tag{2.2.20}$$

The derivative $\partial S_i/\partial H$ can be written as

$$\left(\frac{\partial S_i}{\partial H}\right)_T = \left(\frac{\partial S_i}{\partial B_i}\right)_T \left(\frac{\partial B_i}{\partial H}\right)_T = -\frac{\partial^2 F_i}{\partial B_i \partial T}\left(\frac{\partial B_i}{\partial H}\right)_T \tag{2.2.21}$$

$$= -\frac{1}{4\pi}\left(\frac{\partial H}{\partial T}\right)_{B_i}\left(\frac{\partial B_i}{\partial H}\right)_T, \tag{2.2.22}$$

where eqs.(2.2.12) and (2.2.13) have been used.

On the other hand $\mathrm{d}H_{ij}/\mathrm{d}T$ is given by

$$\frac{\mathrm{d}H_{ij}}{\mathrm{d}T} = \left(\frac{\partial H}{\partial T}\right)_{B_i} + \left(\frac{\partial H}{\partial B_i}\right)_T \frac{\mathrm{d}B}{\mathrm{d}T}, \tag{2.2.23}$$

where $dB/dT = dB_i/dT = dB_j/dT$ is the variation of $B$ along the equilibrium curve (see eq. (2.2.15).

The combination of expression eqs. (2.2.22) and (2.2.23) yields

$$\left(\frac{\partial S_i}{\partial H}\right)_T = -\frac{1}{4\pi}\frac{dH_{ij}}{dT}\frac{\partial B_i}{\partial H} + \frac{1}{4\pi}\frac{dB}{dT} \tag{2.2.24}$$

and the discontinuity of specific heat is given by

$$C_j - C_i = \frac{T}{4\pi}\left(\frac{dH_{ij}}{dT}\right)^2\left[\left(\frac{\partial B_j}{\partial H}\right)_T - \left(\frac{\partial B_i}{\partial H}\right)_T\right]. \tag{2.2.25}$$

This relation is in fact a generalization of Ehrenfest's formula.

A number of conclusions can be drawn from eq. (2.2.25): for the transition (1) $\rightarrow$ (2) (perfect Meissner effect $\rightarrow$ mixed state), $H = H_{c1}(T)$ and we expect from experiment $\partial B_1/\partial H = 0$ and $\partial B_2/\partial H = \infty$ (see Fig. 2.2.1(a)). One should find an infinite discontinuity of the specific heat. Actually, this is difficult to observe because the singularity is masked by hysteresis effects. However, a lamdba transition for $H = H_{c1}$ was found in niobium by Serin[47]; for the transition (2) $\rightarrow$ (3) (mixed state $\rightarrow$ normal state) $H = H_{c2}(T)$ and, from experiment, $\partial B_2/\partial H > 1$ and $\partial B_3/\partial H = 1$. Knowing the value of $dH_{c2}/dT$, $C_2 - C_3$ can be calculated. It is first concluded that $C_2 > C_3$. However, the comparison of eq. (2.2.25) with experiment is not always possible since not all the quantities of interest have been measured. In $V_3Ge$, it was found that there is no latent heat and the discontinuity $C_2 - C_3$ was measured as well as $dH_{c2}/dT$. An extrapolation of $\partial B/\partial H$ for $H = H_{c2}$ gives an agreement of the order of 10.

### *2.2.2 Anisotropic superconductors*

After the first discovery of the heavy fermion superconductor of $CeCu_2Si_2$ by Steglich *et al.*[48], there were found six heavy superconductors ($UPt_3$, $UBe_{13}$, $URu_2Si_2$, $UNi_2Al_3$ and $UPd_2Al_3$). These exhibit many features suggesting a non-BCS-like pairing mechanism. Especially, $UPt_3$ has a multiplicity of superconducting phases which have been inferred, in particular, from the two distinct discontinuities observed in the specific heat and thermal expansion in the zero applied magnetic field.

The microscopic theory of superconductivity, which was provided by Bardeen, Cooper and Schrieffer in 1957, is based on an idea that, when an attractive interaction between fermions is present, the stable ground state is no longer the degenerated Fermi gas but becomes a coherent state in which the electrons are combined into pairs of spin-singlet with zero total momentum (Cooper pairs). BCS theory simplifies calculations by some assumption and approximation. One of the uniqueness of these assumptions is to be treated as electron systems are isotropic in the normal and superconducting states. Namely, the superconducting energy gap is opened over the entire of the Fermi surface.

Heavy fermion superconductors are, however, well known to show the power law in physical properties such as the electronic specific heat $C_e$ and the nuclear spin-lattice

relaxation rate $1/T_1$, not indicating an exponential dependence predicted by BCS theory. This indicates the existence of an anisotropic gap, namely existence of a node in the energy gap. When we compare the phonon-mediated attractive interaction based on the BCS theory to the strong repulsive interaction among the $f$ electrons, it is theoretically difficult for the former interaction to overcome the latter one. To avoid a large overlap of the wave functions of the paired particles, the heavy electron system would rather choose an anisotropic channel, like a $p$-wave spin triplet or a $d$-wave spin singlet state, to form Cooper-pairs.

We will discuss the pairing wave function and symmetry of superconductivity. The pairing wave function can be expressed as a product of two electrons' orbital and spin term:

$$\Psi(r_1, \sigma_1, r_2, \sigma_2) = \psi(r_1, r_2)\chi(\sigma_1, \sigma_2) \quad . \tag{2.2.26}$$

The spin term $\chi(\sigma_1, \sigma_2)$ of the wave function is categorized when the spin is the pairing state of $S = 0$ (spin singlet)

$$\chi^{S=0}(\sigma_1, \sigma_2) = \frac{1}{\sqrt{2}}(|\uparrow\downarrow\rangle - |\downarrow\uparrow\rangle) \tag{2.2.27}$$

or the pairing state of $S = 1$ (spin triplet) is

$$\chi^{S=1}(\sigma_1, \sigma_2) = \begin{cases} |\uparrow\uparrow\rangle & S_Z = 1 \\ \frac{1}{\sqrt{2}}(|\uparrow\downarrow\rangle + |\downarrow\uparrow\rangle) & S_Z = 0 \\ |\downarrow\downarrow\rangle & S_Z = -1 \end{cases} \tag{2.2.28}$$

$\Psi(r_1, \sigma_1, r_2, \sigma_2)$ has to be antisymmetric against exchanging two particles on the whole. In case of $\chi^{S=0}$, an orbital term $\psi(\sigma_1, \sigma_2)$ has a symmetric form like the $s$-wave or $d$-wave pairing. On the other hand, in case of $\chi^{S=1}$, it has an antisymmetric form as in the $p$-wave.

Here, we can express the spin term with the superposition of the plane wave:

$$\chi(\sigma_1, \sigma_2) = \sum_{k_1, k_2} A(\boldsymbol{k}) \exp(i\boldsymbol{k}_1\boldsymbol{r}_1 + i\boldsymbol{k}_2\boldsymbol{r}_2) = \sum_{\boldsymbol{k}} A(\boldsymbol{k}) \exp(i\boldsymbol{k}\boldsymbol{r}). \tag{2.2.29}$$

Here, the coordinate of the center of the paired particle is expressed as $\boldsymbol{R} = (\boldsymbol{r}_1 + \boldsymbol{r}_2)/2$, the momentum of the center of the particles $\boldsymbol{K} = \boldsymbol{k}_1 + \boldsymbol{k}_2$, the relative coordinates $\boldsymbol{r} = \boldsymbol{r}_1 - \boldsymbol{r}_2$ and the relative momentum $\boldsymbol{k} = (\boldsymbol{k}_1 - \boldsymbol{k}_2)/2$. In this case the momentum of the center of the particle for pairing is zero ($\boldsymbol{K} = 0$). This wave function can be solved:

$$\left[-\frac{\hbar^2}{m}\Delta^2 + V(\boldsymbol{r})\right]\Psi(\boldsymbol{r}) = E\Psi(\boldsymbol{r}) \quad , \tag{2.2.30}$$

where $V(\boldsymbol{r})$ is an attractive interaction. As mentioned above, BCS theory accepting isotopic pairing symmetry indicates that the attractive interaction should be constant:

$V(\boldsymbol{k}-\boldsymbol{k}')=0$. Here, if $V(\boldsymbol{k}-\boldsymbol{k}')$ depends on the only relative angle $\theta$ between $\boldsymbol{k}$ and $\boldsymbol{k}'$, it can be expanded on the Legendre function or the spherical harmonics function:

$$V(\boldsymbol{k}-\boldsymbol{k}') = -\sum_l (2l+1)V_l(k,k')P_l(\cos\theta) \tag{2.2.31}$$

$$= -4\pi\sum_l V_l(k,k')\sum_{m=-l}^{l} Y_l^m(\theta,\varphi)Y_l^m(\theta',\varphi'). \tag{2.2.32}$$

The gap function is represented as

$$\Delta(\boldsymbol{k}) = \Delta_0\sum_m \lambda_m Y_l^m(\theta,\varphi) \tag{2.2.33}$$

$$\Delta_0 = 2\hbar\omega_{\mathrm{D}}\exp\left(-\frac{1}{N(E_{\mathrm{F}})V_l}\right). \tag{2.2.34}$$

Here, in the case of $s$-wave ($l=0$, $m=0$) it is to be $\Delta(k)=\Delta_0$. On the other hands, as shown in eq. (2.2.28), in the $p$-wave ($l=1$) there are three pairing states ($m=-1,0,1$). For $l=1$ and $m=-1$, the superconducting gap is the same as the $s$-wave and is isotropic. This condition corresponds to the Balian-Werthamer(BW) state of $^3$He superfluid.[49] For $l=1$ and $m=0$, the gap is represented as $\Delta(\theta)=\Delta_0\cos\theta$ and has a line node in the equator on the Fermi surface. This structure is called the polar type. For $l=1$ and $m=1$, it is shown as $\Delta(\theta)=\Delta_0\sin\theta$ and has a point node in the poles on the Fermi surface. This condition corresponds to the Anderson-Brinkman-Morel(ABM) state of $^3$He superfluid.[50] This is called the axial type. Figure 2.2.3 shows the gap structure for these cases.[31] To describe the spin triplet state, matrix description by the $\boldsymbol{d}$-vector is convenient. The superconducting gap function in eq. (2.2.33) is also represented by the 2×2 matrix:

$$\hat{\Delta}(\boldsymbol{k}) = \begin{pmatrix} \Delta_{\uparrow\uparrow} & \Delta_{\uparrow\downarrow} \\ \Delta_{\uparrow\downarrow} & \Delta_{\downarrow\downarrow} \end{pmatrix} = \begin{pmatrix} -d_x+id_y & d_z \\ d_z & d_x+id_y \end{pmatrix}, \tag{2.2.35}$$

where $\Delta_{\uparrow\downarrow}=\Delta_{\uparrow\downarrow}\equiv\Delta_0$ and $\boldsymbol{k}=(k_x,k_y,k_z)$ is the vector specifying the direction in momentum space. The representation in eq. (2.2.33) is not convenient in dealing with the rotation of spin space. Therefore, the $\boldsymbol{d}$-vector is introduced as in

$$\boldsymbol{d} = d_x\boldsymbol{x}+d_y\boldsymbol{y}+d_z\boldsymbol{x} \tag{2.2.36}$$

$$= 2^{-1/2}\{\Delta_{\uparrow\uparrow}|\uparrow\uparrow\rangle+\Delta_{\downarrow\downarrow}|\downarrow\downarrow\rangle+\Delta_0(|\uparrow\downarrow\rangle+|\downarrow\uparrow\rangle)\}. \tag{2.2.37}$$

The $\boldsymbol{d}$-vector $\boldsymbol{d}(\boldsymbol{k})=(d_x,d_y,d_z)$ can be transformed as a three-dimensional vector under the rotation in spin space.

Next we will explain the density of states in the superconducting state.[51] The density of states (DOS) for the $s$-wave is

$$\frac{N_{\mathrm{s}}(E)}{N_0} = \begin{cases} \frac{E}{\sqrt{E^2-\Delta_0^2}} & (E>\Delta_0) \\ 0 & (E<\Delta_0) \end{cases}. \tag{2.2.38}$$

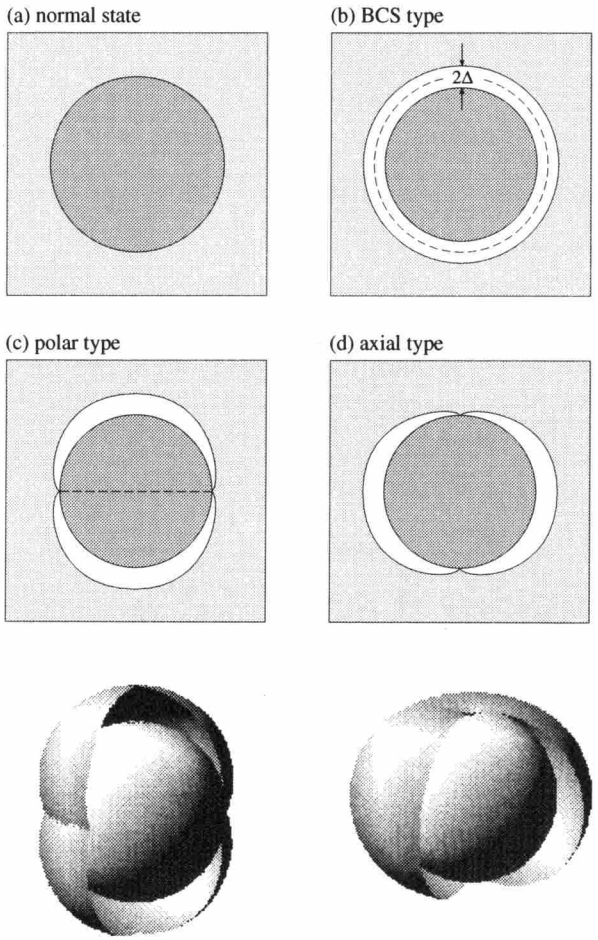


**Fig. 2.2.3** Schematic picture of the gap structures: (a) normal state, (b) BCS-type superconductor, which has an isotropic gap, (c) polar type and (d) axial type.[31)]

where $N_0$ is the density of states of one spin per unit energy at Fermi level in the normal state. It indicates that there is no DOS inside of the gap, diverging at $E = E_{\rm F} + \Delta_0$. In the case of the polar type, DOS is represented as

$$\begin{aligned} \frac{N_{\rm s}(E)}{N_0} &= \frac{E}{4\pi}\int_0^2 \pi \int_0^\pi \frac{\sin\theta}{\sqrt{E^2 - \Delta_0^2\cos\theta}} {\rm d}\theta{\rm d}\phi \qquad (2.2.39) \\ &= \begin{cases} \frac{E}{\Delta_0}\sin^{-1}\frac{\Delta_0}{E} & (E > \Delta_0) \\ \frac{\pi E}{2\Delta_0} & (E < \Delta_0) \end{cases} . \end{aligned}$$

DOS of the axial type is shown as

$$\begin{aligned} \frac{N_{\rm s}(E)}{N_0} &= \frac{E}{4\pi}\int_0^2 \pi \int_0^\pi \frac{\sin\theta}{\sqrt{E^2 - \Delta_0^2\sin\theta}} {\rm d}\theta{\rm d}\phi \qquad (2.2.40) \\ &= \frac{E}{2\Delta_0}\ln\left|\frac{E+\Delta_0}{E-\Delta_0}\right| \\ &\propto E^2 \quad (E \ll \Delta_0) \begin{cases} \frac{E}{\Delta_0}\sin^{-1}\frac{\Delta_0}{E} & (E > \Delta_0) \\ \frac{\pi E}{2\Delta_0} & (E < \Delta_0) \end{cases} . \qquad (2.2.41) \end{aligned}$$

Therefore, in the energy region far below gap edge $\Delta_0$ ($E \ll \Delta_0$), DOS with the anisotropic gap is expressed as

$$\frac{N_s(E)}{N_0} \propto \begin{cases} E & \text{polar type} \\ E^2 & \text{axial type.} \end{cases} \tag{2.2.42}$$

We show $N_s(E)$ in the case of the BCS state ($\Delta = \Delta_0$), the polar state ($\Delta = \Delta_0 \cos\theta$) and the axial state ($\Delta = \Delta_0 \sin\theta$) in Fig. 2.2.3. Next, we will explain the temperature

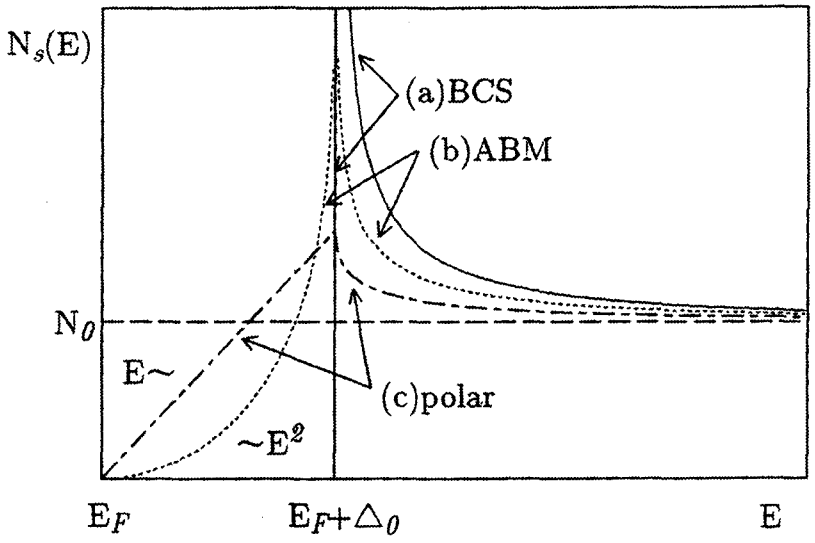


**Fig. 2.2.4** Density of state $N_s$ for (a) the BCS state, (b) the axial ABM state and (c) the polar state.[52)]

dependence of $C_e$ and $1/T_1$ indicating the power law, which reflects the anisotropic DOS.

a) Specific heat

Generally, the electronic specific heat $C_e$ of the metal in the normal state is represented as

$$\begin{aligned} C_e &= \frac{\pi^2 k_B}{3} N(E_F) T \\ &\equiv \gamma T, \end{aligned} \tag{2.2.43}$$

where $\gamma$ is the Sommerfeld coefficient or electronic specific heat coefficient and $N(E_F)$ is DOS at the Fermi energy. Its coefficient in the superconducting state can be expressed as

$$\frac{C_s}{T} = \frac{2}{T^2} \int_0^\infty N_s(E) E^2 \left( -\frac{\partial f}{\partial E_k} \right) dE, \tag{2.2.44}$$

where $f$ is the Fermi-Dirac distribution. Thus, for the BCS($s$-wave), polar and axial types, the electronic specific heat can be represented as

$$\frac{C_s}{T} = \begin{cases} \exp(-\Delta/T) & \text{BCS type} \\ T & \text{polar type} \\ T^2 & \text{axial type.} \end{cases} \tag{2.2.45}$$

b) Nuclear spin-lattice relaxation rate

The nuclear spin-lattice relaxation rate $1/T_1$ in the superconducting state is caused by the scattering of the normal electrons excited above the superconducting energy gap. $1/T_1$ in the BCS state is expressed as

$$\frac{1}{T_1} = \frac{2\pi}{\hbar} A^2 \int_0^\infty (N_s(E)^2 + M_s(E)^2) \left(-\frac{\partial f}{\partial E}\right) dE, \tag{2.2.46}$$

where $M_s$ is the density of states related to the coherence effect. $M_s$ is given by

$$M_s = \begin{cases} \frac{N_0 \Delta}{\sqrt{E^2 - \Delta^2}} & E \geq \Delta \\ 0 & E \leq \Delta. \end{cases} \tag{2.2.47}$$

Thus just below $T_c$ is characterized in $T_1^{-1}$ the so-called "Hebel-Slichter peak" or "coherence peak" originated not only the divergence of $N_s$ at the gap edge $\Delta_0$, but also from the density of states $M_s$. This effect is weakened by the lifetime broadening of the quasiparticles and/or the damping effect due to the electron-phonon coupling. In the temperature region of $T \ll T_c$, $1/T_1$ decreases exponentially with decreasing temperature as

$$\frac{1}{T_1} \sim \exp\left(-\frac{\Delta}{k_B T}\right), \tag{2.2.48}$$

reflecting the isotropic opening of the energy gap.

On the other hand, for the $d$- or $p$-wave pairing, the coherence effect is weakened or disappears owing to the anisotropic gap and/or the lifetime broading of the quasiparticles. From eq.(2.2.44), we can get the relations as follows,

$$\frac{1}{T_1} = \begin{cases} \exp(-\Delta/T) & \text{BCS type} \\ T^3 & \text{polar type} \\ T^5 & \text{axial type} \end{cases} \tag{2.2.49}$$

*2.2.3 Typical examples of anisotropic superconductor*

We take three materials of $CeRu_2$, $UPt_3$ and $UPd_2Al_3$ for typical examples of $s$-, $p$- (or $f$-) and $d$-wave superconductors, respectively.

$CeRu_2$ has the cubic crystal structure with $T_c = 6.3$ K. For NMR and NQR measurements using the powder sample, Matsuda *et al.* and Ishida *et al.* reported important information for superconductivity.[53,54] Figure 2.2.5 shows the temperature dependence of a nuclear spin-lattice relaxation rate $1/T_1$ of $^{101}$Ru. They observed a Habel-Slichter peak just below $T_c$ and an exponential decrease in $1/T_1$. The magnitude of superconducting gap $2\Delta/k_BT_c$ was, however, obtained as 4.0 by Matsuda *et al.* and as 3.8 by Ishida *et al.*, respectively. These values are larger than an expected BCS value ($2\Delta/k_BT_c = 3.54$). Thus, these results indicate that $CeRu_2$ is a strong-coupling BCS superconductor. The exponential decrease in $1/T_1$ is also consistent with the same temperature dependence of the specific heat data obtained by Huxley *et al.* and Hedo *et al.*[55,56]

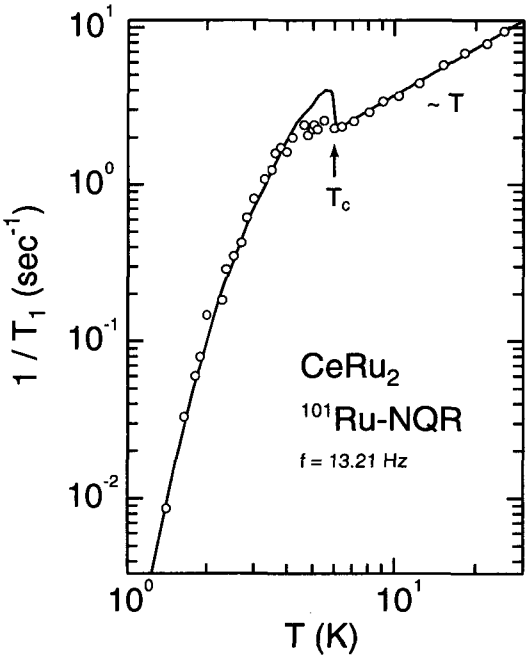


**Fig. 2.2.5** $T$-dependence of $1/T_1$ in $CeRu_2$. A solid curve is a BCS line.[54]

The $T^2$ dependence of the specific heat in the form of $C/T$ under the several constant fields are shown in Fig. 2.2.6. A jump in the specific heat is sharp at the superconducting critical temperature. In fields higher than 55 kOe the sample is changed into the normal state. The electronic specific heat parameters are $\gamma = 27$ mJ/ K$^2 \cdot$ mol and $\Theta_D = 120$ K. The electronic specific heat $C_e$ in the superconducting state is well explained by the BCS theory, as shown in Fig. 2.2.7. The superconducting parameters are obtained as $2\Delta(0)/k_BT_c = 3.7$ and $\Delta(0) = 11.7$K. The value of $2\Delta(0)/k_BT_c$ is compared to the BCS value of 3.53. $\Delta C/\gamma T_c$ is obtained as 2.0, where $\Delta C$ is the jump in the specific heat at

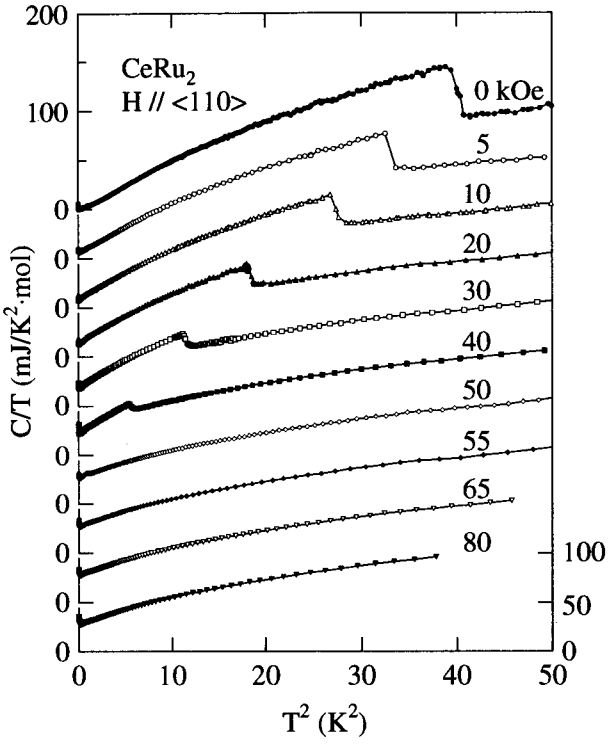


**Fig. 2.2.6** $T^2$ dependence of the specific heat in the form of $C/T$ under several constant fields. Solid lines connecting the data are guidelines.[56)]

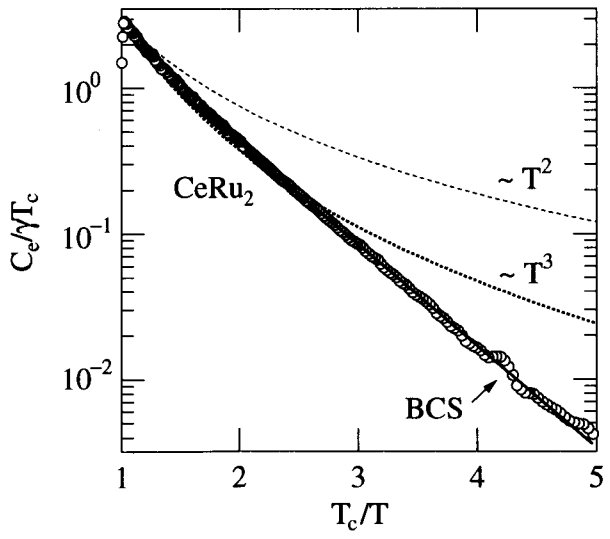


**Fig. 2.2.7** Temperature dependence of the specific heat in the superconducting region. The $T^2$ and $T^3$ dependences of the specific heat correspond to the gap structures with polar and axial nodes, respectively.[56)]

$T_c$. This value is also larger than BCS value of 1.43.

In Fig. 2.2.7 another relation is drawn from a viewpoint of anisotropic superconductivity, where the specific heat follows the $T^2$ and $T^3$ dependences for the superconducting gap with the polar and axial nodes, respectively. This data follows the BCS relation.

The temperature dependence of a Maki parameter $\kappa_2$ is shown by circles in Fig. 2.2.8. The $\kappa_2$ value is 12 around $T_c$ and increases with decreasing the temperature. The behavior is predicted to be no paramagnetic effect. The data do not diverge as $\sqrt{\ln(T_c/T)}$ at low temperatures, but saturate to a finite value when extrapolating the temperature down to 0 K. This means that the sample is, rigorously saying, not in the pure limit.[57] It is, however, close to the pure limit because the theoretical ratio of $\kappa_2$ at 0 K to the one at $T_c$ becomes 2.0 for $\xi/l = 0.05$, where $l$ is the mean free path.[57] The corresponding ratio for the present sample is about 3. In fact, the $\xi/\ell$ value is approximately 0.03-0.04 because the coherence length is determined as 79.3 Å from $H_{c2}(0)$ and the mean free path, which has been determined by the de Hass-van Alphen oscillation, is 2600 Å for branch $\alpha$, 2000 Å for branch $\delta_1$ and 2400 Å for branch $\varepsilon_{1,2,3}$.[58]

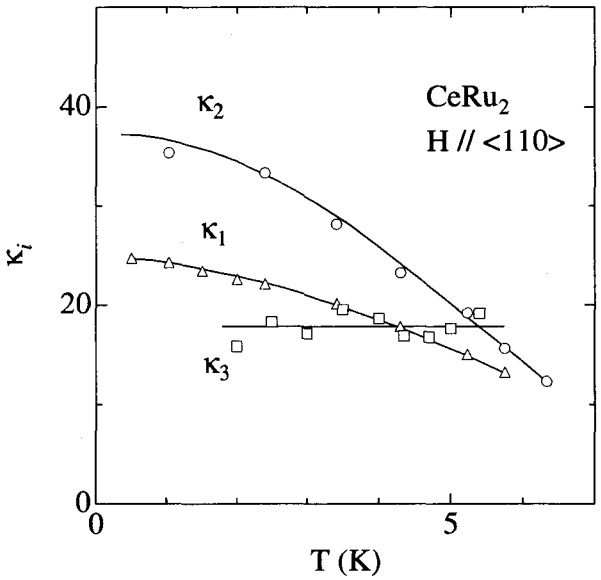


**Fig. 2.2.8** Temperature dependence of Maki parameters $\kappa_1$ and $\kappa_2$ and $\kappa_3$ shown by triangles, circles and squares, respectively. Solid lines connecting the data are guidelines.

The $\kappa_1$ value is almost the same as $\kappa_2$ near $T_c$, but becomes smaller than $\kappa_2$ with decreasing the temperature. This behavior is normal in usual type II superconductors. [57]

Next, we will explain the typical non $s$-wave superconductor $UPt_3$ with the hexagonal structure, which is a strong candicate for a $p$ or $f$-wave superconductor. The double superconducting transition was observed in the specific heat measurements. Figure 2.2.9 shows the superconducting multiple $H$-$T$ phase diagram of $UPt_3$, which was obtained

from magnetization and specific heat measurement under the magnetic field[3,29,61,62]. From this phase diagram, there are three superconducting phases, called A, B and C, and

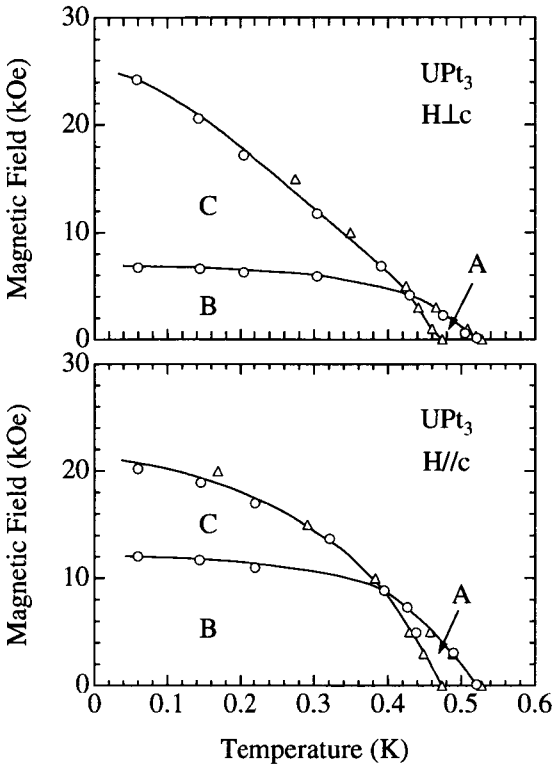


**Fig. 2.2.9** Multiple $H$-$T$ phase diagram of $UPt_3$ determined by the static magnetization and specific heat experiments[3,29,61,62].

the anisotropy between the field directions along [0001] and [11$\bar{2}$0].

Figure 2.2.10 shows the temperature dependence of nuclear spin-lattice relaxation rate $1/T_1$ of $^{195}$Pt.[59] No NMR anomalies associated with AF ordering have been observed near or below $T_N = 5\,K$, suggesting that the static long-range ordering is ruled out. A Habel-Slichter peak was not observed just below $T_c$ and a power law($\sim T^3$) is observed in the temperature dependence of $1/T_1$. This results claims a polar type gap.

The $^{195}$Pt Knight shifts do not decrease at all below $T_c$ within an experimental error of $\pm 0.02\%$ regardless of the crystal directions and of the superconducting multiphases.[2] These novel results have eliminated the possibilities of both even parity superconductivity and odd parity superconductivity with the strong spin-orbit (SO) coupling. As a result, unconventional superconductivity of $UPt_3$ is characterized by odd parity with an equal spin pairing keeping the same anisotropy of the spin susceptibility as in the normal state and following the direction of the magnetic field in a range of $4.4 - 15.6\,kOe$ without an appreciable pinning to the lattice. The Pt Knight shift study has provided an important clue that the SO coupling for the pair is not so strong as to lock the pseudo-spin de-

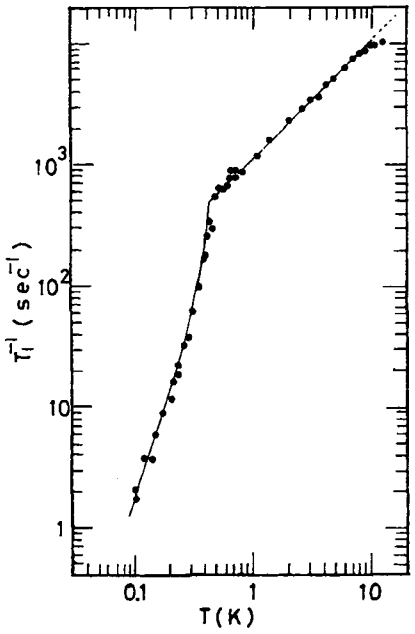


**Fig. 2.2.10** Temperature dependences of $1/T_1$ of $^{195}$Pt.[59]

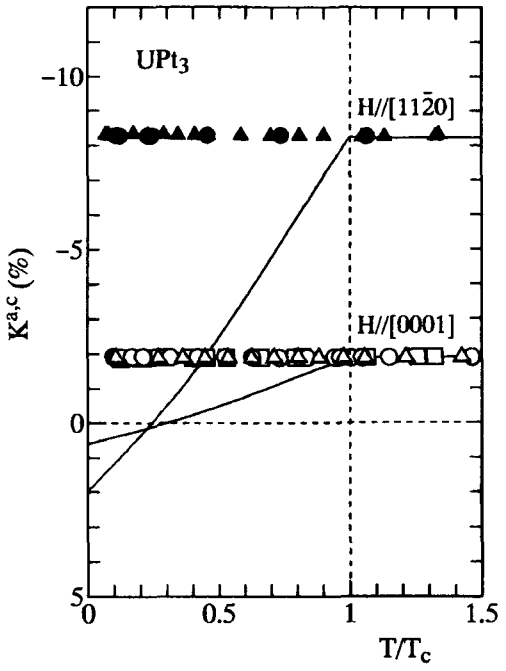


**Fig. 2.2.11** Temperature dependences of $^{195}$Pt $K$ against temperature normalized by $T_c$ with a full scale for the shift.[2]

gree of freedom in the crystal direction. The one-dimensional scenario incorporating the symmetry-breaking-field (SBF) for the weak SO coupling seems to be promising.

The normal state paramagnetic susceptibility $\chi_n$ of $UPt_3$ is large and anisotropic, with the easy direction being $H \perp [0001]$ ($c$-axis). Since a substantial part of $\chi_n$ comes from the pseudo-spin Pauli paramagnetism, the behavior of $M_{eq}$ near $H_{c2}$ may depend strongly on the pairing symmetry.[61] Figure 2.2.12 shows the $M(H)$ curves, measured at 50 mK. The strong irreversibility appearing at low field is due to the ordinary flux pinning effect. The hysteresis rapidly decreases as $H$ increases, and $M(H)$ becomes almost reversible at $H \sim 17$ kOe. The linear magnetization above $H_{c2}$ is due to the normal state paramagnetism. In both field directions, the irreversibility in $M(H)$ increases again in a narrow region just below $H_{c2}$, which is called "peak effect". When the magnetization hysteresis is small, the equilibrium magnetization $M_{eq}$ of the vortex state can be well approximated by the average of the increasing- and decreasing-field data. The results for $M_{eq}$ are shown in Fig. 2.2.12 by thin solid lines.

In general, $M_{eq}^0$ near $H_{c2}$ can be expressed in terms of a Ginzburg-Landau parameter $\kappa_2$. Temperature variation of $\kappa_2$ evaluated from $M_{eq}^0$ is summarized in Fig. 2.2.13, which further confirms the existence of the anisotropic paramagnetic effect. In a conventional superconductor, $\kappa_2$ could be direction-dependent, reflecting the effective mass anisotropy.

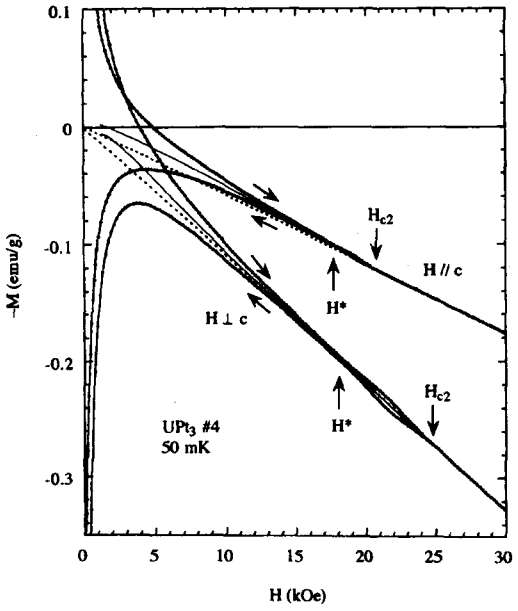


**Fig. 2.2.12** Magnetization curves of the single crystal of $UPt_3$ at 50 mK.[61)]

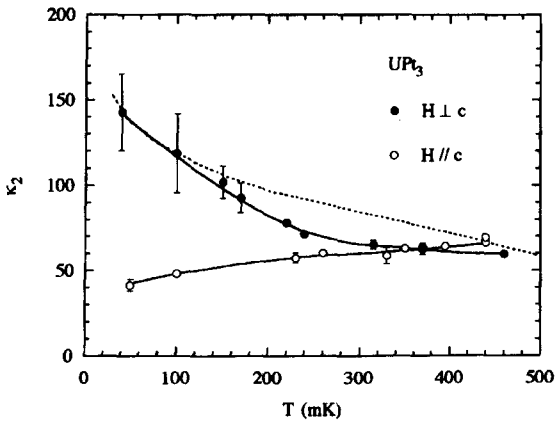


**Fig. 2.2.13** Temperature variation of $\kappa_2$. The dotted line is the theoretical prediction for a clean superconductor without paramagnetic effect.[61)]

Remarkably, $\kappa_2^a(T)$ continues to increase on cooling, without an indication of saturation. This is actually the behavior which is predicted for a clean superconductor in the absence of the paramagnetic effect, where $\kappa_2 \propto \sqrt{\ln(T_c/T)}$ as $T \to 0$ as shown by the dotted line. In contrast, $\kappa_2^c$ continues to decrease on cooling: this is a typical feature in the presence of the paramagnetic effect where the pair breaking by the Zeeman energy becomes important at low temperatures. As a result, there is a crossover in the anisotropy ratio $\kappa_2^a/\kappa_2^c$ at about $T \sim 0.7T_c$.

The probable scenario is the odd parity pairing with anisotropic pair-spin orientation. The apparent lack of the paramagnetic effect in the basal plane would imply an equal spin pairing in this direction, whereas the appreciable paramagnetic effect along the [0001] direction would mean that the pair-spin orientation is somewhat confirmed in the basal plane, implying a non-negligible spin-orbit coupling in the pairing channel. This scenario is consistent with the result of the NMR Knight shift, except for the anisotropy along the [0001] direction: no change is observed in the Knight shift for two principal directions.

$UPd_2Al_3$ with the hexagonal structure is known as a typical heavy fermion superconductor in which antiferromagnetic ordering with a Nèel temperature $T_N$=14.5 K and superconductivity with a critical temperature $T_c$=2 K. Form the results of $^{27}$Al-NMR measurements using the high-quality polycrystalline sample, a Habel-Slichter peak was not observed just below $T_c$, which imply the non $s$-wave superconductor, as shown in Fig. 2.2.14. The $T^3$-law of $1/T_1$ holds down to sufficiently low temperatures, resulting

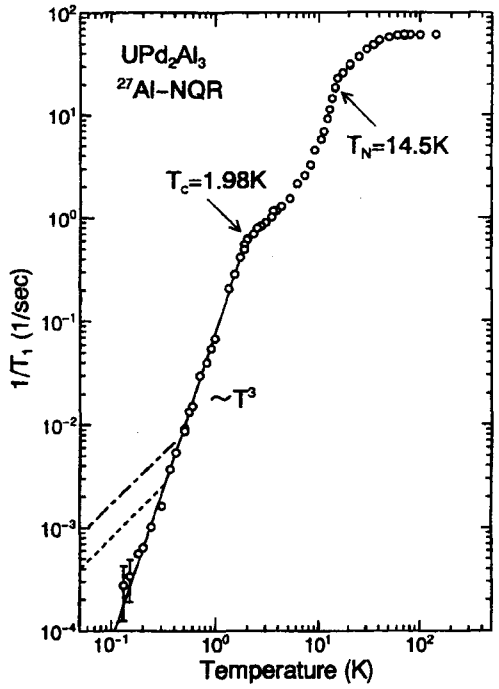


**Fig. 2.2.14** $T$-dependence of $1/T_1$ in $UPd_2Al_3$. A solid line shows $T^3$ dependence. The dash-dotted lines show the low-$T$ behavior reported by Kohori *et al.*.[64,65]

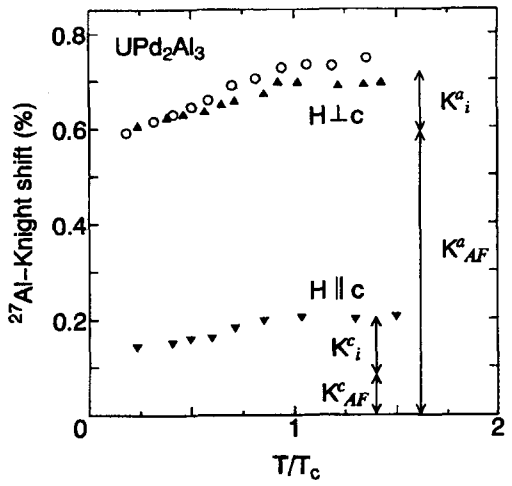


**Fig. 2.2.15** $T$-dependence of the Knight shift below $T_c$ in $UPd_2Al_3$. [65]

from the line-node gap (polar-type).[64,65] Figure 2.2.15 shows the temperature dependence of the Knight shift below $T_c$. The large residual shift originates from the antiferromagnetic susceptibility, while the isotropic reduction of the spin shift below $T_c$ is due to the formation of a singlet pair among quasiparticles near the Fermi level. Combining both the results of $1/T_1$ and Knight shift, it has been clarified that superconductivity in $UPd_2Al_3$ is of the $d$-wave pairing type characterized by line nodes on the Fermi surface.

The magnetization curves in the increasing- and decreasing-field processes at 50 mK are shown in Fig. 2.2.16[66]. A pronounced peak effect are observed in the mixed state. A broken and a thin solid line show the equilibrium magnetization and normal state magnetization, respectively. Figure 2.2.17 shows the temperature dependence of the Maki parameter $\kappa_2$, obtained from the slope of the equilibrium magnetization. The value of $\kappa_2$ decreases monotonously with decreasing the temperature and becomes constant. This indicates the existence of the paramagnetic effect for the field parallel to the hexagonal basal plane.

Next, we show in Fig. 2.2.18 the inelastic scattering profiles measured with $E_f = 4$ meV at the (0 0 0.5) antiferromagnetic Bragg point as a function of the sample temperature.[67]

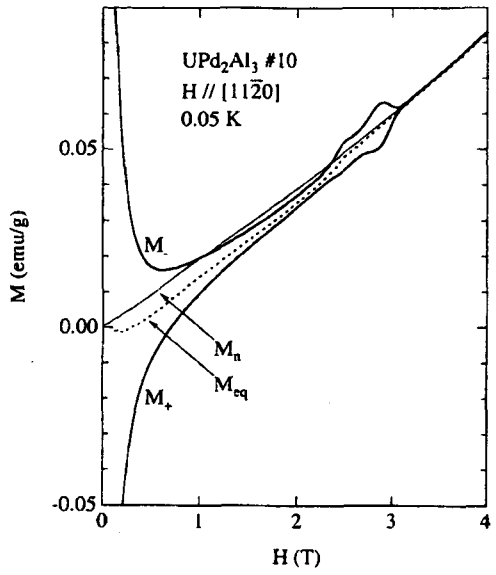


**Fig. 2.2.16** Magnetization curve at 50 mK in $UPd_2Al_3$.[66]

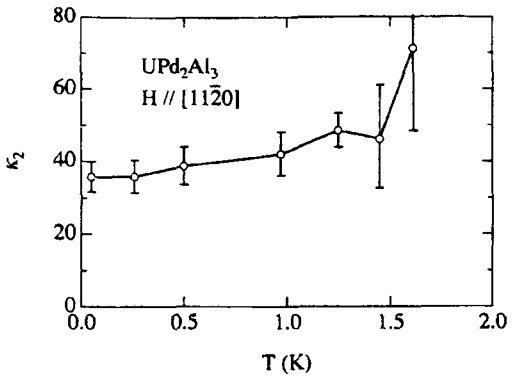


**Fig. 2.2.17** $T$-dependence of the Maki parameter $\kappa_2$ in $UPd_2Al_3$.[66]

At T= 4.2 K, the profile can be described by a combination of a broad quasielastic (dotted line) and an inelastic Lorentzian line shape at $\Delta E = 1.5$ meV (dashed line), as well as a sharp Bragg peak (dashed line) and an incoherent scattering (dash dotted line) both centered at $E = 0.0$ meV. The broad peak at $\Delta E$= 1.5 emV is a spin wave excitation. Below $T_c = 1.9$ K, the position of the quasielastic peak shifts to a higher energy. A clear peak with a maximum at $\Delta E = 0.4$ meV appears at 0.4 K.

Fig. 2.2.19 shows the temperature dependence of the energy of the magnetic excitation gap. The gap starts to open at $T_c = 1.9$ K and increases with decreasing the temperature. This temperature dependence is comparable to the one of the superconducting energy gap expected from the weak coupling BCS theory (dotted line), which is normalized by the maximum energy gap. The energy gap at the low temperature is 0.36 meV, which corresponds to $2\Delta = 2.2k_BT_c$. It is the same order compared with the weak-coupling BCS theory, $2\Delta = 3.5k_BT_c$. In addition we note that the gap disappeared with applying the magnetic field larger than the upper critical field $H_{c2}$.[68]

From these results it is concluded that the observed magnetic excitation gap corresponds to the superconducting gap. At present we don't know the microscopic mechanism why the magnetic excitation gap behaves very similar to the superconducting gap which is obviously a charge gap. It should be noted, however, that this phenomenon is due to the strong coupling between magnetism and superconductivity.

High-$T_c$ cuprates also indicate the similar features as in $UPd_2Al_3$, indicating a $d$-wave superconductor.

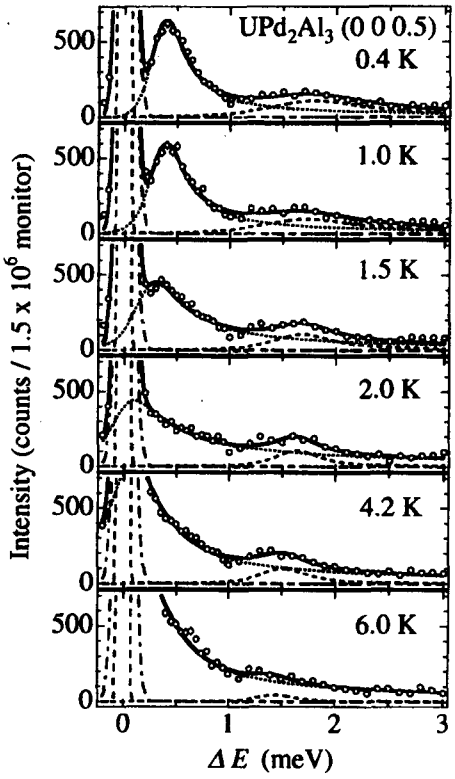


**Fig. 2.2.18** $T$-dependence of the neutron inelastic scattering profile measured at $Q$=(0 0 0.5) in $UPd_2Al_3$.[67]

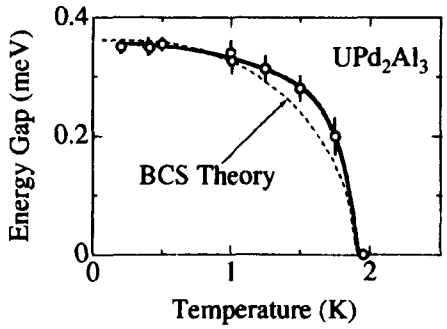


**Fig. 2.2.19** (a)$T$-dependence of the energy gap in $UPd_2Al_3$.[67]

## 2.3 Characteristic properties of $Sr_2RuO_4$

### *2.3.1 Nomal state*

$Sr_2RuO_4$ is the first non-cuprate superconductor with a layered perovskite structure as in $La_{2-x}Sr_xCuO_4$. The superconducting temperature $T_c$ was for the first time about 1 K, but later on it reached to 1.49 K.[4,69]

Reflecting the layered structural character, the transport property is highly anisotropic with the ratio of the resistivity along the $c$-axis or the [001] direction to that of the $ab$-plane, $\rho_c/\rho_{ab} \sim 850$ at 2 K. The temperature dependence of $\rho_{ab}$ is metallic. On the other hand, that of $\rho_c$ is nonmetallic, but becomes metallic below $T_M$ which is the crossover temperature from 2D to 3D metal. The metallic behavior along the $c$-axis is only valid below $T_M \sim 130$ K. Neutron diffraction experiments for the single crystal revealed that any structural transition was not observed across $T_M$.[70]

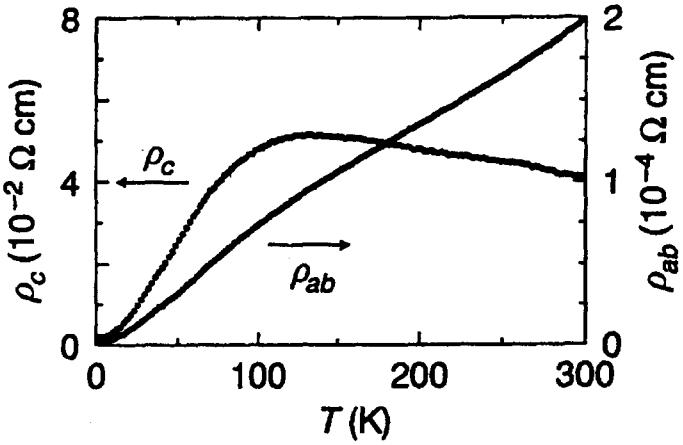


**Fig. 2.3.1** Temperature dependence of the electrical resistivity in $Sr_2RuO_4$.[4]

A $T^2$ dependence of $\rho_{ab}$ and $\rho_c$ below 25 K implies the Fermi liquid nature.[71] The electronic specific heat coefficient $\gamma$ is substantially enhanced from the band calculation by a factor of 3.8, being in satisfactory agreement with the expectation from the enhanced masses obtained from quantum oscillations.[5] Although the magnetic susceptibility shows a Pauli paramagnetic weak $T$-dependence up to 700 K, the spin susceptibility estimated by Ru-NMR measurement is exchange-enhanced by a factor of 5.4. The Wilson ratio is expected to be 1.36, indicating that the enhancements in $\chi$ and $\gamma$ are of the same origin.

According to the band-structure calculations[6,7], the electronic states of $Sr_2RuO_4$ near the Fermi level are derived mainly from four $4d$ electrons of Ru. The hybridization with the oxygen $2p$ electrons is substantial. The quantum oscillations(both the de Haas-van Alphen and Shubnikov-de Haas oscillations) by Mackenzie *et al.*[5] showed that the Fermi surface consists of three pieces of two dimensional sheets, labeled $\alpha$, $\beta$ and $\gamma$. The observed cyclotron masses are in agreement with the observed $\gamma$-value and all enhanced from the

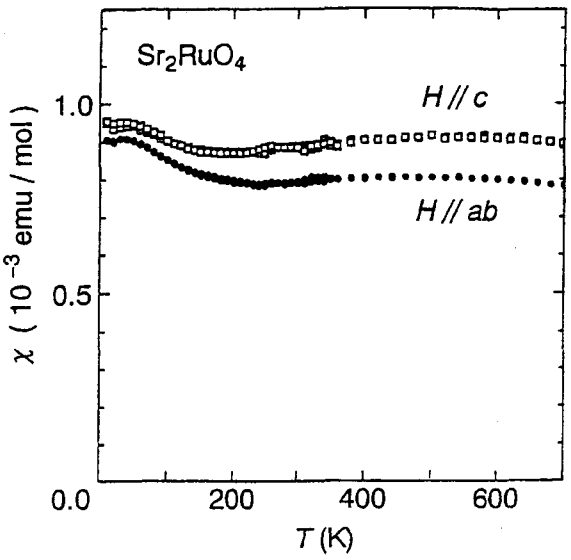


**Fig. 2.3.2** Magnetic susceptibility up to 700 K in $Sr_2RuO_4$.[71]

respective expectations of the band structure calculation by a factor of three to four. The surface $\alpha$ is a small hole Fermi surface, while, the surfaces $\beta$ and $\gamma$ are electron ones.

The Hall coefficient $R_H$ exhibits a complicated temperature dependence.[73,74] It changes from negative to positive below 130 K, and changes again to negative below about 25 K. Mackenzie *et al.*[74] have shown that below 1 K, it saturates at a value of $-1.15\times10^{-10}$ $m^3/C$. According to an analysis for a two-dimensional metal, the negative value at low temperatures where the mean free path can be assumed isotropic, requires that the number of electrons be greater than that of the holes. This means that $Sr_2RuO_4$ is an uncompensated metal. The above assignment is also consistent with the negative sign and the value of the Hall coefficient at low temperatures.

Significantly different Fermi surface has been observed by angle-resolved photoemission spectroscopy(ARPES) by two independent research groups.[75-77] These ARPES results are in agreement with each other and indicate the presence of an extended van Hope singularity (a flat band), much like the ones commonly observed in high-$T_c$ cuprates. The reported Fermi surface consists of one electron Fermi surface and two hole ones, in sharp contrast to the results of the quantum oscillations. Such Fermi surfaces would give the de Haas-van Alphen frequency of only 47% of the actual observation for $\gamma$. Since ARPES has been a powerful and unparalleled method of providing useful information on the electronic states near the Fermi level for high-$T_c$ cuprates, it is quite important to resolve this controversy on this layered perovskite material. ARPES is a surface sensitive technique and the consistency with the bulk properties such as the de Haas-van Alphen effects should be confirmed for each compound under investigation.

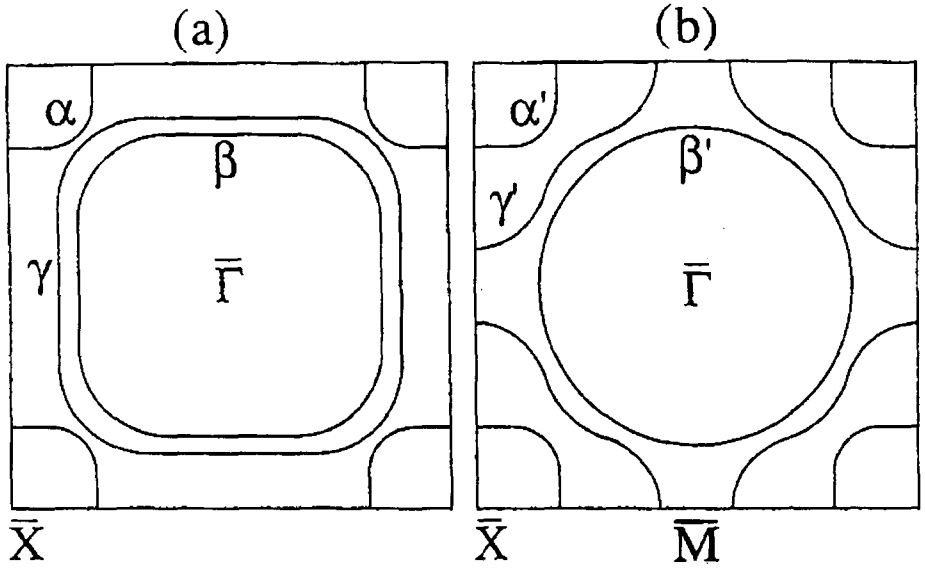


**Fig. 2.3.3** Sketches of the different Fermi surface topographies deduced from (a) dHvA measurements and (b) angle-resolved photoemission spectroscopy.[72)]

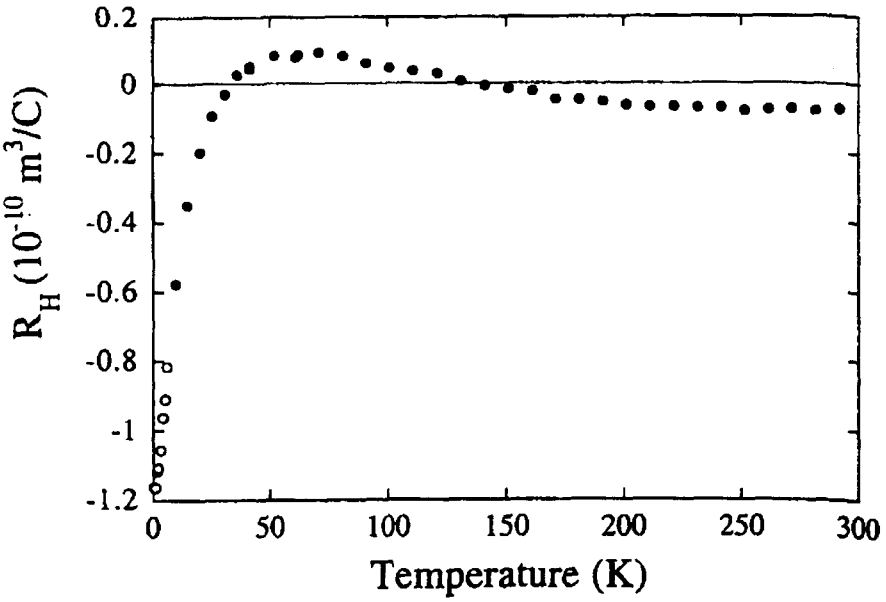


**Fig. 2.3.4** Temperature dependence of the weak-field Hall coefficient $R_H$.[74)]

Recently, an interesting phenomenon has been observed in the Shubnikov-de Haas oscillation at an angle $\theta = 31°$, where $\theta$ denotes a tilt angle measured from [001] to [100]. [8] Both Fermi surfaces $\alpha$ and $\beta$ become perfectly two-dimensional at 31°. Namely, this corresponds to the Yamaji angle. The cyclotron effective masses of the sum and difference oscillatory components $m^*_{\beta\pm\alpha}$ are found to be highly different from $m^*_\beta + m^*_\alpha$, which is derived from the usual magnetic interaction. This phenomenon was explained on the basis of the dHvA oscillation derived under the constant total electron number, so-called chemical potential oscillation, which is in contrast with the Lifshiz-Kosevich formula derived under the constant chemical potential. [9]

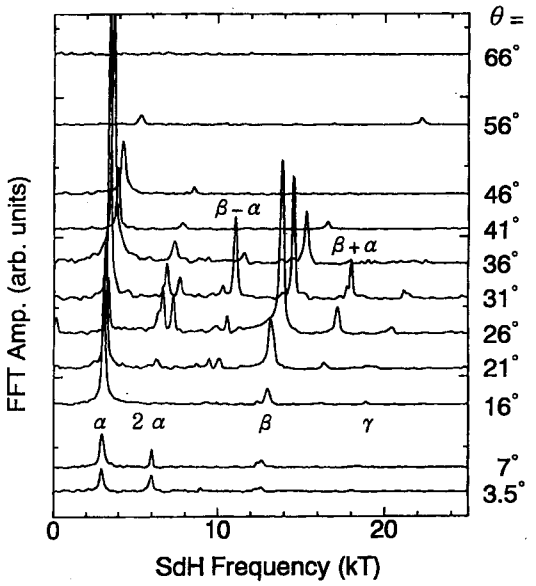


**Fig. 2.3.5** FFT spectra of the oscillations for various angle $\theta$ values.[8]

### *2.3.2 Superconductivity*

The superconducting properties are also highly anisotropic due to quasi-two dimensional electronic character. The ratio of the coherence lengths, $\xi_{ab}/\xi_c$ ~660Å/33Å ~ 20[69], is large. Nevertheless, the coherence length along the $c$-axis is several times longer than the interlayer spacing of $d$=6.4Å. The effect of strong Coulomb repulsion among the electrons, reflected in the Fermi-liquid properties[71], tends to favor pairing states with non-zero orbital angular momentum. From the early Ru-NQR measurement, the absence of the Hebel-Slichter peak in $1/T_1$ just below $T_c$ excluded a possibility of the $s$-wave pairing state.[10] The large residual density of states of 62% was observed at lower temperatures from Ru-NQR, which was consistent with the estimated by the specific heat measurement.[11,12] Even in the better sample with $T_c$ ~1.43 K, the residual electronic specific heat have been observed.[78] The unconventional nature of superconductivity is

reinforced by the observation of the extremely strong suppression of $T_c$ by disorder introduced by nonmagnetic impurities and defects.[79] Recently, the measurements of the $^{17}O$

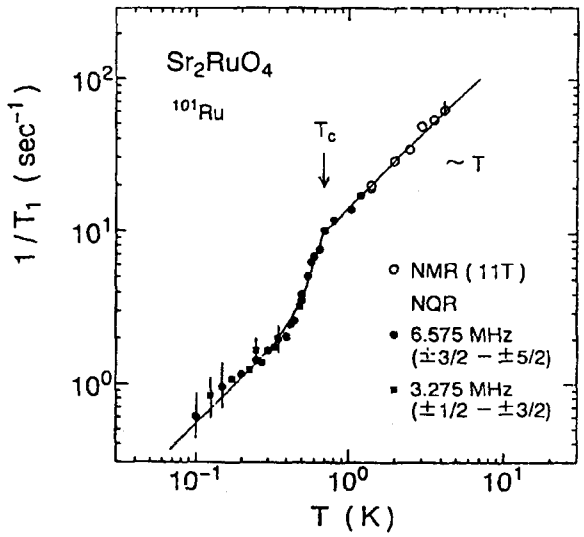


**Fig. 2.3.6** $T$ dependence of $1/T_1$ at Ru site in $Sr_2RuO_4$.[10]

Knight-Shift in $Sr_2RuO_4$ have been performed.[14,80] For the field of 0.65 T parallel to the $ab$-plane, the spin part of the Knight shift does not change down to 15 mK, much below $T_c(H = 0.65\ T) \approx 1.2$ K. Since the system is in the clean limit, the invariance of the Knight shift cannot be attributed to the strong spin-orbit scattering in the $s$-wave superconductor. This constitutes the decisive evidence for the spin-triplet pairing in $Sr_2RuO_4$. Here, the $\boldsymbol{d}$-vector should be perpendicular to the applied field. Considering the tetragonal crystal symmetry, it is concluded that the $\boldsymbol{d}$-vector is most likely $\boldsymbol{d} = \boldsymbol{z}f(\boldsymbol{k})$.

Another important observation is the spontaneous internal magnetic field in the superconducting state, probed by $\mu$SR.[13] When the crystal of $Sr_2RuO_4$ is cooled below $T_c$ under zero external field, the relaxation rate clearly increases below $T_c$. This indicates the spontaneous emergence of an internal field in the superconducting state. Therefore, the superconducting state of $Sr_2RuO_4$ is characterized by the broken time-reversal symmetry(TRS). In principle, the spontaneous field may arise from either the spin part or the orbital part of the wave function. The spin state that breaks TRS is the non-unitary state. Among the allowed spin-triplet states under the tetragonal symmetry of $Sr_2RuO_4$, the wave function compatible with the results of the Knight shift and $\mu$SR is therefore represented by the $\boldsymbol{d}$-vector $\boldsymbol{d} = \boldsymbol{z}f(k_x \pm ik_y)$.

More recently, the specific heat measurement for the sample with $T_c$ =1.48 K was performed under the magnetic fields precisely parallel to the [110] direction.[81] The temperature-sweep measurements of the electronic specific heat clearly show that a profound change

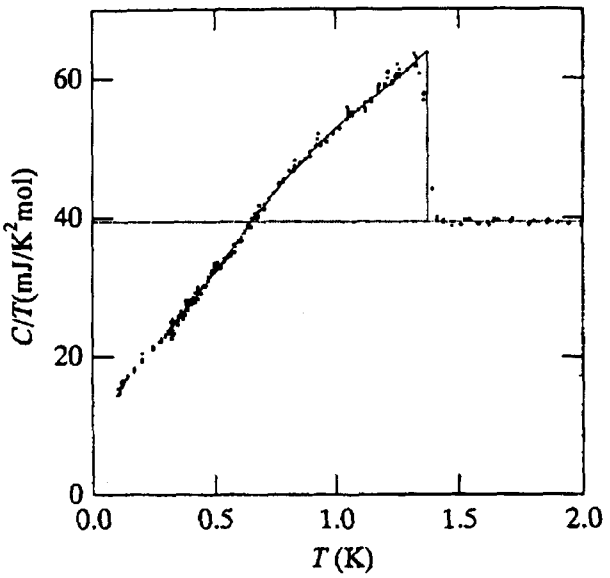


**Fig. 2.3.7** Temperature dependence of the specific heat divided by temperature of $Sr_2RuO_4$.[78)]

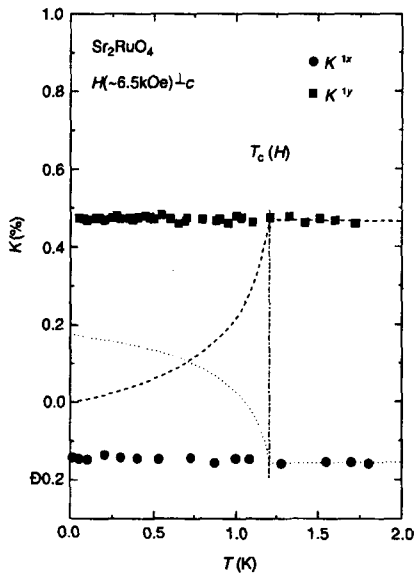


**Fig. 2.3.8** Temperature dependence of the Knight shift $K^{1x}$ and $K^{1y}$ at low temperatures.[14)]

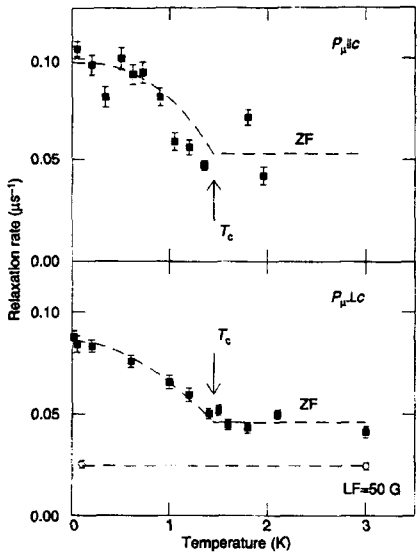


**Fig. 2.3.9** Zero-field relaxation rate for the initial muon spin polarization $\| c$ (top) and $\perp c$ (bottom).[13)]

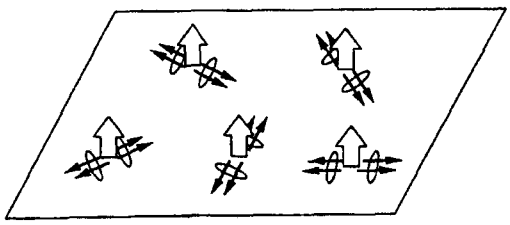

**Fig. 2.3.10** Schematic representation of the spin and orbital parts of the spin-triplet pairing function $\boldsymbol{d} = \boldsymbol{z} f(k_x \pm i k_y)$ on the $RuO_2$ plane.[78)]

in the superconducting state takes place near $T_c$(H) under the fields above 1.2 T. The specific-heat jump at $T_c$(H) contains large entropy release only below 1.1 - 1.2 K. These results indicate that there is a second phase transition in the vincity of $T_c$(H) at low temperatures and under high magnetic fields. In addition, in-plane anisotropy of $H_{c2}$ was reported by Z. Q. Mao *et al.*[82], which shows four-fold symmetry corresponding to the tetragonal crystal structure. The magnitude of the anisotropy shows a sharp decrease above 0.8 K or under slight field misalignment. Then, the anisotropy is enhanced in the region where the second phase transition observed in the $H - T$ phase.

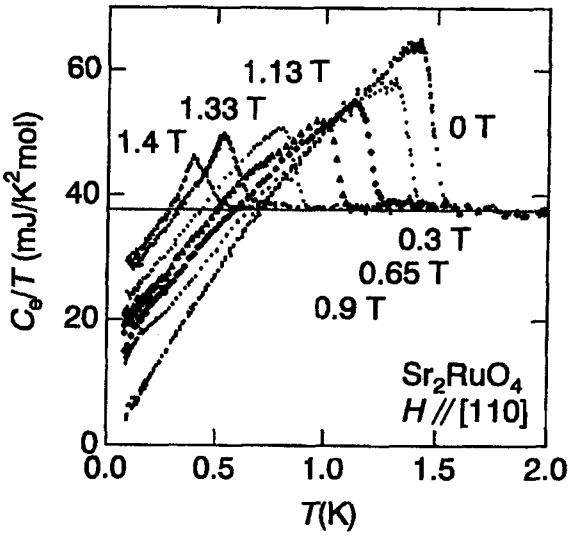


**Fig. 2.3.11** Dependence of the electronic specific heat divided by temperature for the field along [110].[81]

From theoretical studies, the spin-triplet pairing has been suggested over the spin-singlet pairing[15]. Rice and Sigrist had predicted the possibility of the spin-triplet superconductivity stabilized by ferromagnetic spin fluctuation on analogue of superfluid $^3$He[15]. There were proposed five possible $p$-wave pairing states without any gap nodes in a weak spin-orbit coupling scheme. From experimental results mentioned above, the possible pairing state is proposed to be a $p$-wave state expressed by a so-called $\boldsymbol{d}$-vector: $\boldsymbol{d}(\boldsymbol{k}) = \boldsymbol{z}(k_x \pm ik_y)$.[10] This state breaks time-reversal symmetry. The internal field is originated from the orbital part $(k_x \pm k_y)$ of the pair wave function.

Furthermore, the several ideas have been proposed in order to explain the intrinsic residual density of states. One idea is based on the non-unitary $p$-wave superconductivity, which actually realized in $A_1$ phase of $^3$He[83,84]. The other idea is to explain by the orbital dependent superconductivity proposed by Agterberg *et al.*[16] A part of the Fermi surfaces, $(\alpha, \beta)$ or $\gamma$, open up a large superconductivity gap, where $(\alpha, \beta)$ and $\gamma$ sheets are considered to be domained by Ru $d_{xz,yz}$ and $d_{xy}$ orbitals, respectively. It is also proposed

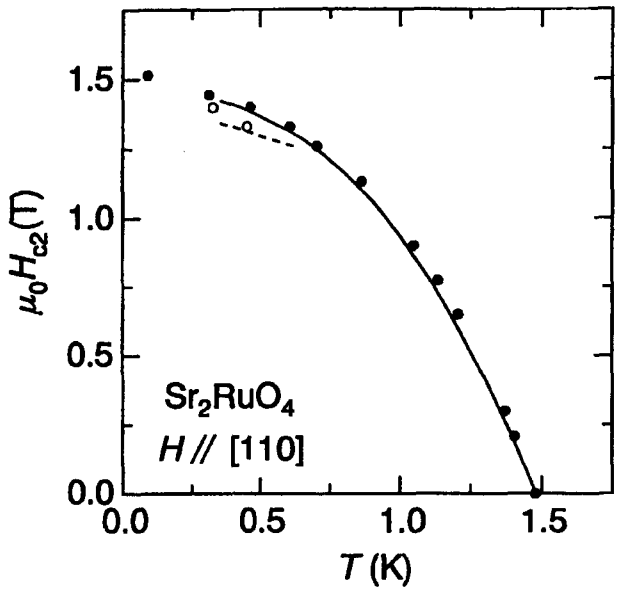


**Fig. 2.3.12** Phase diagram of $Sr_2RuO_4$ for H//[110].[81]

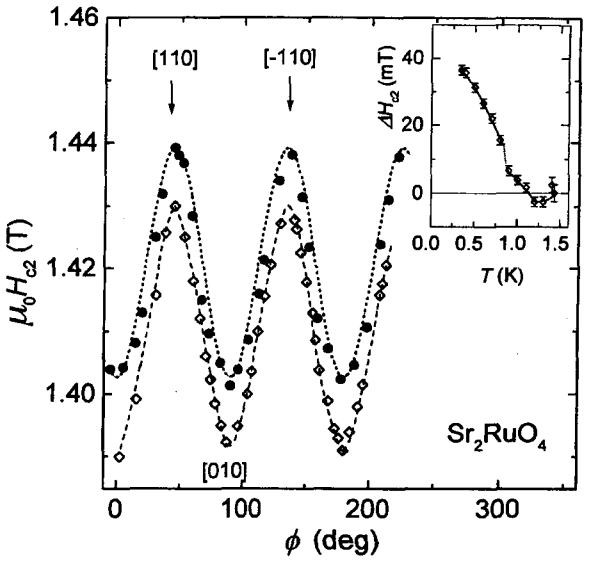


**Fig. 2.3.13** Angular dependence of the in-plane $H_{c2}$.[82]

that the existence of a second phase transition in the mixed state when the magnetic field applied along a high symmetry direction in the basal plane.[85]

Recently, Miyake and Narikiyo have proposed anther theory, in which the exchange-enhanced ferromagnetic coupling dominated between the nearest-neighbor Ru spins leads to the spin-triplet wave function with a strong four-fold anisotropy in the superconducting gap.[17] The ratio between the maximum and minimum of the magnitudes of the gap is of a factor of ten, the specific heat may be explained even if all the bands equally contribute to superconductivity.

### *2.3.3 Energy band structure and Fermi surface*

The band structure calculations were done by some researchers. Among them, to clarify the precise angular dependence of the dHvA frequency, Betsuyaku and Harima have done the energy band structure calculations.[87,88] The Fermi surface was calculated by using an FLAPW method and the local density approximation, which is parametrized by Moruzzi *et al.*[89] Scalar relativistic effects are taken into account for all electrons, and the spin-orbit interaction is included for valence electrons in a second variational procedure. Lattice parameters used in the calculations are the same as the previous report.[6] Self-consistent potential is given from eigen states at sampling 24 k-points in the irreducible Brillouin zone (IBZ), calculated with basis functions truncated at $|\vec{k}+\vec{G}_i| < 4.15\frac{2\pi}{a}$, which correspond to LAPW functions at the $\Gamma$ points. To obtain a final band structure, eigen energies are calculated at 175 k-points in IBZ.

The band structure, as shown in Fig.2.3.14, is very similar to the previous results.[6,7] Total and particial density of states are shown in Fig 2.3.15. Valence bands are formed by the Ru-4*d* and O-2*p* hybridization. Three kinds of cylindrical Fermi surfaces originate in the Ru-4*d* and O-2*p* antibonding bands. The perspective views of the Fermi surfaces are shown in Fig. 2.3.16. The orbits, denoted by $\alpha$, $\beta$ and $\gamma$, are due to the band 17-hole, 19-electron and 18-electron Fermi surfaces, respectively. The band 19-electron Fermi surface is clearly corrugated, which is denoted by $\beta_1$ and $\beta_2$. The theoretical angular dependence of the dHvA frequency are shown in Fig 2.3.17.

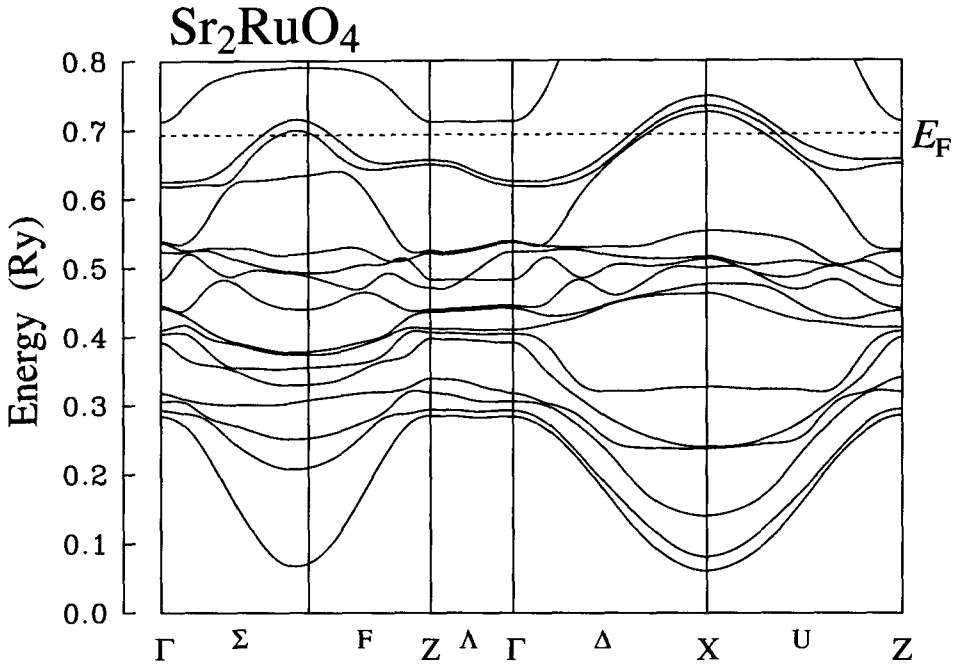


**Fig. 2.3.14** Energy band structure of $Sr_2RuO_4$.The Fermi Energy is 0.6936 Ry denoted by $E_F$. Three bands, which namely consist of Ru-4*d* and O-2*p* components, cross the Fermi energy.

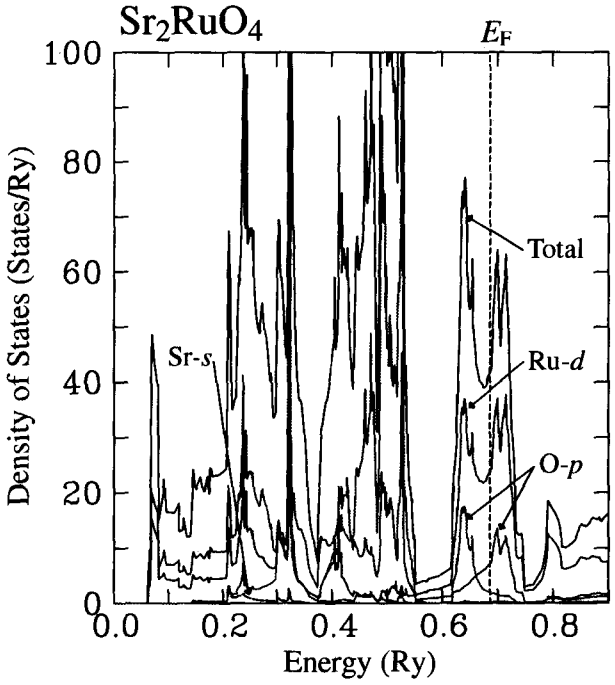


**Fig. 2.3.15** Density of states of $Sr_2RuO_4$. Partial density of states for Sr-*s*, Ru-*d* and O-*p* are also shown.

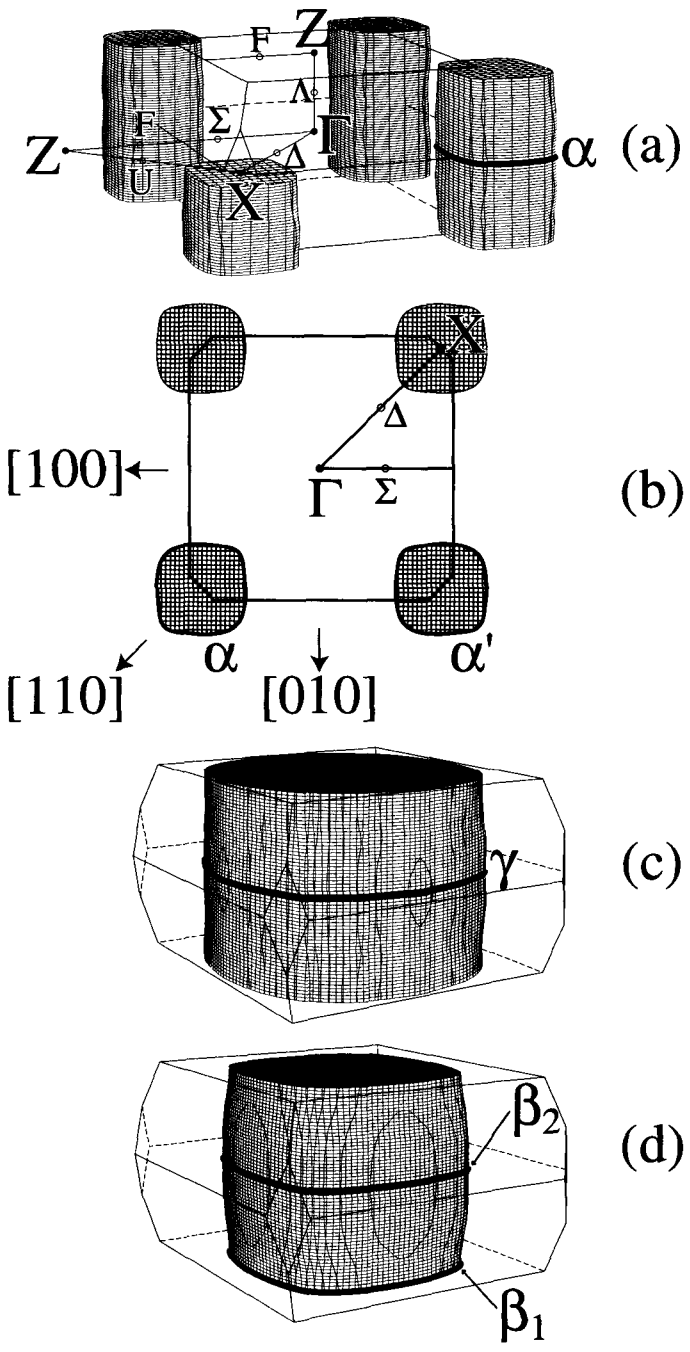


**Fig. 2.3.16** Fermi surfaces of (a) and (b) band 17-hole, (c) band 18-electron and (d) band 19-electron in $Sr_2RuO_4$.

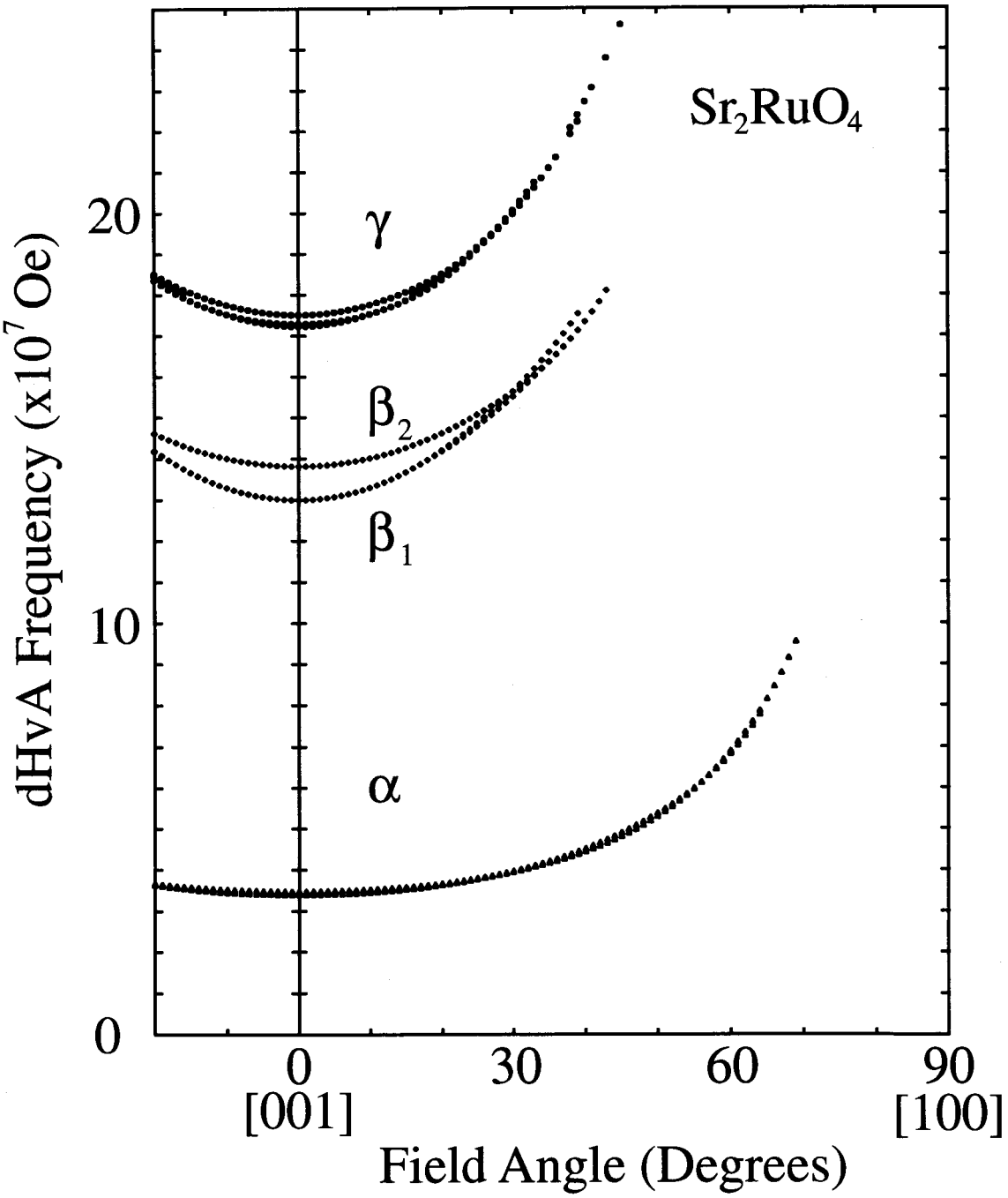


**Fig. 2.3.17** Theoretical angular dependence of the dHvA frequency in $Sr_2RuO_4$.

# Chapter 3 Experimental

## 3.1 Single crystal growth

### *3.1.1 Crystal structure*

$Sr_2RuO_4$ has the tetragonal $K_2NiF_4$-type crystal structure, which is the same as the high $T_c$-superconductor $La_{2-x}Sr_xCuO_4$, as shown in Fig. 3.1.1. The characteristic feature is that the quasi-two dimensional network of $CuO_2$ plane is replaced by the $RuO_2$ one. It

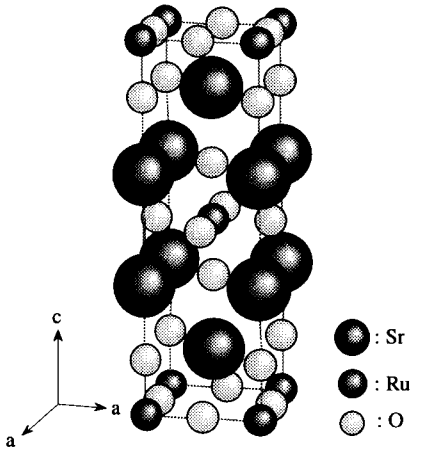


**Fig. 3.1.1** Crystal structure of $Sr_2RuO_4$

has the space group $I4/mmm$ and contains two molecules per unit cell. Crystallographic parameters of $Sr_2RuO_4$ are tabulated in Table3.1-I.

**Table 3.1-I** Crystallographic parameters of $Sr_2RuO_4$

| | | | |
|---|---|---|---|
| **Crystal structure** | $K_2NiF_4$-type | | |
| **Space group** | No.139 $D_{4h}^{17}$ - $I4/mmm$ | | |
| **Lattice constant** | $a = 3.8603$ Å[a] | | |
| | $c = 12.729$ Å | | |
| **Atomic positions** | | | |
| Sr | 4*e*-site $z$=0.3532 | $(0,0,z)$ | $(0,0,\bar{z})$ |
| Ru | 2*a*-site | $(0,0,0)$ | |
| O(1) | 4*c*-site | $(0,1/2,0)$ | $(1/2,0,0)$ |
| O(2) | 4*e*-site $z$=0.1619 | $(0,0,z)$ | $(0,0,\bar{z})$ |

[a]ref. 81

*3.1.2 Sample preparation*

Single crystals of $Sr_2RuO_4$ were grown by a floating-zone technique using a commercial infrared radiation image furnace. The photograph of the furnace was shown in Fig. 3.1.2.

Figure 3.1.3 shows the schematic picture of infrared radiation image furnace. In general, the method of a floating-zone technique is as follows:

1) Set the seed crystal and nutrient rod in the quartz tube.

2) Control the gas condition for the crystal growth.

3) Set the focus of the radiation at the bottom of the nutrient rod.

4) Increase the power until the rod is melt partially, with the seed and nutrient rod rotating.

5) After melting seed crystal partially, connect the both melting zone.

6) Move the focus upward along the nutrient rod. A sweeping speed is usually 3~5 mm/hr.

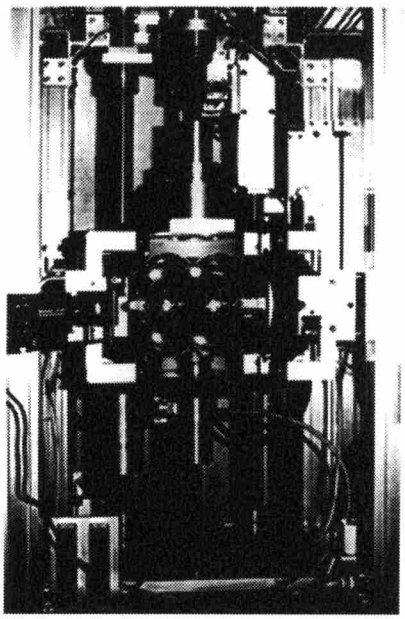

**Fig. 3.1.2** Photograph of a FZ-furnace.

In this study, starting materials were 4N4(99.994%)-$SrCO_3$ and 3N-$RuO_2$. The nutrient rods was made as follows. The reagant powders of $SrCO_3$ and $RuO_2$ were weighted and were mixed in an agate mortar. The mixtures, put into an almina boat, were heated in a muffle furnace in the conditions at 950 °C for 24 hours. The powder was reground and pressed into rods of about 5 mm in diameter and 70 mm in length. The rods were sintered at 1350 °C for 3 hours under a flow of oxygen and/or air. At the first time, a

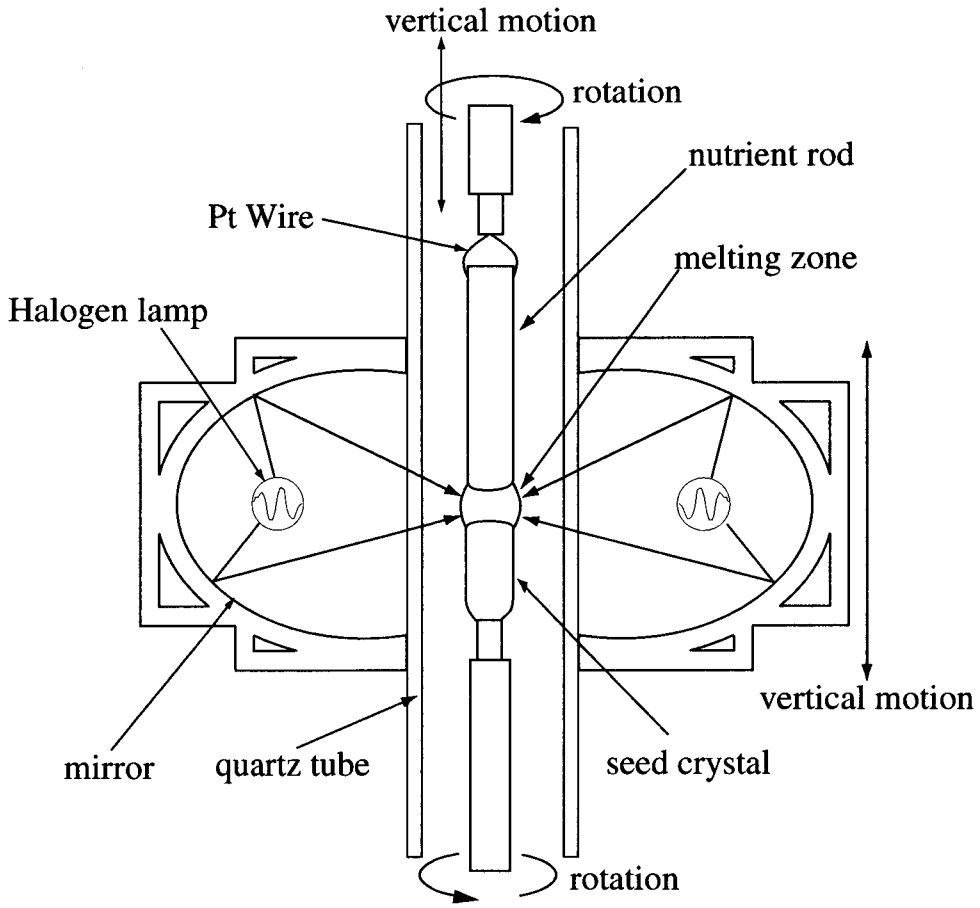


**Fig. 3.1.3** Schematic picture of an infrared radiation image furnace.

short nutrient rod was used as a seed crystal, which was polycrystalline. After several times of growth, a single crystal could be used for the seed crystal. The typical single crystal ingot was about 5 mm in diameter and 50 mm in length, as shown in Fig 3.1.4.

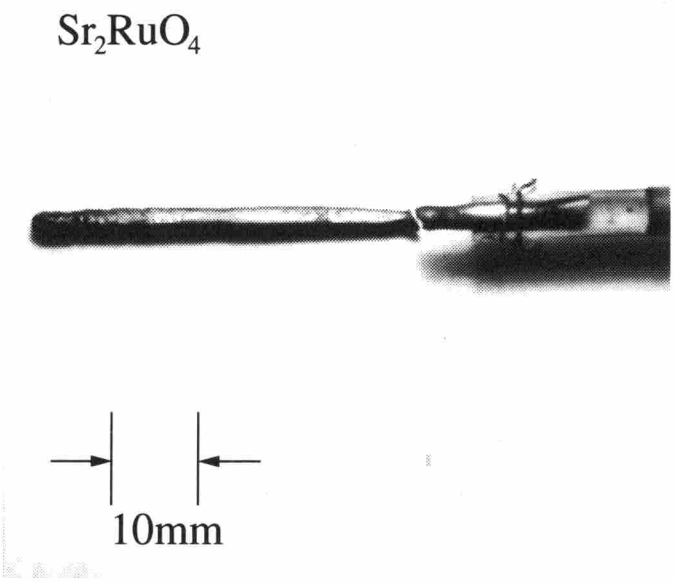


**Fig. 3.1.4** Typical single crystal ingot of $Sr_2RuO_4$.

The growth of $Sr_2RuO_4$ is complicated by evaporation of $RuO_2$, which leads to the segregation of SrO. Considering this evaporation, the ratio in the nutrient rod of $SrCO_3$ to $RuO_2$ was systematically changed from the ratio of 2 to 1. We also tried various condition to the crystal growth, as summarized in Table 3.1-II.

**Table 3.1-II** Condition of the crystal growth of $Sr_2RuO_4$.

| **growth-speed** | **ratio of Sr:Ru** | **atomosphere** | | $T_c$ |
|---|---|---|---|---|
| 6 mm/hr | 2:1.2∼1.3 | 16%$O_2$/84%$N_2$ | 1[atm] | no superconductivity |
| 12 mm/hr | 2:1.15∼1.3 | 16%$O_2$/84%$N_2$ | 1[atm] | no superconductivity or 0.8 K |
| 18 mm/hr | 2:1.1∼1.3 | 16%$O_2$/84%$N_2$ | 1[atm] | 0.8∼1.18 K |
| 40 mm/hr | 2:1.06∼1.24 | 16%$O_2$/84%$N_2$ | 1[atm] | 0.8∼1.2 K |
| | 2:1.1 | 10∼28%$O_2$/90∼72%Ar | 2[atm] | 1.15∼1.3 K |
| | 2:1.06∼1.24 | 14%$O_2$/86%Ar | 4[atm] | 1.0∼1.52 K |
| 60 mm/hr | 2:1.06∼1.12 | 13%$O_2$/87%Ar | 2[atm] | 0.7∼1.24 K |
| | 2:1.1 | 10∼28%$O_2$/90∼72%Ar | 3[atm] | 0.9∼1.24 K |

From this table, the quality of $Sr_2RuO_4$ tends to increase with increasing the growth-speed until 40 mm/hr. It is closely related to the evaporation of $RuO_2$. As the growth-speed becomes slower, evaporation increases more severely. Large evaporation causes a

large quantity of segregation of SrO. In this case, crystals can be easily cleaved at the (001) plane. The similar situation occurs in the case of lack of $RuO_2$.

On the other hand, in the case of too excess of $RuO_2$, the crystal includes metallic Ru in a shape of fine lamellae, as shown by optical microscopy in Fig 3.1.5. It suggests that dissociation of $RuO_2$ occurred during the crystal growth. The dissociation of $RuO_2$ mainly depends on the partial pressure of oxygen. Giving high pressure is an effective way to prevent from dissociation and evaporation. It is also effective to make a melting zone stable during the crystal growth. The high-quality single crystal of $Sr_2RuO_4$ with

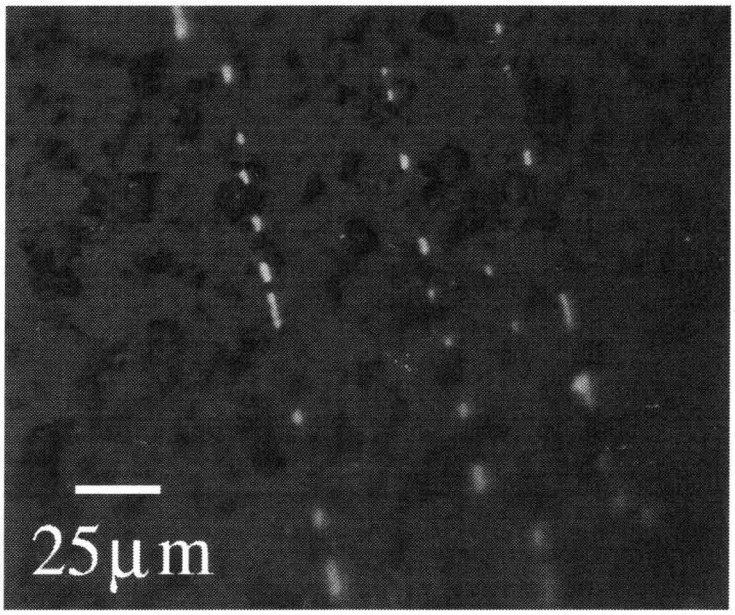


**Fig. 3.1.5** Optical microscopy picture of polished surface of $Sr_2RuO_4$.

$T_c$ = 1.52 K was reproducibly obtained at a speed of 40 mm/hr in a 14%-$O_2$/86%-Ar gas mixture with the total pressure of 4 atm, where the ratio of $SrCO_3$ to $RuO_2$ was 2 to 1.12. For the single crystal growth of the ruthenium oxide, it is important to control evaporation and dissociation of $RuO_2$.

### *3.1.3 Determination of the crystallographic direction of the sample*

We characterized all the obtained samples by the X-ray back Laue method. We show the Laue patterns for the typical planes, (100), (110) and (001) planes of $Sr_2RuO_4$ in Fig 3.1.6. If both ends of an ingot show the same pattern, where we should obtain a mirror image, the ingot is regarded as a single crystal. After determining a sample direction, the pieces of crystals were carefully spark-cut from the ingot.

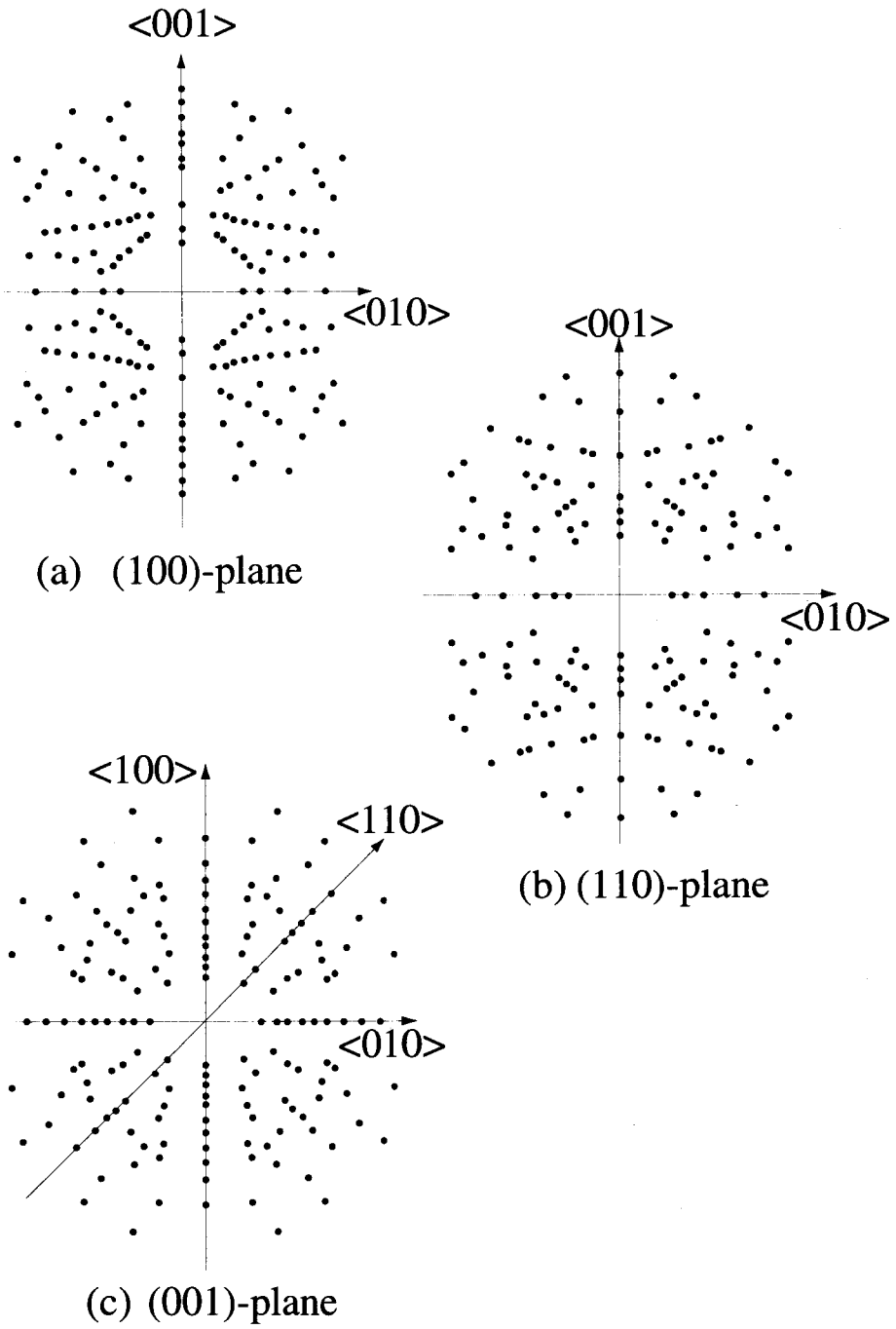


**Fig. 3.1.6** Laue patterns for the typical planes, (a) (100), (b) (110) and (c) (001) of $Sr_2RuO_4$.

## 3.2 Experimental method

### *3.2.1 Electrical resistivity*

1) Introduction

An electrical resistivity consists of four contributions: the electron scattering due to impurities or defects $\rho_0$, the electron-phonon scattering $\rho_{\rm ph}$, the electron-electron scattering $\rho_{\rm e-e}$ and the electron-magnon scattering $\rho_{\rm mag}$ as in

$$\rho = \rho_0 + \rho_{\rm ph} + \rho_{\rm e-e} + \rho_{\rm mag} \quad . \tag{3.2.1}$$

This relation is called a Matthiessen's rule.

The $\rho_0$-value, which is originated from the electron scattering from impurities and defects, is constant for a variation of the temperature. This value is important to determine whether an obtained sample is good or not, because if $\rho_0$ is large, it contains many impurities and defects. A quality of sample can be estimated by determining a so-called residual resistivity ratio (RRR=$\rho_{\rm RT}/\rho_0$), which is a value of a resistivity at room temperature $\rho_{\rm RT}$ divided by $\rho_0$. Of course, a large value of RRR indicates that the quality of sample is good.

Let us introduce a scattering life time $\tau_0$ and a mean free path $l_0$ from the residual resistivity. The residual resistivity $\rho_0$ can be written as

$$\rho_0 = \frac{m^*}{ne} \cdot \frac{1}{\tau_0} \quad , \tag{3.2.2}$$

where $n$ is a density of carrier and $e$ is the electric charge. Then $\tau_0$ and $l_0$ values are

$$\tau_0 = \frac{m^*}{ne\rho_0} \quad , \tag{3.2.3}$$

$$l_0 = v_{\rm F}\tau_0 = \frac{\hbar k_{\rm F}}{ne\rho_0} \quad . \tag{3.2.4}$$

The temperature dependence of $\rho_{\rm ph}$, which is originated from the electron scattering by phonon, changes monotonously. $\rho_{\rm ph}$ is proportional to $T$ above the Debye temperature, while it is proportional to $T^5$ far below the Debye temperature, and $\rho_{\rm ph}$ will be zero at $T = 0$.

In the strongly correlated electron system, the contribution, $\rho_{\rm e-e}$, which can be expressed in terms of the reduction factor of the quasiparticle and the Umklapp process, is dominant at low temperatures. Therefore, we can regard the total resistivity in the non-magnetic compounds at low temperatures as follows:

$$\begin{aligned} \rho(T) &= \rho_0 + \rho_{\rm e-e}(T) \\ &= \rho_0 + AT^2 \quad , \end{aligned} \tag{3.2.5}$$

where the coefficient $\sqrt{A}$ is proportional to the effective mass. Yamada and Yosida obtained the rigorous expression of $\rho_{\rm e-e}$ in the strongly correlated electron system on the

basis of the Fermi liquid theory[38]. According to their theory, $\rho_{e-e}$ is proportional to the imaginary part of the $f$ electron self-energy $\Delta\boldsymbol{k}$, and $\Delta\boldsymbol{k}$ is written as

$$\rho_{e-e} \propto \Delta\boldsymbol{k} \simeq \frac{4}{3}(\pi T)^2 \sum_{k'q} \pi D^f_{\boldsymbol{k}-\boldsymbol{q}}(0) D^f_{\boldsymbol{k}'}(0) D^f_{\boldsymbol{k}'+\boldsymbol{q}}(0) \times \left\{ {\Gamma_{\uparrow\downarrow}}^2(\boldsymbol{k},\boldsymbol{k}';\boldsymbol{k}'+\boldsymbol{q},\boldsymbol{k}-\boldsymbol{q}) + \frac{1}{2}{\Gamma_{\uparrow\uparrow}}^{A2}(\boldsymbol{k},\boldsymbol{k}';\boldsymbol{k}'+\boldsymbol{q},\boldsymbol{k}-\boldsymbol{q}) \right\}, \quad (3.2.6)$$

where $\Gamma_{\sigma\sigma}$ is the four-point vertex, which means the renormalized scattering interaction process of $\boldsymbol{k}(\sigma)\boldsymbol{k}'(\sigma) \rightarrow \boldsymbol{k}'+\boldsymbol{q}(\sigma)\boldsymbol{k}-\boldsymbol{q}(\sigma)$, $\Gamma^{A}_{\uparrow\uparrow}$ is denoted as $\Gamma_{\uparrow\uparrow}(\boldsymbol{k}_1,\boldsymbol{k}_2;\boldsymbol{k}_3,\boldsymbol{k}_4) - \Gamma_{\uparrow\uparrow}(\boldsymbol{k}_1,\boldsymbol{k}_2;\boldsymbol{k}_4,\boldsymbol{k}_3)$, and $D^f_{\boldsymbol{k}}(0)$ is the true (perturbed) density of states of $f$ electrons with mutual interaction in the Fermi level. This $\Delta\boldsymbol{k}$ is proportional to the square of the enhancement factor and gives a large $T^2$-dependence to the heavy fermion system.

2) Experimental method of the resistivity measurement

We have done the resistivity measurement using a standard four probe DC current method. The sample is fixed on a plastic plate by GE7031 varnish. The gold wire ($0.02\,\mathrm{mm}\phi$) and silver paste were used to form contacts on the sample. The sample is mounted on a sample-holder and installed in a $^3$He cryostat. We measured the resistivity in the temperature range from 0.5 K to the room temperature. The applied current is about 1-3 mA. The thermometers are a $RuO_2$ resistor at lower temperatures (below 15 K) and a diode thermocouple at higher temperatures.

### *3.2.2 Transverse magnetoresistance*

1) Introduction to transverse magnetoresistance

High field transverse magnetoresistance $\Delta\rho/\rho = \{\rho(H) - \rho(0)\}/\rho(0)$, in which the directions of the magnetic field and the current are perpendicular each other, provides important information on the overall topology of the Fermi surface, although the experimental technique is simple[45]. Under the high field condition of $\omega_c\tau \gg 1$, it is possible to know whether the sample under investigation is a compensated metal with an equal carrier number of electrons and holes, $n_e = n_h$, or an uncompensated metal, $n_e \neq n_h$, and whether the open orbit exists or not. Here, $\omega_c = eH/m^*_c$ is the cyclotron frequency, $\tau$ the scattering lifetime, $m^*_c$ the effective cyclotron mass and $\omega_c\tau/2\pi$ is the number of cyclotron cycles performed by the carrier without being scattered. The characteristic features of the high field magnetoresistance are summarized as follows for $\omega_c\tau \gg 1$:

(1) For a given field direction, when all of the cyclotron orbits are closed orbits, (a) for the uncompensated metal the magnetoresistance saturates ($\Delta\rho/\rho \sim H^0$), and (b) for the compensated metal the magnetoresistance increases quadratically ($\Delta\rho/\rho \sim H^2$).

(2) For a given magnetic field direction, when some of the cyclotron orbits are not closed but form open orbits, the magnetoresistance increases quadratically and depends on

the current direction as $\Delta\rho/\rho \sim H^2 \cos^2 \alpha$, where $\alpha$ is the angle between the current direction and the open orbit direction in $\boldsymbol{k}$-space. This is true regardless of the state of compensation.

In Fig. 3.2.1 we show this transverse magnetoresistance behavior for a metal with a partially cylindrical Fermi surface whose cylinder axis is in the $k_z$-plane and deviates by an angle $\alpha$ from the $k_x$-axis. Here, the current $\boldsymbol{J}$ is directed along the $k_x$-axis and the magnetic field $\boldsymbol{H}$ rotates in the $k_x$-plane.

If we count the number of valence electrons of various compounds in the unit cell, most of them are even in number, meaning that they are compensated metals. In this case the transverse magnetoresistance increases as $H^n$ $(1 < n \leq 2)$ for a general direction of the field. When the magnetoresistance is saturated for a particular field direction, often a symmetrical direction, some open orbits exist whose directions are parallel to $\boldsymbol{J} \times \boldsymbol{H}$, namely $\alpha = \pi/2$ in $\boldsymbol{k}$-space. We summarize in Table 3.2-I the behavior of magnetoresistance in a high field at each condition.

As the magnetoresistance in the general direction is roughly equal to $(\omega_c \tau)^2$, we can estimate the $\omega_c \tau$ value.

The presence of open orbits is revealed by (a) spikes against a low background for the uncompensated metal (Fig. 3.2.1(c)) and (b) dips against a large background for the compensated metal (Fig. 3.2.1(d)).

2) Experimental method

The magnetoresistance experiment was carried out with a $^3$He cryostat and dilution refrigerator. Measurements were done at temperatures down to 0.4 K and in fields up to 14 T by using a 15 T -superconducting magnet with a $^3$He cryostat, while at temperatures down to 50 mK and in fields up to 17 T by using a 17 T -superconducting magnet with the dilution refrigerator. A technique of the magnetoresistance measurement is almost the same as in the resistivity one. As shown in Fig. 3.2.2, the current direction is fixed to a crystal symmetrical axis of the sample and the sample is rotated in a constant magnetic field.

### *3.2.3 de Hass-van Alphen effect*

1) Introduction to de Haas-van Alphen effect

Under a strong magnetic field the orbital motion of the conduction electron is quantized and forms Landau levels[45]. Therefore various physical quantities show a periodic variation with $H^{-1}$ since increasing the field strength $H$ causes a sharp change in the free energy of the electron system when a Landau level crosses the Fermi energy. In a three-dimensional system this sharp structure is observed at the extremal areas in $\boldsymbol{k}$-plane, perpendicular to the field direction and enclosed by the Fermi energy because the density of state also becomes extremal. From the field and temperature dependences of various physical

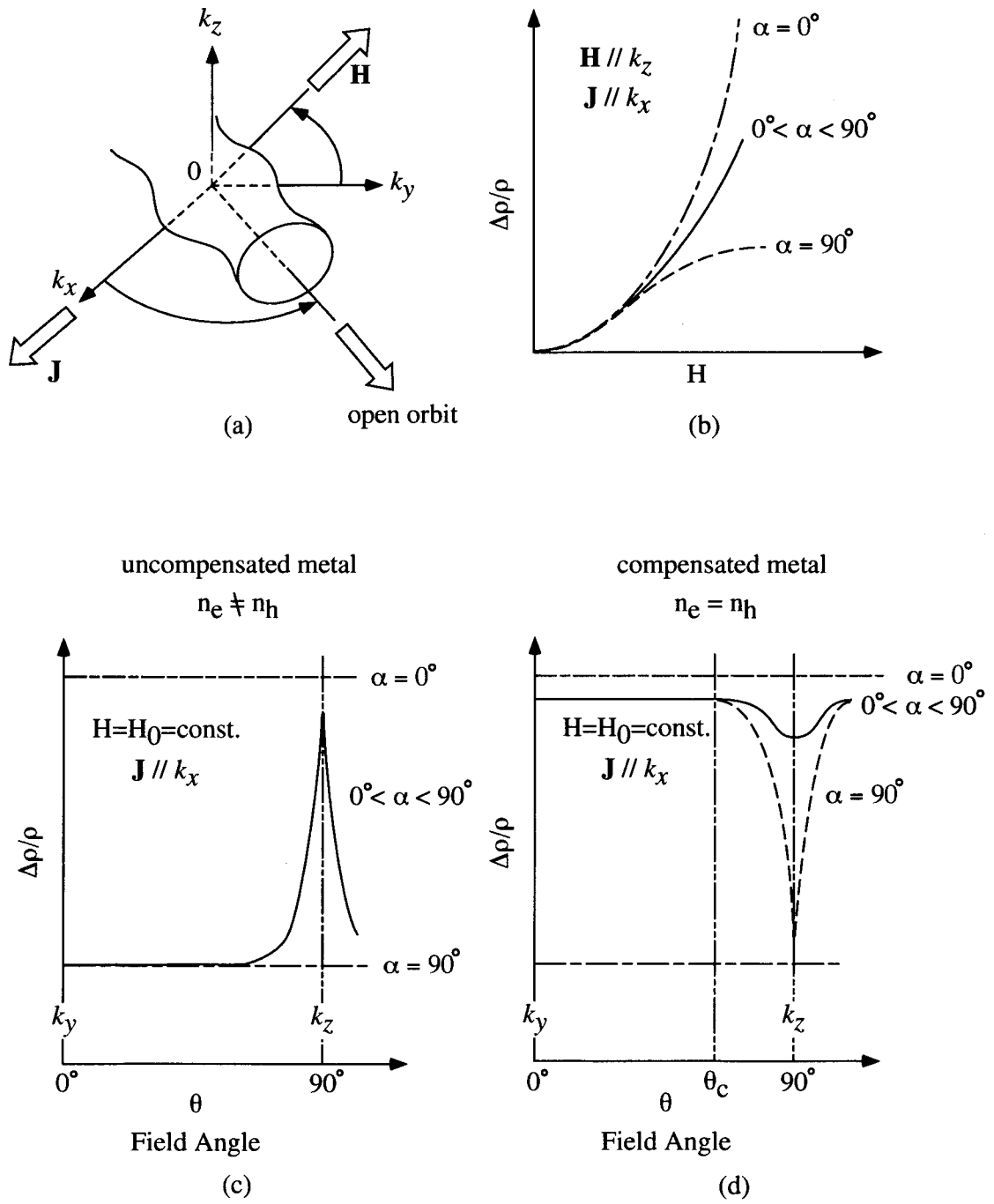


**Fig. 3.2.1** Schematic picture of the transverse magnetoresistances in uncompensated and compensated metals when a partially cylindrical Fermi surface exists. The magnetic field H rotates in the $k_x$-plane.

| open orbit (in k-space) | uncompensated metal | compensated metal |
|---|---|---|
| none | 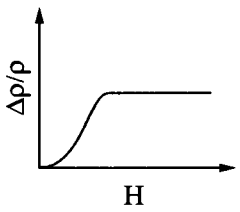  | 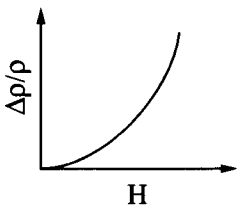  |
| open orbit // **J** | 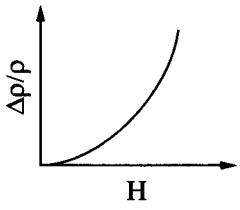  | 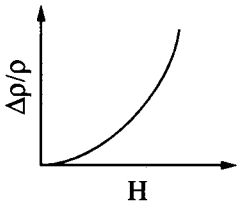  |
| open orbit ⊥ **J** | | |
| When an open orbit exists on the plane sliced vertical with **H** | 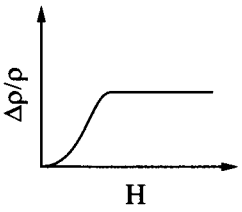  | 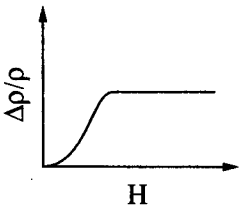  |
| When no open orbit exists on the plane sliced vertical with **H** | 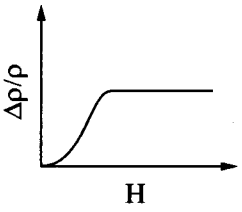  | 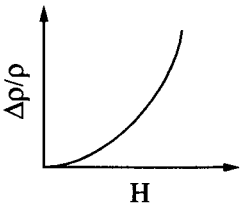  |

**Table 3.2-I** Magnetoresistance in a high field at each condition.

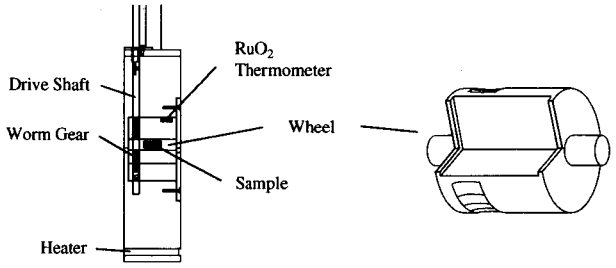


**Fig. 3.2.2** Detailed picture of the sample holder and the inside wheel.

quantities, we can obtain the extremal area $S$, the cyclotron mass $m_c^*$ and the scattering lifetime $\tau$ for this cyclotron orbit. The magnetization or the magnetic susceptibility is the most common one of these physical quantities, and its periodic character is called the de Haas-van Alphen (dHvA) effect. It provides one of the best tools for the investigation of Fermi surfaces of metals.

The theoretical expression for the oscillatory component of magnetization $M_{\rm osc}$ due to the conduction electrons was given by Lifshitz and Kosevich as follows:

$$M_{\rm osc} = \sum_r \sum_i \frac{(-1)^r}{r^{3/2}} A_i \sin\left(\frac{2\pi r F_i}{H} + \beta_i\right) \quad , \tag{3.2.7}$$

$$A_i \propto H^{1/2} \left|\frac{\partial^2 S_i}{\partial k_{\rm H}^2}\right|^{-1/2} R_{\rm T} R_{\rm D} R_{\rm S} \quad , \tag{3.2.8}$$

$$R_{\rm T} = \frac{\lambda r m_{ci}^* T/H}{\sinh(\lambda r m_{ci}^* T/H)} \quad , \tag{3.2.9}$$

$$R_{\rm D} = \exp(-\lambda r m_{ci}^* T_{\rm D}/H) \quad , \tag{3.2.10}$$

$$R_{\rm S} = \cos(\pi g_i r m_{ci}^*/2m_0) \quad , \tag{3.2.11}$$

$$\lambda = 2\pi^2 c k_{\rm B}/e\hbar \quad . \tag{3.2.12}$$

Here the magnetization is periodic on $1/H$ and has a dHvA frequency $F_i$

$$\begin{aligned} F_i &= \frac{\hbar c}{2\pi e} S_i \\ &= 1.05 \times 10^{-8} \quad [\mathrm{Oe \cdot cm^2}] \cdot S_i \quad , \end{aligned} \tag{3.2.13}$$

which is directly proportional to the $i$-th extremal (maximum or minimum) cross-sectional area $S_i$ $(i = 1, \ldots, n)$. The extremal area means a mesh plane in Fig. 3.2.3, where there is one extremal area in a spherical Fermi surface. On the other hand, three extremal areas exist in a dumbbell-shape Fermi surface.

The factor $R_{\rm T}$ in the amplitude $A_i$ is related to the thermal damping at finite temperatures $T$. The factor $R_{\rm D}$ is also related to the Landau level broadening $k_{\rm B}T_{\rm D}$. Here $T_{\rm D}$ is due to both the lifetime broadening and inhomogeneous broadening caused by impurities, crystalline imperfections or strains. $T_{\rm D}$ is called the Dingle temperature and is given by

$$\begin{aligned} T_{\rm D} &= \frac{\hbar}{2\pi k_{\rm B}} \tau^{-1} \\ &= 1.22 \times 10^{-12} \quad [\mathrm{K \cdot sec}] \cdot \tau^{-1} \quad . \end{aligned} \tag{3.2.14}$$

The factor $R_{\rm S}$ is called the spin factor, and related to the difference of phase between the Landau levels due to the Zeeman split. When $g_i = 2$ (free electron value) and $m_c^* = 0.5m_0$, this term becomes zero for $r = 1$. The fundamental oscillation vanish for all values of the field. This is called the zero spin-splitting situation in which the up and down spin contributions to the oscillation cancel out, and this can be useful for determining the value of $g_i$. Note that in this situation the second harmonics for $r = 2$ should gave a full amplitude.

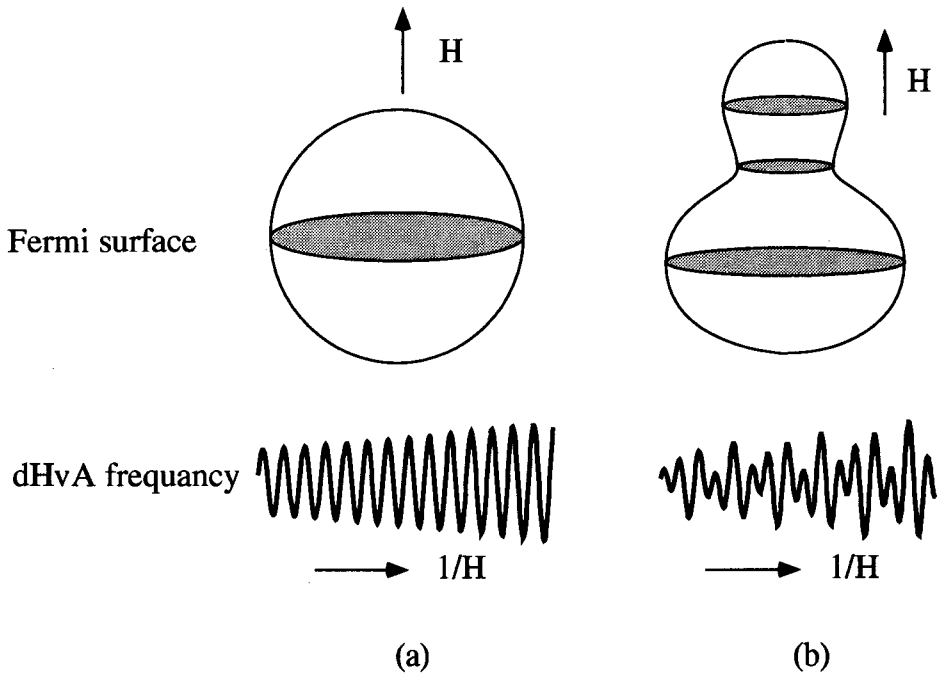


**Fig. 3.2.3** Simulations of the cross-sectional area and its dHvA signal for a simple Fermi surface. There is one dHvA frequency in (a), while there are three different frequencies in (b).

The quantity $\left|\partial^2 S/\partial {k_{\rm H}}^2\right|^{-1/2}$ is called the curvature factor. The rapid change of the cross-sectional area around the extremal area along the field direction diminishes the dHvA amplitude for this extremal area.

The detectable conditions of dHvA effect are as follows:

(1) The distance between the Landau levels $\hbar\omega_{\rm c}$ must be larger than the thermal broadening width $k_{\rm B}T$; $\hbar\omega_{\rm c} \gg k_{\rm B}T$ (high field, low temperature).

(2) At least one cyclotron motion must be performed during the scattering, namely $\omega_{\rm c}\tau/2\pi > 1$ (high quality sample). In reality, however, it can be observed even if a cyclotron motion is about ten percent of one cycle in average.

(3) The fluctuation of the static magnetic field must be smaller than the field interval of one cycle of the dHvA oscillation (homogeneity of the magnetic field).

2) Shape of Fermi surface

The angular dependence of dHvA frequencies gives very important information about a shape of the Fermi surface. As a volume of Fermi surface corresponds to a carrier number, we can obtain the carrier number of metal directly.

We show the typical Fermi surfaces and their angular dependences of dHvA frequencies in Fig. 3.2.4. In a spherical Fermi surface, the dHvA frequency is constant for any field

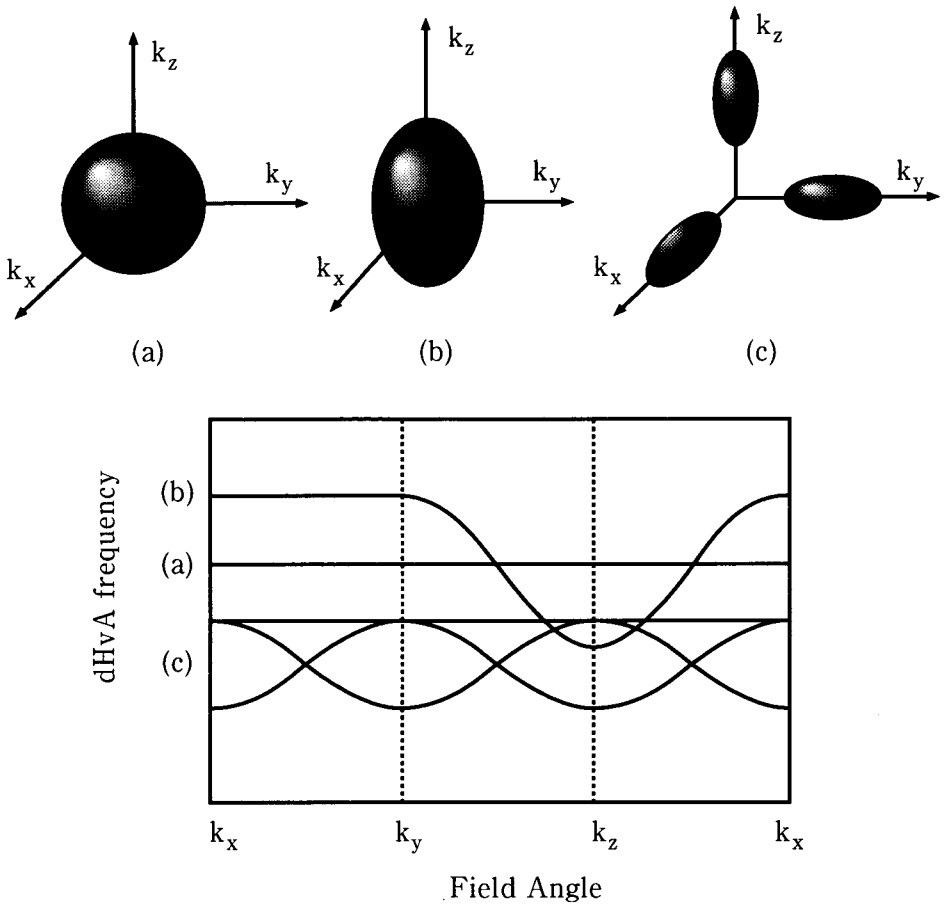


**Fig. 3.2.4** Angular dependence of the dHvA frequency in three typical Fermi surfaces (a) sphere, (b) ellipsoide (on center) and (c) ellipsoide (on axes).

direction. On the other hand, in an ellipsoidal Fermi surface such as in Fig. 3.2.4(b), it takes a minimum value for the field along the $z$-axis. These simple shape of the Fermi surfaces can be determined only by the experiment. However, information from an energy band calculation is needed to determine a complicated one.

3) Cyclotron effective mass

We can determine the cyclotron effective mass $m_{ci}^*$ from measuring a temperature dependence of a dHvA amplitude. Equation (3.2.9) is transformed into:

$$\ln\left\{A_i\left[1-\exp\left(\frac{-2\lambda m_{ci}^* T}{H}\right)\right]/T\right\} = \frac{-\lambda m_{ci}^*}{H}T + \text{const.} \tag{3.2.15}$$

From the slope of a plot of $\ln\left\{A_i\left[1-\exp\left(\frac{-2\lambda m_{ci}^* T}{H}\right)\right]/T\right\}$ versus $T$ at constant field $H$, the effective mass can be obtained.

Let us consider the relation between the cyclotron mass and the electronic specific

heat coefficient $\gamma$. Using a density of states $D(E_F)$, $\gamma$ is written as

$$\gamma = \frac{\pi^2}{3} {k_B}^2 D(E_F) \quad . \tag{3.2.16}$$

In a spherical Fermi surface, using $E_F = \hbar^2 {k_F}^2 / 2m_c^*$ takes

$$\begin{aligned} \gamma &= \frac{\pi^2}{3} {k_B}^2 \cdot \frac{V}{2\pi^2} \left( \frac{2m_c^*}{\hbar^2} \right)^{3/2} {E_F}^{1/2} \\ &= \frac{{k_B}^2 V}{3\hbar^2} \cdot m_c^* \cdot k_F \quad , \end{aligned} \tag{3.2.17}$$

where $V$ is molar volume. $k_F = (S/\pi)^{1/2}$ from eq.(3.2.13), then

$$\begin{aligned} \gamma &= \frac{{k_B}^2 m_0}{3\hbar^2} \left( \frac{2e}{\hbar c} \right)^{1/2} \cdot V \frac{m_c^*}{m_0} F^{1/2} \\ &= 2.87 \times 10^{-6} [\mathrm{mJ/K^2 mol} \cdot (\mathrm{cm^3/mol}) \cdot \mathrm{Oe}] \cdot V \frac{m_c^*}{m_0} F^{1/2} \quad . \end{aligned} \tag{3.2.18}$$

In the case of the cylindrical Fermi surface,

$$\begin{aligned} \gamma &= \frac{\pi^2}{3} {k_B}^2 \cdot \frac{V}{2\pi^2 \hbar^2} \cdot m_c^* k_z \\ &= \frac{{k_B}^2 V}{6\hbar^2} \cdot m_c^* k_z \quad , \end{aligned} \tag{3.2.19}$$

where the Fermi wave number $k_z$ is parallel to axial direction of the cylinder.

4) Dingle temperature

We can determine the Dingle temperature $T_D$ from measuring a field dependence of a dHvA amplitude. Equations (3.2.8)-(3.2.10) yield

$$\ln \left\{ A_i H^{1/2} \left[ 1 - \exp \left( \frac{-2\lambda m_{ci}^* T}{H} \right) \right] \right\} = -\lambda m_{ci}^* (T + T_D) \cdot \frac{1}{H} + \text{const.} \tag{3.2.20}$$

From the slope of a plot of $\ln \left\{ A_i H^{1/2} \left[ 1 - \exp \left( \frac{-2\lambda m_{ci}^* T}{H} \right) \right] \right\}$ versus $1/H$ at constant $T$, the Dingle temperature can be obtained. Here, the cyclotron effective mass must have been already obtained.

We can estimate the mean free path $l$ or the scattering life time $\tau$ from the Dingle temperature. The relation between an effective mass and life time takes the form

$$\hbar k_F = m^* v_F \quad , \tag{3.2.21}$$

$$l = v_F \tau \quad . \tag{3.2.22}$$

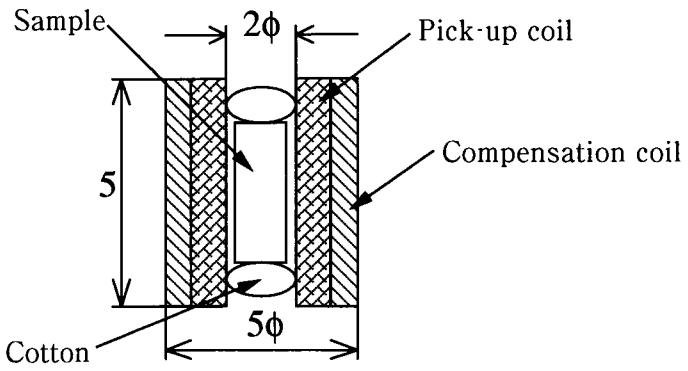


**Fig. 3.2.5** Detecting coil and the sample location.

Then eq. (3.2.14) is transformed into

$$l = \frac{\hbar^2 k_{\mathrm{F}}}{2\pi k_{\mathrm{B}} m_{\mathrm{c}}^* T_{\mathrm{D}}} \quad . \tag{3.2.23}$$

When the extremal area can be regarded as a circle approximately, using eq. (3.2.13), the mean free path is written as

$$\begin{aligned} l &= \frac{\hbar^2}{2\pi k_{\mathrm{B}} m_0} \left(\frac{2e}{\hbar c}\right)^{1/2} \cdot F^{1/2} \left(\frac{m_{\mathrm{c}}^*}{m_0}\right)^{-1} T_{\mathrm{D}}^{-1} \\ &= 0.776 \quad [\text{Å} \cdot \mathrm{Oe}^{-1/2} \cdot \mathrm{K}] \cdot F^{1/2} \left(\frac{m_{\mathrm{c}}^*}{m_0}\right)^{-1} T_{\mathrm{D}}^{-1} \quad . \end{aligned} \tag{3.2.24}$$

5) Field modulation method

Experiments of the dHvA effect were conducted by using the usual ac susceptibility field modulation method. Now we give an outline of the field modulation method in the present study.

A small ac field $h_0 \cos \omega t$ is varied on an external field $H_0$ ($H_0 \gg h_0$) in order to obtain the periodic variation of the magnetic moment. The sample is placed in a pair of balanced coils (pick up and compensation coils) as shown in Fig. 3.2.5, induced emf $V$ will be proportional to

$$\begin{aligned} V &= c\frac{dM}{dt} \\ &= c\frac{dM}{dH}\frac{dH}{dt} \\ &= -ch_0\omega \sin \omega t \sum_{k=1}^{\infty} \frac{{h_0}^k}{2^{k-1}\,(k-1)!} \left(\frac{d^k N}{dH^k}\right)_{H_0} \sin k\omega t \quad , \end{aligned} \tag{3.2.25}$$

where $c$ is the constant which is fixed by the number of turns in the coil and so on, and the higher differential terms of the coefficient of $\sin k\omega t$ are neglected. Calculating the

$(d^kM/dH^k)$ it becomes

$$V = -c\omega A \sum_{k=1}^{\infty} \frac{1}{2^{k-1}(k-1)!} \left(\frac{2\pi h_0}{\Delta H}\right)^k \sin\left(\frac{2\pi F}{H} + \beta - \frac{k\pi}{2}\right) \cdot \sin k\omega t \quad . \tag{3.2.26}$$

Here, $\Delta H = H^2/F$. Considering ${h_0}^2 \ll {H_0}^2$ the time dependence of magnetization $M(t)$ is given by

$$M(t) = A\left[J_0(\lambda)\sin\left(\frac{2\pi F}{H_0} + \beta\right) + 2\sum_{k=1}^{\infty} kJ_k(\lambda)\cos k\omega t \cdot \sin\left(\frac{2\pi F}{H_0} + \beta - \frac{k\pi}{2}\right)\right] \quad , \tag{3.2.27}$$

where

$$\lambda = \frac{2\pi F h_0}{{H_0}^2} \quad . \tag{3.2.28}$$

Here, $J_k$ is $k$-th Bessel function. Finally we can obtain the output emf as follows:

$$V = c\left(\frac{dM}{dt}\right) = -2c\omega A \sum_{k=1}^{\infty} kJ_k(\lambda)\sin\left(\frac{2\pi F}{H_0} + \beta - \frac{k\pi}{2}\right) \cdot \sin k\omega t \quad . \tag{3.2.29}$$

The signal was detected at the second harmonic of the modulation frequency $2\omega$ using a lock-in-amplifier, since this condition may cut off the offset magnetization and then detect the component of the quantum oscillation only. We usually choose the modulation field $h_0$ to make the value of $J_2(\lambda)$ maximum, namely $\lambda = 3.1$. We used a modulation frequency of 334 Hz for the $^3$He cryostat or 36.3 Hz for the dilution refrigerator, respectively. Fig. 3.2.6 shows a block diagram for the dHvA measurement in the present study.

### *3.2.4 Specific heat*

1) General

At low temperatures, the specific heat in the normal state $C_{\rm n}$ is written as the sum of electronic, lattice, magnetic and nuclear contributions as follows:

$$\begin{aligned} C_{\rm n} &= C_{\rm e} + C_{\rm ph} + C_{\rm mag} + C_{\rm nuc} \\ &= \gamma T + \beta T^3 + C_{\rm mag} + \frac{A}{T^2}, \end{aligned} \tag{3.2.30}$$

where $A$, $\gamma$ and $\beta$ are constants characteristic of the material.

The electronic term is linear as a function of temperature and is dominant at sufficiently low temperatures. If we can neglect the the magnetic and nuclear contributions, it is convenient to exhibit the experimental values of $C_{\rm n}$ in the normal state as a plot of $C_{\rm n}/T$ versus $T^2$:

$$C_{\rm n}/T = \gamma + \beta T^2, \tag{3.2.31}$$

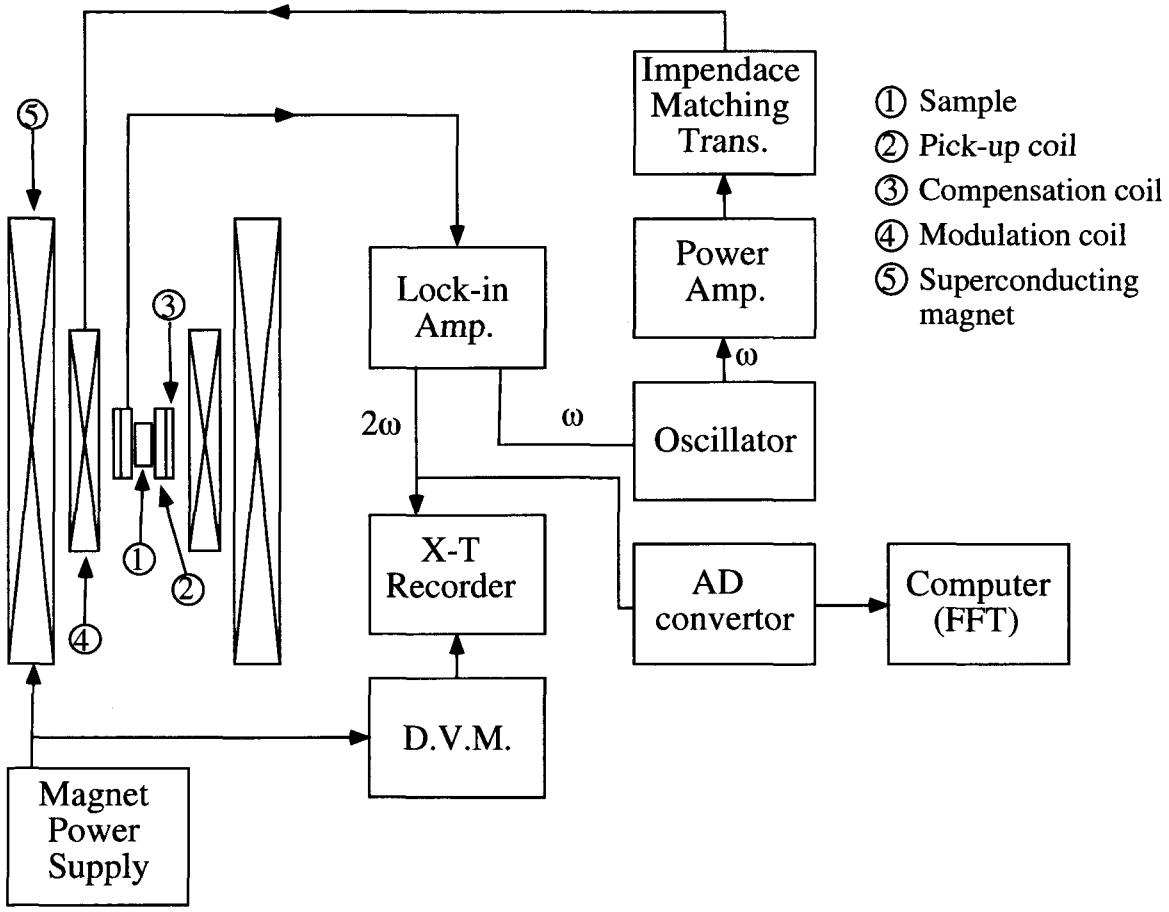


**Fig. 3.2.6** Block diagram for the dHvA measurement.

, where $\gamma$ is called the electronic specific heat coefficient or Sommerfeld coefficient. Using free-electrons gas model, for $k_{\mathrm{B}}T \ll \varepsilon_{\mathrm{F}}$, the electronic specific heat $C_{\mathrm{e}}$ in the normal state can be expressed as

$$C_{\mathrm{e}} = \frac{\pi^2}{3} k_{\mathrm{B}} D(\varepsilon_{\mathrm{F}}) T \equiv \gamma T, \tag{3.2.32}$$

where $\gamma$ is related to the density of state at the Fermi energy $D(\epsilon_{\mathrm{F}})$. For the free-electron with a mass $m_0$ the $\gamma$-value can be represented as follows:

$$\gamma = \frac{\pi^2}{3} k_{\mathrm{B}}^2 D(\varepsilon_{\mathrm{F}}) = \frac{\pi^2 k_{\mathrm{B}}^2 m_0 N_{\mathrm{A}}}{\hbar^2 (3\pi^2 N/V)^{2/3}}, \tag{3.2.33}$$

where $N_{\mathrm{A}}$ is Avogadro's number and $N/V$ is the number of conduction electrons per unit volume.

As mentioned above in section 2.2.2, the electronic specific heat in the superconducting state $C_{\mathrm{s}}$ can be expressed an exponential form for the BCS superconductor and power laws for anisotropic superconductors such as heavy fermion superconductors.

According to the Debye $T^3$ law, for $T \ll \Theta_{\mathrm{D}}$, the specific heat based on the phonon contribution is written as follows:

$$C_{\mathrm{ph}} \cong \frac{12\pi^4 N k_{\mathrm{B}}}{5} \left( \frac{T}{\Theta_{\mathrm{D}}} \right)^3 \equiv \beta T^3, \tag{3.2.34}$$

where $N$ is the number of atoms and $R$ the gas constant. Therefore, the Debye characteristic temperature $\Theta_{\mathrm{D}}$ can be represented as follows:

$$\Theta_{\mathrm{D}} = \sqrt[3]{\frac{12\pi^4 N k_{\mathrm{B}}}{5\beta}} \tag{3.2.35}$$

For actual lattices the temperatures at which the $T^3$ approximation holds are quite low. It may be necessary to be below $T = \Theta_{\mathrm{D}}/50$ to get a reasonable $T^3$ law.

2) Experimental

The specific heat was measured in collaboration with laboratories of Prof. N. Wada in University of Tokyo and of Prof. H. Sato in Tokyo Metropolitan University. It was measured by the quasi-adiabatic heat pulse method using a dilution refrigerator in magnetic fields up to 20 kOe and at low temperatures down to 70 mK.

In Wada laboratory, the sample was put on the Ag-addenda, which is arranged horizontally, with APIEZON N grease. The addenda and Cu-heat bath have thermal links through copper lead wire. In Sato laboratory, the sample was put on the Cu-addenda, which is arranged lengthways, with GE vanish. The addenda and Cu-heat bath have thermal links through a very thin silver wire. There is slightly a flow of heat.

To equilibrate the system, we can use the heater set on the addenda. After the addenda sufficiently reached thermal equibrium, we started a specific heat measurement. We can

measure the temperature of a sample with constant heating and the specific heat, deduced as follows:

$$C = \frac{\Delta Q}{\Delta T} = \frac{I \cdot V \cdot \Delta t}{\Delta T}. \tag{3.2.36}$$

Here, $\Delta Q$ is the amount of heat, $I$ and $V$ are the current and the voltage flowing to the heater, respectively, $\Delta t$ is the duration of heating and $\Delta T$ is a change of temperature due to heating. The temperature was measured by the $RuO_2$(Sato laboratory) resistor or carbon(Wada laboratory) resistor at the addenda. The specific heat of the sample is derived by subtracting the specific heat of the addenda measured. All of the these experiments were carried out after field cooling process.

We note that the usual temperature dependence of the specific heat in the temperature range from 0.5 K to 3 K was measured in our laboratory by the usual quasi-adiabatic heat pulse method mentioned above. This measurement is important to determine the critical temperature $T_c$ for each sample.

# *Chapter 4* Experimental Results and Discussion

## 4.1 Electrical resistivity

We measured the temperature dependence of the electrical resistivity of a sample #A with two different current directions, as shown in Fig. 4.1.1. The current was applied along the [100] and [001] directions, corresponding to the open circles and triangles, respectively. A large anisotropy was observed in the normal-state resistivity, which is the same as the previous report.[4] The characteristic behavior was a broad maximum at about 130 K in the interlayer resistivity $\rho_{[001]}$. The in-plane resistivity $\rho_{[100]}$ shows metallic behavior in the whole temperature range. On the other hand, $\rho_{[001]}$ changes to non-metallic behavior at high temperatures. A crossover occurs from 2D metallic behavior to 3D metallic behavior at the broad maximum temperature. The anisotropy ratio increase from about 140 at 300 K to about 650 at 4.2 K. Because of this large anisotropy, it was crucial to achieve a uniform current distribution for the measurements of $\rho_{[100]}$. The temperature dependence of $\rho_{[100]}$ slightly contains the contribution of $\rho_{[001]}$ in our measurements.

The resistivities at room temperature are about 260$\mu\Omega$·cm for $\rho_{[100]}$ and about 35m$\Omega$·cm for $\rho_{[001]}$, while the resistivity at low temperatures is quite different: 0.54 $\mu\Omega$·cm at 0 K and 0.35m$\Omega$·cm, respectively. Here the residual resistivity is estimated following a Fermi liquid formula $\rho = \rho_0 + AT^2$ below 20K. The residual resistivity ratio $\rho_{RT}/\rho_0$ is thus 480 for $\rho_{[100]}$ and 90 for $\rho_{[001]}$. These values indicate high quality for the present sample.

The temperature dependence of both $\rho_{[100]}$ and $\rho_{[001]}$ at low temperatures are shown in Fig. 4.1.2. In the current direction along [001], we show the temperature dependence of the different two samples in quality, named #A and #B. With the sample #A, superconductivity occurs below 1.45 K for both current directions. On the other hand, the critical temperature of the sample #B is 1.2 K.

## 4.2 Magnetoresistance

We show in Fig. 4.2.1 the magnetoresistance of the sample #A with the current along [001] for the field along [100], [110] and [001] at 50 mK. The magnetoresistance for the field along [100], which is the transverse magnetoresistance, increases linearly with increasing the field. For the field along [110] the magnetoresistance increases $H^{1.5}$-dependence with increasing the field. It is because that $Sr_2RuO_4$ is not a compensated metal and the direction of the carriers is perpendicular to the current direction in real space. There is an anisotropy of the field direction between [100] and [110]. This will be discussed later. On the other hand, a saturated behavior in H//[001] is usual in the longitudinal magnetoresistance.

We show in Fig. 4.2.2(a) the angular dependence of the magnetoresistance under the stationary magnetic fields of 80 and 170 kOe at 80 mK. Here the field is tilted from [001]

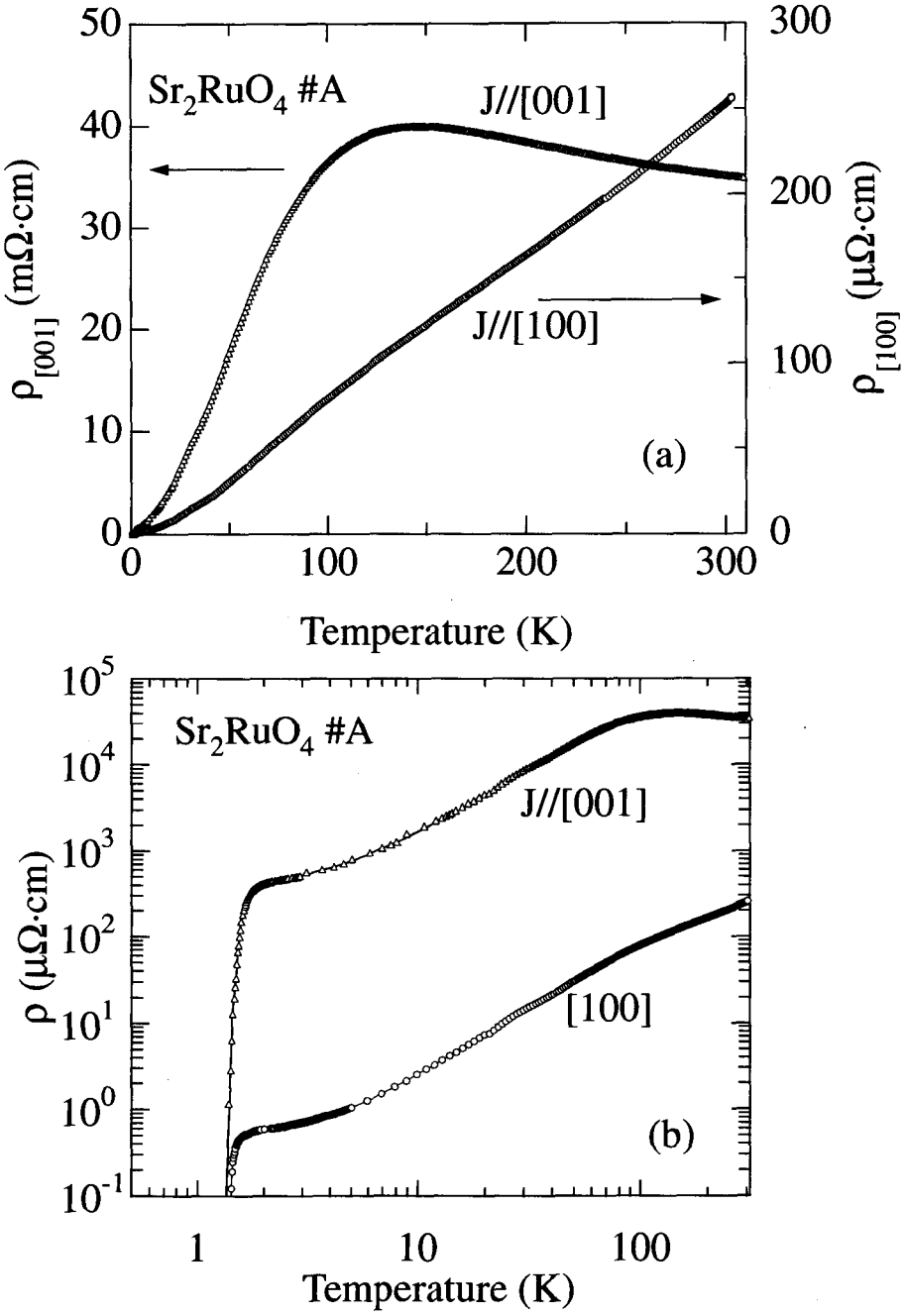


**Fig. 4.1.1** Temperature dependence of the electrical resistivity in $Sr_2RuO_4$.

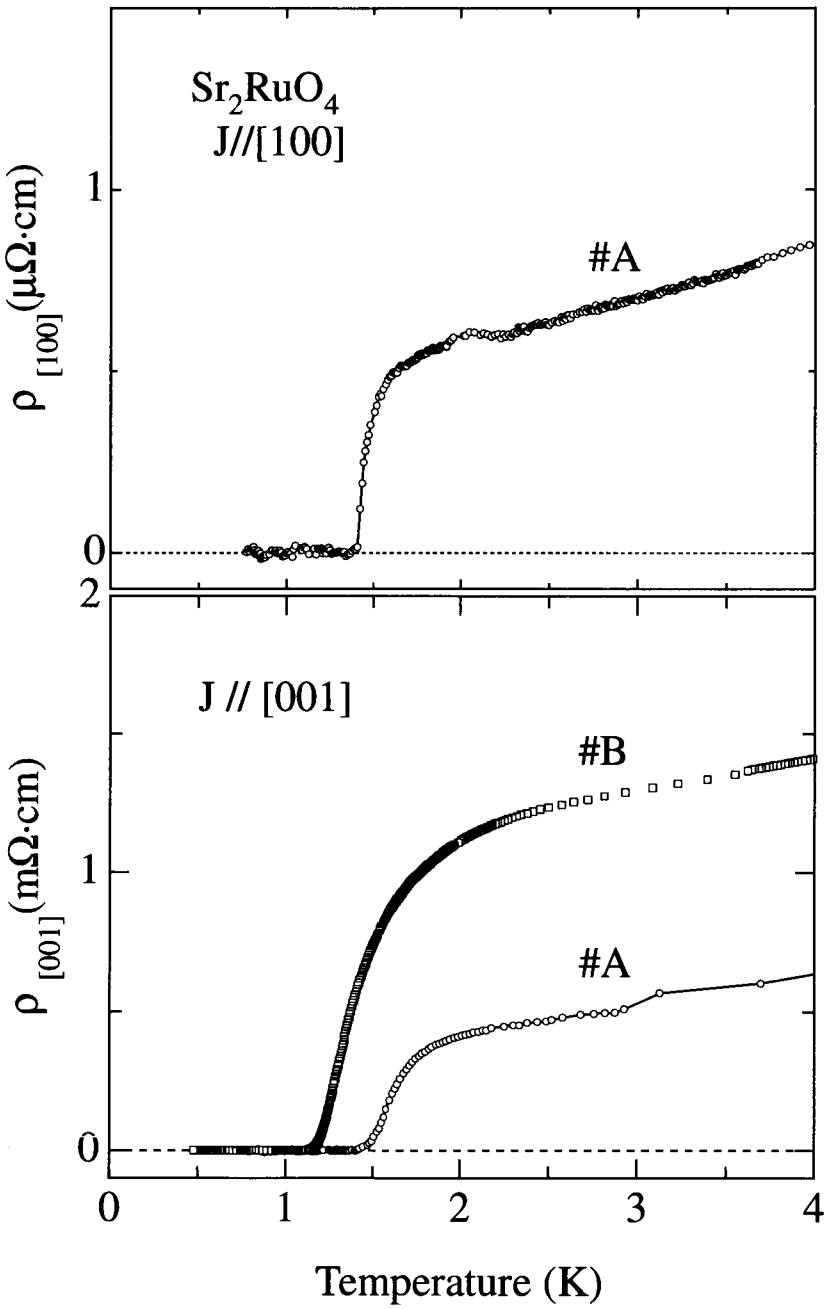


**Fig. 4.1.2** Temperature dependence of the electrical resistivity in $Sr_2RuO_4$.

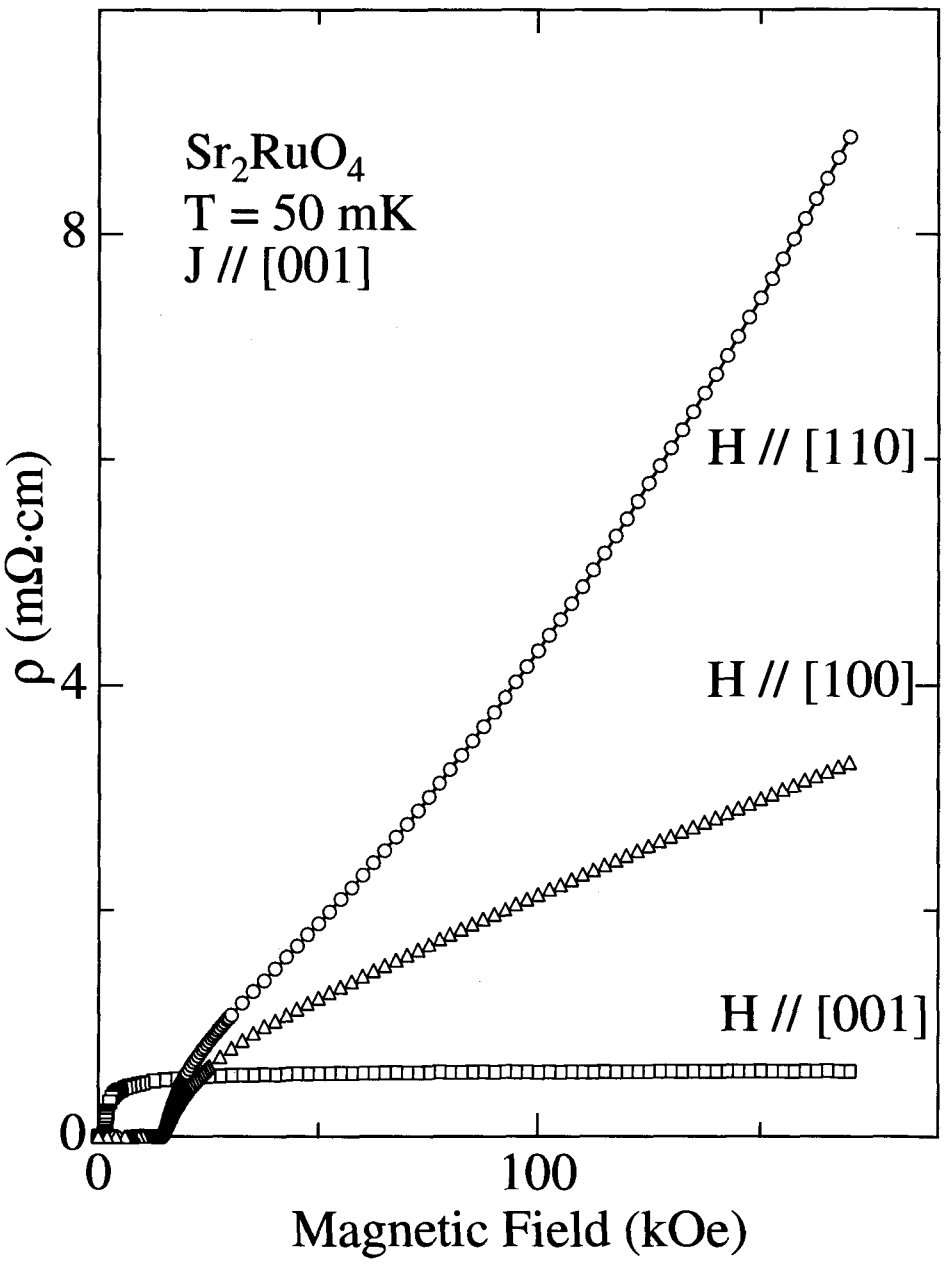


**Fig. 4.2.1** The magnetoresistance for the field along [100], [110] and [001] at 50 mK in $Sr_2RuO_4$(sample #A).

to [100]. A characteristic oscillatory behavior is found in the angular dependence of the magnetoresistance. Many peaks are observed at 31°, 55°, 66° 71° and 75°. These peaks are enhanced when the field is increased. We note that this oscillatory behavior of the magnetoresistance is mainly due to the Yamaji effect for two Fermi surfaces, as discussed in Chap.2. The Yamaji effect generally occurs when the following condition is satisfied:

$$ck_{\mathrm{F}} \tan\theta_n = \pi(n - 1/4), \tag{4.2.1}$$

where $c$=12.73 Å is the lattice constant along the $z$-axis or [001] and $k_{\mathrm{F}}$=0.30, 0.61 and 0.74Å$^{-1}$ are the Fermi wave numbers of the Fermi surface $\alpha$, $\beta$ and $\gamma$, respectively, which are obtained from dHvA experiments, shown in the next section. The spacing of the Brillouin zone along the $c$-axis in eq. (4.2.1) is $2\pi/c$. In the present $Sr_2RuO_4$, the crystal structure is body-centered tetragonal. The corresponding spacing is thus $4\pi/c$, which is applied to the Fermi surfaces $\beta$ and $\gamma$ centered at the $\Gamma$ point. In this case, eq. (4.2.1) is changed into $ck_{\mathrm{F}} \tan\theta_n = 2\pi(n - 1/4)$. On the other hand, the Fermi surface $\alpha$ is located at the X point, as shown in Fig. 2.3.16. The spacing becomes half of that centered at the $\Gamma$ point. Therefore, eq. (4.2.1) is applied to all Fermi surfaces. In fact, the peak position in Fig. 4.2.2(b) is in good agreement with a theoretical straight solid line derived by eq. (4.2.1).

Next, we show in Fig. 4.2.3(a) the angular dependence under the stationary magnetic fields, tilted from [001] to [110]. The similar oscillatory behavior based on the Yamaji effect is observed at 30°, 53°, 65° and 70°. The peak position in Fig. 4.2.3(b) is also in good agreement with a theoretical straight line. We note that the similar experiment was done by Ohmichi *et al.*, most likely indicating a combined oscillatory feature between the Fermi surfaces $\alpha$ and $\beta$. [91]

Angular dependences of the magnetoresistance at 0.5 K are also shown in Figs. 4.2.4(a) and (b).[87] In this condition, the peak is broad and small in amplitude, compared to that in Figs. 4.2.2(a) and 4.2.3(a) and the oscillation of the magnetoresistance is mainly due to the Fermi surface $\alpha$. It is because that the dHvA oscillation at the present condition of fields and temperature of 0.5 K mainly come from the branch $\alpha$. The branch $\beta$ has a small amplitude. This will be discussed later. A high-field condition is satisfied for the branch $\beta$ when a much lower temperature than 0.5 K is hold for the present sample. We could not observe the oscillatory behavior based on the Fermi surface $\gamma$.

In addition to the oscillatory behavior due to the Yamaji effect, a sharp peak is found for the field along [110], as shown in Fig. 4.2.3(a). This effect occurs when the carriers move along the field direction, namely perpendicularly to the current direction $J$. This is closely related to the curvature of the cylindrical Fermi surface $\alpha$. The Fermi surface $\alpha$ has a convex part along [110], as shown in Fig. 4.2.5. This is the reason for in-plane anisotropy of the magnetic field dependence.

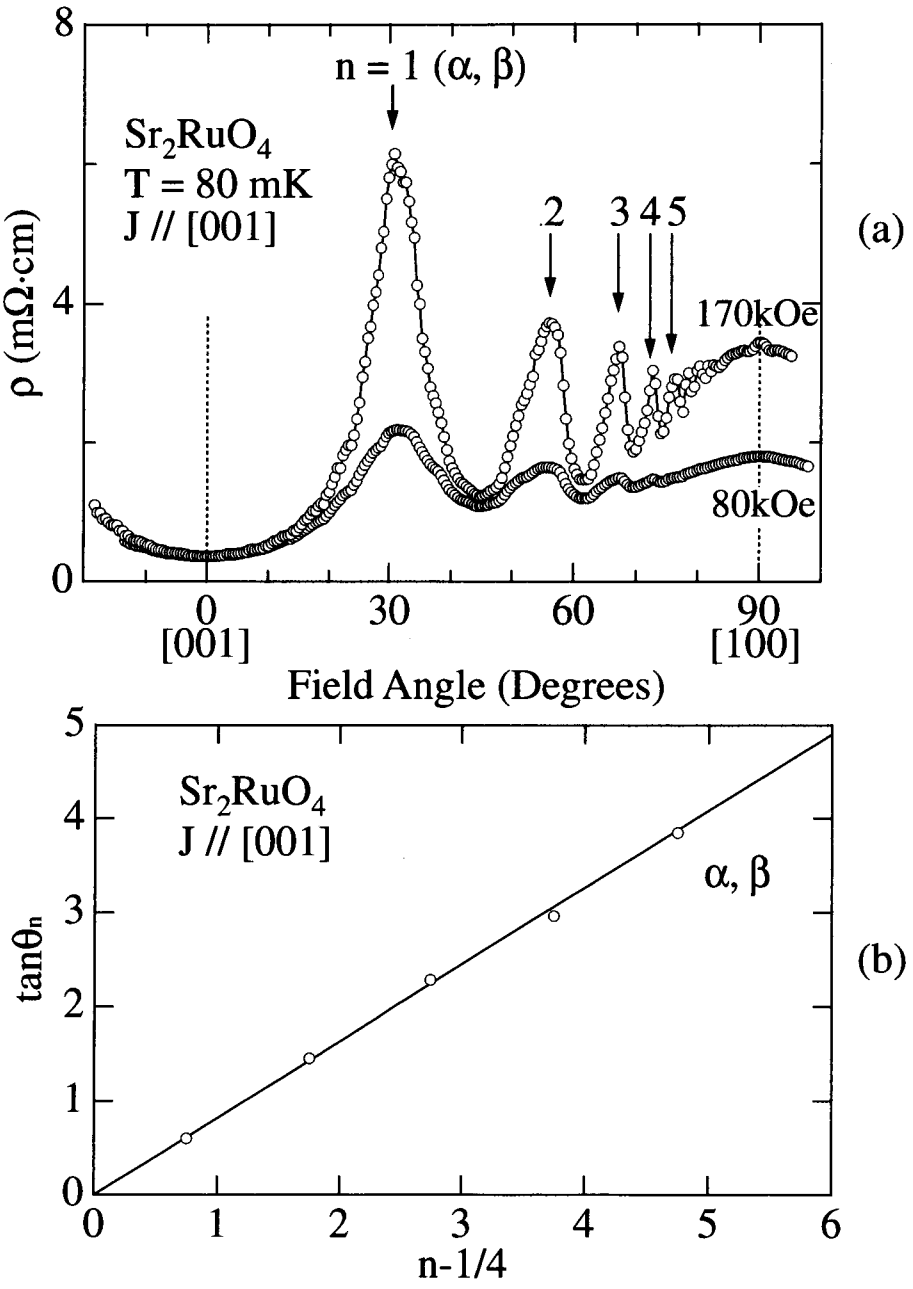


**Fig. 4.2.2** (a)Angular dependence of the magnetoresistance under several magnetic field tilted from [001] to [100] at 80 mK and (b)the Yamaji relation for two branches in $Sr_2RuO_4$.

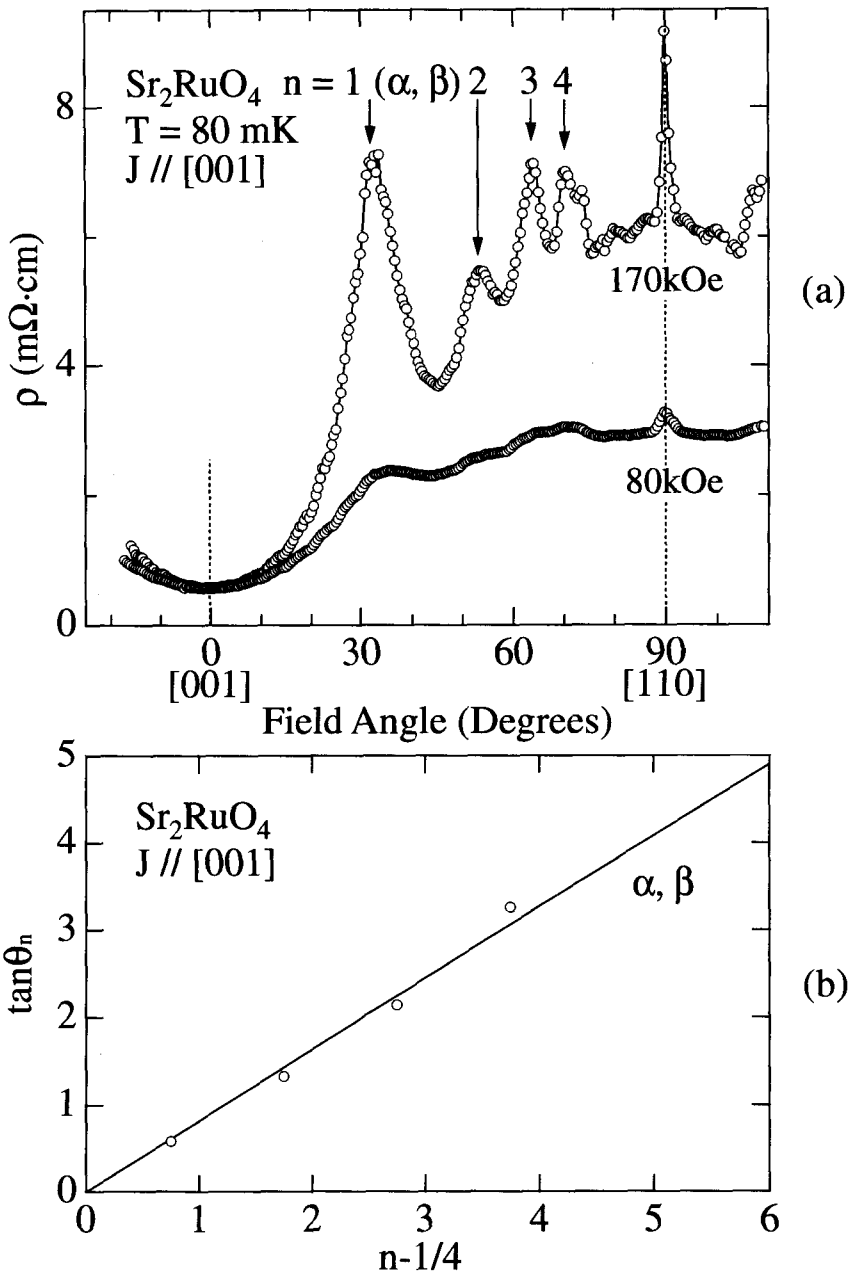


**Fig. 4.2.3** (a)Angular dependence of the magnetoresistance under several magnetic field tilted from [001] to [110] at 80 mK and (b)the Yamaji relation for two branches in $Sr_2RuO_4$(sample #A).

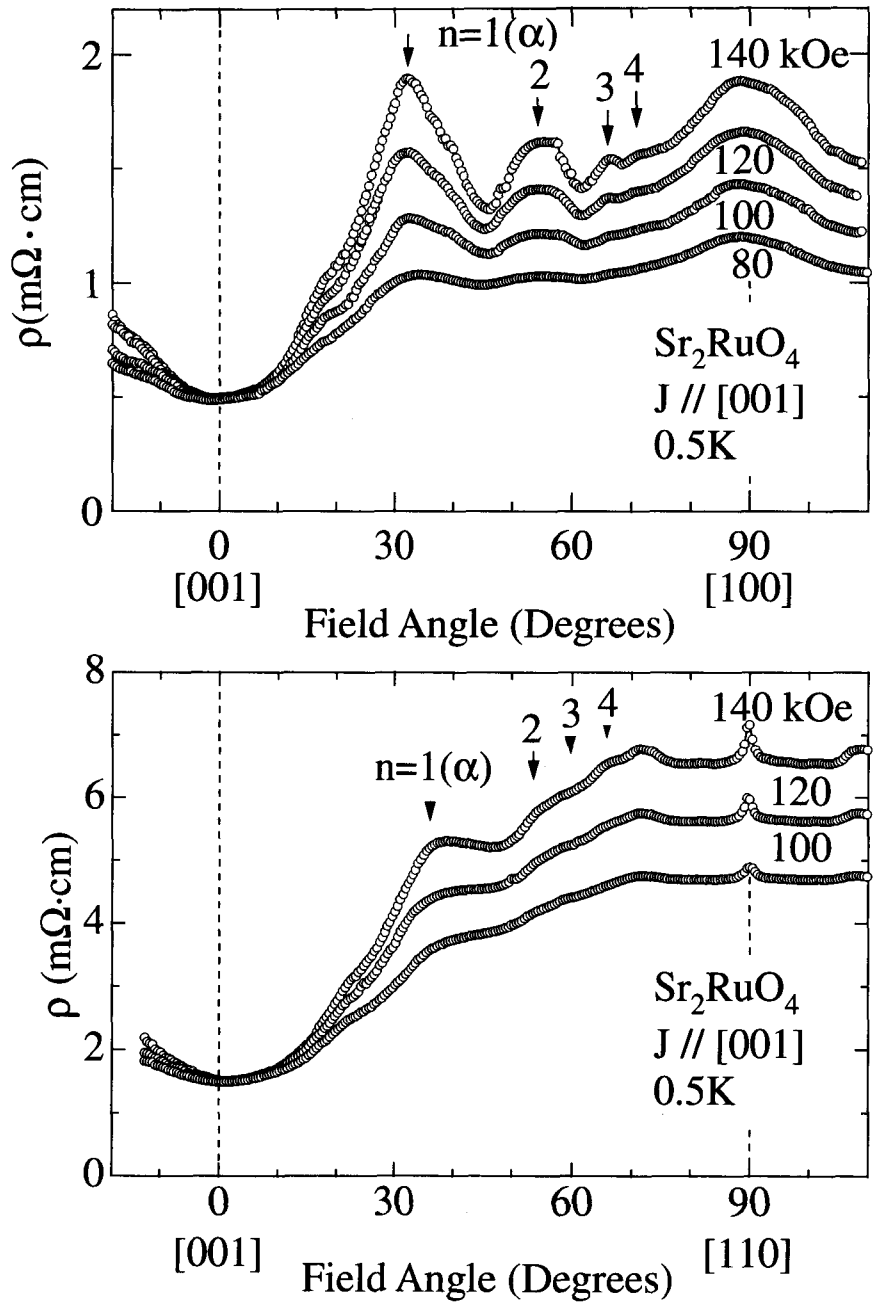


**Fig. 4.2.4** Angular dependence of the magnetoresistance under several magnetic field (a)tilted from [001] to [110] and (b)tilted from [001] to [110] at 0.5 K in $Sr_2RuO_4$(sample #A).

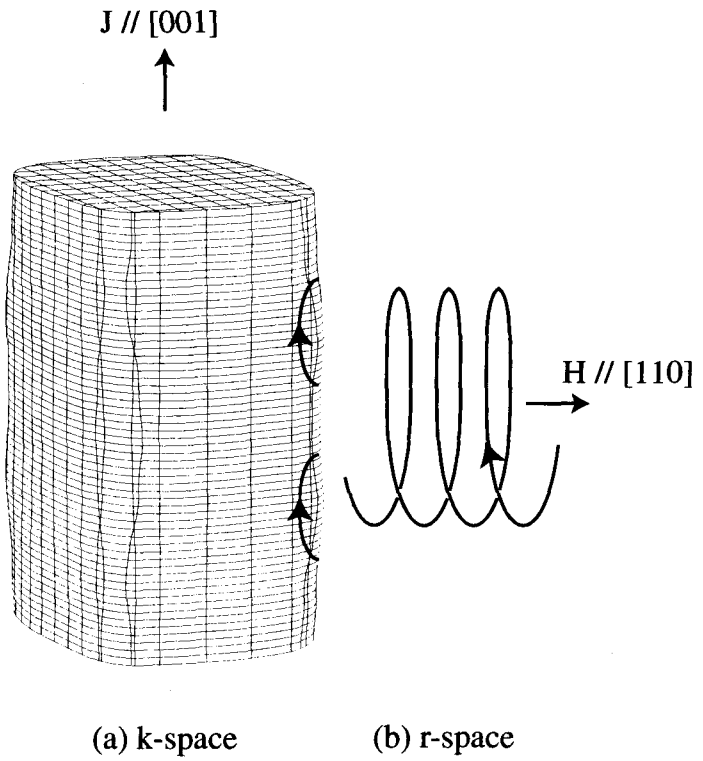


**Fig. 4.2.5** Cyclotron motion of the carrier due to the convex part of the Fermi surface $\alpha$ when the field is applied perpendicularly to the cylindrical axis in both $k$- and real space.

## 4.3 de Haas-van Alphen effect

We show in Fig. 4.3.1 the typical dHvA oscillation of the sample #A with $T_c = 1.5$ K for the magnetic field along the [001] direction and its fast Fourier transformation (FFT) spectrum in the field range from 130 to 170 kOe at 25 mK. We observed three fundamental dHvA branches, named $\alpha$, $\beta$ ($\beta_1$ and $\beta_2$) and $\gamma$ as well as higher harmonics of $\alpha$, namely $2\alpha$, $3\alpha$, $4\alpha$, and the combined harmonics of the fundamental ones; $\beta_2 \pm \alpha$ and $\gamma \pm \alpha$.[92] On the other hand, in the case of the sample #C with $T_c$ about 1.1 K, we observed only three fundamental branches and 2nd harmonics of branch $\alpha$, as shown in Fig. 4.3.2.[87]

Figures 4.3.3 and 4.3.4 show the angular dependences of the dHvA frequency. The large circles correspond to the fundamental branches, while the small circles indicate the harmonics. The solid lines for the fundamental branches represent the $1/\cos\theta$-dependence, where $\theta$ is a tilt angle from [001] to [100] in Fig. 4.3.3 and from [001] to [110] in Fig. 4.3.4. The $1/\cos\theta$-dependence means a cylindrical Fermi surface. The $1/\cos\theta$-dependence for two branches, named $\alpha$ and $\gamma$, is in good agreement with the experimental results. The branch $\beta$ follows also the $1/\cos\theta$-dependence, but around [001] it splits into two branches, denoted by $\beta_1$ and $\beta_2$ in Fig 4.3.1. The two branches $\beta_1$ and $\beta_2$, however, merge into one at $\theta \simeq 30°$. These results are the same as the previous reports. [5]

The dHvA frequency of the branch $\alpha$ follows the $1/\cos\theta$-dependence up to each tilt angle of about 70°. The amplitudes of the dHvA oscillation are, however, extremely angle-dependent, as shown in Figs. 4.3.5(a) and (b). In Fig. 4.3.5(a), we plot not only the amplitude of the fundamental branch $\alpha$ but also those of higher harmonics. The amplitude of the branch $\alpha$ strikingly depends on the tilt angle $\theta$. It possesses maxima around 18°, 30.6°, 44° and 52° and minima around 9°, 24°, 40°, 49° and 58° on the tilt angle from [001] to [100]. On the other hand, it has maxima around 18°, 29°, 38° and 48° and minima around 9°, 22°, 32°, 45° and 57° on the tilt angle from [001] to [110].

The almost zero-amplitude in Fig. 4.3.5(a) around 24° is due to a spin factor, which is the interference effect of the dHvA oscillations by the conduction electrons possessing the up- and down-spin states. The zero spin factor around 24° is supported by the result that the second harmonic $2\alpha$ shows a maximum in amplitude around 25°, as shown in Fig. 4.3.5(a). This explanation is based on the following theory. As the cyclotron effective mass $m_c^*(\theta)$ increases with increasing the tilt angle $\theta$ as in $m_c^*(\theta) = m_c^*(0°)/\cos\theta$, the spin factor $R_S = \cos(\pi m_c^*(\theta) g/2m_0)$ in eq. (3.2.11) becomes zero at a characteristic angle where the argument $\pi m_c^*(\theta) g/2m_0 = \pi(2n+1)/2 (n = 0, 1, 2...)$ is satisfied. Here $g$ is the $g$-factor of the branch $\alpha$. The spin factor of the second harmonic takes a maximum value $R_S = 1$ when the fundamental one becomes zero, because the effective mass of the second harmonic becomes twice as large as that of the fundamental one. However, the amplitude of the fundamental one around 30° is extremely large. This is not realized in the usual case because the amplitude is exponentially reduced as a function of $m_c^*$.

We have to consider another approach, namely, the Yamaji effect to clarify the angular

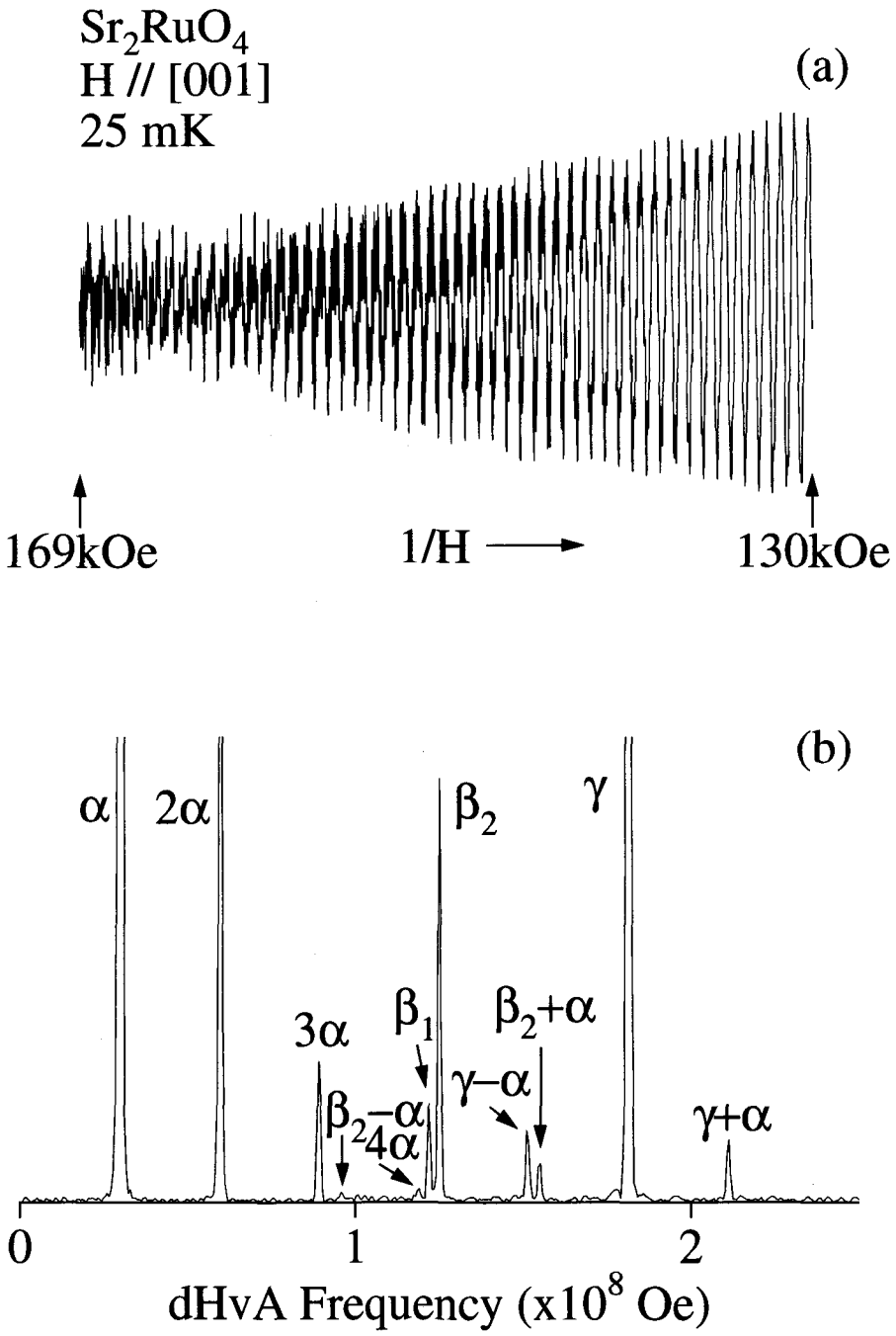


**Fig. 4.3.1** (a)dHvA oscillation of the sample with $T_c = 1.5$ K and (b)its FFT spectrum for the field along [001] in $Sr_2RuO_4$(sample #A).

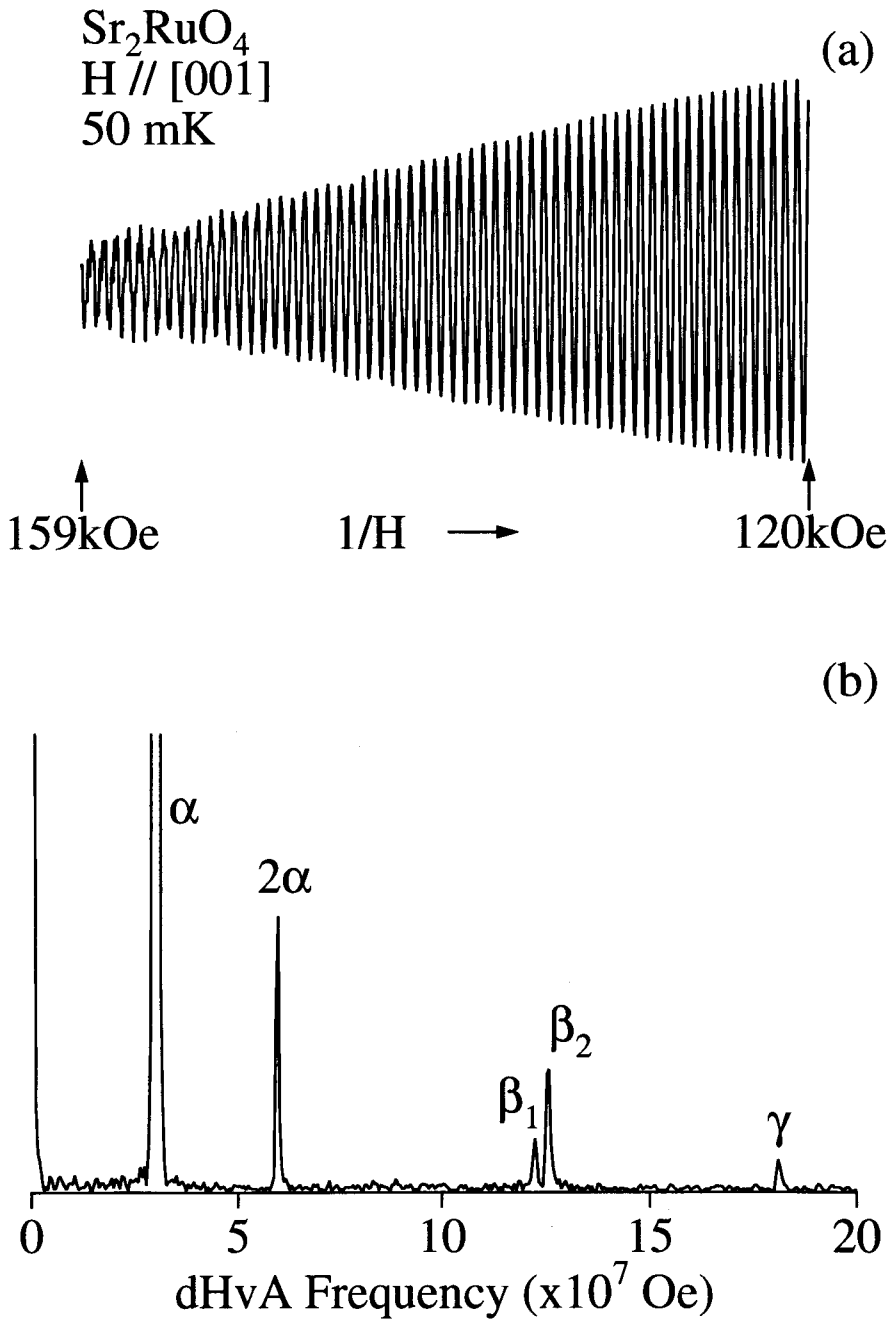


**Fig. 4.3.2** (a)dHvA oscillation of the sample with $T_c$ about 1.1 K and (b)its FFT spectrum for the field along [001] in $Sr_2RuO_4$(sample #C).

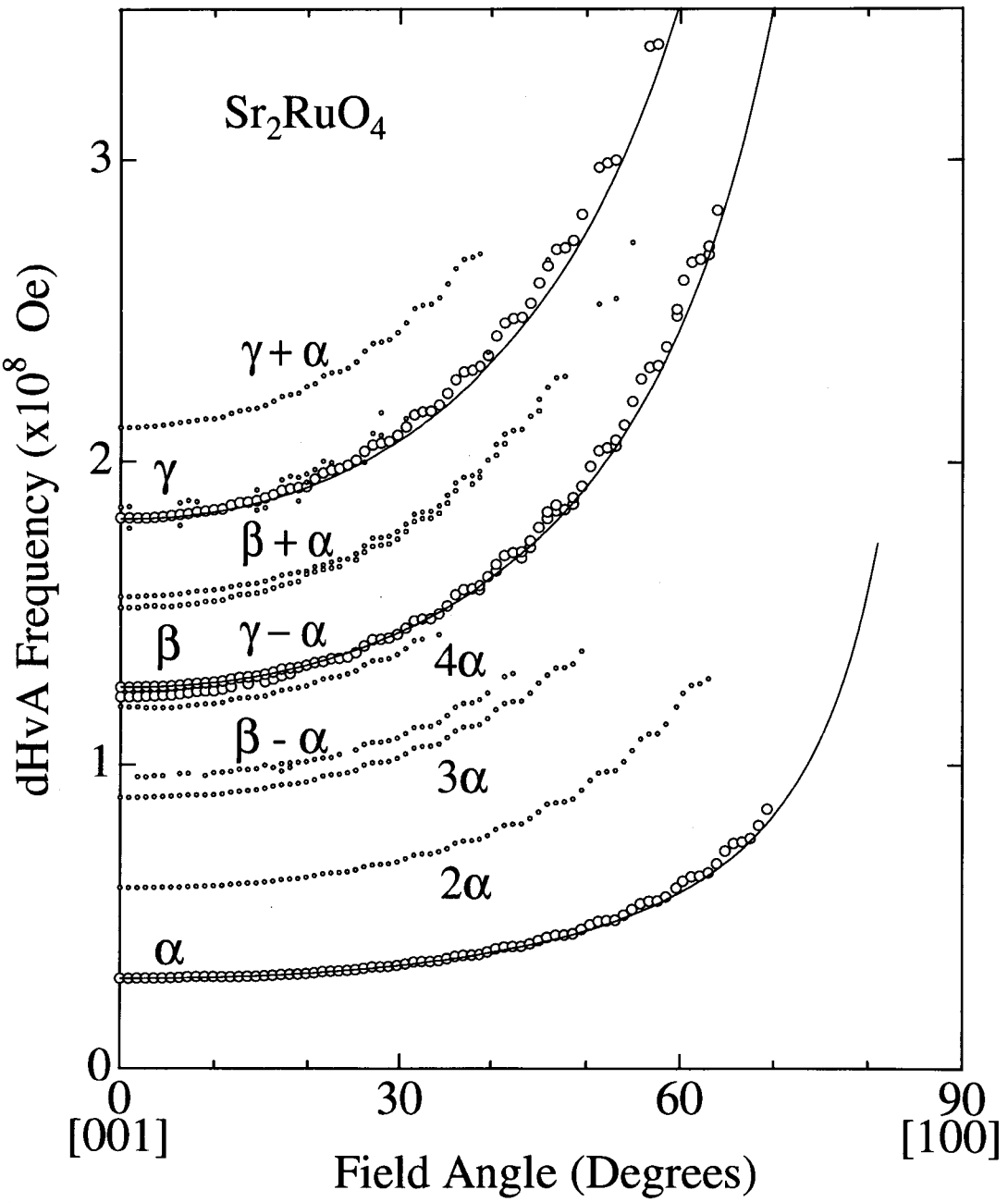


**Fig. 4.3.3** Angular dependence of the dHvA frequency tilted from [001] to [100] in $Sr_2RuO_4$(sample #A).

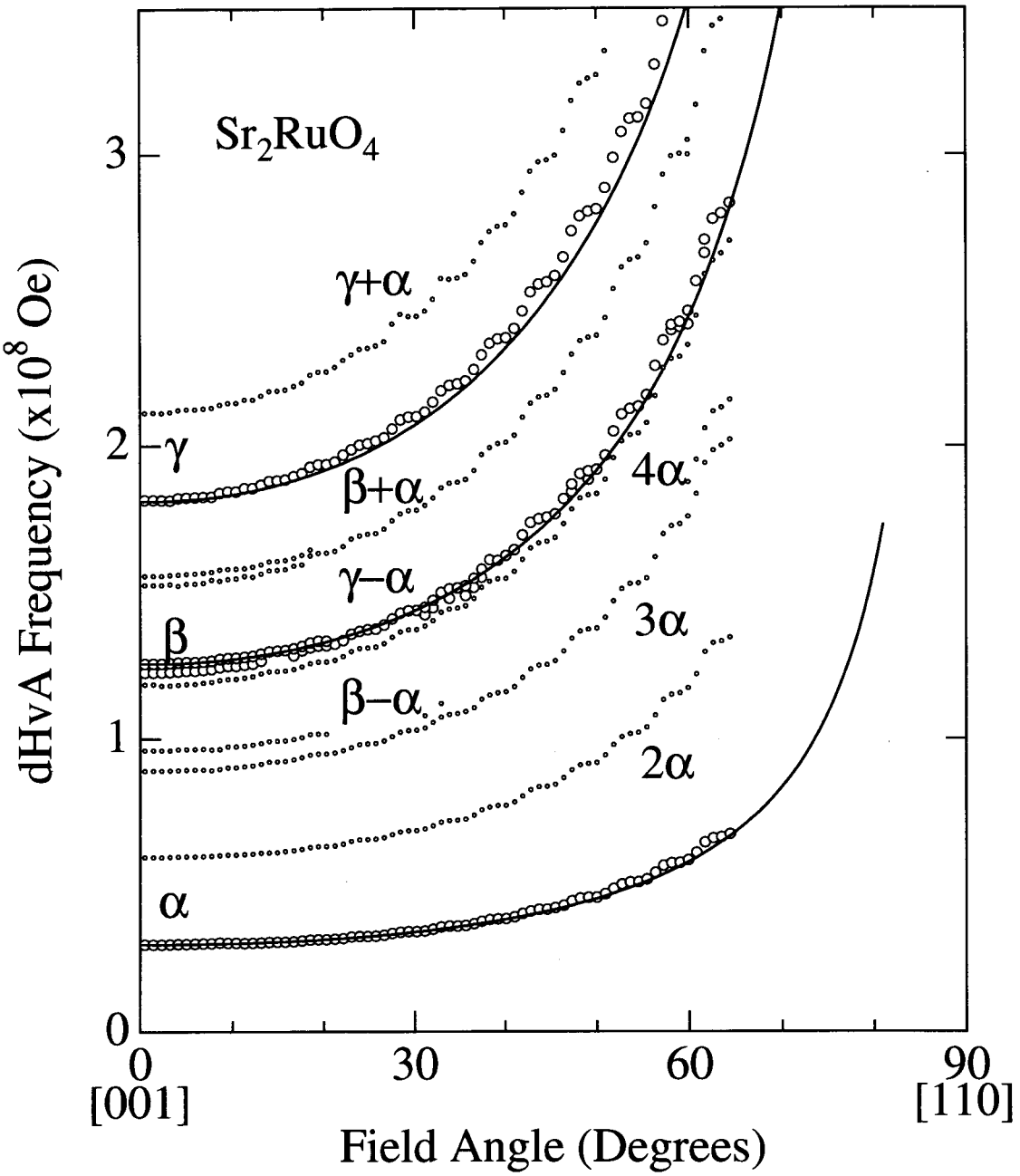


**Fig. 4.3.4** Angular dependence of the dHvA frequency tilted from [001] to [110] in $Sr_2RuO_4$(sample #A).

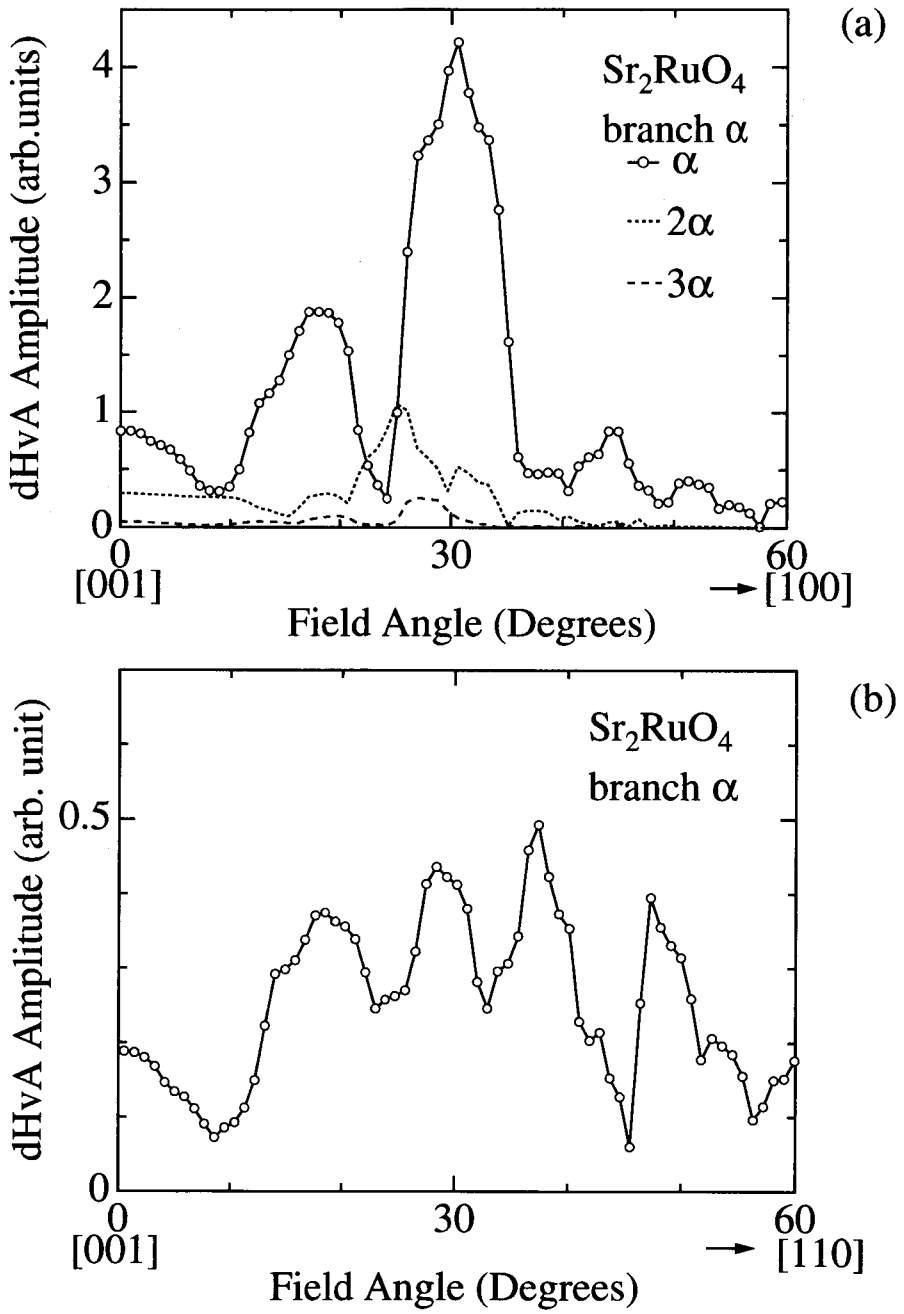


**Fig. 4.3.5** Angular dependences of the dHvA amplitude for the branch $\alpha$ tilted (a)from [001] to [100] and (b)from [001] to [110] in $Sr_2RuO_4$(sample #A).

dependence of dHvA amplitude. When we consider a cylindrical Fermi surface, the Lifshiz-Kosevich formula in eq. (3.2.8) is not right. More rigorously, the curvature factor including $H^{1/2}$ in eq. (3.2.8) is replaced by

$$R_{\rm Y} = J_0(\frac{\pi\Delta F(\theta)}{H}), \tag{4.3.1}$$

$$\Delta F(\theta) = \Delta F(\theta = 0°) J_0(ck_{\rm F}\tan\theta)/\cos\theta, \tag{4.3.2}$$

where $\Delta F(\theta = 0°)$ is a difference between a maximum dHvA frequency and a minimum one, $c$ is the lattice constant along the cylindrical $z$-axis and $S_{\rm F} = \pi k_{\rm F}^2$.

To clarify the angular dependence of the dHvA amplitude for the branch $\alpha$, we determined $\Delta F(\theta = 0°)$. If the maximum dHvA frequency is highly different from the minimum one as in the branches $\beta_1$ and $\beta_2$, it can be distinguished easily from the FFT spectrum. The present $\Delta F$ is, however, small. We searched for a node of the beat oscillation due to the maximum and minimum frequencies. Figure 4.3.6 shows the field dependence of the dHvA amplitude for the branch $\alpha$. Each data point was obtained from the FFT spectrum for twenty oscillations. The node is found at 72 kOe. From this node, we determined $\Delta F(\theta) = 1.27 \times 10^5$ Oe for the branch $\alpha$.

Another information on the Dingle temperature and the cyclotron mass is necessary to analyze the dHvA amplitude. Usually, the Dingle temperature in eq. (3.2.10) can be determined from the field dependence of the dHvA amplitude. In the present case, the dHvA oscillation due to the branch $\alpha$ has a beat pattern. By using eq. (3.2.8), we tried to fit the dHvA amplitude. A solid line in Fig. 4.3.6 is a calculated result. An adjusting value $T_{\rm D}$ was determined to be $T_{\rm D} = 0.63$ K. In calculations, we used the cyclotron mass $m_{\rm c}^* = 3.27 m_0$, estimated later. The mean free path $\ell$ was thus calculated to be 2050 Å from the following relations; $\ell = v_{\rm F}\tau, \tau = (\hbar/2\pi k_{\rm B})T_{\rm D}^{-1}$ and $\hbar k_{\rm F} = m_{\rm c}^* v_{\rm F}$. In addition, in the case of another sample with $T_{\rm c}$=1.1 K, the Dingle temperature and mean free path were 0.88 K and 1200 Å, respectively. The oscillation of the branch $\alpha$ has a node due to the beat at $\theta = 0°$, but has no node from beat around $\theta = 30°$, as shown in Fig. 4.3.7. Then, we obtained the Dingle temperature by using eq. (3.2.10).

In addition to this, we show the dHvA oscillation at the angular dependence of previous magnetoresistance condition of fields and temperature of 0.5 K in Fig. 4.3.8. The main dHvA branch is $\alpha$. The branch $\beta$ has a small amplitude.

From these data, we calculated the angular dependence of the dHvA amplitude based on eq. (3.2.8), as shown by a solid line in Fig. 4.3.9(d). An adjusting value of the $g$-factor is determined to be $g = 4.2$, which is larger than a free electron value $g = 2$. The minimum of the dHvA amplitude at 9° and the maximum at 30.6° correspond to $R_{\rm Y} = 0$ and 1, respectively. On the other hand, the minima at 24° and about 40° are due to the zero spin factor, $R_{\rm S} = 0$.

The difference between Figs. 4.3.5(a) and (b) is mainly due to the difference of the shape of its Fermi surface. The Fermi surface $\alpha$ is cylindrical but the cross-sectional area

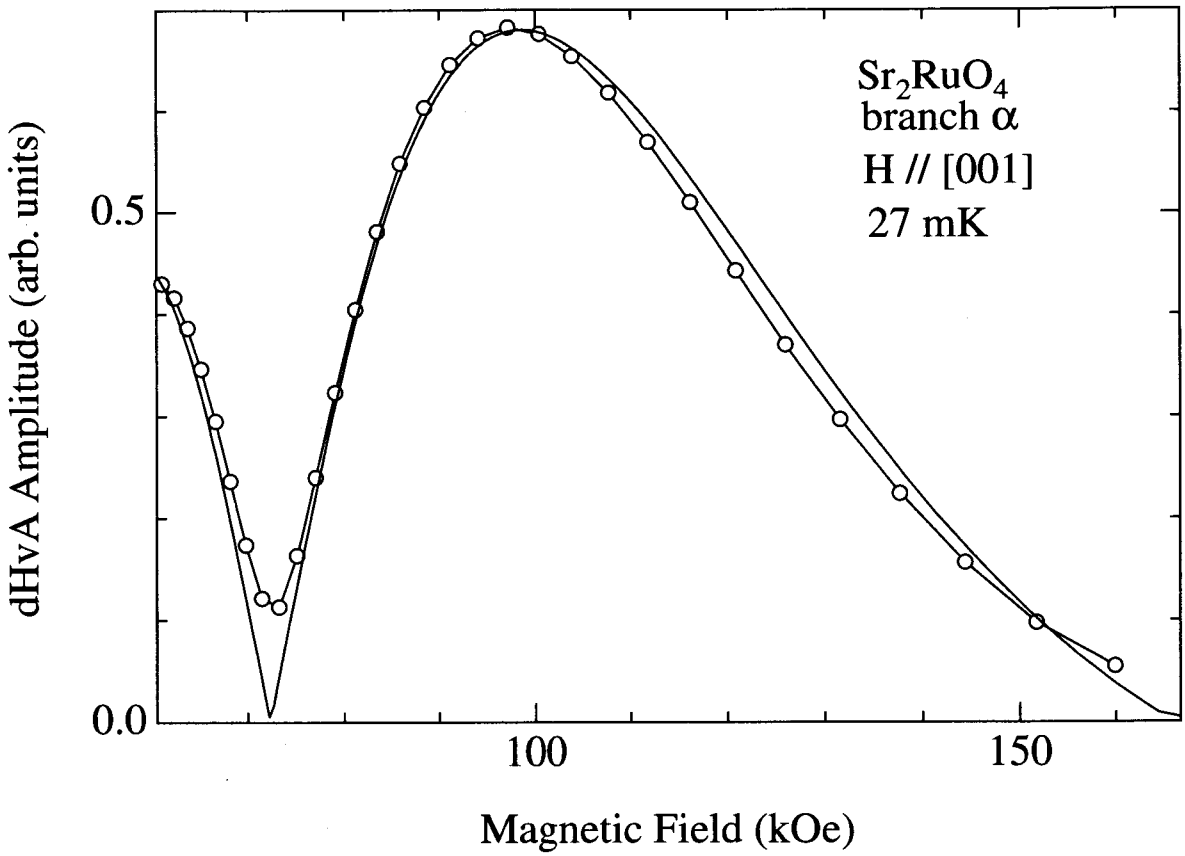


**Fig. 4.3.6** Field dependence of the dHvA amplitude for the branch $\alpha$ in $Sr_2RuO_4$(sample #A).

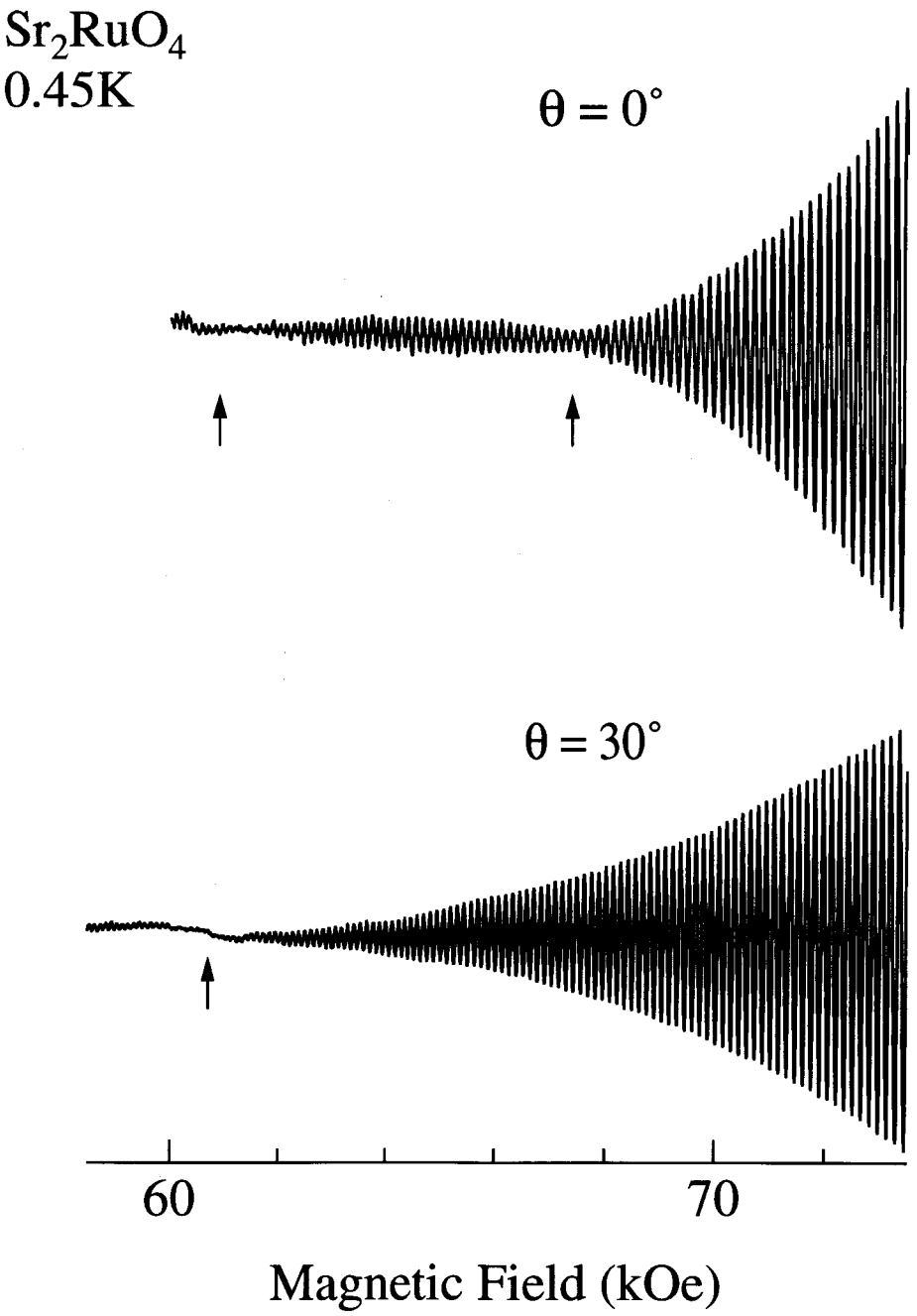


**Fig. 4.3.7** dHvA oscillation for field of $\theta = 0°$ and $\theta = 30°$ at 0.45 K in $Sr_2RuO_4$(sample #C).

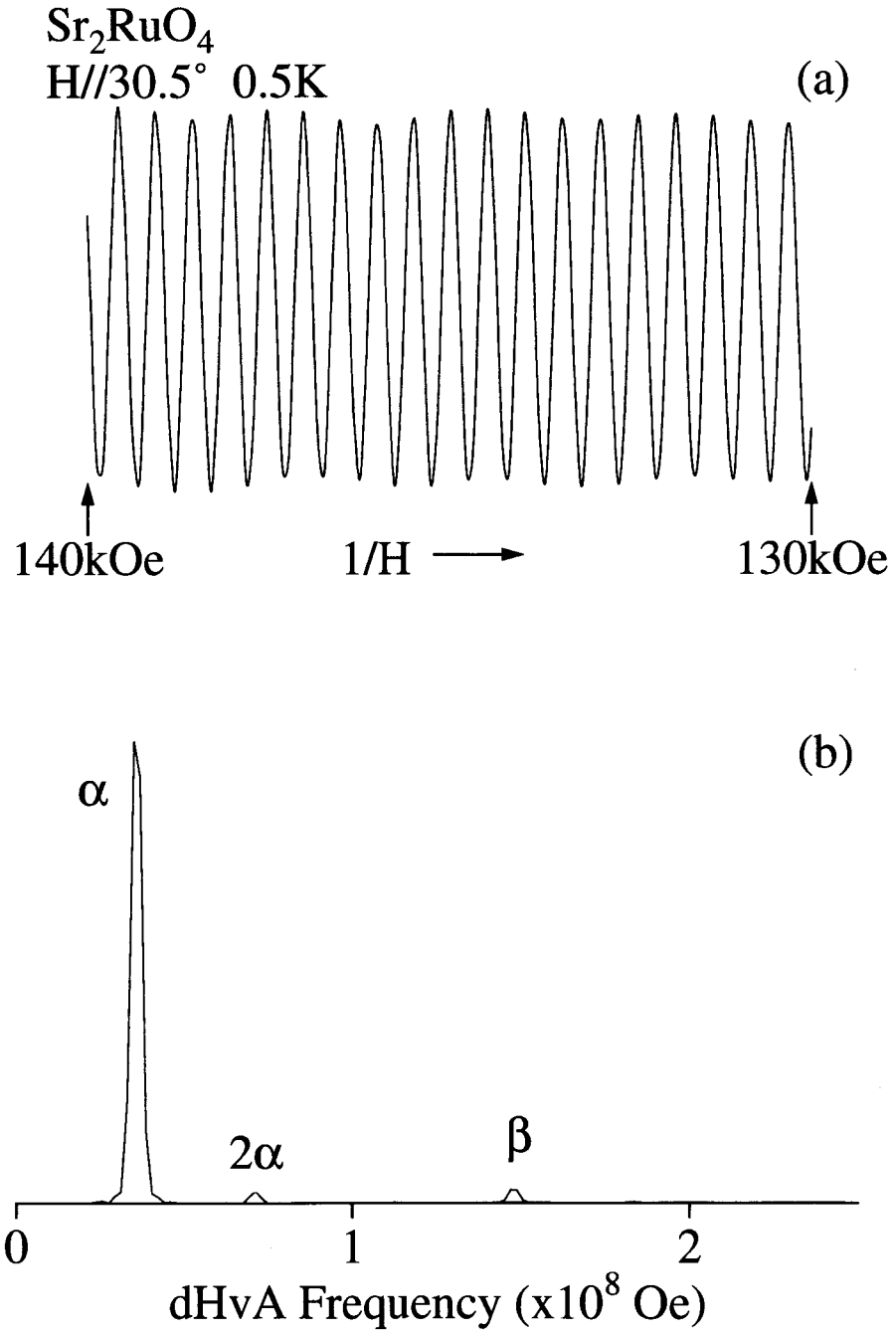


**Fig. 4.3.8** (a)dHvA oscillation and (b)its FFT spectrum at 30.5° in $Sr_2RuO_4$(sample #C).

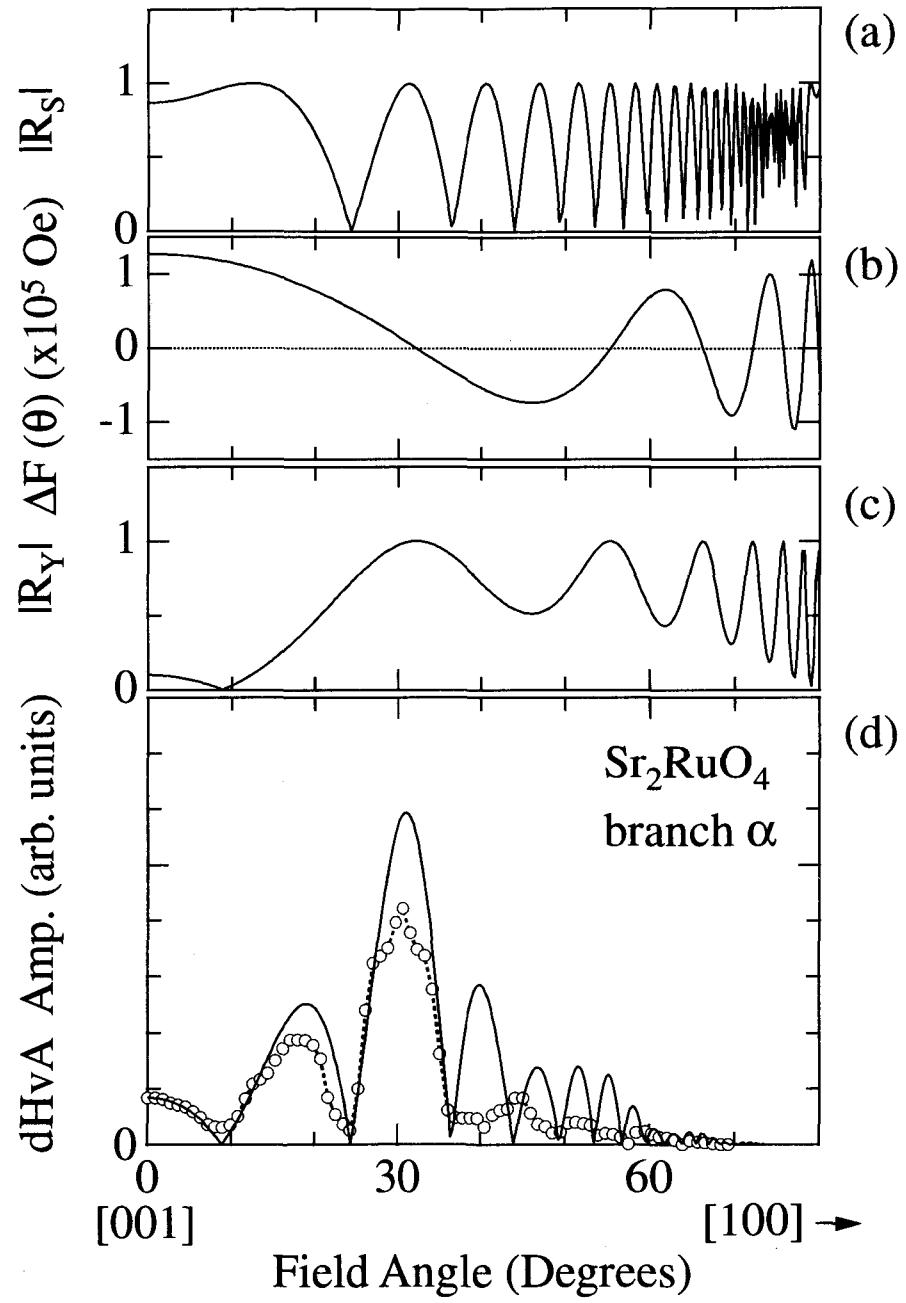


**Fig. 4.3.9** Angular dependence of (a)the spin reduction factor$R_S$, (b)a difference between the maximum and minimum dHvA frequencies, (c)the Yamaji reduction factor, (d)the dHvA amplitude for the branch $\alpha$ in $Sr_2RuO_4$(sample #A).

perpendicular to [001] is not circular, as shown in Fig. 2.3.16(a) and (b). Therefore, there are two kinds of cross-sectional areas at the X point, $\alpha$ and $\alpha'$, as shown in Fig. 2.3.16(b), when the field is tilted from [001] to [110]. This can be represented by the angular dependence of the theoretical dHvA frequency, as shown in Fig. 4.3.10. A thin solid line corresponds to the maximum cross-sectional area, while both a broken line named $\alpha$ and a dotted line named $\alpha'$ in Fig. 4.3.10 correspond to the minimum cross-sectional areas centered at the X point. The latter two lines are the same and cross the solid line at 27° when the field is tilted from [001] to [100]. Theoretically, the Yamaji angle is 27° in this configuration. On the other hand, the solid line does not cross the dotted line but crosses the broken line, when the field is tilted from [001] to [110]. The Yamaji angle in this configuration is 31°, as shown in an inset of Fig. 4.3.10. Note that the experimental results of the Yamaji angle deviates a little between the measurements of the magnetoresistance and that of dHvA. It is because that the Yamaji angle of the dHvA experiments is caused by both the spin and curvature factors.

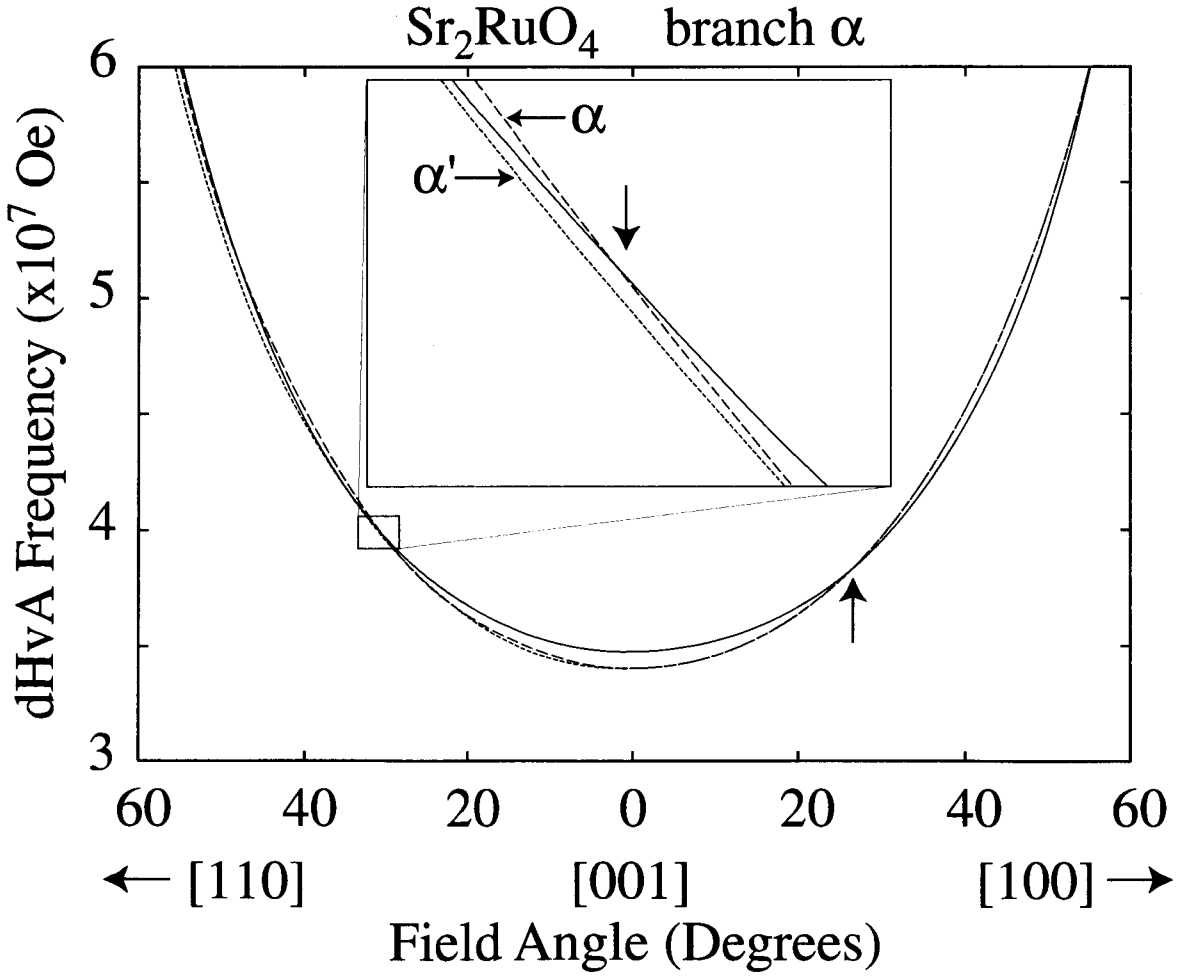


**Fig. 4.3.10** Angular dependence of the theoretical dHvA frequency for the branch $\alpha$ in $Sr_2RuO_4$.

Next, we determined the cyclotron effective mass from the temperature dependence of the dHvA amplitude. Figure 4.3.11 shows the cyclotron effective masses of the branch $\alpha$ and higher harmonics at the tilt angles of (a) 0° ($H$//[001]), (b) 15.3° and (c) 30.6° tilted to [100]. Note that 30.6° corresponds to the Yamaji angle of the branch $\alpha$. The effective masses are also shown in Table I. The effective mass of the branch $\alpha$, which are $3.3\,m_0$ at 0°, $3.4\,m_0$ at 15.3° and $4.0\,m_0$ at 30.6°, increases following the $1/\cos\theta$-dependence. The effective mass along [001] is proportional to the harmonic index number, as shown in Fig. 4.3.11(a). At the Yamaji angle of 30.6°, however, the effective mass of the higher harmonic slightly deviates from a linear relation, as shown in Fig. 4.3.11(c). This is most likely related to the chemical potential oscillation, as discussed later.

**Table 4.3-I** dHvA frequency and the corresponding cyclotron mass at field angles of 0° ($H$ // [001]), 15.3° and 30.6° in $Sr_2RuO_4$. (*) and (**) are cited from refs. (5) and (8), respectively.

| | 0° | | 15.3° | | 30.6° | |
|---|---|---|---|---|---|---|
| | F($\times 10^7$Oe) | $m_c^*(m_0)$ | F($\times 10^7$Oe) | $m_c^*(m_0)$ | F($\times 10^7$Oe) | $m_c^*(m_0)$ |
| $\alpha$ | 2.97 | 3.27 ± 0.06 (3.4*) | 3.07 | 3.42 ± 0.03 | 3.46 | 3.96 ± 0.02 (4.2**) |
| $2\alpha$ | 5.95 | 6.46 ± 0.07 | 6.15 | 6.76 ± 0.2 | 6.92 | 7.42 ± 0.03 |
| $3\alpha$ | 8.92 | 10.0 ± 0.1 | 9.22 | 10.3 ± 0.2 | 10.4 | 10.5 ± 0.2 |
| $4\alpha$ | 11.9 | 13.5 ± 0.8 | | | | |
| $\beta_1$ | 12.2 | 6.8 ± 0.2 | | | | |
| | | | | | 14.5 | 8.24 ± 0.06 |
| $\beta_2$ | 12.5 | 7.04 ± 0.07 (6.6*) | 13.0 | 7.25 ± 0.04 | | (10.3**) |
| $\beta+\alpha$ | 15.5 | 7.5 ± 0.3 | 16.1 | 8.1 ± 0.2 | 18.0 | 9.2 ± 0.2 (11.9**) |
| $\beta-\alpha$ | | | | | 11.1 | 9.5 ± 0.6 (12.2**) |
| $\gamma$ | 18.2 | 17.1 ± 0.2 (12.0*) | 18.8 | 17.1 ± 0.1 | 21.2 | 19.8 ± 0.2 (16.3**) |
| $\gamma+\alpha$ | 21.1 | 18.0 ± 0.4 | 21.9 | 17.5 ± 0.07 | 24.6 | 19.7 ± 0.4 |
| $\gamma-\alpha$ | 15.2 | 17.3 ± 0.4 | 15.7 | 17.6 ± 0.2 | 17.7 | 20.3 ± 0.4 |

In Figs. 4.3.12(a) and (b) we show the angular dependence of the dHvA amplitude for the branch $\beta$ ($\beta_1$ and $\beta_2$). There exist so many maxima and minima in the dHvA amplitude, as for the branch $\alpha$. The branches $\beta_1$ and $\beta_2$ merge into one around 30°. This angle is also the Yamaji angle for the branch $\beta$.

Figure 4.3.13 shows the angular dependence of the dHvA amplitude for the branch $\gamma$. The amplitude of the branch $\gamma$ also strikingly depends on the angle $\theta$, as in the branch $\alpha$. Especially, the dHvA amplitude due to the branch $\gamma$ is enhanced at 15.3°. We think that a Yamaji angle for the branch $\gamma$ is 15.3°, reflecting the largest dHvA amplitude.

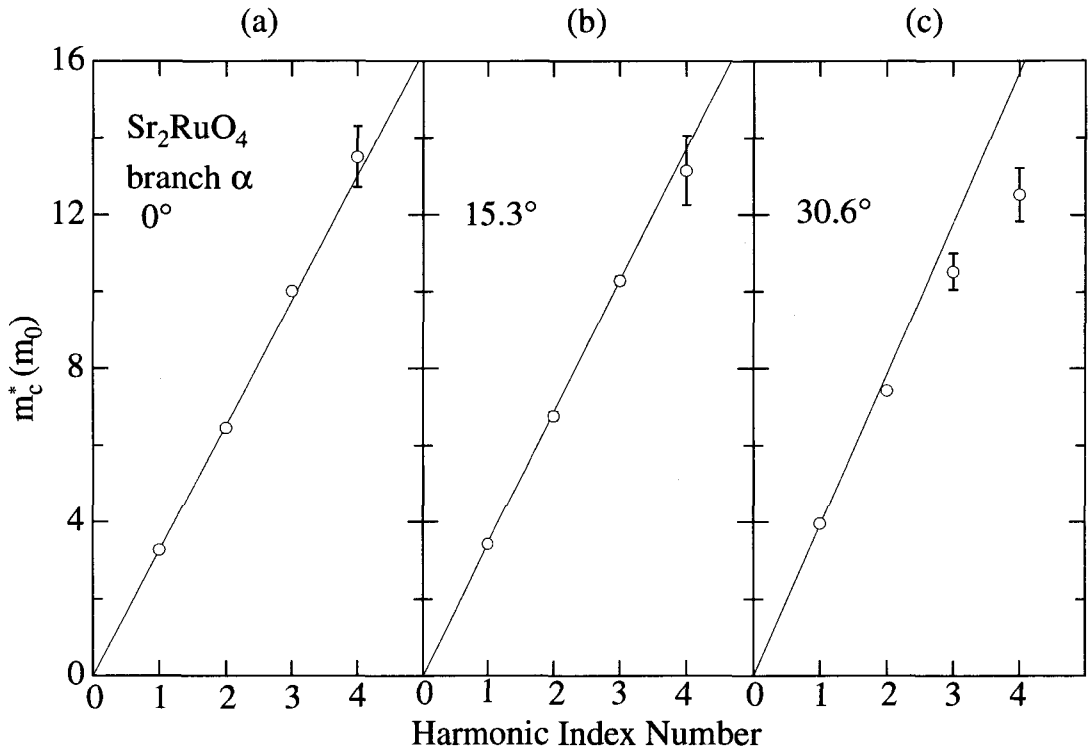


**Fig. 4.3.11** Harmonic index number dependence of the cyclotron effective masses of the branch $\alpha$ and its harmonics, (a) for the field along the [001] direction (0°), (b) 15.3° and (c) 30.6 °, tilted from [001] to [100], in $Sr_2RuO_4$.

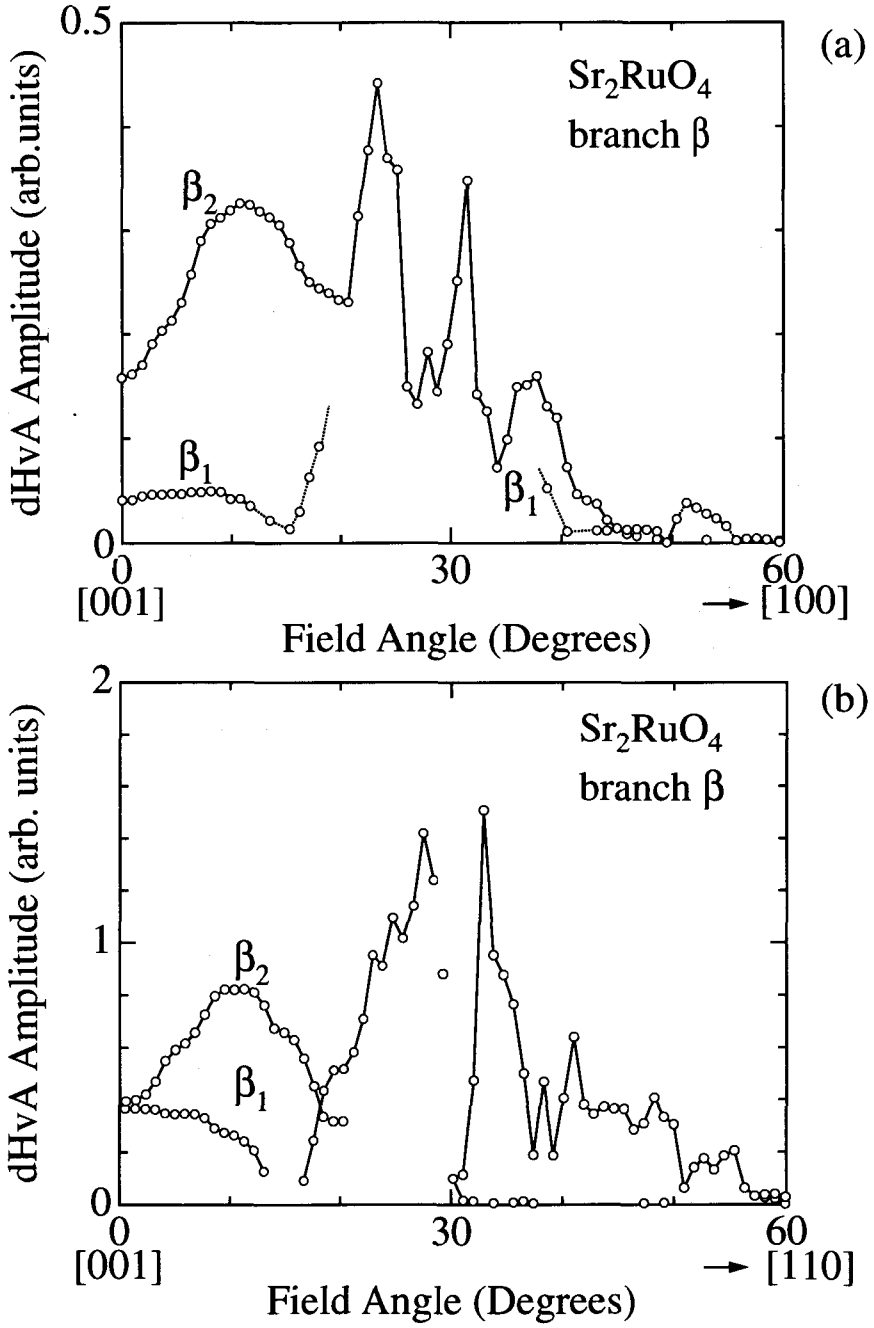


**Fig. 4.3.12** Angular dependence of the dHvA amplitude for the branch $\beta$ in $Sr_2RuO_4$(sample #A).

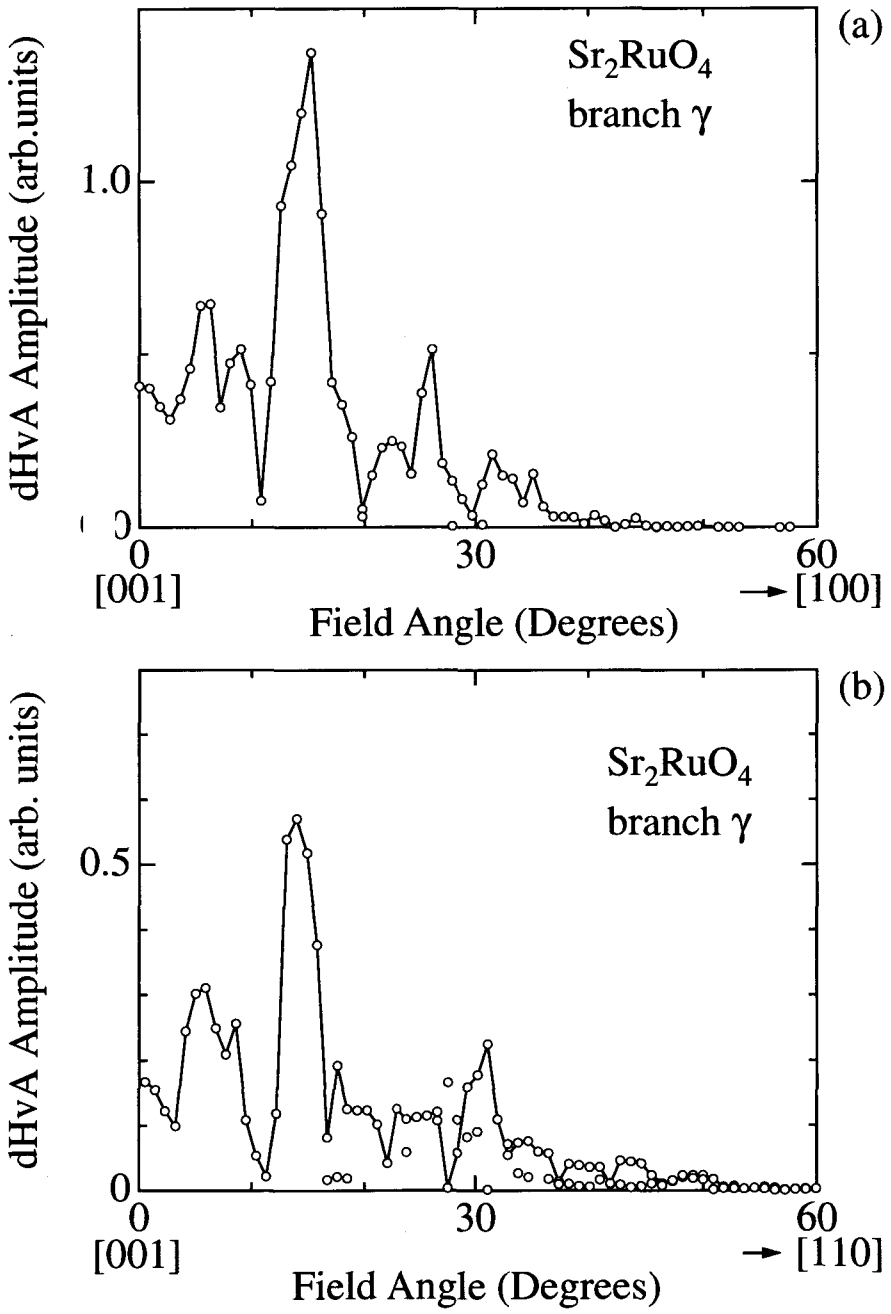


**Fig. 4.3.13** Angular dependence of the dHvA amplitude for the branch $\gamma$ in $Sr_2RuO_4$(sample #A).

Next, we show in Fig. 4.3.14 the angular dependence of the dHvA amplitude for the sum and difference branches $\beta+\alpha$ and $\beta-\alpha$. Both branches exhibit a broad peak around 17° and a sharp peak around 31°. These peaks are mainly ascribed to those of the branch $\alpha$. The amplitude of the latter peak at 31° is enhanced by the Yamaji effect for both Fermi surfaces $\alpha$ and $\beta$.

Figure 4.3.15 shows the similar angular dependence of the dHvA amplitude for the sum and difference branches $\gamma+\alpha$ and $\gamma-\alpha$. Both branches exhibit sharp three peaks at 15°, 27° and 32°, reflecting the combined amplitudes of the branches $\alpha$ and $\gamma$.

We determined the cyclotron effective masses of the branches $\beta$ and $\gamma$ and their harmonics $\beta\pm\alpha$ and $\gamma\pm\alpha$, as shown in Table I and also Fig. 4.3.16. Usually the cyclotron masses of the sum and difference branches $m^*_{\alpha\pm\beta}$ are given as $m^*_\alpha + m^*_\beta$, which is derived from the magnetic interaction. The present $m^*_{\alpha\pm\beta}$ and $m^*_{\gamma\pm\beta}$ values are highly different from $m^*_\beta+m^*_\alpha$ and $m^*_\gamma+m^*_\alpha$, respectively, for any tilt angle. For example, $m^*_\gamma+m^*_\alpha$ is 20.4 $m_0$ at $\theta$=0°, which is compared to $m^*_{\gamma+\alpha}$ = 18.0 $m_0$ and $m^*_{\gamma-\alpha}$ = 17.3 $m_0$. The similar result was reported for the branches $\beta\pm\alpha$, which are cited in Table I [8]. These results can not be explained by the usual magnetic interaction, but are due to the chemical potential oscillation. We note that the cyclotron mass of the Fermi surface $\gamma$, 17 $m_0$ is a little larger than the previous value of 12 $m_0$. [5]

Finally, we note the relation between the cyclotron mass and the electronic specific heat coefficient $\gamma$. As three branches are almost cylindrical, the $\gamma$-value from each branch is easily calculated: the branch $\alpha$ with $m^*_c = 3.3m_0$ corresponds to a $\gamma$-value of 4.9 mJ/K$^2$·mol, the branch $\beta$ with $m^*_c = 6.9m_0$ corresponds to 10 mJ/K$^2$·mol and the branch $\gamma$ with $m^*_c = 17m_0$ corresponds to 25 mJ/K$^2$·mol. The total $\gamma$-value becomes 40 mJ/K$^2$·mol, which is in excellent agreement with the measured $\gamma$-value of 39.8 mJ/K$^2$·mol, as shown later.

The dHvA oscillation for the $i$-th extremal cross-sectional area of the Fermi surface is written as follows:

$$\tilde{M}_i = \sum_{p=1}^{\infty} A_i(H,T,p)\sin\left\{2\pi p\left(\frac{F_i}{H}+\phi_i\right)\right\} \tag{4.3.3}$$

Here, the dHvA frequency $F_i$ is proportional to the the extremal cross-sectional area $S_{F,i}$ and is experimentally determined from the FFT spectrum. The dHvA oscillation is not a single sinusoidal curve but the sum of the harmonics $p$. The dHvA amplitude $A_i(H,T,p)$ corresponds to $A$ in eq. (3.2.8). The curvature $\partial^2 S_i/\partial k_H^2$ is zero for a perfect cylindrical Fermi surface or a sinusoidally modulated cylindrical one at the Yamaji angle. Therefore, the dHvA amplitude becomes large, as observed in $Sr_2RuO_4$.

The cyclotron effective mass is obtained from the so-called mass plot, which is the plot of the temperature dependence of dHvA amplitude under a constant average magnetic field as follows:

$$\ln\frac{A_i(H,T,p)}{T} = const. - \ln\left(\sinh\left(\alpha\frac{T}{H}\cdot pm^*_{c,i}\right)\right) \tag{4.3.4}$$

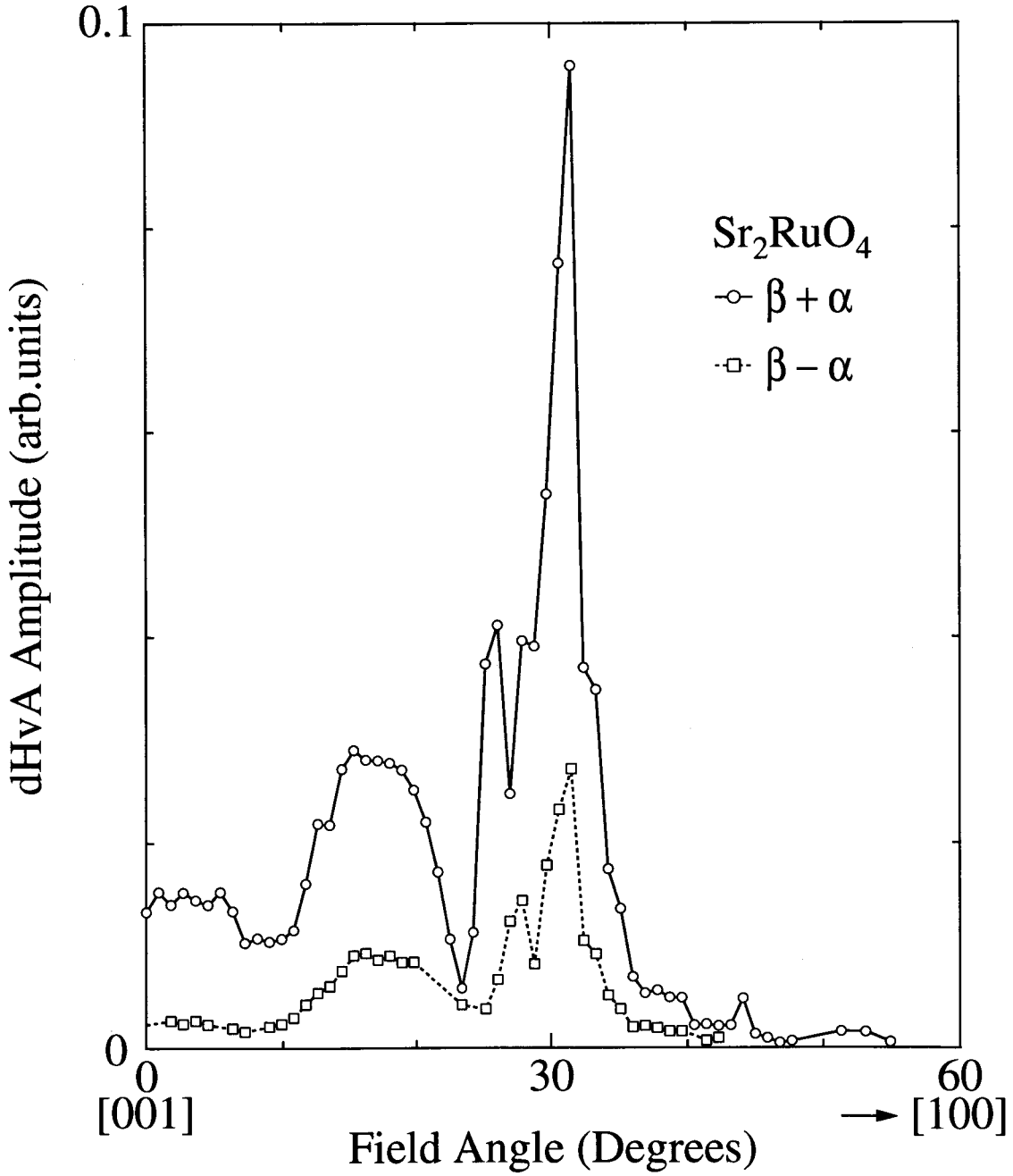


**Fig. 4.3.14** Angular dependence of the dHvA amplitude for the branches $\beta + \alpha$ and $\beta - \alpha$ in $Sr_2RuO_4$(sample #A).

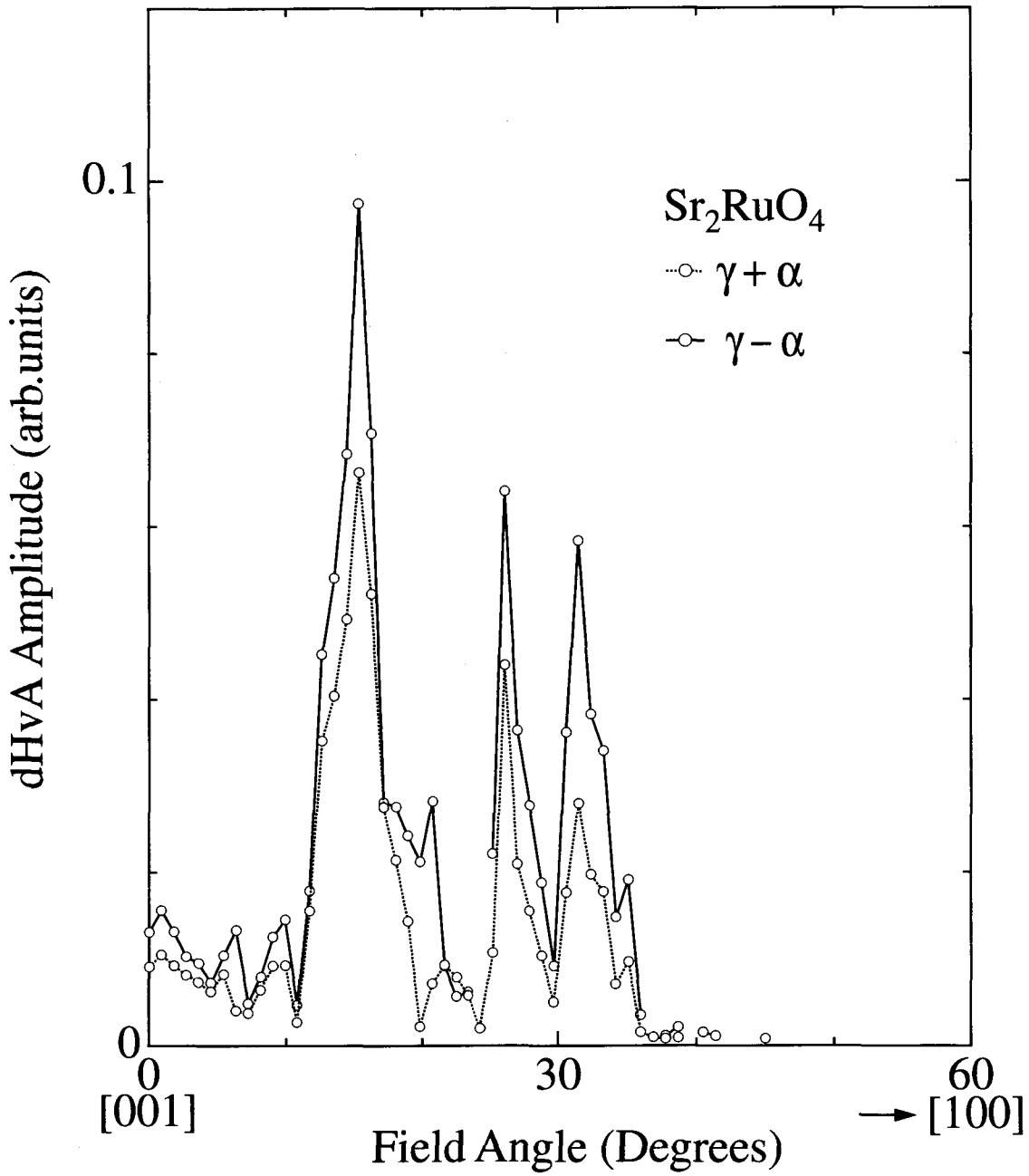


**Fig. 4.3.15** Angular dependence of the dHvA amplitude for the branches $\gamma + \alpha$ and $\gamma - \alpha$ in $Sr_2RuO_4$(sample #A).

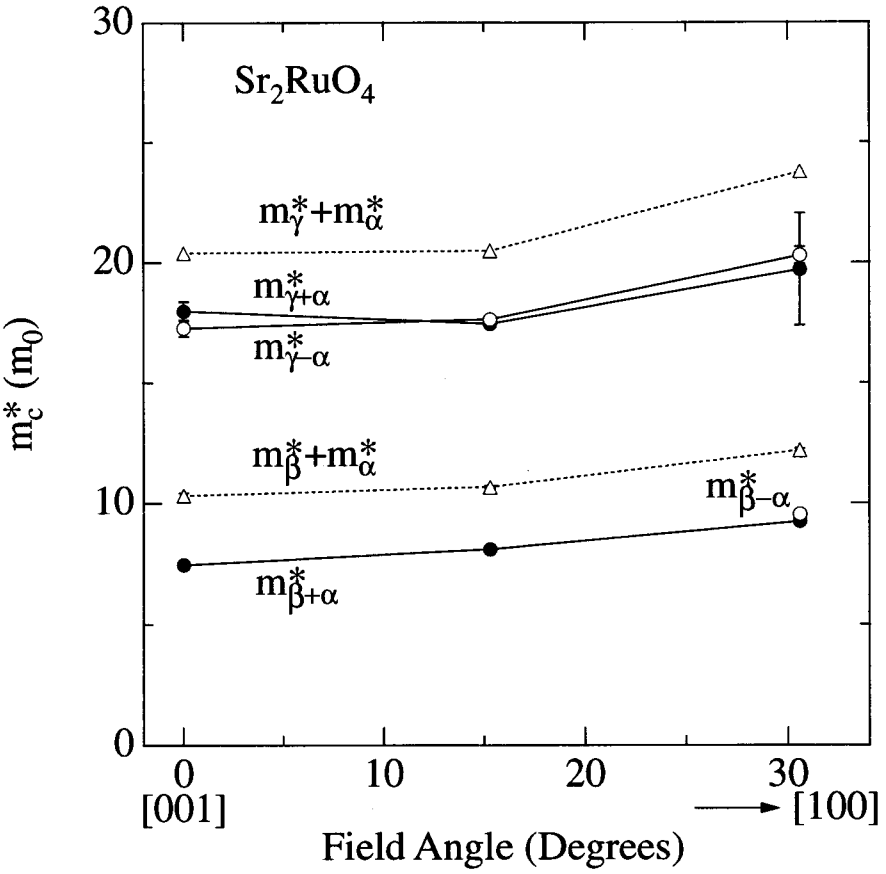


**Fig. 4.3.16** Angular dependence of the cyclotron effective mass for the branches $\beta \pm \alpha$ and $\gamma \pm \alpha$ in $Sr_2RuO_4$(sample #A).

Usually, the mass is determined by a method of successive approximation. We note that the cyclotron effective mass of $p$-th higher harmonic is $p$ times larger than the fundamental one.

Next, we will discuss the magnetic interaction effect which yields the sum and difference dHvA frequencies of different fundamental ones. Here we consider following two dHvA frequencies $F_\alpha$ and $F_\beta$:

$$\tilde{M} = \tilde{M}_\alpha + \tilde{M}_\beta \tag{4.3.5}$$

$$= A_\alpha \sin\left\{2\pi\left(\frac{F_\alpha}{H} + \phi_\alpha\right)\right\} + A_\beta \sin\left\{2\pi\left(\frac{F_\beta}{H} + \phi_\beta\right)\right\} \tag{4.3.6}$$

In the actual substances, however, the magnetic field $H$ should be replaced by the magnetic flux density $B = H + 4\pi(\tilde{M}_\alpha + \tilde{M}_\beta)$. The magnetic oscillation is expanded as follows:

$$\begin{aligned}\tilde{M} &= A_\alpha \sin\left\{2\pi\left(\frac{F_\alpha}{H}\right)\right\} + A_\beta \sin\left\{2\pi\left(\frac{F_\beta}{H}\right)\right\} \\ &- \frac{1}{2}\frac{8\pi F_\alpha}{H^2}(A_\alpha)^2 \sin\left\{2\cdot 2\pi\left(\frac{F_\alpha}{H}\right)\right\} - \frac{1}{2}\frac{8\pi F_\beta}{H^2}(A_\beta)^2 \sin\left\{2\cdot 2\pi\left(\frac{F_\beta}{H}\right)\right\} \\ &- \frac{1}{2}\frac{8\pi}{H^2}A_\alpha A_\beta\left[(F_\beta + F_\alpha)\sin\left\{2\pi\left(\frac{F_\beta + F_\alpha}{H}\right)\right\} - (F_\beta - F_\alpha)\sin\left\{2\pi\left(\frac{F_\beta - F_\alpha}{H}\right)\right\}\right] \\ &+ \cdots\end{aligned} \tag{4.3.7}$$

Here we neglect the phases $\phi_\alpha$ and $\phi_\beta$ for simplicity. Eq. (4.3.7) indicates that we could observe the sum and difference frequencies in addition to the 2nd harmonic. We note that the sum and difference frequencies $F_{\alpha\pm\beta}$ are $F_\alpha \pm F_\beta$, but the cyclotron effective mass is given as $m^*_{c,\beta\pm\alpha} = m^*_{c,\alpha} + m^*_{c,\beta}$ because the factor $A_\alpha A_\beta$ changes with $T\exp\left\{-\alpha\frac{T}{H}\cdot\left(m^*_{c,\alpha} + m^*_{c,\beta}\right)\right\}$. From the viewpoint of the magnetic interaction effect, the effective mass of $m^*_{\alpha\pm\beta}$ should be $m^*_\alpha + m^*_\beta$, as shown in eq. (4.3.7), but the experimental results in Fig. 4.3.16 do not satisfy this relation.

The chemical potential oscillation (CPO), which was based on the dHvA oscillation derived under the constant total electron number, is essentially important in the present quasi-two dimensional system. In the two dimensional system, all the electrons on a perfect cylindrical Fermi surface contribute to the de Haas-van Alphen oscillation, producing the oscillation of the chemical potential. This is in contrast with the three-dimensional system or the Lifshiz-Kosevich formula derived under the constant chemical potential, where the electrons with higher energies than the Fermi level flow continuously to lower-number Landau tubes with increasing the magnetic field and only the electrons on an extremal cross-sectional Landau tube contribute to the dHvA oscillation. Recently, Nakano applied the CPO effect to a quasi-two dimensional two-band system, considering $Sr_2RuO_4$. [9] The CPO effect of one band influences to the magnetic oscillation of the other band, because the electrons flow to the other band so as to minimize the free energy. The temperature dependence of the combination frequency due to the CPO effect is different from that

based on the magnetic interaction effect. The mass $m^*_{\alpha\pm\beta}$ is found to be not equal to $m^*_\alpha$ + $m^*_\beta$. According to the numerical calculations done by Nakano, the mass ratio becomes $m^*_\beta$ : $m^*_{\alpha-\beta}$ : $m^*_{\alpha+\beta}$ : $m^*_\beta + m^*_\alpha$ = 1.00 : 1.20 : 1.14 : 1.43. The corresponding mass ratio of the present experimental results is 1.00 : 1.15 : 1.12 : 1.48 at the Yamaji angle of 30.6°, being in good agreement with the theoretical one.

We observed the similar result for the cyclotron masses $m^*_{\gamma\pm\alpha}$, as shown in Fig. 4.3.16. A striking difference between $m^*_\gamma + m^*_\alpha$ and $m^*_{\gamma\pm\alpha}$ is also not explained by the magnetic interaction but by the CPO effect as in $m^*_{\beta\pm\alpha}$. Important is that $m^*_{\beta\pm\alpha}$ and $m^*_{\gamma\pm\alpha}$ are highly different from $m^*_\beta + m^*_\alpha$ and $m^*_\gamma + m^*_\alpha$, respectively, in the wide field direction, even along the cylindrical axis, namely [001]. It means that Fermi surfaces observed here are very close to cylinders.

Finally we note that the mass of the higher harmonic is not strongly influenced by the CPO effect, holding $pm^*_c$ for the $p$-th harmonic, although a slight CPO effect is observed for the 3rd harmonic of the branch $\alpha$ at the Yamaji angle of 30.6°. The self-band (intra-band) CPO effect is weak compared to the inter-band one.

## 4.4 Elastic anomalies and acoustic de Haas-van Alphen effect

*- Other group's results -*

The ultrasound velocity measurements are based on a phase comparison method that achieves relative resolution of $10^{-7}$.[94,95] The $LiNbO_3$ transducer which generates and detects the ultrasound waves is glued to parallel surfaces of a sample by RTV silicone (Sinetsu-Chemical Co, Ltd.) available below $\approx$ 150 K, together with a liquid polymer (Thiokol LP-32) which hardens below 240 K. The fundamental frequencies of the longitudinal and transverse transducers are 15 and 7 MHz, respectively.

There are six components of the elastic constant $C_{ij}$ ($i, j$ = 1-6) for a tetragonal crystal. Ultrasound waves of four different modes can be generated into the sample; longitudinal modes of $C_{11}(k, u//[100])$ and $C_{33}(k, u//[001])$, and transverse one of $C_{44}(k//[100], u//[001])$ and $C_{66}(k//[100], u//[010])$, where $k$ and $u$ represent the ultrasound directions of propagation and polarization, respectively. The absolute value of the ultrasound velocity $v$ is estimated by the time interval between echo signals. The elastic constants are determined to be $C_{11} \approx 10 \times 10^{11}$, $C_{33} \approx 9 \times 10^{11}$, $C_{44} \approx 1 \times 10^{11}$ and $C_{66} \approx 1 \times 10^{11}$ erg/cm$^3$ at 4.2 K by the relation $C = \rho_m v^2$. Here the density $\rho_m$ = 5.853 g/cm$^3$ at 300 K is used.

Figure 4.4.1 shows the temperature dependence of the elastic constants below 220 K. With decreasing temperature, $C_{44}$ and $C_{66}$ increase monotonically, while $C_{11}$ and $C_{33}$ take a broad maximum at 108 K, followed by a shallow minimum at 61 K ($C_{11}$) and 48 K ($C_{33}$). For the tetragonal point group $D_{4h}$, $C_{44}$ and $C_{66}$ induce the strain $\epsilon_{zx}$ with $\Gamma_5$ representation and $\epsilon_{xy}$ with $\Gamma_4$, respectively. Remarkable anomalies are not observed in these transverse modes. On the other hand, there appears a large lattice softening of about 1 % in longitudinal $C_{11}$ and $C_{33}$. $C_{11}$ includes the strain $\epsilon_{xx}$ with a linear combination fo

$\Gamma_1$ and $\Gamma_3$. $C_{33}$ is a response to the strain $\epsilon_{zz}$ with $\Gamma_1$. Although $(C_{11} - C_{12})/2$ with $\Gamma_3$ is not measured yet, we can conclude that the strain $\epsilon_{zz}$ with $\Gamma_1$ strongly couples to the electronic states in $Sr_2RuO_4$.

From neutron diffraction measurements,[96,97] the lattice constants along [001] and [100] rapidly decrease down to 100 K. In comparison with our results, these anomalies are directly related to the elastic softening in $C_{11}$ and $C_{33}$. Moreover, anomalies are found around 100 K in the electrical resistivity $\rho_{[001]}$,[4] the Hall coefficient[74] and the magnetic susceptibility,[71] which correspond to the competition between metallic and non-metallic states. Therefore, the elastic anomalies observed here are associated with the charge of the electronic states via $\Gamma_1$ representation.

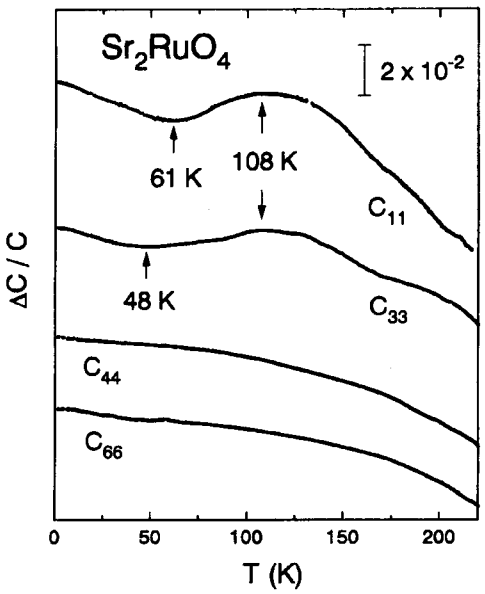


**Fig. 4.4.1** Temperature dependence of relative change of elastic constants $C_{11}, C_{33}, C_{44}$ and $C_{66}$ below 220 K. Anomalous softening is observed in longitudinal modes.

The temperature dependence of $C_{11}$ and $C_{33}$ below 3 K is illustrated in Fig. 4.4.2. As shown by the solid circles in Fig. 4.4.2(a), $C_{11}$ takes a maximum around $T_c$ at zero magnetic field. A monotonic increase (open squares) is observed below $T_c$ in the normal states induced by 2 T ( $> H_{c2}$, see Fig. 4.4.4) applied parallel to [100]. $C_{33}$ changes linearly with temperature above $T_c$. but a discontinuous change in the slope is observed at $T_c$.

A discontinuous change in the longitudinal elastic constant has been observed at $T_c$ in many heavy fermion and high-$T_c$ superconductors, which originates from the first-order strain dependence of $T_c$, $\partial T_c/\partial \epsilon_{uk}$. In the present study, the remarkable step at $T_c$ cannot be obtained, so that the first-order contribution are negligible. The slope, however, changes at $T_c$ in both modes. The discontinuity appears in the temperature deriva-

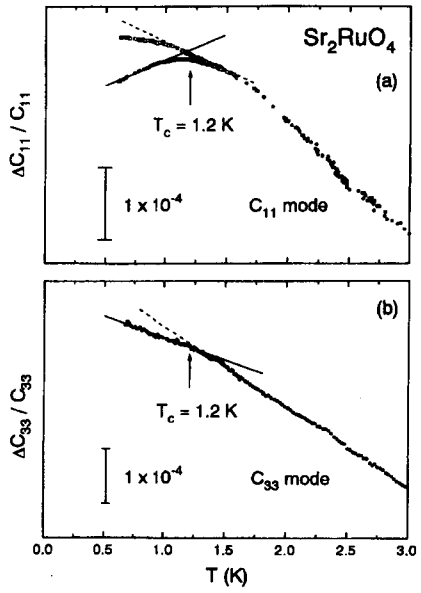


**Fig. 4.4.2** Relative change of elastic constants caused by the superconducting transition for longitudinal modes $C_{11}$(a) and $C_{33}$(b). Solid and broken lines have been fitted to obtain the slope at $T_c$.

tive, coming from second-order strain dependence of $T_c$ described by the thermodynamic relation:[98,99]

$$\left.\frac{dC_{ii}^S}{dT}\right|_{T_c} - \left.\frac{dC_{ii}^N}{dT}\right|_{T_c} \approx \frac{\Delta C_e}{T_c}\frac{d^2T_c}{d\epsilon_{uk}^2}. \tag{4.4.1}$$

Here the first-order contribution at $T_c$ is neglected. The specific heat jump is $\Delta C_e \approx$ 19 mJ/K$^2$·mol.[12,83] Superscripts S and N represent the superconducting and normal states, respectively. The difference of the slope $\Delta[1/C_{ii}(dC_{ii}/dT)_{T_c}]$ below and above $T_c$, is estimated to be $14.3\times10^{-5}$ K$^{-1}$ for $C_{11}$ and $6.9\times10^{-5}$ K$^{-1}$ for $C_{33}$. Using eq. (4.4.1), the second-order strain dependence is obtained as $\partial^2T_c/\partial\epsilon_{xx}^2 = 5\times10^4$ K and $\partial^2T_c/\partial\epsilon_{zz}^2 = 2\times10^4$ K. The large contribution of the former in comparison with the latter reflects the response of $\epsilon_{xx} - \epsilon_{zz}$ with $\Gamma_3$.

The elastic anomalies accompanied by the superconducting transition consist of mean-field and fluctuation contributions from the theory proposed by Millis and Rabe.[99] The above calculation with eq. (4.4.1) is to obtain the former contribution and is well applicable to $C_{33}$. However, the gradual change seen around $T_c$ in $C_{11}$ cannot be explained only by the mean-field contribution. It might be attributed to the fluctuation contribution for the response of $\epsilon_{xx} - \epsilon_{zz}$.

Figure 4.4.3 shows the magnetic field dependence of $C_{11}$ and $C_{33}$ for the different temperatures. The magnetic fields are applied parallel to [100] in (a) and to [001] in (b). With increasing temperatures, the kink-like transition, which is assumed to give the upper critical field $H_{c2}(T)$ as shown by arrows, moves to the lower magnetic field and becomes

broad. The change in $C_{11}$ observed from $H = 0$ to $H_{c2}$ is comparable to the difference between normal and superconducting states shown in Fig. 4.4.2.

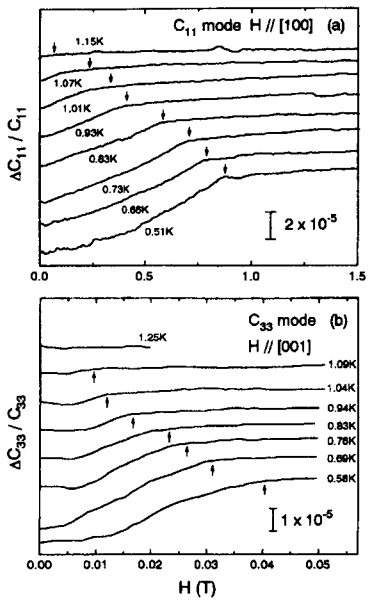


**Fig. 4.4.3** Relative change of longitudinal modes $C_{11}$ and $C_{33}$ as a function of a magnetic field applied parallel to [100] in (a) and to [001] in (b).

The temperature dependence of $H_{c2}$ is plotted in Fig. 4.4.4 for H//[100] and [001]. The inset shows an expanded view of $H_{c2}^{[001]}$. The initial slopes given by the straight lines at $T_c$ are $dH_{c2}^{[100]}/dT|_{T_c}$=-1.7 T/K and $dH_{c2}^{[001]}/dT|_{T_c}$=-0.06 T/K. The ratio is: $\gamma = (dH_{c2}^{[100]}/dT|_{T_c})/(dH_{c2}^{[001]}/dT|_{T_c})$=28. From the effective mass model based on the Ginzburg-Landau theory for an anisotropic superconductor,[100,101] $\gamma$ represents an anisotropy ratio of the penetration depth $\lambda$, the coherence length $\xi$ and the effective mass $m^*$: $\gamma = (m^*_{[001]}/m^*_{[100]})^{1/2} = \lambda_{[001]}/\lambda_{[100]} = \xi_{[001]}/\xi_{[100]}$. The anisotropy ratio in the coherence length of 28 agrees with the previous value of 26 obtained by AC susceptibility measurements.[102] This ratio is one order of magnitude smaller than that in usual high-$T_c$ and organic superconductors. The coherence lengths are evaluated to be $\xi_{[100]}$=680 Å and $\xi_{[001]}$=24 Å using the relation $-dH_{c2}^{[001]}/dT|_{T_c} = \phi_0/2\pi\xi^2_{[100]}T_c$.[103] Here, $\xi_{[001]}$ is larger than the interlayer distance of 6.37 Å, in contrast to the high-$T_c$ and organic superconductors. From the superconducting vortex point of view, $Sr_2RuO_4$ is an anisotropic but three-dimensional superconductor and the flux lines are rigid along the interlayer direction as well as a classical bulk superconductor.

Figure 4.4.5 shows the magnetic field dependence up to 10 T for the magnetic field parallel to [100] for $C_{11}$ and to [001] for $C_{33}$ at 0.58 K. It is noted that the anomaly, which is weakly temperature-dependent up to 0.93 K, is observed around 5 T in the normal state.

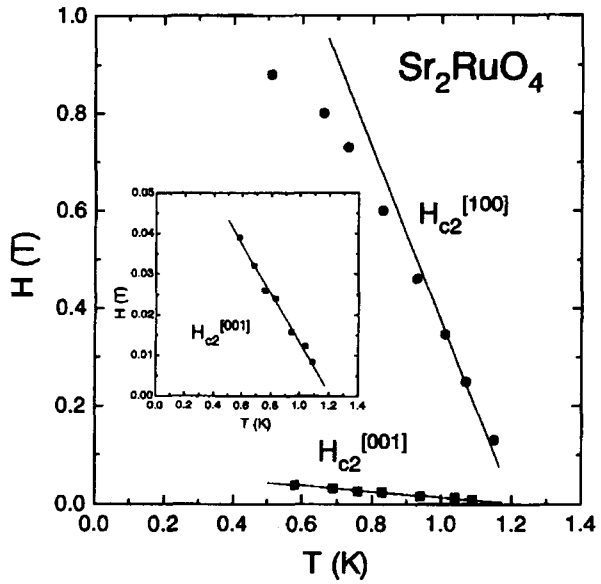


**Fig. 4.4.4** Temperature dependence of the upper critical fields $H_{c2}$ down to 0.51 K for the magnetic fields parallel to [100](solid circles) and [001](solid squares). In the inset, the low-field data of $H_{c2}^{[001]}$ are enlarged.

As shown in the inset of Fig 4.4.5, acoustic dHvA oscillations are observed above 8 T in $C_{33}$ measured with the third harmonic frequency of 44.9 MHz. The first Fourier transform (FFT) spectrum indicates that these oscillations are attributed to the $\alpha$-hole FS. The dHvA frequency $F(=(c\hbar/2\pi e)S$, where $S$ denotes the cross-sectional area) estimated as $3.00\times10^7$Oe is in good agreement with the pervious values of $3.01\times10^7$[87] and $3.04\times10^7$Oe.[5] The effective mass is evaluated to be $m^*= 3.2(\pm0.2)m_0$ from the temperature dependence of the oscillatory amplitude, which is close to $3.4m_0$.[5] However, this value deviates from $4.3m_0$.[87] The Dingle temperature $T_D$ is estimated to be about 1.5±0.1 K. From the angular dependence of the dHvA amplitude, the spin factor becomes zero at the magnetic field directions of $\theta$=16° and 35°.[87] If we define the angular dependence of the effective mass as $m^* = 3.2m_0/\cos\theta$, the $g$-factor becomes 3.32.

$$\Delta C_{33}(H) = \left(\frac{eH}{2\pi c\hbar}\right)^{3/2}\left|\frac{\partial^2 S}{\partial k_z^2}\right|^{-1/2}\frac{\hbar\omega_c}{\pi^2}R_T R_D R_S \times |\Lambda_{zz}|^2\left(\frac{2\pi F}{H}\right)^2\cos\left(\frac{2\pi F}{H}+\eta\frac{\pi}{4}\right), \quad (4.4.2)$$

where the cyclotron angular frequency $\omega_c = eH/m^*c$, and $R_T, R_D$ and $R_S$ represent the conventional reduction factors at $T$= 0.58 K and $H$= 8.9 T are determined to be $R_T$= 0.29, $|R_S|$= 0.56 and $R_D$= 0.01. The oscillatory amplitude of the acoustic dHvA effect is evaluated as $\Delta C_{33}= 1.7\times10^6$ erg/cm$^3$ from the FFT spectrum.

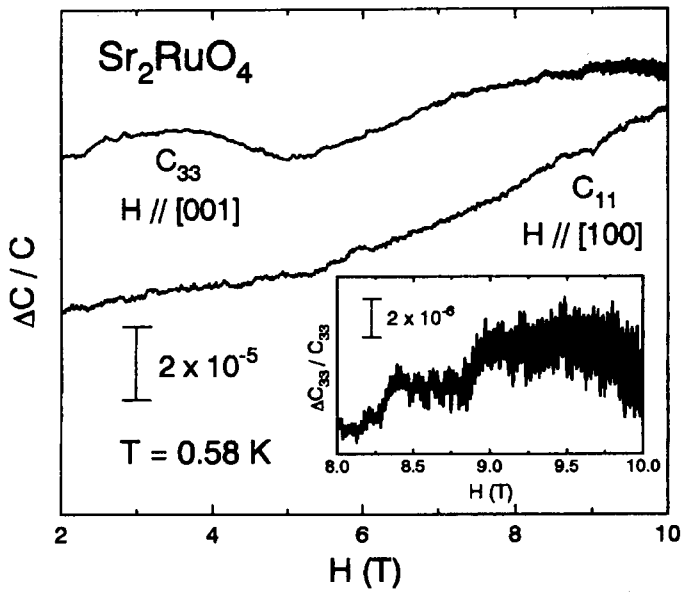


**Fig. 4.4.5** Magnetic field dependence of $C_{11}$(H//[100]) and $C_{33}$(H//[001]) up to 10 T at 0.58 K. As shown in the inset, the acoustic dHvA effect is measured in $C_{33}$ above 8 T.

The difference in the dHvA frequency between two extremal orbits for the warped cylinder of $\alpha$-FS is obtained to be $\Delta F_\alpha = 1.25 \times 10^5$ Oe.[87] According to the Yamaji theory,[20] the interlayer transfer energy for the cylindrical $\alpha$-FS is estimated as $t_\perp^\alpha$= 0.1 meV, which is one order of magnitude smaller than $t_\perp^\beta$= 1.2 meV in $\beta$-FS with $\Delta F_\beta = 3.1 \times 10^6$ Oe.[5,87] The $\alpha$-FS with extremely small warping has more 2D character than $\beta$-FS. The $t_\perp^\alpha$ in the present $Sr_2RuO_4$ is comparable to 0.2 meV for Q2D $\alpha$-(BEDT-TTF)$_2$NH$_4$Hg(SCN)$_4$.[105] The curvature factor of the $\alpha$-orbit for H//[001] is given by

$$\left|\frac{\partial^2 S}{\partial k_z^2}\right|^{-1/2} = \left|\frac{4\pi m^* t_\perp^\alpha d^2}{\hbar^2}\right|^{-1/2} \tag{4.4.3}$$

where $d$= 12.73Å, and thus we obtain $|\partial^2 S/\partial k_z^2|^{-1/2}$= 3.2. By excluding the contribution of the reduction and curvature factors from the oscillatory amplitude $\Delta C_{33}$, the area coefficient is finally determined to be $|\Lambda_{zz}| = 20 \pm 5$. $|\Lambda_{zz}|$ is about six times larger than the area coefficient of $|\Lambda_{b^*b^*}| = 3.5$ for the Q2D FS of similar cylindrical shape with $m^* = 2.7m_0$ and $F = 5.76 \times 10^6$ Oe in $\alpha$-(BEDT-TTF)$_2$NH$_4$Hg(SCN)$_4$.[105]

According to the KG model,[104] $|\Lambda_{zz}|$ is basically composed of the deformation term $\Lambda_{zz}^d$ and the multiband term $\Lambda_{zz}^m$ for longitudinal waves. It is rather complicated to separate these contributions for the present situation. $\Lambda_{zz}^d$ represents the strain dependence of the effective mass with conserving the carrier number. The shape of $\alpha$-FS is perfectly cylindrical, so that the deformation of the FS along the $k_z$-direction is negligible. The

contribution of $\Lambda_{zz}^{d}$ should not be dominant. Therefore, $\Lambda_{zz}^{m}$ is overwhelming in $\alpha$-FS with $\Lambda_{zz}^{m} \approx \Lambda_{zz}$= 20. The multiband term without varying the effective mass is attributed to a charge transfer. In this case, charge transfer takes place between the 17th hole band forming the $\alpha$-FS and the 18th or 19th electron band respectively for $\beta$- or $\gamma$-FS. We expected that the large $\Lambda_{zz}$ obtained in the $\alpha$-FS reflects the strong hybridization of these bands.

## 4.5 Specific heat

Figure 4.5.1 shows the temperature dependence of the electronic specific heat $C_e$ in the form of $C_e/T$ for three samples with critical temperatures $T_c$ = 1.52, 1.24 and 1.14 K, named #A, #B and #C, respectively. A sharp jump in the specific heat is observed at $T_c$ in each sample. The specific heat in the normal state follows a simple relation of $C/T = \gamma + \beta T^2 + A/T^3$ below $T < \Theta_D/50$, where $\Theta_D$ is the Debye temperature. Namely, the specific heat at low temperatures consists of the electronic, phonon and nuclear contributions. A nuclear contribution to the specific heat from Ru in $Sr_2RuO_4$ is, however, negligibly small and can be neglected now. If we apply this relation to the specific heat data, we can obtain the electronic specific heat coefficient $\gamma$ =39.8 mJ/K$^2$·mol and $\Theta_D$ = 430 K. These results are almost the same as reported previously. [11,12] The phonon contribution is subtracted in Fig. 4.5.1. The $\gamma$-value is also obtained in the magnetic field of 20 kOe. In fields higher than about 16 kOe, the sample is in the normal state, as shown later in detail.

The specific heat shows a jump at $T_c$ for each sample #A, #B and #C, but $\Delta C/\gamma T_c$ = 0.50, 0.53 and 0.66 are small when compared to the BCS value of 1.43. The residual $C_e/T$-values of the samples of #B and #C at about 0.2 K are extremely large, 22 mJ/K$^2$·mol, remaining half of the $\gamma$-value. On the other hand, a residual value $\gamma_{res}$ of the sample #A is a small, decreasing with increasing the quality of the sample. The $\gamma_{res}$-value, estimated at 0 K, is 8 mJ/K$^2$·mol. It is thus expected that the $\gamma_{res}$-value becomes zero for a much higher-quality sample. Recently, Nishizaki *et al.* reported that the $\gamma_{res}$-value was nearly zero, 3± 3 mJ/K$^2$·mol, by using the sample with $T_c$ = 1.48 K[81]. We conclude that the existence of $\gamma_{res}$ is not intrinsic in superconductivity of $Sr_2RuO_4$.

A large $\gamma_{res}$-value is closely related to the pair-breaking due to non-magnetic impurities and defects. This is usually inevitable to the $p$-wave superconductor, as demonstrated experimentally by the relation of $T_c$ to the residual $\gamma_{res}$-value [12]. Moreover, it is closely related to a characteristic energy gap in $Sr_2RuO_4$. As mentioned in Chap. 2, it was theoretically argued that the unconventional paring in the part of the Fermi surface with Ru-4$d_{xy}$ orbital character, named the Fermi surface $\gamma$, is weakly coupled to that with Ru-4$d_{xz}$ and 4$d_{yz}$ orbital character, named the Fermi surfaces $\alpha$ and $\beta$. Superconductivity in the temperature range from 1.2 to 0.1 K is thus originated mainly from the Cooper-pairs on the Fermi surface $\gamma$, because the gap size on the Fermi surfaces $\alpha$ and $\beta$, about 0.1 K,

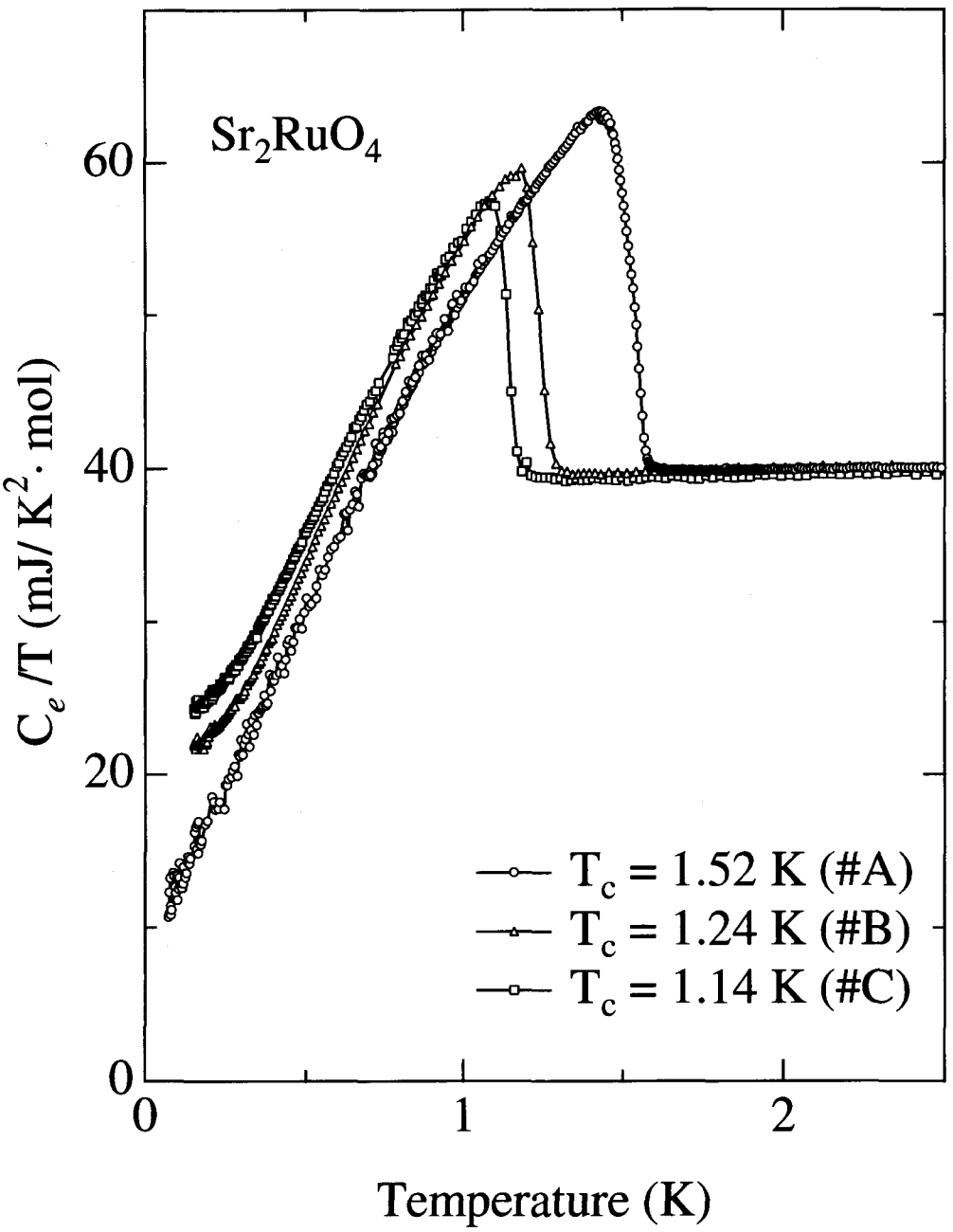


**Fig. 4.5.1** Temperature dependence of the electronic specific heat $C_e$ in the form of $C_e/T$ for three samples in $Sr_2RuO_4$.

.e order smaller than that on the Fermi surface $\gamma$, about 1 K, as schematically shown in Fig. 4.5.2(a). The recent theory [85] and the corresponding observation of a square flux-line lattice [86] also suggest that superconductivity resides mainly on the Fermi surface $\gamma$. However, there is found no anomaly around 0.1 K in the specific heat, which is expected from the $p$-wave theory with different gap sizes.

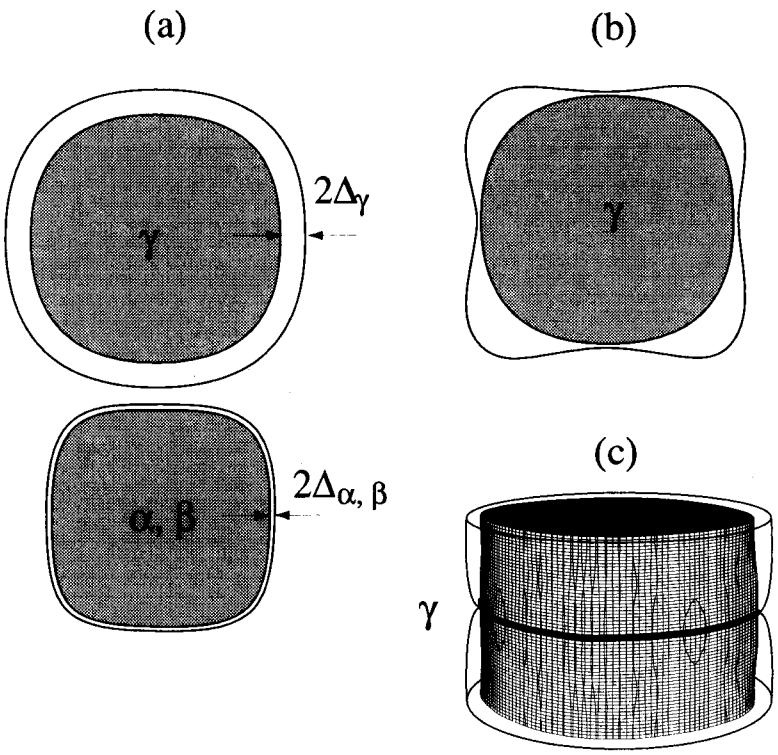


**Fig. 4.5.2** (a) Superconducting energy gaps for the Fermi surfaces $\alpha$, $\beta$ and $\gamma$. (b) and (c) Anisotropic energy gapes for the Fermi surface $\gamma$ in $Sr_2RuO_4$.

Furthermore, the temperature dependence of $C_e$ shows the $T^2$ dependence at low temperatures and the exponential behavior near $T_c$. A relation of $C_e \sim T^2$ at low temperatures claims line nodes in the superconducting gap. In general, unconventional superconductors often have nodes in the gap. The Ru-NQR and NMR relaxation rate experiments also suggest that the gap vanishes on the line of the Fermi surface. [10] From this point, another theory was presented by Miyake and Narikiyo, proposing a polar like-gap for the main Fermi surface $\gamma$, [17] as shown Fig. 4.5.2(b). The present data might be consistent with this theory with a non-uniform gap. Furthermore, Hasegawa *et al.* also proposed another theory showing a gap with a line node at $k_z = 0$, as shown in Fig. 4.5.2(c).[106] This theory is also in principle consistent with the specific heat data.

Next, we obtained the thermodynamical critical field $H_c(T)$ from the well-known re-

lation:

$$\int_T^{T_c} dT \int_T^{T_c} \frac{C_e(T') - \gamma T'}{T'} dT' = \frac{H_c^2(T)}{8\pi} \tag{4.5.1}$$

Thus obtained $H_c$ is plotted in Fig. 4.5.3 as a function of the temperature for three samples. The temperature dependence of $H_c$ deviates from a simple relation of $H_c(0)(1-t^2)$, where $t = T/T_c$ and $H_c(0)$ at 0 K is estimated to be 0.23 kOe for the sample #A, 0.16 kOe for the sample #B and 0.14 kOe for the sample #C. A deviation of the data from the parabolic behavior is represented as follows:

$$D(t) = H_c(t)/H_c(0) - (1 - t^2). \tag{4.5.2}$$

The deviation plot is given in Fig. 4.5.4. A deviation from the parabolic behavior is similar to a weak-coupling BCS curve for the sample #B and #C. On the other hand, the absolute magnitude of the sample #A is larger than the BCS curve. This is most likely related to the fact that a value of $\Delta C/\gamma T_c$ is smaller than a BCS value.

Figures 4.5.5, 4.5.6 and 4.5.7 show the temperature dependence of the electronic specific heat in the form of $C_e/T$ under several magnetic fields for the field along [100], [110] and [001], respectively. The $T_c$-value decreases with increasing the field. There is highly anisotropic behavior in the upper critical field $H_{c2}$ between the field along parallel and perpendicular to the quasi-two dimensional plane, reflecting to the quasi-two dimensional electronic state. In-plane anisotropy was also observed as shown in Figs. 4.5.5 and 4.5.6, which are the same as the results of the AC susceptibility[82].

Figure 4.5.8 shows the field dependence of $C/T$ at 0.25 K and 0.5 K for the sample #A. At 0.25 K, the $C_e/T$ with a residual value of about 18 mJ/K$^2$·mol indicates a $\sqrt{H}$-like increase at low fields, increases rather linearly with increasing the field and reaches the $\gamma$-value at the normal state. On the other hand, $C_e/T$ at 0.5 K increases linearly with increasing the field but increase steeply near the $H_{c2}$.

We carried out the similar specific heat experiments for the other samples named #B and #C. Figure 4.5.9 shows the field dependence of $C_e/T$ at several temperatures for the sample #B. $C_e/T$ with a residual value of 26 mJ/K$^2$·mol at 0.3 K indicates a $\sqrt{H}$-like increase at low fields, increases rather linearly with increasing the field and reaches the $\gamma$-value at the normal state. With increasing temperature, $C_e/T$ increases more linearly, which is the same as the case of sample #A. We also show in Fig. 4.5.10 the temperature dependence of the electronic specific heat of the sample #C in the form of $C_e/T$ under several magnetic fields for the field along [100].

From these data shown in Figs. 4.5.5, 4.5.6 and 4.5.7, we can obtain the temperature dependence of the upper critical field $H_{c2}$ for three typical crystalline directions of the tetragonal structure, as shown in Fig. 4.5.11. Open circles, triangles and squares indicate $H_{c2}$ for the field along [100], [110] and [001], respectively. The data at 0.25 K were obtained from the field dependence of the specific heat measurements. The solid lines

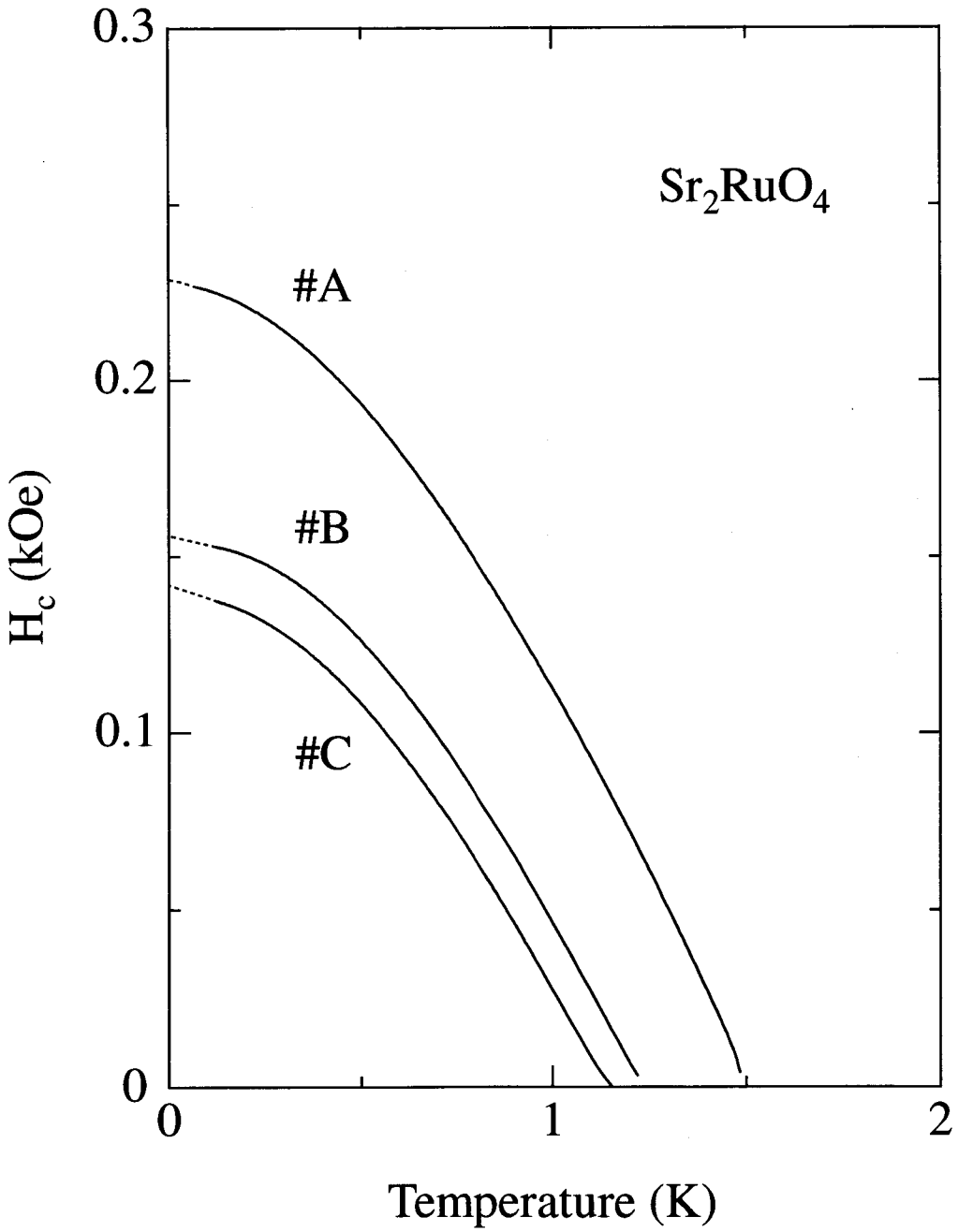


**Fig. 4.5.3** Temperature dependence of the thermodynamical critical field $H_c$ for three samples in $Sr_2RuO_4$.

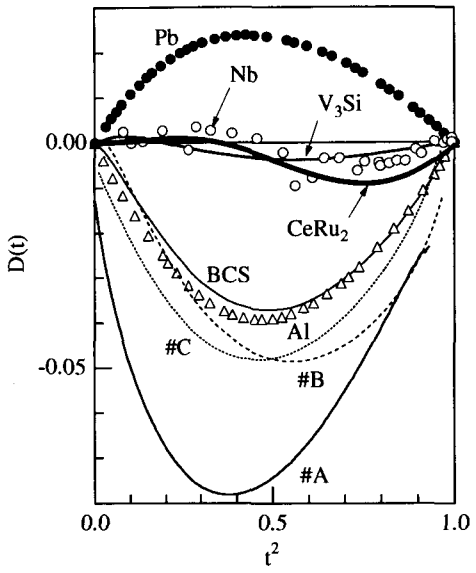


**Fig. 4.5.4** Temperature dependence of $D(t)$ for $Sr_2RuO_4$ and other materials.

in the Fig. 4.5.11 are guide for eyes. $H_{c2}$ for the field along [001] are enlarged in scale, as shown in Fig. 4.5.12. Anisotropic behavior between H//[100] and H//[110] can be observed in the whole temperature range below $T_c$. This is different from the result of the AC susceptibility measurements.[82] $H_{c2}(0)$ is estimated as 15.7 kOe for [110], 14.2 kOe for [100] and 0.83 kOe for [001], respectively.

Using the Ginzbug-Landau formula for an anisotropic three-dimensional superconductor, we can estimate the coherence length. The used formulas are as follows:

$$H_{c2//c} = \Phi_0/(2\pi\xi_{ab}^2), \tag{4.5.3}$$

$$H_{c2//ab} = \Phi_0/(2\pi\xi_{ab}\xi_c), \tag{4.5.4}$$

where $\Phi_0$ is the flux quantum. We assume that no anisotropy of the effective mass appears along the field direction between [100] and [110]. We define $H_{c2//ab}(0)$ as an average between $H_{c2//[110]}(0)$=15.7 kOe and $H_{c2//[100]}(0)$=14.2 kOe, namely 15.0 kOe. The obtained coherence lengths are $\xi_{ab}(0) = 630$Å and $\xi_c(0) = 35$Å. The superconducting anisotropy ratio is $\xi_{ab}(0)/\xi_c(0) = 19$ for the present sample with $T_c = 1.52$ K. These values are almost same as the results reported by Akima *et al.*[69]

The anisotropic GL parameter $\kappa_{GL}(0)$ are evaluate from $H_{c2}(0) = \sqrt{2}\kappa_{GL}(0)H_c(0)$ to $\kappa_{GL}(0) = 44$ for H//[100], $\kappa_{GL}(0) = 48$ for H//[110] and $\kappa_{GL}(0) = 2.6$ for H//[001]. The lower critical fields are also estimated using $H_{c1}(0)H_{c2}(0) = H_c^2(0)(\ln\kappa + 0.08)$ for $\kappa \gg 1$ and $H_{c1}(0)H_{c2}(0) \approx H_c^2(0)$ for $\kappa \approx 1$. Thus obtained $H_{c1}(0)$ is 0.014 kOe for H//[100], 0.013 kOe for H//[110] and 0.064 kOe for H//[001]. We summarize in Table 4.5-I the obtained parameters of the superconducting property.

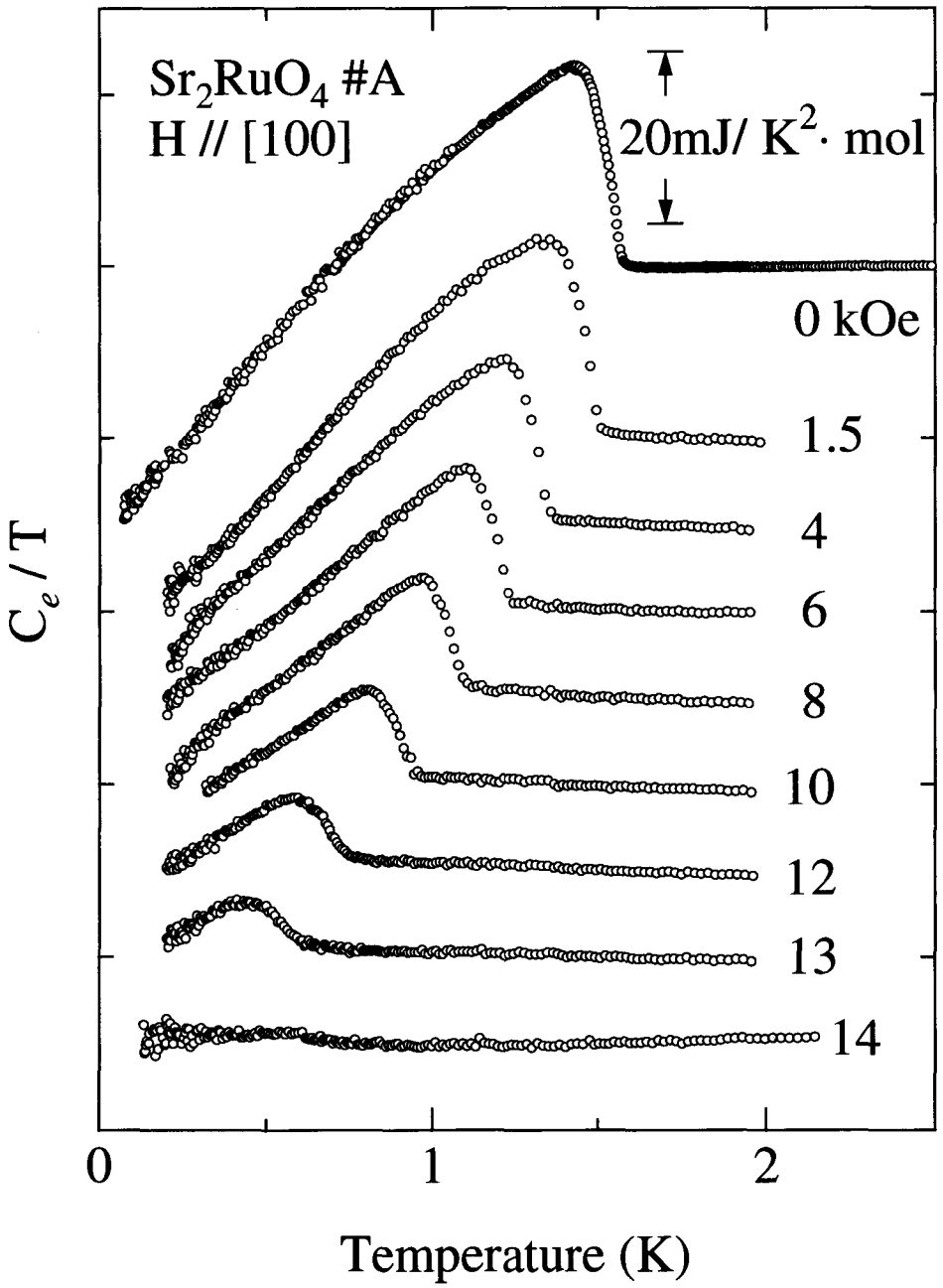


**Fig. 4.5.5** Temperature dependence of the specific heat $C_e$ in the form of $C_e/T$ under several fields for the field along [100] in $Sr_2RuO_4$.

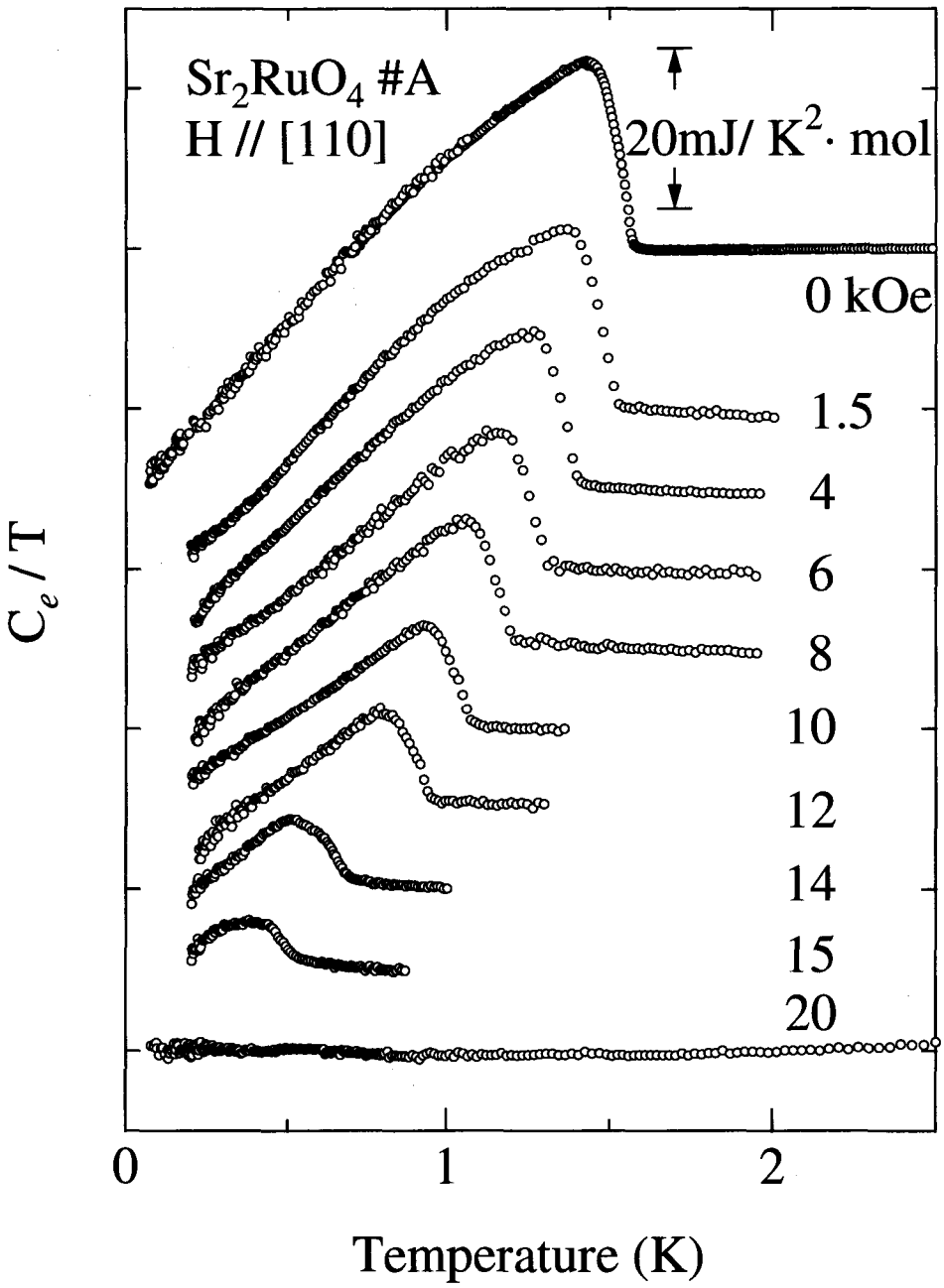


**Fig. 4.5.6** Temperature dependence of the specific heat $C_e$ in the form of $C_e/T$ under several fields for the field along [110] in $Sr_2RuO_4$.

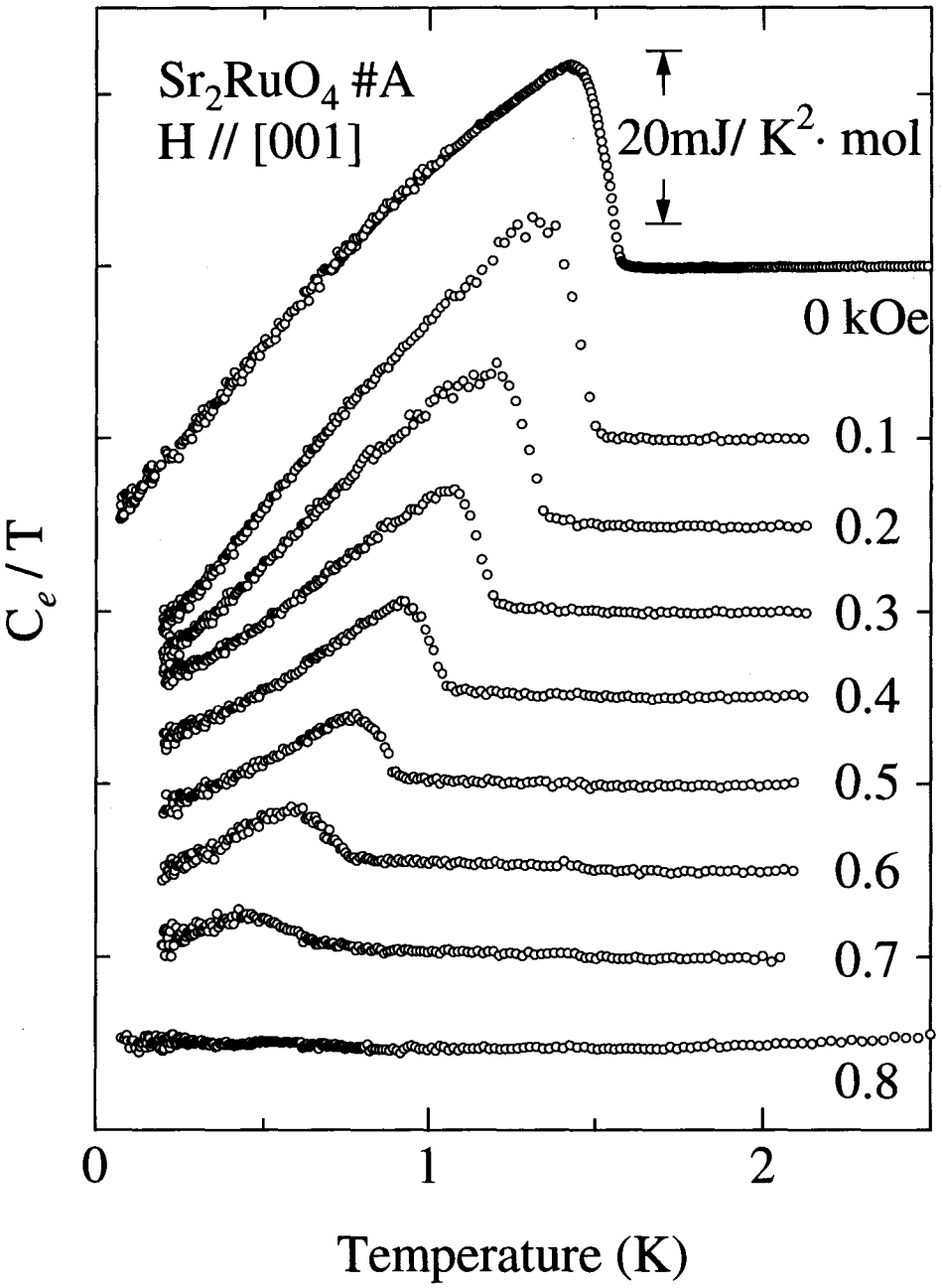


**Fig. 4.5.7** Temperature dependence of the specific heat $C_e$ in the form of $C_e/T$ under several fields for the field along [001] in $Sr_2RuO_4$.

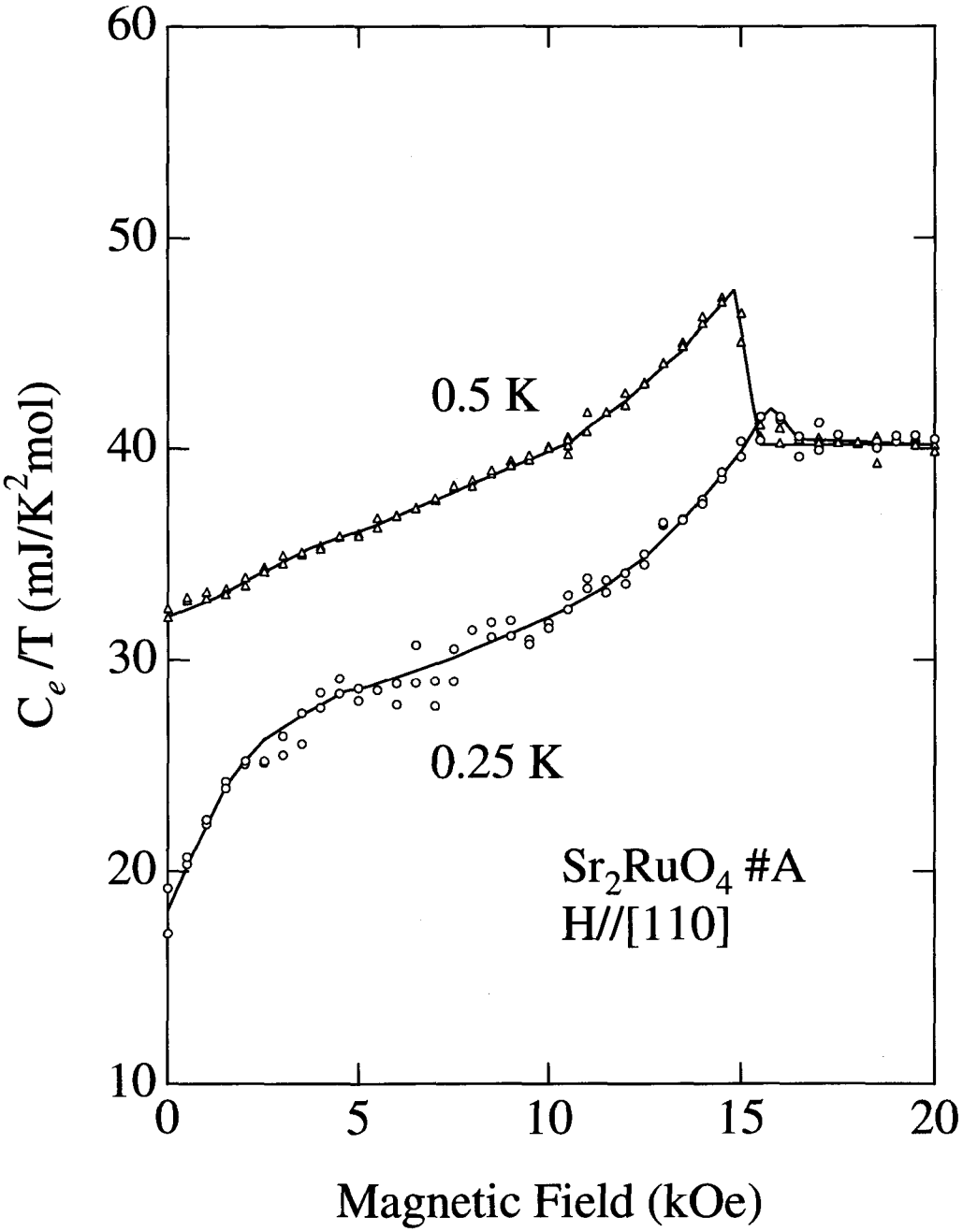


**Fig. 4.5.8** Field dependence of the specific heat $C_e$ in the form of $C_e/T$ under several constant temperatures in $Sr_2RuO_4$.

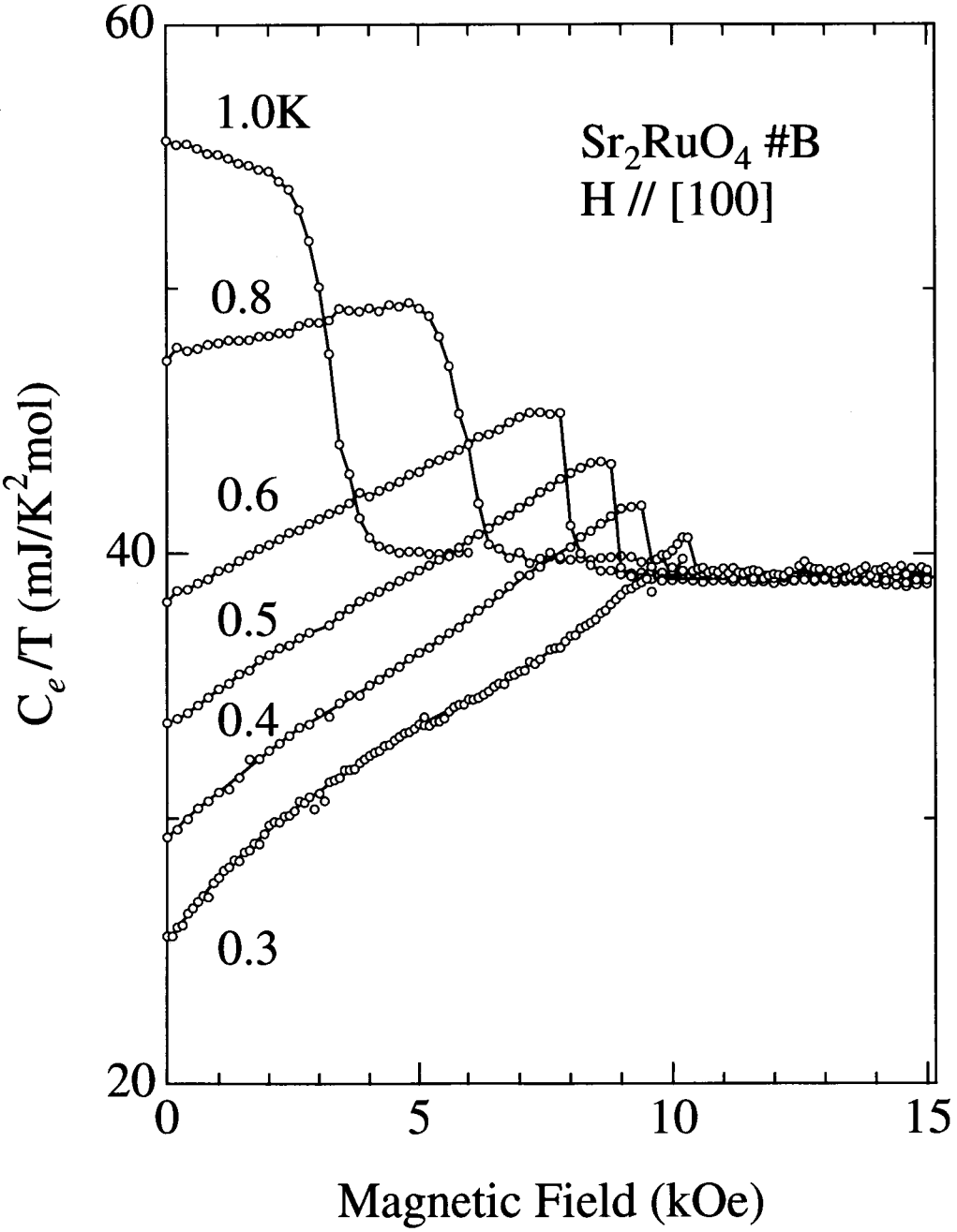


**Fig. 4.5.9** Field dependence of the specific heat $C_e$ in the form of $C_e/T$ under several constant temperatures for the sample #B in $Sr_2RuO_4$.

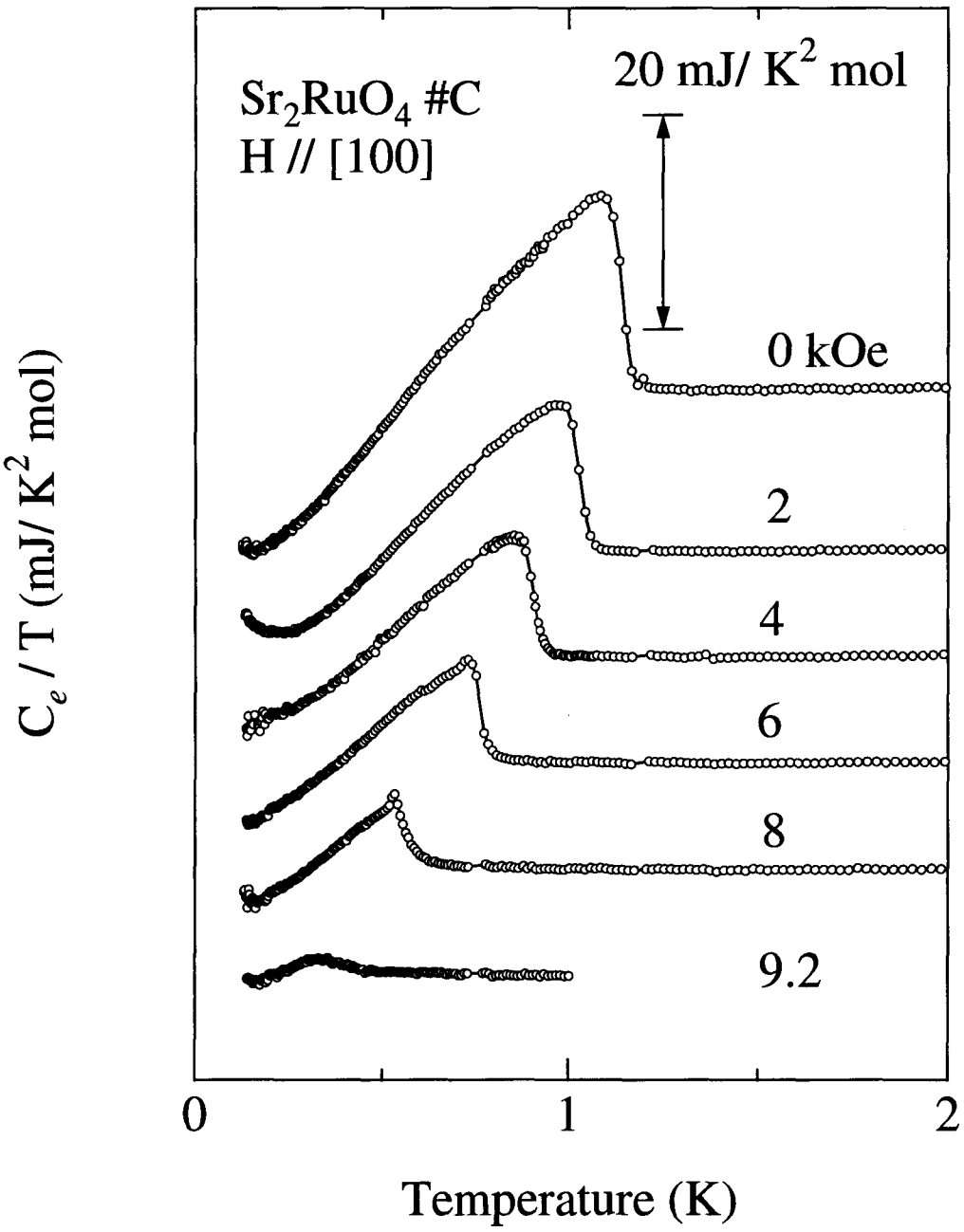


**Fig. 4.5.10** Temperature dependence of the specific heat $C_e$ in the form of $C_e/T$ under several fields for the field along [100] with the sample #C in $Sr_2RuO_4$.

**Table 4.5-I** Obtained parameters of the superconducting property in $Sr_2RuO_4$.

| | | H//[100] | [110] | [001] |
|---|---|---|---|---|
| $T_c$ (K) | 1.52 | | | |
| $H_c(0)$ (kOe) | 0.23 | | | |
| $H_{c2}(0)$ (kOe) | | 14.2 | 15.7 | 0.83 |
| $H_{c1}(0)$ (kOe) | | 0.014 | 0.013 | 0.064 |
| $\kappa_{GL}(0)$ | | 44 | 48 | 2.6 |
| $\xi_{GL}(0)$ (Å) | | 630 | | 35 |
| $l$ (Å) | | | | 2050 for $\alpha$ |
| | | | | 1700 for $\gamma$ |

We also obtain the temperature dependence of $H_{c2}$ of three different samples for the field along [100], as shown in Fig. 4.5.13. The solid lines in the Fig. 4.5.13 are also guide for eyes. $H_{c2}(0)$ is roughly estimated as 14.2 kOe for the sample #A with $T_c$ = 1.52 K, 12 kOe for the sample #B with $T_c$ = 1.24 K and 11 kOe for the sample #C with $T_c$ = 1.14 K. $H_{c2}(0)$ increases with increasing the sample quality.

From the data on the slope of $H_{c2}$ against the temperature at $T = T_H$, $(dH_{c2}/dT)_{T_H}$ in Fig. 4.5.11 and the jump of the specific heat $\Delta C$ at $H = T_H$ in Figs. 4.5.5, 4.5.6 and 4.5.7, we can obtain the Maki parameter $\kappa_2$ by using the following relation:

$$\left(\frac{\Delta C}{T}\right)_{T_H} = \frac{1}{4\pi\beta_A\left(2\kappa_2^2 - 1\right)}\left(\frac{dH_{c2}}{dT}\right)^2_{T_H}, \tag{4.5.5}$$

where $\beta_A$ is about 1. The temperature dependence of $\kappa_2$ is shown in Fig 4.5.14 for the sample #A. Open triangles, circles and squares are corresponding to the field direction. The $\kappa_2$-value is highly anisotropic for the field direction. The anisotropy between the in-plane and inter-plane is mainly due to the two-dimensional electronic states. The in-plane anisotropy between [100] and [110] is also related to the electronic states.

For the field along [100] and [110], the $\kappa_2$-value decreases with decreasing the temperature. Generally speaking, this indicates the existence of the paramagnetic effect. Namely, it is a typical feature in the presence of the paramagnetic effect where the pair breaking by the Zeeman energy becomes important at low temperatures. On the other hand, the $\kappa_2$-value increases slightly with decreasing the temperature for the field along [001], which is shown in Fig. 4.5.15. This is actually the characteristic feature which is predicted for a clean superconductor in the absence of the paramagnetic effect, although the data do not diverge as $\sqrt{\ln(T_c/T)}$ at low temperatures. This means that it is difficult to determine definitely whether the sample is in the clean limit or not.[57] The $\xi_{ab}$ and $\xi_c$ values, however, are 630 and 33 Å, while the mean free path is $\ell$=1700-2050Å, which was obtained from dHvA effect.This fact indicates that the present sample is close to the clean limit.

The anisotropic paramagnetic effect itself is not unusual. For instance, in $ErRh_4B_4$

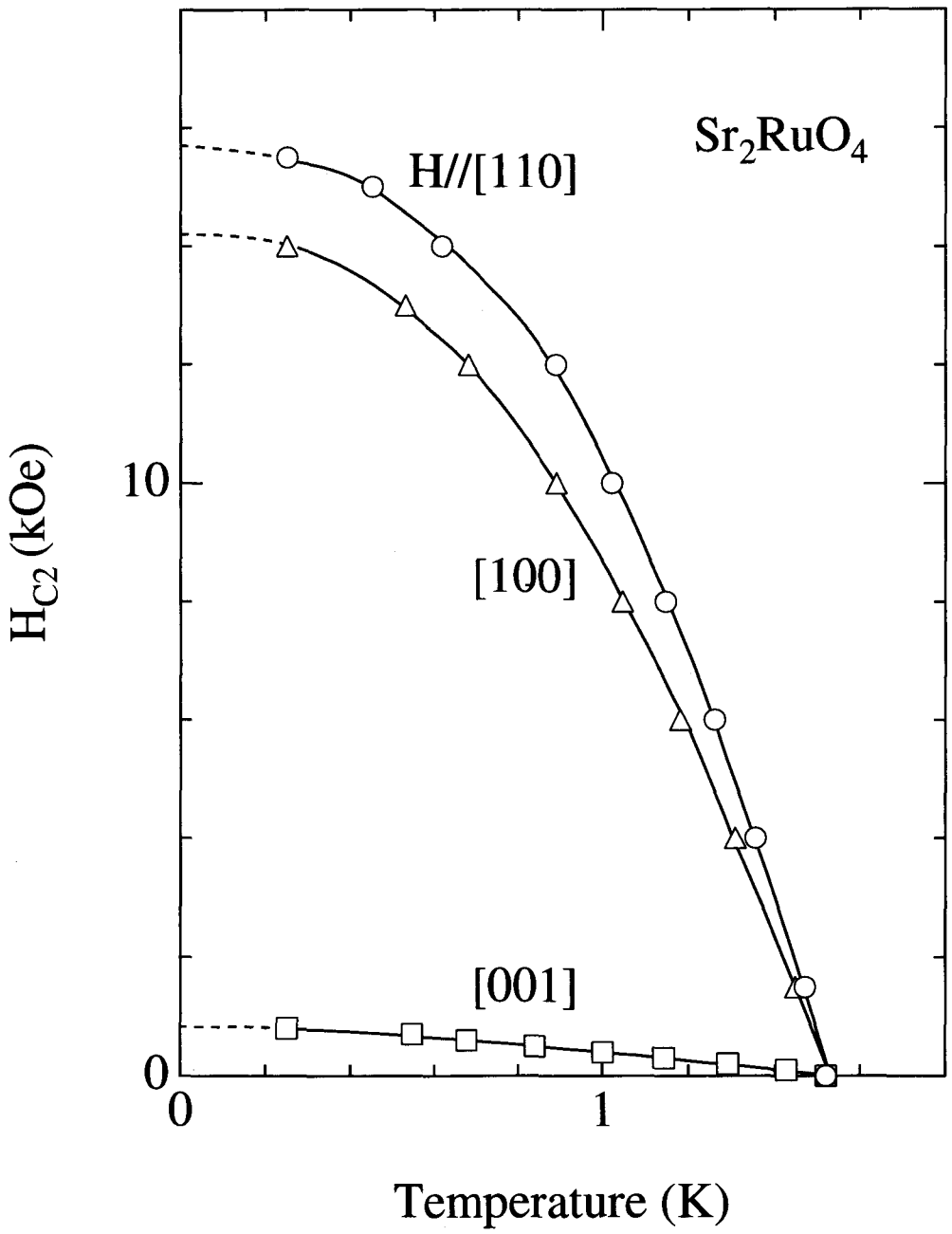


**Fig. 4.5.11** Temperature dependence of the upper critical field $H_{c2}$ in $Sr_2RuO_4$.

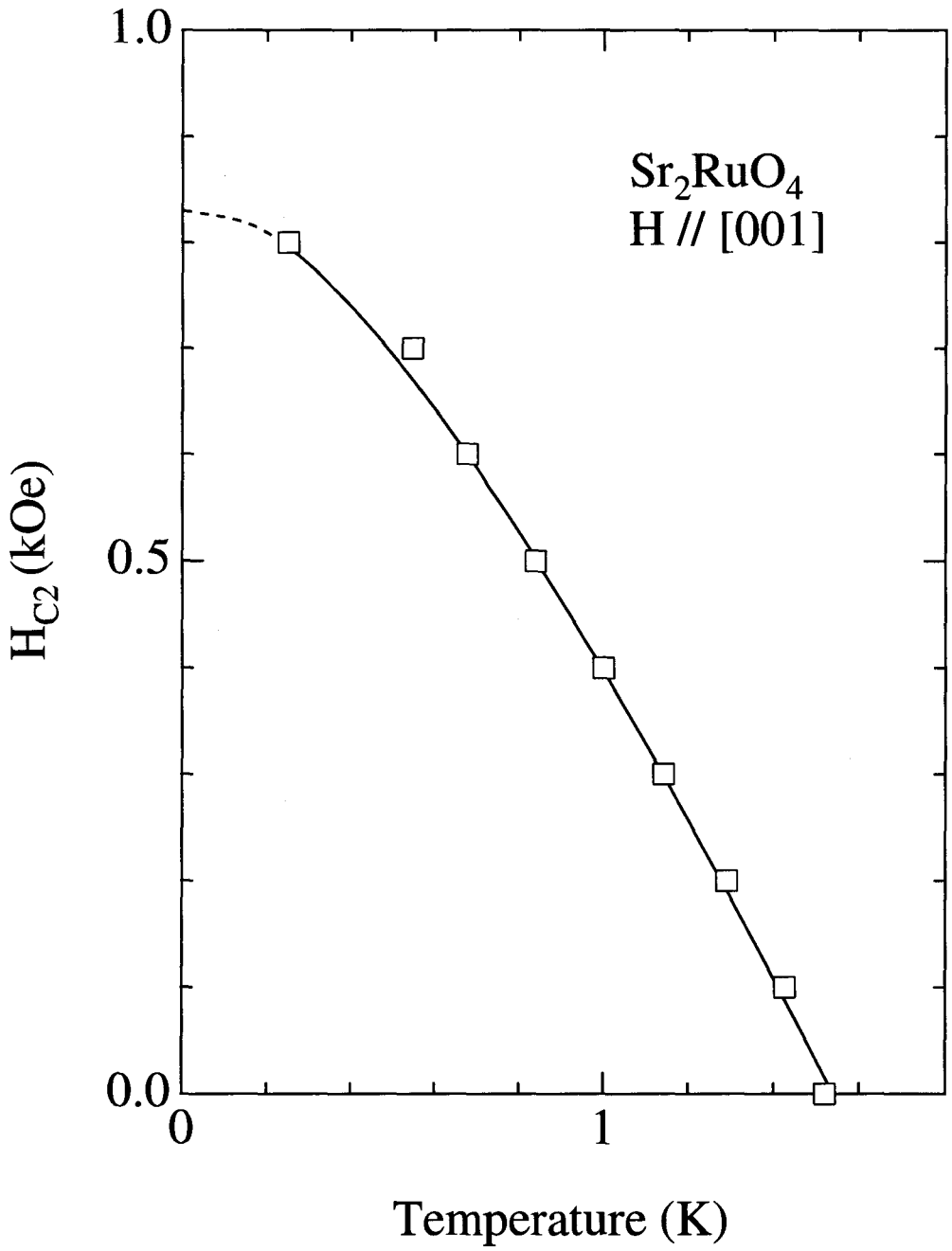


**Fig. 4.5.12** Temperature dependence of the upper critical field $H_{c2}$ for the field along [001] in $Sr_2RuO_4$.

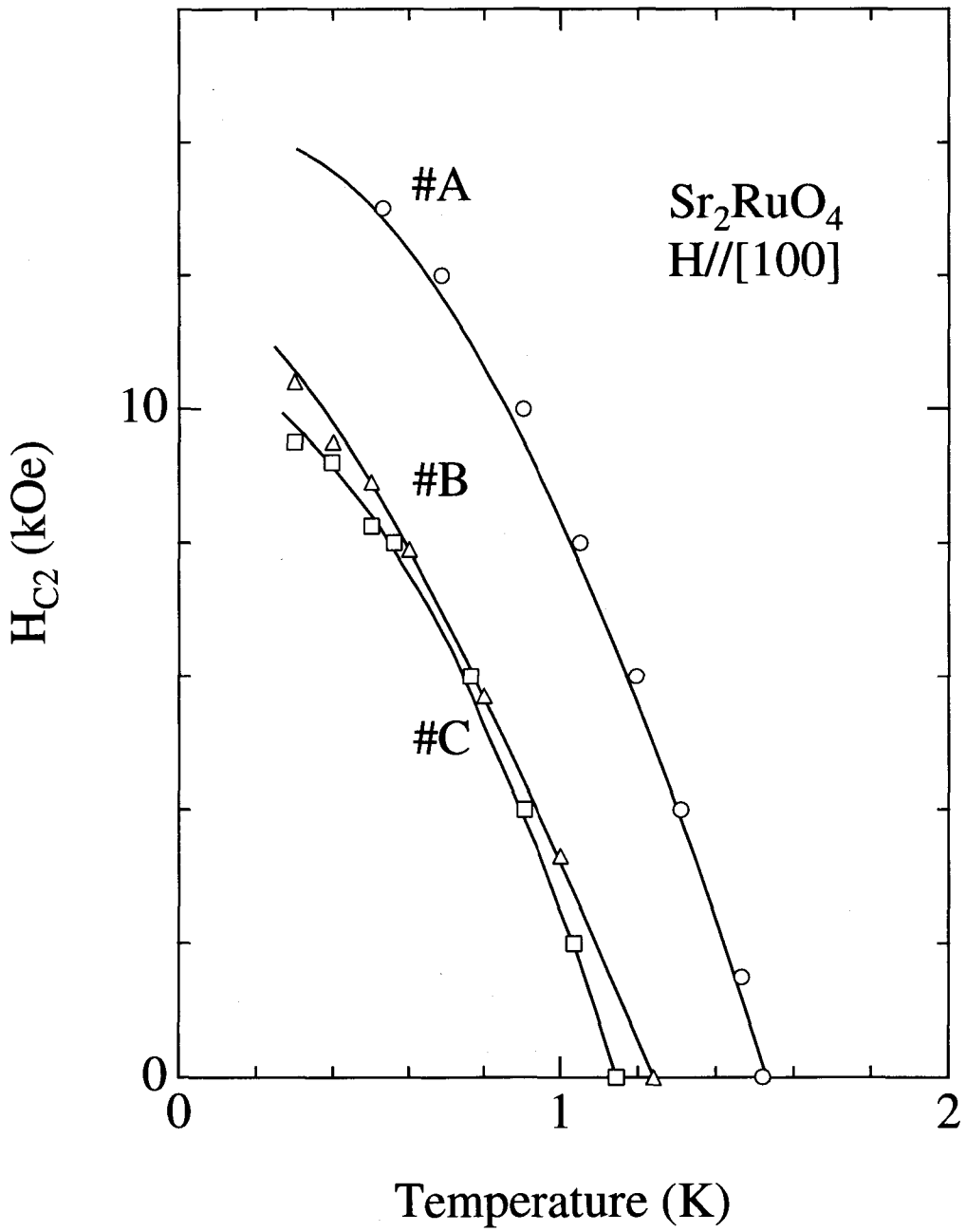


**Fig. 4.5.13** Temperature dependence of the upper critical field $H_{c2}$ for three samples for the field along [100] in $Sr_2RuO_4$.

where ferromagnetic interactions between Er ions compete with superconductivity of conduction electrons, a strong paramagnetic effect is observed in the magnetization for the spin-easy axis ($H//a$), while the effect is weak for the hard axis ($H//c$).[107] $UPt_3$ is also another example. When the field is directed along the [11$\bar{2}$0] direction in the hexagonal structure of $UPt_3$, the $\kappa_2$ value increases with decreasing temperature as a function of $\sqrt{\ln(T_c/T)}$. This means no existence of the paramagnetic effect. On the other hand, it decreases slightly with the decreasing the temperature for the field along [0001], indicating the existence of the paramagnetic effect. We note that $UPt_3$ is now clarified to be the odd-parity ($p$- or $f$-wave) superconductor. In general, a large $\kappa$ value and high magnetic fields often cause the paramagnetic effect. In this case, the absence of the paramagnetic effect for H//[001] of $Sr_2RuO_4$ is mainly due to a small magnetic field and to a small $\kappa$ value. On the other hand, a high $\kappa$ value might cause the paramagnetic effect for H//[100] and H//[110].

In addition to this, $\kappa_2$ for the sample #C is obtained in the same way. The $\kappa_2$-value of the sample #C is about 60 and is almost constant against the temperature.

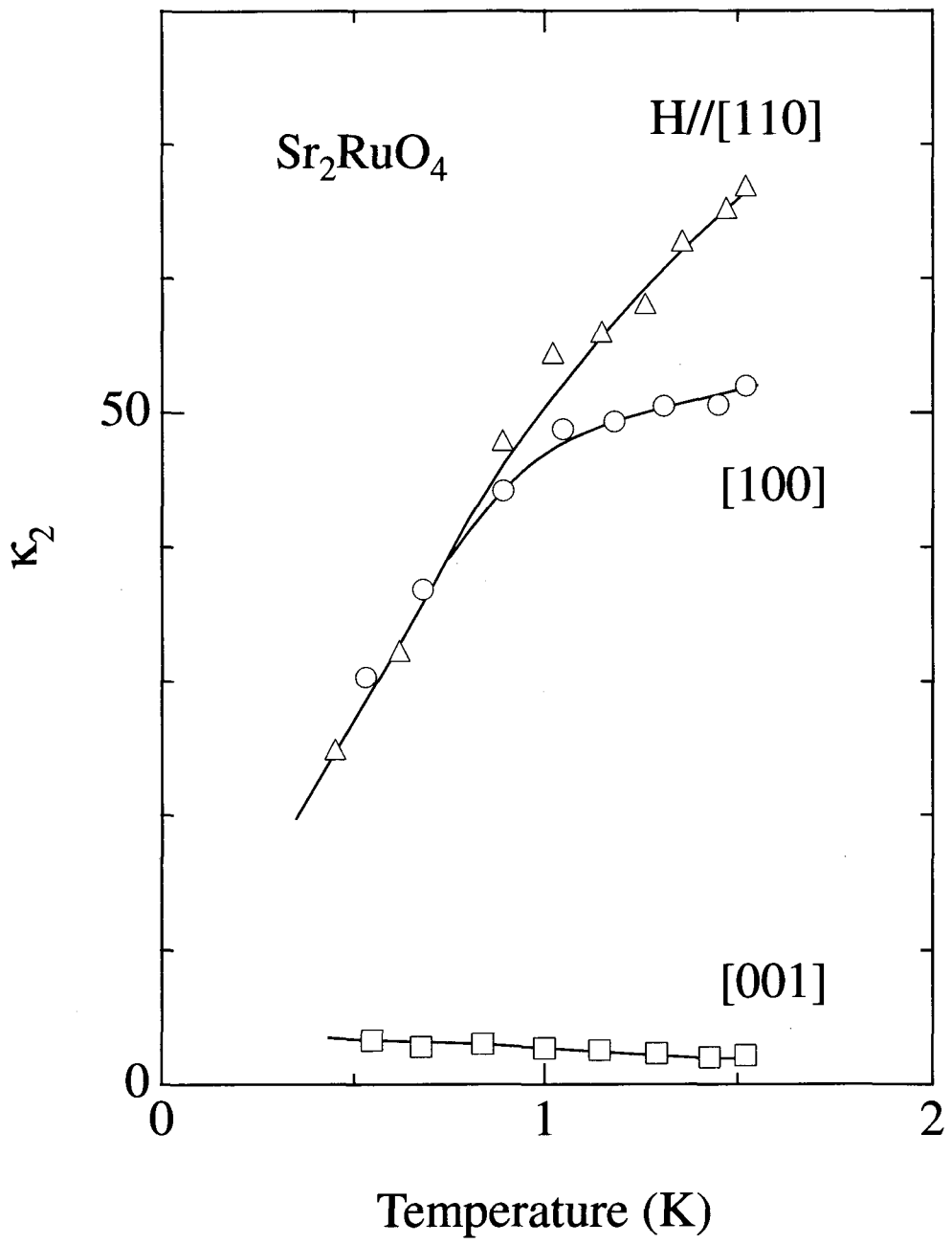


**Fig. 4.5.14** Temperature dependence of the Maki parameters $\kappa_2$ for the sample #A in $Sr_2RuO_4$.

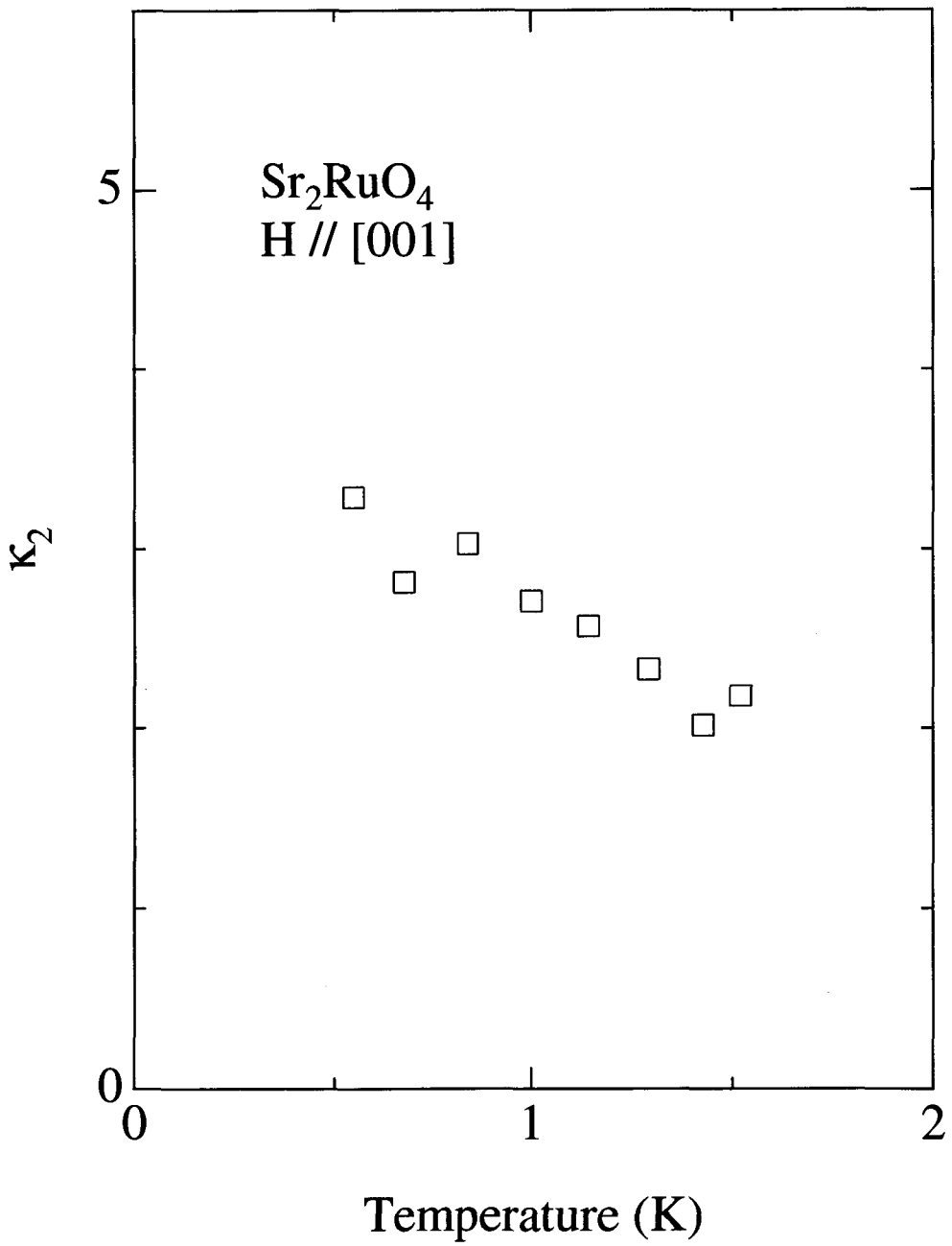


**Fig. 4.5.15** Temperature dependence of the Maki parameters $\kappa_2$ for the field along [001] with the sample #A of $Sr_2RuO_4$.

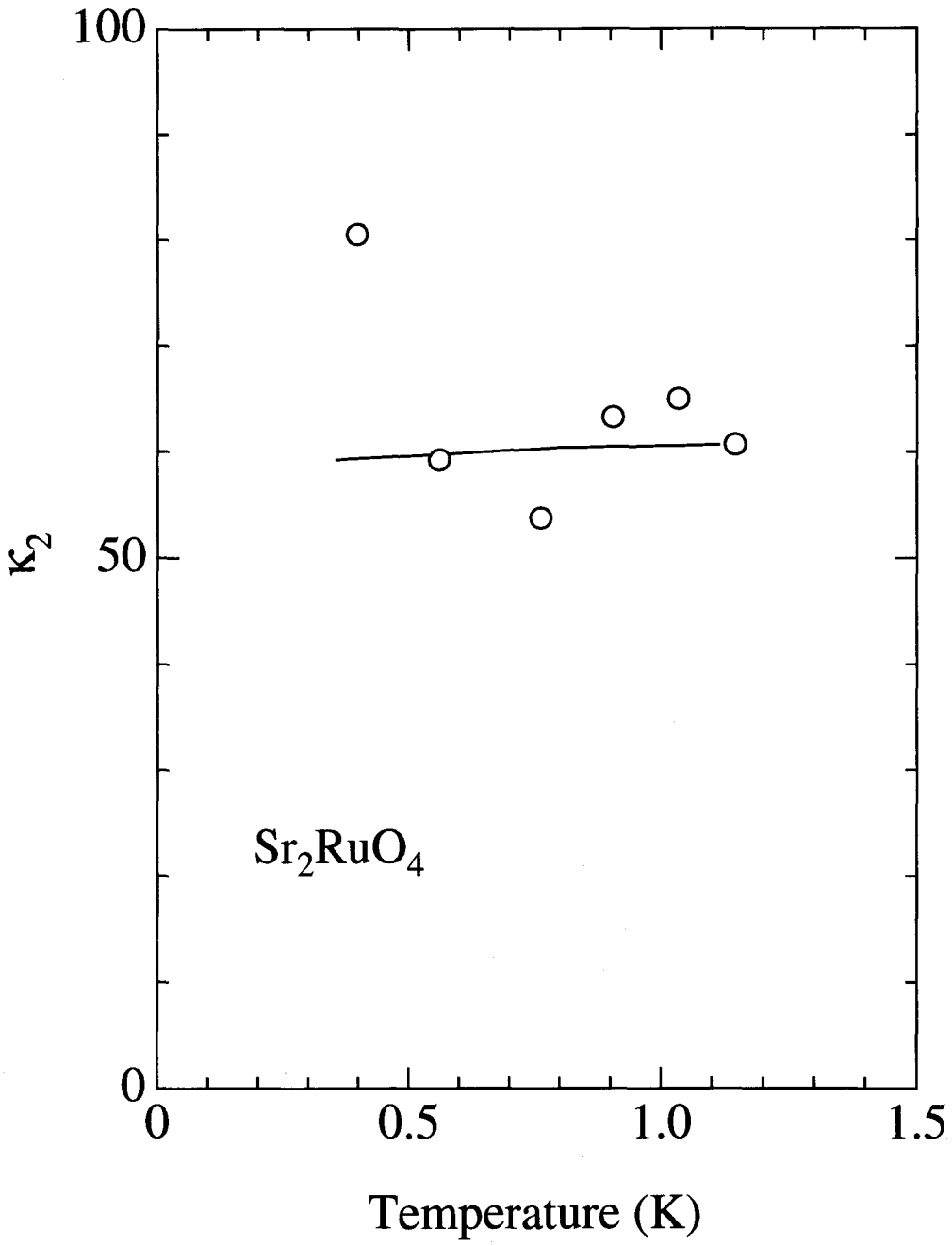


**Fig. 4.5.16** Temperature dependence of the Maki parameters $\kappa_2$ for the sample #C in $Sr_2RuO_4$.

# *Chapter 5* Conclusion

We succeeded in growing high-quality single crystals of $Sr_2RuO_4$ and carried out the dHvA, magnetoresistance and specific heat experiments. Experimental results are summarized as follows:

1) High quality single crystals of $Sr_2RuO_4$ with $T_c$=1.52 K were grown by using a floating-zone technique.

2) The Yamaji effect is observed as the oscillatory angular dependence of the magnetoresistance. A sharp peak found at [110] occurs when the carriers move along the field direction. This is closely related to the corrugated curvature of the cylindrical Fermi surface $\alpha$.

3) In the dHvA experiments, we determined precisely the angular dependence of the dHvA amplitude for three cylindrical Fermi surfaces $\alpha$, $\beta$ and $\gamma$. We considered the Yamaji effect to clarify the angular dependence of dHvA amplitude. The first Yamaji angle is determined to be 30.6° for the dHvA branch $\alpha$, about 30° for the branch $\beta$ and 15.3° for the branch $\gamma$. A striking effect of the chemical potential oscillation (CPO) is found in the wide range of field direction. The cyclotron masses $m^*_{\beta\pm\alpha}$ and $m^*_{\gamma\pm\alpha}$ are highly different from $m^*_\beta + m^*_\alpha$ and $m^*_\gamma + m^*_\alpha$, respectively. On the other hand, the CPO effect is negligibly small for higher harmonics of the branch $\alpha$, although it is slightly found at a Yamaji angle $\theta = 30.6°$ for the 3rd harmonic. We determined the cyclotron mass: $3.3\,m_0$ for the branch $\alpha$, $6.9\,m_0$ for the branch $\beta$ and $17\,m_0$ for the branch $\gamma$ for the field along [001]. From these values, we can estimate the electronic specific heat coefficient of $40\,\mathrm{mJ/K^2{\cdot}mol}$, which is in good agreement with $39.8\,\mathrm{mJ/K^2{\cdot}mol}$, determined from the specific heat experiments.

4) We measured the specific heat in the temperature range from 70 mK to 2 K in magnetic fields, ranging from 0 to 20 kOe for three samples with $T_c$=1.52 K, 1.24 K and 1.14 K. A residual electronic specific heat coefficient $\gamma_{res}$ of the sample with $T_c$=1.52 K decreases with increasing $T_c$. The $\gamma_{res}$-value, estimated at 0 K, is 8 $\mathrm{mJ/K^2{\cdot}mol}$. The temperature dependence of the $C_e$ shows the $T^2$ dependence at low temperatures and the exponential behavior near $T_c$. A characteristic power law dependence of $C_e \sim T^2$ at low temperatures claims line nodes in the superconducting gap. We determined the upper critical field $H_{c2}$ for the field along [100], [100] and [001] from the specific heat in fields. $H_{c2}$ is highly anisotropic between H//[100]([110]) and [001], reflecting the quasi-two dimensional electronic states. The Maki parameter $\kappa_2$ is also anisotropic. For the field along [100] and [110], the $\kappa_2$-value decreases with decreasing the temperature, indicating the existence of the

paramagnetic effect. On the other hand, the $\kappa_2$-value increases slightly with decreasing the temperature for the field along [001]. This corresponds to no existence of the paramagnetic effect for [001].

## Acknowledgements

This work was performed in collaboration with many researchers. That was a very wonderful and fortunate experience for me.

I would like to express sincere thanks to Prof. Yoshichika Ōnuki for valuable and pertinent advices and great encouragements throughout my study.

Special thanks are also devoted to Prof. Rikio Settai for stimulating and technical advices. I am fortunate to collaborate with him who showed a wonderful technique and accomplishment of the experimental program.

I wish to express great thanks to Prof. Kiyohiro Sugiyama and Dr. Yoshihiko Inada for stimulating and technical advices.

I am deeply indebted to Prof. Humihiko Takei for growing samples and helpful discussion. My special thanks are also expressed to Mr. Mikito Mamiya for his kind technical advices and discussion.

I will express special thanks to Prof. Hisatomo Harima for helpful discussion, showing me the results of the band calculation. My special thanks are also expressed to Dr. Kiyoshi Betsuyaku for drawing very beautiful illustrations of the Fermi surface.

Specific heat experiments were performed at Graduate School of Arts and Sciences, University of Tokyo. I would like to express special thanks to Prof. Nobuo Wada for their many advices, stimulating discussion and encouragements. My special thanks are also expressed to Mr. Junji Kiuchi and Mr. Yasuhisa Miyamoto for their assistance.

Specific heat experiments were also performed at Faculty of Science, Tokyo Metropolitan University. For these investigations, I would like to express special thanks to Prof. Hideyuki Sato, Dr. Yuji Aoki and Dr. Hitoshi Sugawara for their many advices, stimulating discussion and encouragements. My special thanks are also expressed to Mr. Tatsuma D. Matsuda for his helpful assistance.

I would like to thank Prof. Naoki Toyota and Dr. Hiroshi Matsui for ultrasonic measurements.

I would like to express special thanks to Prof. Yoshiteru Maeno for his helpful comments.

Thanks are also expressed to Dr. Noriaki Kimura and Dr. Masato Hedo for their kind technical advices, discussion and encouragements. I wish to thank Mr. Atsushi Mukai for his helpful assistance, and enjoyed working and discussing with him. Acknowledgements are also expressed to Mr. Hitoshi Ohkuni, Mr. Dai Aoki, Mr. Shingo Araki for their interesting discussion.

This work was partially supported by the Japan Society for the Promotion of Science in frames of the *Research Fellowship for Young Scientists.*

Finally, I wish also to express great thanks to my family and friends.

## References


1) S. Adenwalla, S. W. Lin, Z. Zhao, Q. Z. Ran, J. B. Ketterson, J. H. Sauls, L. Taillefer, D. G. Hinks, M. Levy and B. K. Sarme: Phys. Rev. Lett. **65** (1990) 2298.

2) H. Tou, Y. Kitaoka, K. Asayama, N. Kimura, Y. Ōnuki, E. Yamamoto and K. Maezawa: Phys. Rev. Lett. **77** (1996) 1374.

3) K. Tenya, M. Ikeda, T. Tayama, T. Sakakibara, E. Yamamoto, K. Maezawa, N. Kimura, R. Settai and Y. Ōnuki: Phys. Rev. Lett. **77** (1996) 3193.

4) Y. Maeno, H. Hashimoto, K. Yoshida, S. Nishizaki, T. Fujita, J. G. Bednorz and F. Lichtenberg: Nature **372** (1994) 532.

5) A. P. Mackenzie, S. R. Jullian, A. J. Diver, G. J. McMullan, M. P. Ray, G. G. Lonzarich, Y. Maeno, S. Nishizaki and T. Fujita: Phys. Rev. Lett. **76** (1996) 3786.

6) T. Oguchi: Phys. Rev. B **51** (1995) 1385.

7) I. Hase and Y. Nishihara: J. Phys. Soc. Jpn. **65** (1996) 3957.

8) E. Ohmichi, Y. Maeno and T. Ishiguro: J. Phys. Soc. Jpn. **68** (1999) 24.

9) M. Nakano: J. Phys. Soc. Jpn.**68** (1999) 1801.

10) K. Ishida, Y. Kitaoka, K. Asayama, S. Ikeda, S. Nishizaki, Y. Maeno, K. Yoshida and T. Fujita: Phys. Rev. B **56** (1997) 505.

11) Y. Maeno, S. Nishizaki, K. Yoshida, S. Ikeda and T. Fujita: J. Low. Temp. Phys.**105** (1996) 1577.

12) S. Nishizaki, Y. Maeno, S. Farner, S. Ikeda and T. Fujita: J. Phys. Soc. Jpn. **67** (1998) 560.

13) G.M. Luke, Y. Fudamoto, K.M. Kojima, M.I. Larkin, J. Merrin, B. Nachumi, Y.J. Uemura, Y. Maeno, Z.Q. Mao, Y. Mori, H. Nakamura and M. Sigrist: Nature **394** (1998) 558.

14) K. Ishida, H. Mukuda, Y. Kitaoka, K. Asayama, Z.Q. Mao, Y. Mori and Y. Maeno: Nature **396** (1998) 658.

15) T.M. Rice and M. Sigrist: J. Phys. Condens. Matter **7** (1995) L643.

16) D.F. Agterberg, T.M. Rice and M. Sigrist: Phys. Rev. Lett. **78** (1997) 3374.

17) K. Miyake and O. Narikiyo: Phys. Rev. Lett.**83** (1999) 1423.

18) T. Ishiguro, K. Yamaji, G. Saito in *Organic Superconductors* (Spinger Press, Germmany, 1998)

19) K. Kajita, Y. Nishio, T. Takahashi, W. Sasaki, R. Kato, H. Kobayashi, A. Kobayashi and Y. Iye: Solid State Commun. **70** (1989) 1189.

20) K. Yamaji: J. Phys. Soc. Jpn. **58** (1989) 1520.

21) M. Nakano: J. Phys. Soc. Jpn. **66** (1997) 19.

22) F. A. Meyer, E. Steep, W. Biberacher, P. Christ, A. Lerf, A. G. Jansen, W. Joss, P. Wyder and K. Andres: Europhys. Lett. **32** (1995) 681.

23) K. Kishigi, M. Nakano, K. Machida and Y. Hori: J. Phys. Soc. Jpn. **64** (1995) 3034.

24) L. M. Falicov and H. Stachowiak: Phys. Rev. **147** (1966) 505.

25) A. B. Pippard: Proc. R. Soc. London A **270** (1962) 1.

26) R. W. Stark and L. M. Falicov: Prog. Low Temp. Phys. **5** (1967) 235.

27) R. W. Stark and C. B. Friedberg: J. Low Temp. Phys. **14** (1974) 111.

28) D. Shoenberg: *Mangnetic oscillations in Metals* (Cambridge University Press, Cambridge, 1984).

29) N. Kimura: Doctral Thesis Osaka Univ. (1997)

30) Y. Ōnuki, A. Hasegawa, in *Handbook on the Physics and Chemistry of Rare Earths* Vol. 20, eds. K. A. Gschneidner Jr., L. Eyring (North-Holland, Amsterdam, 1995) p. 1

31) Y. Ōnuki, K. Ueda, T. Komatsubara, in *Slected Papers in Physics IV: Heavy Electron System* (1994) *in Japanese*

32) D. D. Koelling, B. D. Dunlap, G. W. Crabtree, Phys. Rev **B 31** (1985) 1966.

33) K. H. J. Buschow, H. J. van Daal, F. E. Maranzana, P. B. van Aken, Phys. Rev**3** (1971) 1662.

34) R. D. Parks, in *Valence Instabilities and Related Narrow-Band* (Plenum Press, New York, 1977)

35) L. M. Falicov, W. Hanke, M. B. maple, in *Valence Fluctuations in Solids* (North-Holland, Amsterdam, 1981)

36) A. Sumiyama, Y. Oda, H. nagano, Y. Ōnuki, K. Shibutani, T. Komatsubara, J. Phys. Soc. Jpn. **55** (1986) 1294.

37) K. Yamada, K. Yosida, K. Hanzawa, Prog. Theor. Phys. **71** (1984) 450.

38) K. Yamada, K. Yosida, Prog. Theor. Phys. **76** (1986) 621.

39) K. A. Gschneidner Jr., S. K. Dhar, R. J. Stierman, T. W. E. Tsang, O. D. McMasters, J. Mag. Mag. Mat. **47&48** (1985) 51.

40) A. de Visser, A. Menovsky, J. J. M. Franse, Physica B **147** (1987) 81.

41) G. R. Stewart, Rev. Mod. Phys. **56** (1984) 755.

42) P. A. Lee, T. M. Rice, J. W. Serene, L. J. Sham, J. W. Wilkins, Comments on Condensed Matter Phys. **12** (1986) 99.

43) K. Kadowaki, S. B. Woods, Solid State Commun. **58** (1986) 507.

44) M. R. Norman, D. D. Koelling, in *Handbook on the Physics and Chemistry of Rare Earths* Vol. 17, eds K. A. Gschneidner Jr., L. Eyring, G. H. Lander, G. R. Choppin (North-Holland, Amsterdam, 1993) p. 1

45) Y. Ōnuki, T. Goto, T. Kasuya, in *Materials Science and Technology* Vol. 3A, ed. K. H. Buschow (VCH Weinheim, 1992) ch. 7, p. 545.

46) B. B. Goodman: Phys. Lett.**1** (1962) 215.

47) B. Serin: Phys. Lett.**16** (1965) 112.

48) F. Steglich and J. Aarts and C. D. Bredl and W. Lieke and D. Meschede and W. Franz and H. Schafer: Phys. Rev. Lett. **43** (1979) 1892.

49) R. Balian and N. R. Werthame: Phys. Rev.**131** (1963) 1553.

50) P. W. Anderson and W. F. Brinkman: eds. by K. H. Benneman and J. B. Koterson (John Wiley & Sons, New York),p. 177.

51) M. Sigrist and K. Ueda: Rev. Mod. Phys **63** (1991) 239.

52) M. Hedo: Doctral Thesis Osaka Univ. (1998)

53) K. Matsuda and Y. Kohori and T. Kohara: J. Phys. Soc. Jpn. **64** (1995) 2750.

54) K. Ishida and H. Mukuda and Y. Kitaoka and K. Asayama and Y. Onuki: Z. Naturforsch.**51a** (1996) 793.

55) A. D. Huxley and C. Paulsen and O. Laborde and J. L. Tholence and D. Sanchez and A. Junod and R. Calemczuk: J. Phys. :Condens. Matter **5** (1993) 3825.

56) M. Hedo, Y. Inada, E. Yamamoto, Y, Haga, Y. Ōnuki, Y. Aoki, T.D. Matsuda, H. Sato and S. Takahashi: J. Phys. Soc. Jpn. **67** (1998) 272.

57) G. Eilenberger: Phys. Rev.**153** (1967) 584.

58) M. Hedo, Y. Inada, K. Sakurai, E. Yamamoto, Y. Haga, Y. Ōnuki, S. Takahashi, M. Higuchi, T. Maehira and A. Hasegawa: Philo. Mag. B **77** (1997) 975.

59) Y. Kohori, H. Shibai, T. Kohara, Y. Oda, Y. Kitaoka, K. Asayama: J. Mag. Mag. Mat. **76&77** (1988) 478.

60) H. Tou, Y. Kitaoka, K. Asayama, N. Kimura, Y. Ōnuki, E. Yamamoto, K. Maezawa, Phys. Rev. Lett. **77** (1996) 1374.

61) T. Sakakibara, K. Tenya, M. Ikeda, T. Tayama, H. Amitsuka, E. Yamamoto, K. Maezawa, N. Kimura, R. Settai, Y. Ōnuki, J. Phys. Soc. Jpn. **65** (1996) suppl. B 202.

62) K. Tenya, M. Ikeda, T. Tayama, H. Mitamura, H. Amitsuka, T. Sakakibara, K. Maezawa, N. Kimura, R. Settai, Y. Ōnuki J. Phys. Soc. Jpn. **64** (1995) 1063.

63) H.Tou, Y. Kitaoka, K. Asayama, N. Kimura, Y. Ōnuki, E. Yamamoto, K. Maezawa, Int. Conf. of Low Temperature Physics (Prague 1996); Czech. J. Phys. **46** (1996) Suppl. S2 779.

64) Y. Kohori, K. Matsuda and T. Kohara: Solid State Commun. **95** (1995) 121.

65) H.Tou, Y. Kitaoka, K. Asayama, C. Geibel, C. Schank and F. Steglich: J. Phys. Soc. Jpn. **64** (1995) 725.

66) Y. Haga, E. Yamamoto, Y. Inada, D. Aoki, K. Tenya, M. Ikeda, T. Sakakibara and Y. Ōnuki: J. Phys. Soc. Jpn. **65** (1996) 3646.

67) N. Metoki, Y. Haga, Y. Koike and Y. Ōnuki: Phys. Rev. Lett. **80** (1998) 5417.

68) N. Metoki, Y. Haga, Y. Koike, N. Aso and Y. Ōnuki: J. Phys. Soc. Jpn. **66** (1997) 2560.

69) T. Akima, S. Nishizaki and Y. Maeno: J. Phys. Soc. Jpn. **68** (1999) 694.

70) M. Barden, A. H. Moudden, S. Nishizaki, Y. Maeno and T. Fujita: Phisica C **273** (1997) 248.

71) Y. Maeno, K. Yoshida, H. Hashimoto, S. Nishizaki, S. Ikeda, M. Nohara, T. Fujita, A. P. Mackenzie, N. E. Hussey, J. G. Bednorz and F. Lichtenberg: J. Phys. Soc. Jpn. **66** (1997) 1405.

72) A. P. Mackenzie, S. Ikeda, Y. Maeno, T. Fujita, S. R. Jullian and G. G. Lonzarich: J. Phys. Soc. Jpn. **67** (1998) 385.

73) N. Shirakawa, K. Murata, Y. Nishimura, S. Nishizaki, Y. Maeno, T. Fujita, J. G. Bednorz, F. Lichtenberg and N. Hamada: J. Phys. Soc. Jpn. **64** (1995) 1072.

74) A. P. Mackenzie, N. E. Hussey, A. J. Diver, S. R. Jullian, Y. Maeno, S. Nishizaki and T. Fujita: Phys. Rev. B **54** (1996) 7425.

75) T. Yokota, A. Chainami, T. Takahashi, H. Katayama-Yoshida, M. Kasai and Y. Tokura: Phys. Rev. Lett. **76** (1996) 3009.

76) T. Yokota, A. Chainami, T. Takahashi, H. Ding, J. C. Campzano, H. Katayama-Yoshida, M. Kasai and Y. Tokura: Phys. Rev. B **54** (1996) 13311.

77) D. H. Lu, M. Schmit, T. R. Cummins, S. Schuppler, F. Lichtenberg and J. G. Bednorz: Phys. Rev. Lett. **76** (1996) 4845.

78) Y. Maeno, S. NishiZaki and Z. Q. Mao: J. *Superconductivity* **12** (1999) 535.

79) A. P. Mackenzie, R. K. W. Haselwimmer, A. W. Tyler, G. G. Lonzarich, Y. Mori, S. Nishizaki and Y. Maeno: Phys. Rev. Lett. **80** (1998) 161.

80) H. Mukuda: Doctral Thesis Osaka Univ. (1999)

81) S. NishiZaki, Y. Maeno and Z. Q. Mao: to be published in J. Phys. Soc. Jpn.

82) Z. Q. Mao, Y. Maeno, S. NishiZaki, T. Akima and T. Ishiguro: to be published in Phys. Rev. Lett.

83) K. Machida, M. Ozaki and T. Ohmi: J. Phys. Soc. Jpn. **65** (1996) 3720.

84) M. Sigrist and M. E. Zhitomirsky: J. Phys. Soc. Jpn. **65** (1996) 3452.

85) D.F. Agterberg: Phys. Rev. Lett. **80** (1998) 5184.

86) T.M. Riseman, P.G. Kealey, E.M. Forgan, A.P. Machenzie, L.M. Galvin, A.W. Tyler, S.L. Lee, C. Ager, D. McK. Paul, C.M. Aegerter, R. Cubitt, Z.Q. Mao, T. Akima and Y. Maeno: Nature **396** (1998) 242.

87) Y. Yoshida, R. Settai, Y. Ōnuki, H. Takei, K. Betsuyaku and H. Harima: J. Phys. Soc. Jpn. **67** (1998) 1677.

88) K. Betsuyaku: Doctral Thesis Osaka Univ. (1999)

89) V. L. Moruzzi, J. F. Janak and A. R. Williams : Calculated Electronic Properties of Metals (Pergamon Press Inc. , 1978)

90) F. Lichtenberg, A. Catana, J. Mannhart and D. G. Schom: Appl. Phys. Lett **60** (1992) 1138.

91) E. Ohmichi,H. Adachi, Y. Mori, Y. Maeno, T. Ishiguro and : Phys. Rev. B **59** (1999) 7263.

92) Y. Yoshida, A. Mukai, R. Settai, K. Miyake, Y. Inada, Y. Ōnuki, K. Betsuyaku, H. Harima, T. D. Matsuda, Y. Aoki and H. Sato: J. Phys. Soc. Jpn. **68** (1999) 3041.

93) K. Kishigi, Y. Hasegawa and M .Miyazaki: submitted to J. Phys. Soc. Jpn.

94) H. Matsui, M. Yamaguchi, Y. Yoshida, A. Mukai, R. Settai, Y. Ōnuki, H. Takei and N. Toyota: J. Phys. Soc. Jpn. **67** (1998) 3687.

95) T. Goto, A. Sawada and S. Sakatsume: Jpn. J. Appl. Phys. Series **8** (1993) 140.

96) T. Vogt and D. J. Buttrey: Phys. Rev. B **52** (1995) R9843.

97) J. S. Gardner, G. Balakrishnan, D. McK. Paul and C. Haworth: Physica C **265** (1996) 251.

98) L. R. Testardi: Phys. Rev. B **3** (1971) 95.

99) A. J. Mills and K. M. Rabe: Phys. Rev. B **38** (1988) 8908.

100) R. C. Morris, R. V. Coleman and R. Bhandari: Phys. Rev. B **5** (1972) 895.

101) N. Toyota, H. Nakatsuji, K. Noto, A. Hoshi, N. Kobayashi, Y. Muto and Y. Onodera: J. Low Tmp. Phys. **25** (1976) 485.

102) K. Yoshida, Y. Maeno, S. Nishizaki and T. Fujita: J. Phys. Soc. Jpn. **65** (1996) 2220.

103) T. P. Orlando, E. J. McNiff, S. Foner and M. R. Beasley: Phys. Rev. B **19** (1979) 4545.

104) M. Kataoka and T. Goto: Phisica B **219 & 220** (1996) 92.

105) H. Matsui, M. Yamaguchi, S. Endo, T. Inuzuka, H. Uozaki and N. Toyota: J. Phys. Soc. Jpn. **67** (1998) 2586.

106) Y. Hasegawa, K. Machida and M. Ozaki: submitted to J. Phys. Soc. Jpn.

107) G. W. Crabtree, F. Behroozi, S. A. Cambell and D. G. Hinks: Phys. Rev. **147** (1966) 295.

## List of Publications.

1. Metamagnetic transition in $PrCu_2$ studied by the de Haas-van Alphen effect
   R. Settai, M. Abliz, P. Ahmet, H. Azuma, D. Aoki, Y. Yoshida, K. Sugiyama and Y. Ōnuki:
   *Physica B* **216** (1996) 326.

2. Metamagnetic magnetization in $DyCu_2$
   K. Sugiyama, Y. Yoshida, D. Aoki, R. Settai, T. Takeuchi, K. Kindo and Y. Ōnuki:
   *Physica B* **230-232** (1997) 748.

3. Neutron Scattering Study of the Magnetic Structure of $DyCu_2$
   Y. Koike, N. Metoki, Y. Morii, Y. Yoshida, R. Settai and Y. Ōnuki
   *J. Phys. Soc. Jpn.* **66** (1997) 4053.

4. Magnetic structure of $CeCu_{6-x}Au_x$
   H. Okumura, K. Kakurai, Y. Yoshida, Y. Ōnuki and Y. Endoh:
   *J. Magn, Magn. Mater* **177-181** (1998) 405.

5. Metamagnetism based on the quadrupolar interaction in $RCu_2$
   K. Sugiyama, Y. Yoshida, A. Koyanagi, R. Settai, T. Takeuchi, K. Kindo and Y. Ōnuki:
   *J. Magn, Magn. Mater* **177-181** (1998) 361.

6. Metamagnetic transition based on the Quadrupole Moment in $DyCu_2$
   Y. Yoshida, K. Sugiyama, T. Takeuchi, Y. Kimura, D. Aoki, M. Kouzaki, R. Settai, K. Kindo and Y. Ōnuki:
   *J. Phys. Soc. Jpn.* **67** (1998) 1421.

7. Fermi Surface and Yamaji Effect in $Sr_2RuO_4$
   Y. Yoshida, R. Settai, Y. Ōnuki, H. Takei, K. Betsuyaku and H. Harima:
   *J. Phys. Soc. Jpn.* **67** (1998) 1677.

8. Magnetic and Electrical Properties of $GdCu_2$
   A. Koyanagi, Y. Yoshida, Y. Kimura, R. Settai, K. Sugiyama and Y. Ōnuki:
   *J. Phys. Soc. Jpn.* **67** (1998) 2510.

9. Oscillatory Angular Dependence of the Magnetoresistance in $Sr_2RuO_4$
   Y. Yoshida, A. Mukai, R. Settai, Y. Ōnuki and H. Takei:
   *J. Phys. Soc. Jpn.* **67** (1998) 2551.

10. De Haas-van Alphen Effect and Energy Band Structure in $UB_2$
    E. Yamamoto, Y. Haga, T. Honma, Y. Inada, D. Aoki, M. Hedo, Y. Yoshida, H. Yamagami and Y. Ōnuki:
    *J. Phys. Soc. Jpn.* **67** (1998) 3171.

11. High-Field Magnetization and Metamagnetic Transition in $TbCu_2$ and $HoCu_2$ Single Crystals
K. Sugiyama, M. Nakashima, Y. Yoshida, Y. Kimura, K. Kindo, T. Takeuchi, R. Settai and Y. Ōnuki:
*J. Phys. Soc. Jpn.* **67** (1998) 3244.

12. Elastic Anomalies and Acoustic de Haas-van Alphen Effects in $Sr_2RuO_4$
H. Matsui, M. Yamaguchi, Y. Yoshida, A. Mukai, R. Settai, Y. Ōnuki, H. Takei and N. Toyota:
*J. Phys. Soc. Jpn.* **67** (1998) 3687.

13. Metamagnetic transitions based on the quadrupole moment in $RCu_2$ single crystals
K. Sugiyama, M. Nakashima, Y. Yoshida, R. Settai, T. Takeuchi, K. Kindo and Y. Ōnuki:
*Physica B* **259-261** (1999) 896.

14. Fermi surface of $UB_2$ studied by the de Haas-van Alphen oscillation
E. Yamamoto, T. Honma, Y. Haga, Y. Inada, D. Aoki, M. Hedo, Y. Yoshida, H. Yamagami and Y. Ōnuki:
*Physica B* **259-261** (1999) 1085.

15. Field-Induced Ferropuadrupolar Ordering in $RCu_2$
R. Settai, K. Sugiyama, S. Araki, Y. Yoshida, P. Ahmet, M. Abliz, K. Kindo and Y. Ōnuki:
*Jpn. J. Appl. Phys. Series* **11** (1999) 194.

16. Fermi Surface Properties in $Sr_2RuO_4$
Y. Yoshida, A. Mukai, R. Settai, K. Miyake, Y. Inada, Y. Ōnuki, K. Betsuyaku, H. Harima, T. D. Matsuda, Y. Aoki and H. Sato:
*J. Phys. Soc. Jpn.* **68** (1999) 3041.

17. Fermi surface and superconducting properties in $Sr_2RuO_4$
Y. Yoshida, A. Mukai, K. Miyake, N. Watanabe, R. Settai, Y. Ōnuki, T. D. Matsuda, Y. Aoki, H. Sato, Y. Miyamoto and N. Wada:
printed in *Physica B.*